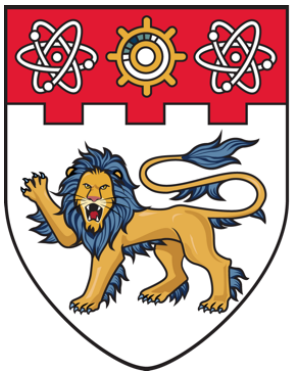

NANYANG TECHNOLOGICAL UNIVERSITY
SINGAPORE

RELATIVE BIOLOGICAL EFFECTIVENESS AND DOSE-AVERAGED LINEAR ENERGY TRANSFER STUDIES FOR PROTON THERAPY MONTE CARLO TREATMENT PLANNING

KOH WEI YANG, CALVIN

SCHOOL OF PHYSICAL AND MATHEMATICAL SCIENCES

2021

RELATIVE BIOLOGICAL EFFECTIVENESS AND DOSE-AVERAGED LINEAR ENERGY TRANSFER STUDIES FOR PROTON THERAPY MONTE CARLO TREATMENT PLANNING

KOH WEI YANG, CALVIN

SCHOOL OF PHYSICAL AND MATHEMATICAL SCIENCES

A thesis submitted to the Nanyang Technological University in partial fulfilment of the requirement for the degree of Doctor of Philosophy

2021

Statement of Originality

I hereby certify that the work embodied in this thesis is the result of original research done by me except where otherwise stated in this thesis. The thesis work has not been submitted for a degree or professional qualification to any other university or institution. I declare that this thesis is written by myself and is free of plagiarism and of sufficient grammatical clarity to be examined. I confirm that the investigations were conducted in accord with the ethics policies and integrity standards of Nanyang Technological University and that the research data are presented honestly and without prejudice.

18 Jan 2022

Date

Koh Wei Yang, Calvin

Supervisor Declaration Statement

I have reviewed the content and presentation style of this thesis and declare it of sufficient grammatical clarity to be examined. To the best of my knowledge, the thesis is free of plagiarism and the research and writing are those of the candidate's except as acknowledged in the Author Attribution Statement. I confirm that the investigations were conducted in accord with the ethics policies and integrity standards of Nanyang Technological University and that the research data are presented honestly and without prejudice.

20 Jan 2022

. . . . . .

Date

. . . . . .

Assoc. Prof. James Lee Cheow Lei

20 Jan 2022

. . . . . .

Date

. . . . . .

Prof. Lew Wen Siang

Authorship Attribution Statement

This thesis contains material from 3 paper(s) published in the following peer-reviewed journal(s) / from papers accepted at conferences in which I am listed as an author.

Chapter 3 is published as Hong Qi Tan, Wei Yang Calvin Koh , Lloyd Kuan Rui Tan, Jun Hao Phua, Khong Wei Ang, Sung Yong Park, Wen Siang Lew, James Cheow Lei Lee, Dependence of LET on Material and its Impact on Current RBE Model, Phys. Med. Biol.(2019). DOI: 10.1088/1361-6560/ab1c90.

The contributions of the co-authors are as follows:

- Dr Tan Hong Qi proposed the idea and designed the study
- I performed the literature review and simulation study
- Dr Tan Hong Qi, Lloyd Tan Kuan Rui, Phua Jun Hao and Ang Khong Wei and I discussed the results
- Prof. Park Sung Yong, Prof. Lew Wen Siang and Prof. James Cheow Lei Lee supervised the study.
- All authors contributed to the discussion and preparation of the manuscript

Chapter 4 is published as Wei Yang Calvin Koh[1], Hong Qi Tan[2], Khong Wei Ang[2], Sung Yong Park[2], Wen Siang Lew[1] and James Cheow Lei Lee[12], Standardizing Monte Carlo Simulation parameters for a reproducible Linear Energy Transfer, The British Journal of Radiology, 93(1112), 20200122.

The contributions of the co-authors are as follows:

- I proposed the idea and designed the study.
- I performed all the simulation and data analysis
- Dr Tan Hong Qi and I analyzed the data
- Prof. Park Sung Yong, Prof. Lew Wen Siang and Prof. James Cheow Lei Lee supervised the study.
- All authors contributed to the discussion and preparation of the manuscript

Chapter 5 is published as Wei Yang Calvin Koh, Hong Qi Tan, Yan Yee Ng, Yen Hwa Lin, Khong Wei Ang, Wen Siang Lew, James Cheow Lei Lee and Sung Yong Park, Quantifying systematic RBE-weighted dose uncertainty arising from multiple variable RBE models in organ-at-risk. *Advances in Radiation Oncology*, 100844. https://doi.org/10.1016/j.adro.2021.100844

The contributions of the co-authors are as follows:

- I proposed the idea and designed the study.
- I performed all the simulation and data analysis
- Ng Yan Yee performed the treatment planning
- Dr. Lin Yen Hwa Rachel performed the CT data clean up
- Dr Tan Hong Qi and I analyzed the data
- Prof. Park Sung Yong, Prof. Lew Wen Siang and Prof. James Cheow Lei Lee supervised the study.
- All authors contributed to the discussion and preparation of the manuscript

18 Jan 2022

Date

Koh Wei Yang, Calvin

Abstract

Proton Therapy shows dosimetric advantages over conventional X-Ray Therapy in terms of the control of doses to normal tissues. In fact, it should be the preferred treatment in most paediatrics and local recurrent cancer when available. This is due to the physical characteristics of proton interactions where they have a finite range as they traversed through a medium. This gives rise to a steep increase in dose distribution with a sharp fall-off known as the Bragg Peak. Despite the dosimetric advantage, physical and radiobiological uncertainties are a concern in Proton Therapy. In other words, it is not sufficient to know it stops, instead, it is important to know *where* it stops and the biological effects that follow.

This thesis aims to address the issue of radiobiological uncertainties with Relative Biological Effectiveness (RBE) for treatment planning which is defined as a scalar quantity Proton Therapy. Currently, a constant RBE of 1.1 is used clinically to include the differential biological effect of protons as compared to photons during treatment planning. However, the counter-argument against the use of a constant RBE of 1.1 stems from the possibility of under- or over-dosing in the target volume. As suggested by AAPM-TG-256[1], there is a need to understand the spatial variations of RBE within and outside the target volume. It is also recommended for the use of variable RBE models for certain clinical situations such as target volumes that are close to Organ-At-Risks (OARs). Numerous RBE models were developed to account for the uncertainties arising from dependent quantities of patient radio-sensitivity alpha-beta ratio $\left(\frac{\alpha}{\beta}\right)_x$, linear energy transfer (LET), cell lines used in experiments and experimental set-up.

The biological uncertainties are investigated via Monte Carlo (MC) Simulation through three projects using Linear Quadratic (LQ)-based RBE models, where the model is dependent on proton dose (D_p), dose-averaged LET (LET_D) and alpha-beta ratio $\left(\frac{\alpha}{\beta}\right)_x$ ratio. The first project

investigated the estimation of LET_D in these RBE model and the dosimetric impact of LET_D uncertainty on a clinical case. The second project investigated the MC simulation parameters for simulating LET_D and its mathematical functions when calculating LET_D. The final project investigated the systematic dose variation from different RBE models in the clinical case where OARs are located near the target.

The results from these studies showed the importance of calculating LET_D via MC simulation and how it can lead to an increase in biological uncertainties in Proton Therapy. The dosimetric impact of simulating LET_D when there is insufficient knowledge of cellular composition could lead to huge uncertainty during the simulation and this uncertainty could propagate down to the resulting RBE models. The results show that using cellular materials instead of water during LET_D MC simulation is important under low $\left(\frac{\alpha}{\beta}\right)_x$ and low dose $(2\ Gy)$ conditions. In addition, a standard protocol is proposed for sampling LET_D in MC simulation which is required as this would affect secondary electrons production and will improve the accuracy of the dose distribution and LET_D. Therefore, the MC simulation protocols and LET_D scoring method is defined and standardized to facilitate future cross-institutional studies. Lastly, based on the two previous projects, it was established that RBE values are bound to be associated with large uncertainties due to variations in biological experiments and LET_D calculations reported in the literature. It is thus challenging to *select* a single RBE model based on experimental data. Instead, in our last project, we focus our effort on arriving at an RBE model-agnostic approach treatment planning with Multi-Field Optimization (MFO) vs Single-Field Optimization (SFO) to minimize the systematic dose variation between different RBE models. In this study, brain tumor cases are used. MFO planning technique showed a better option for overlapping brain tumors with OARs in eliminating RBE-weighted dose uncertainties.

In conclusion, this thesis examined the uncertainties in RBE arising from different experimental set-up and LET_D calculations from different MC simulation parameters. The studies have concluded that RBE uncertainties are still challenging and the choice of MFO treatment planning technique may possibly yield an RBE-model agnostic dose distribution. Standadization for LET_D calculations are important for MC simulation. The knowledge gained from these studies will be beneficial for the future development of RBE-based treatment planning system for proton beam therapy using MC simulation.

Acknowledgements

I am grateful to my family, friends and colleagues for encouraging me in going down this route, persevering through this journey and finally publishing this work. It was not an easy journey but the training improved my soft skills and technical abilities tremendously and I am grateful for that. I have also come to realize that this is not solely about work and research, this journey also taught me about balance. Balancing between everything in life is what we all should be aiming for. I am glad for who I am now as a person.

I am thankful for my professors - Assoc. Prof. James Lee, Prof. Lew Wen Siang, Prof. Park Sung Yung and Khong Wei, whose guidance and academic support elevated this experience. In addition, to the colleagues in NCCS and NTU, I could have never asked for a better bunch of people.

To my mentor, Hong Qi, this would not have happened if not for his guidance in all aspects. He had been there during the toughest times of this journey and has continued to guide me through even in my career. I am very grateful for whatever he has done for me, taking his time out whenever I needed help.

Last but not least, to all my dear family and friends, my pillars of support, who had helped in whichever way you had, you know who you are. And to my dear friend, I hope you are doing well up there.

List of Abbreviations

Abbreviation	Description
RBE	Relative Biological Effectiveness
OAR	Organ-At-Risks
LET	Linear Energy Transfer
MC	Monte Carlo
LQM	Linear Quadratic Model
MFO	Multi-Field Optimization
SFO	Single-Field Optimization
RT	Radiation Therapy
DNA	Deoxyribonucleic Acid
EBRT	External Beam Radiation Therapy
3DCRT	3 Dimensional Conformal Radiation Therapy
IMRT	Intensity Modulated Radiation Therapy
PT	Proton Therapy
BP	Bragg Peak
SOBP	Spread-Out Bragg Peak
TCP	Tumor Control Probability
NTCP	Normal Tissue Complication Probability
IMPT	Intensity Modulated Proton Therapy
MCS	Multiple Coulomb Scattering
CSDA	Continuous Slowing Down Approximation
TPS	Treatment Planning System
PCS	Proton Convoluation Superposition
DICOM	Digital imaging and Communications in Medicine
GEANT4	Geometry and Tracking 4
TOPAS	Tool for Particle Simulation
IDD	Integrated Depth Dose
FWHM	Full Width Half Maximum
DTA	Distance To Agreement
CAX	Central Axis
MU	Monitor Unit
DVH	Dose Volume Histogram
CTV	Clinical Target Volume
BS	Brainstem
CH	Optic Chiasm
RO	Robust Optimization

Table of Contents

Chapter 1 Introduction to Proton Beam Therapy and Relative Biological Effectiveness Treatment Planning

1.1 Cancer

Rapid technological advancement allows for significant improvements in almost all aspects of human health over the years. However, there remain several pressing issues for which universal remedies have yet to be discovered and certain areas where we have yet to find the perfect solution. One crucial area of interest concerns cancer treatment. Without a doubt, the advancement of medical treatment for this much feared condition has come a long way. Despite the present medical advances that the world's best medical doctors possess, there is still no absolute cure for cancer which continues to claim many lives. In Singapore, the past five years daily average of new cancer diagnosis and fatality as a result of cancer is 40 and 15 people respectively. The common cancers among males include colorectal, lung and prostate cancer while females are more commonly diagnosed with breast, colorectal, and lung cancer[2]. There is also an increase in the world's fatality rate and incidence rate for cancers[3].

Cancer cells are living cells that continuously divide and grow uncontrollably. These cancer cells are referred to as malignant tumor. They can appear almost anywhere in the body and can affect the neighboring tissues and metastasize. If left untreated, it might potentially result in death.

Radiation Therapy (RT) was developed upon the discovery of X-ray in 1896[4] and it was first used by Emil Grubbe[5] on a woman with breast cancer in Chicago as a form of treatment that same year. The aim of RT is to eliminate cancer cells in the body using ionizing radiation while minimizing harm to normal or critical tissues or organs. During the process of RT, photons are delivered as an indirect ionising radiation and consequently resulting in the production of charged particles (directly ionizing radiation)

to the tumor which then kills the cancer cells by damaging their DNA. When the DNA is beyond repair, the cancer cells die and are eventually recycled or degraded into non-toxic components in our body[6]. With the advances of radiation medicine, RT can be used as a primary treatment modality to fight cancer in conjunction with other treatment modalities such as surgery and chemotherapy. RT is very effective when the cancer type is particularly radiosensitive.

1.1.1 Types of Radiotherapy (RT)

Internal RT

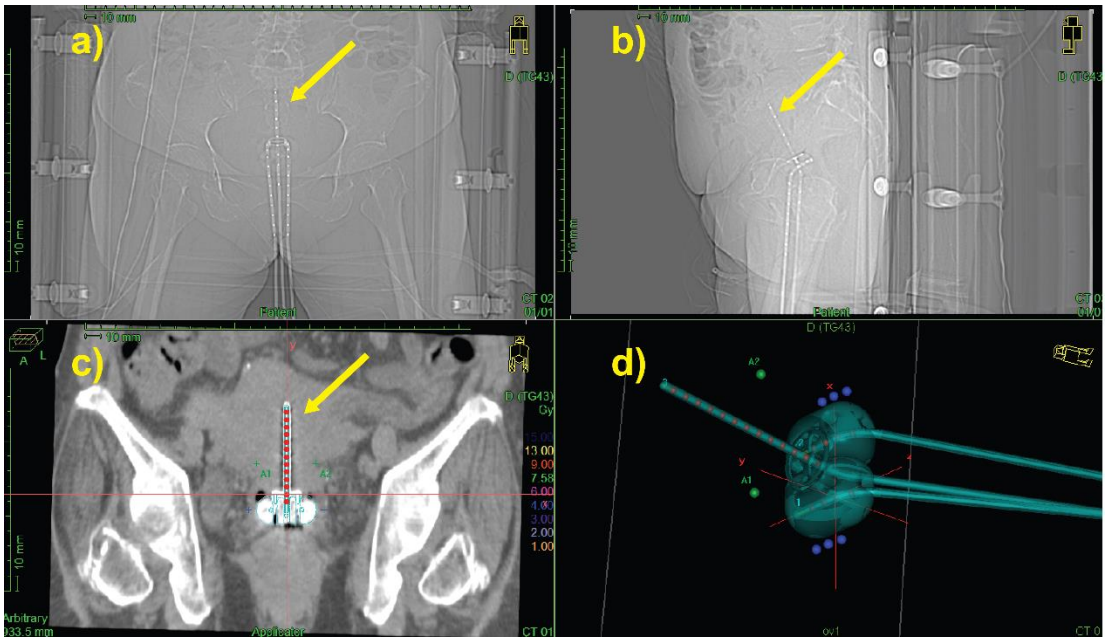

Figure 1.1 (a) and (b) shows the topogram of the patient with the Rotterdam cervix applicator and 2 ovoids. (c) shows the applicator model and the radiation seeds position in the CT image (d) shows the applicator model created with red circles defining the radiation seeds position and blue circles represent the optimization points.

Internal RT such as Brachytherapy (e.g. radiation seeds implants), delivers a high dose of radiation directly at the tumor tissues. It can be categorized into Low- (LDR), Medium- (MDR) or High- (HDR) dose rate brachytherapy where the dose rates are 0.4-

2Gy/hr, 2-12Gy/hr and >0.2Gy/min, respectively[7] as determined by the type of radioactive source used. A radioactive source, such as Iridium-192 or Iodine-125 is placed or inserted directly at the tumor site or interstitial cavity in the patient for a pre-set time or permanently depending on treatment prescription. An example of brachytherapy for cervical cancer is shown in Figure 1.1.

External Beam RT (EBRT)

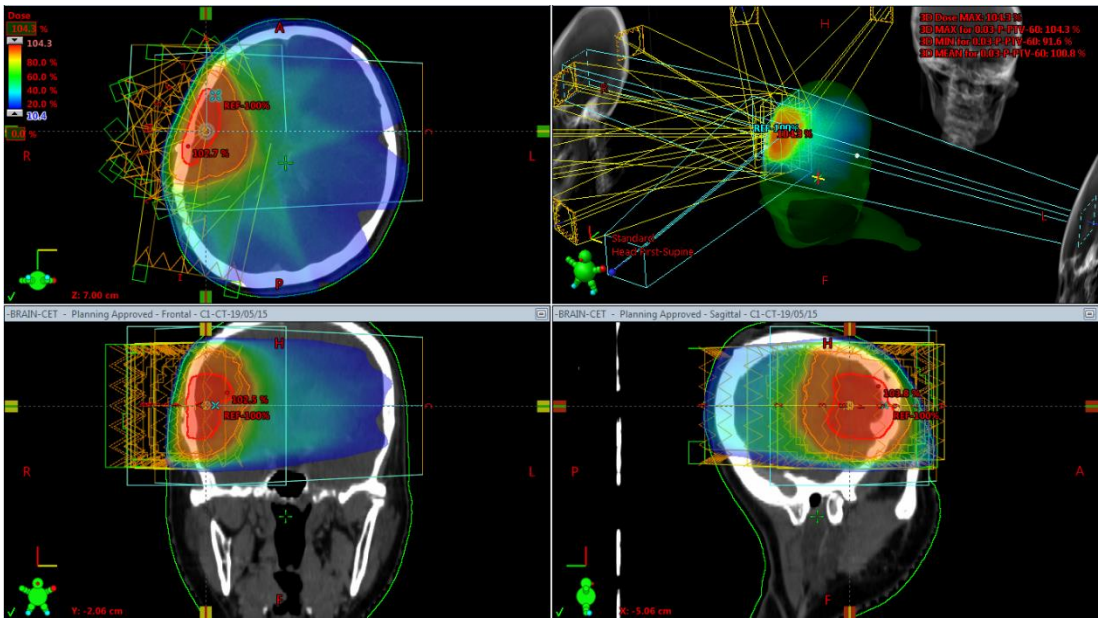

Figure 1.2 shows an external beam radiotherapy plan on a brain tumor. The color wash represents the dose distribution in the head and the red contour represent the target tumor.

EBRT is the irradiation from a source outside of the body, passing through the skin and towards the tumor tissues shown in Figure 1.2. The energy typically ranges from $4-20\ MeV$. From this section onwards, RT refers to high energy X-rays for treatment unless stated (e.g., electrons). A few common types of external radiotherapy treatment are Radiotherapy (RT), Stereotactic Body RT (SBRT), Stereotactic RadioSurgery (SRS) and particle therapy such as Proton Therapy (PT) and Carbon Ion Therapy (CIT). In SBRT, the dose is escalated to 8 to 30Gy per fraction and over a course of 1 to 5 fractions to complete treatment as compared to normal RT where the number of

fractionations might be higher, allowing healthy tissues to heal. SRS is usually limited to the brain regions where the entire dose is typically given in a single fraction.

In the area of RT, they are usually delivered using Linear Accelerator (LINAC) while Gamma Knife and CyberKnife are usually used to deliver SRS. The main difference between Gamma Knife and Cyberknife is that the latter is capable of delivering SBRT.

The common treatment techniques are 3D Conformal RT (3D-CRT), Intensity Modulated RT (IMRT) and Volumetric-Modulated Arc Therapy (VMAT). In 3D-CRT, the shape of the beam is changed at every angle to match the shape of the tumor. For IMRT however, the intensity of the beam is modulated using Multi-Leaf Collimator (MLC) that move dynamically whereas the intensity in 3D-CRT is uniform and delivered in MLC-shaped open fields. In the National Cancer Centre Singapore (NCCS), IMRT is delivered at static gantry angles and dynamic MLC. VMAT is similar to IMRT where it is treated with a dynamic gantry. VMAT often results in reduced treatment time for the patients as the gantry and MLCs are both dynamic during delivery. Depending on tumor type and treatment prescription, a patient was treated with 1.8-2Gy per fraction over 30-35 fractions. On the other hand, Electron Beam RT is used to treat superficial tumor using electrons. Unlike RT, due to the electron interactions, electrons do not penetrate more than a few centimeters beyond the skin surface.

Following the conventional high energy X-ray, Proton Therapy (PT) was introduced by Lawrence Berkeley Laboratory[8] in 1954 as a form of treatment for cancer. Even though it is still being administered for more than 60 years, the high cost and insufficient data available for wide acceptance and further research on the efficacy of treatment has limited its advancement. While initial clinical results from other centres appear promising when treating tumors close to critical structures, the use of PT is still widely

debated given its physical and radiobiological uncertainties. Despite this, there is increased use of PT due to the clear advantages over RT for good tumor control probability and lower normal tissue complications probability. To make PT accessible in Singapore, NCCS is setting up its first PT facility in Singapore which is expected to be ready by 2022.

1.2 Proton Therapy

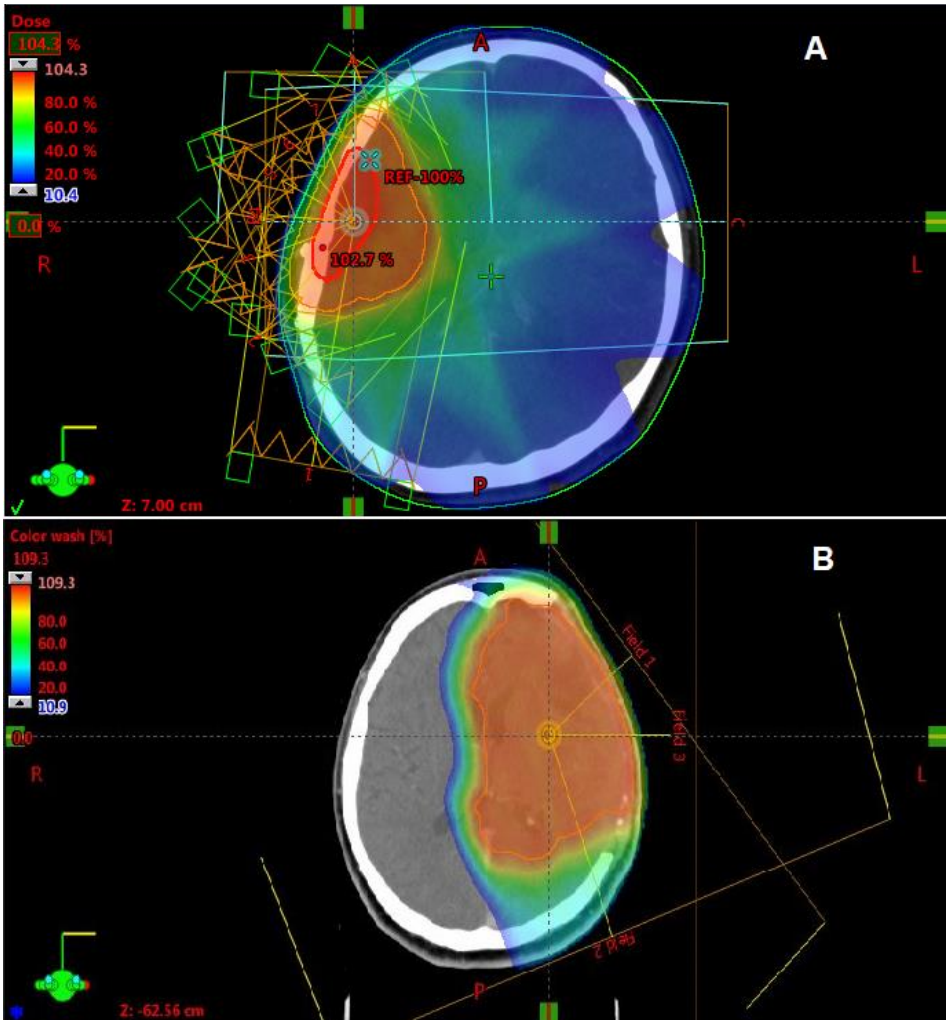

Figure 1.3 (A) shows a EBRT plan while (B) shows a proton beam plan on a brain tumor. The color wash represents the dose distribution in the head and the red contour represent the target tumor. We can see the main difference in the exit dose of the beam where there is low dose spill on the whole brain in the EBRT plan as compared to no exit dose in the PT plan.

Proton Therapy (PT) is a type of particle or hadron therapy that delivers similarly to EBRT as shown in Figure 1.3. Here, a high-energy ionizing proton beam ($70 - 250\ MeV$) from outside the body is directed precisely at the tumor volume in the body in controlled and specific amounts to deliver absorbed dose to kill the cancer cells. Due to the physical and radiobiological properties of the protons, PT presents distinct differences from x-ray and electron beam therapy. One important factor to be

considered for radiotherapy is the absorbed dose delivered to the surrounding healthy tissues or critical organs. These dosages should be minimized to reduce or avoid radiation toxicity to these healthy tissues. In conventional RT, this often limits the amount of dose to the tumour volume due to the high X-ray entrance dose deposition to the surrounding healthy tissues (Figure 1.4). However, it can be circumvented with PT with the low entrance dose and the high dose near the end of range, the Bragg Peak (BP). PT is therefore favoured over RT for its treatment effectiveness as shown by Figure 1.4.

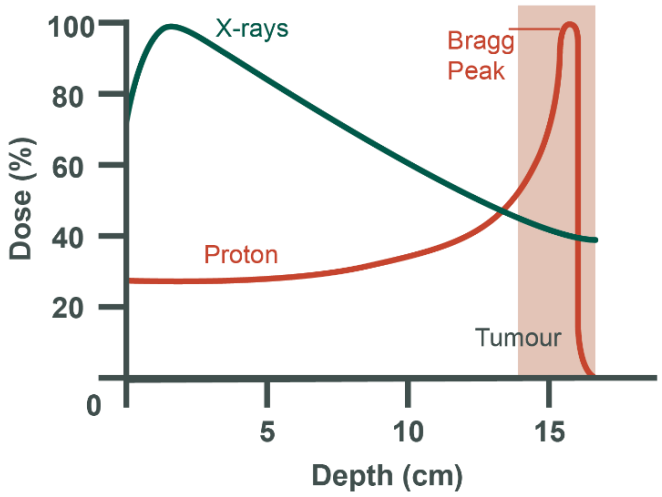

Figure 1.4 shows the Bragg Peak for proton against Percentage Depth Dose (PDD) curve for megavoltage X-rays

The Bragg peak curve (red curve) describes the dose deposited in the body at each depth for a proton beam. This shows that a low entrance dose can be achieved in front of the tumour, while a maximum dose is deposited within the tumour near the proton's end of range. The latter can be made to conform to the depth of the tumour by a Spread Out Bragg Peak (SOBP) which will be discussed in the next section, in order to spare the neighbouring tissues with negligible exit dose. On the contrary, X-ray (green curve) deposits a high dose near the surface of the body (build-up region) and decreases as it approaches the treated volume at depth. The beam continues to fully penetrate the

patient due to its limited attenuation. This causes both a high entrance and exit dose on the healthy tissues located at the front and after the tumour which might eventually lead to radiation toxicity or normal tissue complication.

Therefore, based on the physics (stopping power) of the proton beam, PT should be in principle the desirable solutions for treating tumours near to important Organ-at-risks (OARs) and where low integral dose may be preferred, in particular pediatric patients. With potentially better dose conformity to be achieved with PT relative to RT, it could potentially increase the tumor control probability (TCP) while significantly reducing normal tissue complication probability (NTCP)[9,10]. This also allows the radiation oncologist the option of dose escalation for better TCP. The corresponding reduction in harmful side effects allows a better quality of life for the patients[11,12].

1.2.1 Proton Accelerators

There are two common types of accelerators used for PT treatment, namely, Cyclotrons and Synchrotrons.

Cyclotron

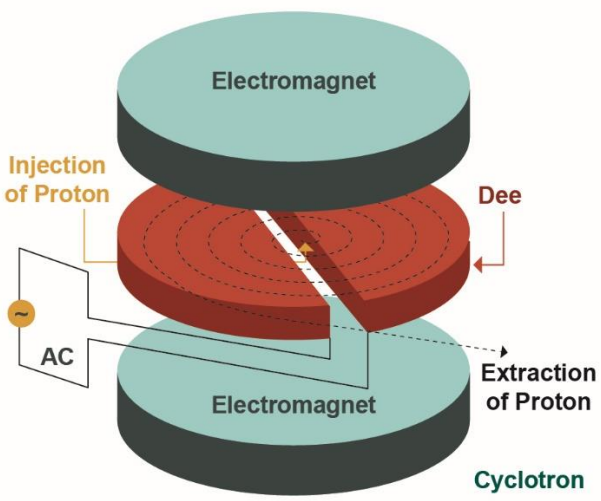

Figure 1.5 shows the schematic of a simple proton cyclotron

Cyclotron is a type of magnetic resonance accelerator where the protons are constrained to the circular motion by the strong *fixed* magnetic field produce by the electromagnet. The protons are first extracted from the hydrogen atom and injected into the centre between the Dees (D-shaped hollow electrodes of $3 - 5\ m$ in diameter). The protons are then accelerated by the small voltage increment between the Dees each time the gap is crossed. The voltage is a sinusoidal alternating voltage in which the frequency of the sinusoidal wave is at revolution frequency (cyclotron frequency). The accelerated protons then spiral outwards and are eventually extracted when it reaches the full *fixed* energy of $230 - 250\ Mev$ ($33 - 38\ cm$ in water) producing a continuous wave of protons. Energy degraders (e.g. variable thickness polycarbonate wheel) are then used to reduce the energy of the protons to the desired range for treatment.

Synchrotron

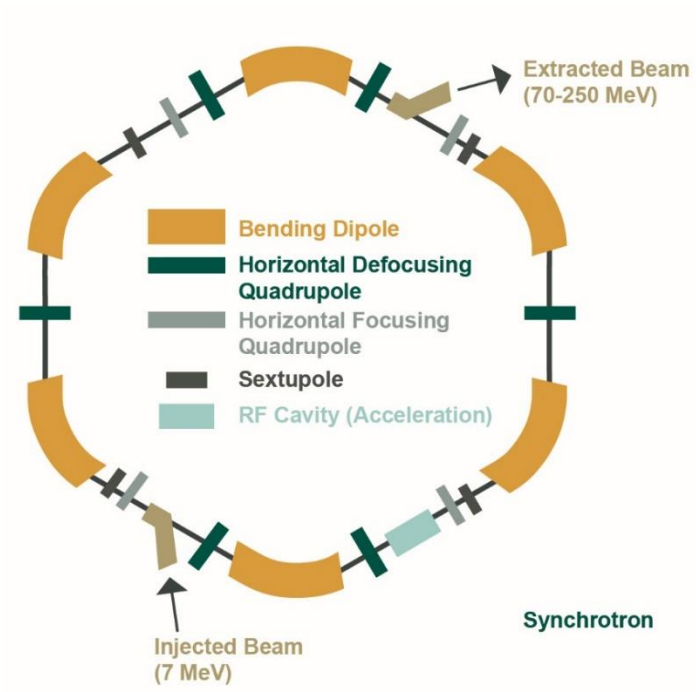

Figure 1.6 shows the schematic of a HITACHI proton synchrotron consisting of a radio frequency (RF) cavity for proton acceleration and six bending dipole magnets to drive the particle in a circular orbit.

Compared to the cyclotron, the orbital radius of the proton in the synchrotron remains constant as the proton is guided by the bending magnet as shown in Figure 1.6. The $7\ MeV$ protons are injected through the injection line and being accelerated at each turn. The diameter of the synchrotron varies from $6-8\ m$ with an injection line of $6-10\ m$. The RF frequency to the cavity and the magnetic field of the dipole bending magnets increases synchronously to hold the proton in the orbit. This limits the energy of the proton being produced as the energy increases with the size of the magnet. In NCCS, the HITACHI synchrotron can extract proton energies from $70-250\ MeV$ ($4-38\ cm$ in water). When the proton reaches the desired energy for treatment, it will then be extracted out from the beamline. Thereafter, depending on the design of the delivery techniques adopted by the centre, a scattered proton beam or pencil beam scanning will be produced in the treatment room through a pulse beam.

1.2.2 Delivery Techniques

In PT, there are two types of delivery methods, namely (1) Passive Scattering and (2) Pencil Beam Scanning.

Passive Scattering (PS)

PS is the early method for PT delivery and has been used since the beginning. Upon acceleration of protons through a cyclotron or synchrotron to required energy, the protons are transported to the delivery room. A high-Z material (e.g. lead) is placed in the path of the proton beam which then broadly scatters the proton to the desired dimension. The first scatterer broadens the Gaussian-shaped beam laterally while the second scatterer further broadens the beam and flatten its radial intensity profile for therapeutic use[13]. Range modulator is used to modulate the energy of the incoming proton to generate a Spread-Out Bragg Peak (SOBP) as it rotates. The scattered protons

then pass through the collimator (e.g. brass aperture) and compensator (e.g. lucite block) which consequently shapes the proton beam laterally in depth to the shape of the tumor. A schematic of the system is shown in Figure 1.7.

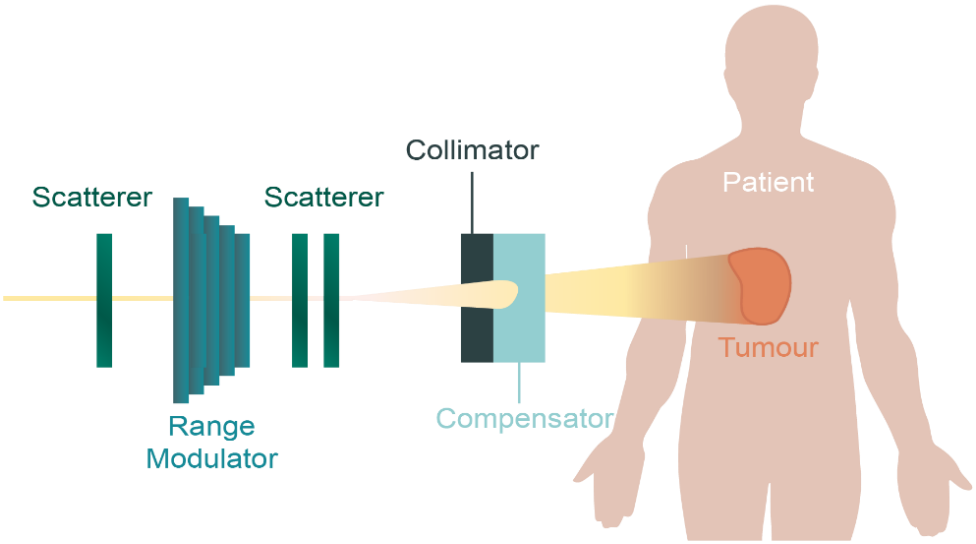

Figure 1.7 shows a Passive Scattering System

On the contrary, due to the number of material components such as the scatterers and collimators, high-energy secondary neutrons are produced from the interactions between protons and these components[14,15]. Neutrons are highly penetrative which may lead to neutron dose exposure throughout the body causing late stochastic effects such as secondary cancers, especially in paediatric patients[16,17]. However, a recent review on neutron dose and its measurement in proton therapy show that it is unlikely that neutron dose will result in a large impact on secondary cancers especially in pencil beam scanning therapy[18].

Pencil Beam Scanning (PBS)

As compared to PS, PBS uses a pair of X- and Y-scanning magnets to adjust the proton beam position in the vertical and horizontal direction to conform the dose to the target. Therefore, the majority of the contribution to neutron dose arises from the patient's body themselves. As shown in Figure 1.8 below, the beam passes through the vertical

and horizontal scanning magnet before proceeding towards the tumor. The proton energy has to be modulated or changed to achieve conformity to the target shape at different depths.

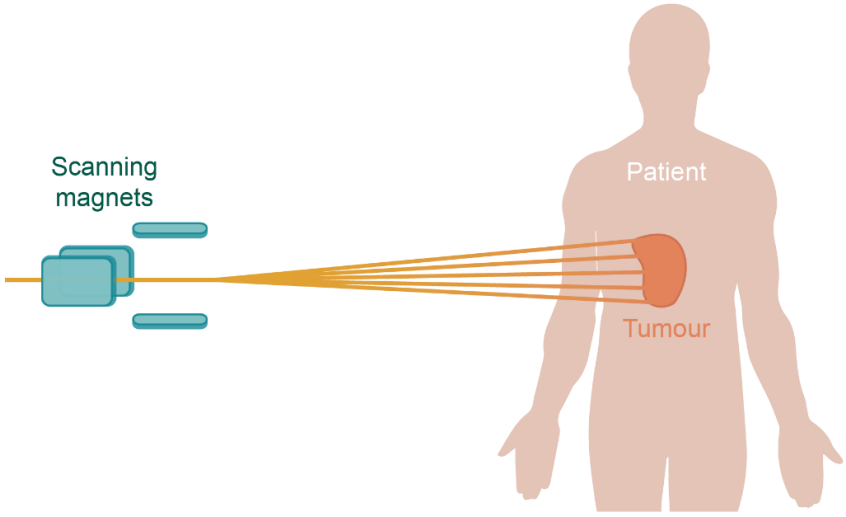

Figure 1.8 shows a Pencil Beam Scanning System

The beam usually moves in a zigzag direction as shown in Figure 1.9 where the proton beam paints the tumor layer by layer by switching energy. The beam can be delivered via discrete spot scanning or a continuous/raster scanning approach. The tumor is divided into iso-energy layers where each layer corresponds to a specific energy of the proton beam. The proton energy is controlled directly by the synchrotron or indirectly via an energy degrader at the exit of the cyclotron.

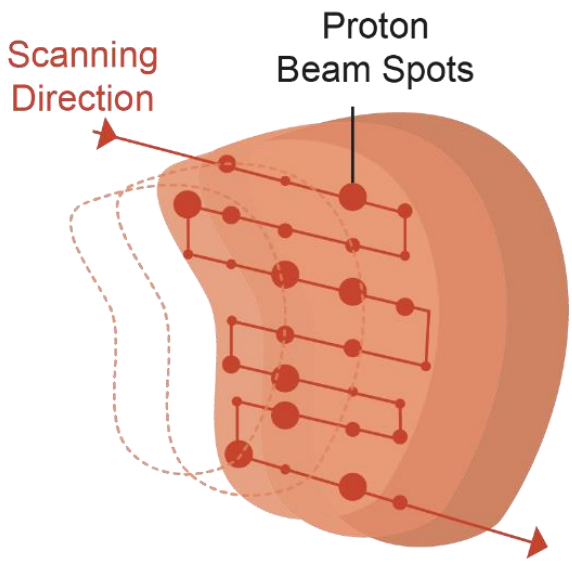

Figure 1.9 shows the scanning beam path on each layer of the tumor

Compared to PS, the PBS technique allows better dose sparing to normal tissues at the entrance of the tumor and also provides better conformity to irregular targets[19–22]. By modulating the intensity in each spot, it can also deliver Intensity Modulated Proton Therapy (IMPT) for even higher target conformity (Figure 1.9). However, PBS is susceptible to moving targets during delivery. Strict safety precautions must be taken to exploit the advantages of PBS in proton therapy. NCCS will have a full PBS system for the PBT delivery technique.

1.3 Physics of Proton Therapy

The advantages of PT over RT are based on the concepts of radiation physics and radiobiology. The physics of PT and absorbed dose calculation will be discussed in the following sections.

1.3.1 Proton Interactions with matter

In PT, proton and other charged particle interactions are categorised into electronic and nuclear interactions. When electromagnetic or Coulomb interaction is present, a stopping process or scattering process could occur.

Stopping (Inelastic Collision)

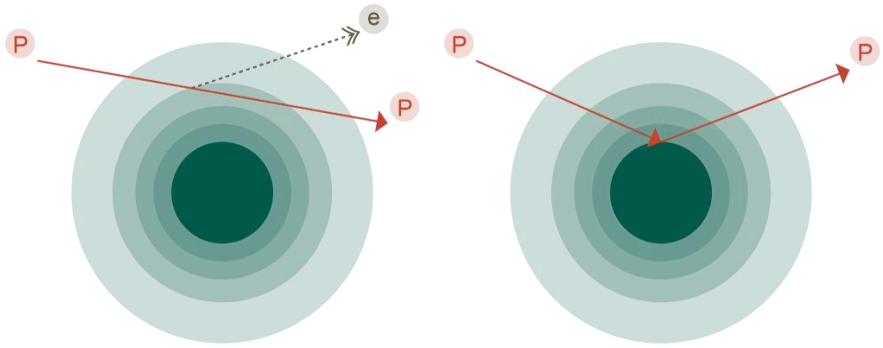

Figure 1.10 shows the electromagnetic Interactions: Stopping Process and Scattering Process where p and e^- refer to proton and electron respectively

The stopping process happens when an incident proton interacts with an atomic electron. The proton slows down through many collisions causing ionisation or excitation in the medium and its rate of energy loss increases. This is due to the velocity dependence of the scattering cross-section and the greater amount of momentum being transferred to the electron when the proton stays in the medium for a longer period. The rate of energy loss, therefore, depends on the initial energy of the incident proton and the material of the medium.

Scattering (Elastic Collision)

In a scattering process, an incident proton interacts with the nucleus and is being deflected or elastically scattered by the many collisions with the nucleus. This is commonly known as the Multiple Coulomb Scattering (MCS). The deflection angle is usually extremely small (order of a few degrees) and the proton loses a negligible amount of energy. However, in clinical practice, millions of protons are involved and the net change in the trajectory of the proton beam is significant. Therefore, it is important to consider this when designing proton beamlines, treatment heads and algorithms or simulations of dose calculations.

Nuclear (Non-elastic Collision)

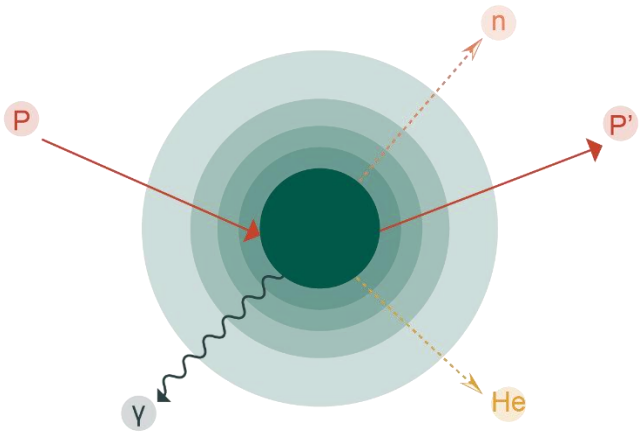

Figure 1.11 shows the Nuclear Interaction where He, n and γ refers to Helium, neutron, and gamma-ray respectively

On the other hand, in a nuclear interaction, the incident proton has a head-on collision with the nucleus. The non-elastic nuclear reaction results in the production of secondary particles as shown in Figure 1.11. One of the main interaction concerns is neutron production by protons of energies exceeding $10\,MeV$. Neutrons are extremely penetrative by virtue of their neutral charge and their resulting radiobiological effects

can be up to 20 times higher than that of protons[23]. Thus, adequate protection from overexposure to neutrons must be ensured for patients and staff in PBT facility design.

Range Straggling

When the protons are mono-energetic and traverse through a homogeneous medium, they lose energy through Coulomb collisions in a continuous slowing down approximation based on the mean energy loss (see Equation 1.2, 1.3 and 1.4). However, not all protons lose the same amount of energy as the nature of their interaction is statistical. Therefore, the number of collisions the protons encounter to bring it to a stop varies. When proton range straggling is accounted for, the range straggling distribution gives a Gaussian distribution.

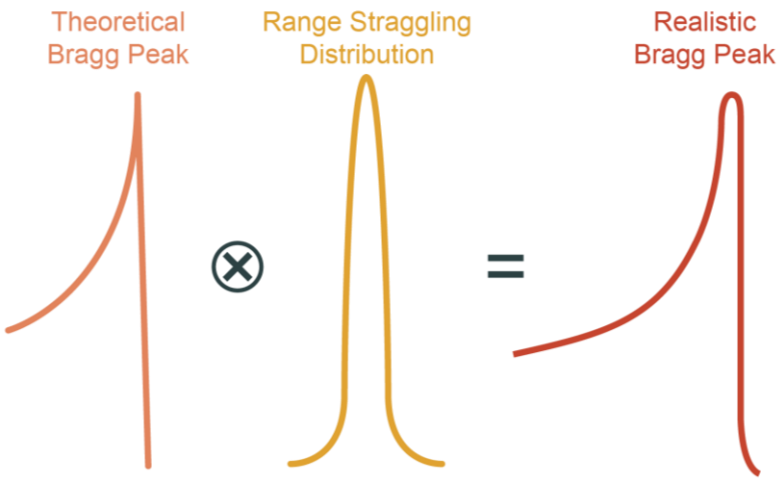

Figure 1.12 shows the Range Straggling (RS)

Theoretically, when a proton stops, the dose should drop to zero, but due to range straggling, a more realistic Bragg Peak is shown in Figure 1.12. There is a spread in range as the dose falls off. This effect is also known as range straggling which is represented by the Range Straggling Distribution.

The width of the spread in the Bragg peak is calculated as

$$d_{20} - d_{80} = 1.3 \times (\sigma_{RS}^2 + \sigma_{beam}^2)^{\frac{1}{2}} \qquad (1.1)$$

where d_{20} and d_{80} represent the proximal and distal point of the Bragg Peak when 20% and 80% of the dose are deposited respectively. Range straggling deviation, $\sigma_{RS} \approx 0.0012 \times range\ of\ proton$ and σ_{beam} is the beam energy spread[24].

1.3.2 Stopping Power, Absorbed Dose and Fluence

Stopping power describes the rate of energy transfer to the medium between the charged particles and the medium with distance travelled. It is defined in Equation 1.2 where it consists of electronic, nuclear, and radiative components.

$$S(x) = -\frac{dE}{dx} = \frac{dE}{dx}_{ele} + \frac{dE}{dx}_{nuc} + \frac{dE}{dx}_{rad} \ MeVcm^2/g \qquad (1.2)$$

The first two terms have been discussed in proton interactions with matter, and the radiative stopping power is due to the Bremsstrahlung production by the interaction between proton and the nuclei. However, the radiative term of stopping power can be neglected since protons are much heavier particles than electrons and the nuclear term can be neglected since it only dominates only at low energies below 1 MeV as presented in ICRU Report 49[25]. This reduces Equation 1.2 to having a total mass stopping power depending solely on the electronic term given as.

$$\frac{S}{\rho} = \frac{1}{\rho}\frac{dE}{dx}\ MeV\ cm^2/g \qquad (1.3)$$

Stopping Power is described by Bethe[26] who derived the equation using quantum mechanical perturbation theory given by.

$$\frac{S}{\rho} = -\frac{dE}{\rho dx} = 4\pi N_A r_e^2 m_e c^2 \frac{Z}{A}\frac{z^2}{\beta^2}\left[\ln\frac{2m_e c^2\gamma^2\beta^2}{I} - \beta^2 - \frac{\delta}{2} - \frac{C}{Z}\right] cm^2 g^{-1} \qquad (1.4)$$

where m_e is the mass of an electron, c is the speed of light, n is the electron density of the material, z is the charge of the incident particle, $\beta = \frac{v}{c}$, e is the electron charge, ϵ_0

is the vacuum permittivity and I is the mean excitation potential. Stopping power is a quantity closely related to Linear Energy Transfer (LET). The main difference is that the stopping power is described as the energy loss per unit thickness while LET is the rate of transfer of energy to the medium locally. LET will be further discussed in the later section.

Since the Bethe formula depends on the z^2 factor, the stopping power will increase by a factor of four if the charge of the incident particle doubles. It also depends on the velocity of the incident particle where the stopping power will decrease by a factor of four if the velocity is doubled due to the β^2 component. Thus, in proton therapy, as the proton slows down (velocity decreases), the linear energy transfer will increase. Since it scatters much less than light charge particles (e.g. electrons), it moves close to a straight line, hence we get the BP. This results in the physical property of a charged particle, the Bragg peak.

In ICRU Report 85[27], the Fluence (Φ) and absorbed dose (D) are defined as

$$\Phi = \frac{dN}{da}\ m^{-2} \tag{1.5}$$

where dN refers to the number of incident particles on a sphere with a cross-sectional area da, and

$$D = \frac{d\bar{\epsilon}}{dm}\ Gy \tag{1.6}$$

where $d\bar{\epsilon}$ refers to the mean energy deposited through ionizing radiation to a matter of mass dm. Dose to medium, D_{med}, can also be expressed with a relationship with Φ and collision stopping power, (S_{col}), as

$$D_{med} = \Phi \times \left(\frac{S_{col}}{\rho}\right)_{med}\ Gy \tag{1.7}$$

1.3.3 Continuous Slowing Down Approximation (CSDA)

When protons transverse through a medium, they experience multiple ionization events over their track length. Energy is transferred in each interaction until the protons stop. Due to range straggling, there are small variations in each proton energy loss. The range in which half of the protons come to rest is the CSDA range as computed by Berger and Seltzer[28]. The CSDA range is given in Equation 1.8

$$R = \int_0^{E_k} \left(\frac{S}{\rho}(E_k)\right)^{-1} dE_k \, cm \tag{1.8}$$

where E_k is the kinetic energy of the proton. For this approximation, the rate at which a proton loses its energy at every point along its track is assumed to be equal to the total stopping power and the fluctuation in energy loss from a proton is negligible[29].

Range uncertainty is a concern in Proton Therapy as it plays an important role in the range calculation in Treatment Planning System (TPS) and the discrepancies between planned and delivered doses during a patient's treatment[30]. This uncertainty is dependent on the energy distribution of the incident proton and the properties of the medium that it is travelling through.

1.3.4 Spread-Out Bragg Peak (SOBP)

Figure 1.4 shows a single BP from a single proton beam. In realistic cases, the tumor covers a certain area in the body. Therefore, in order to fully cover the whole target volume with a proton beam, the proton beam energy is modulated to obtain a Spread-Out Bragg Peak (SOBP) as shown in Figure 1.13.

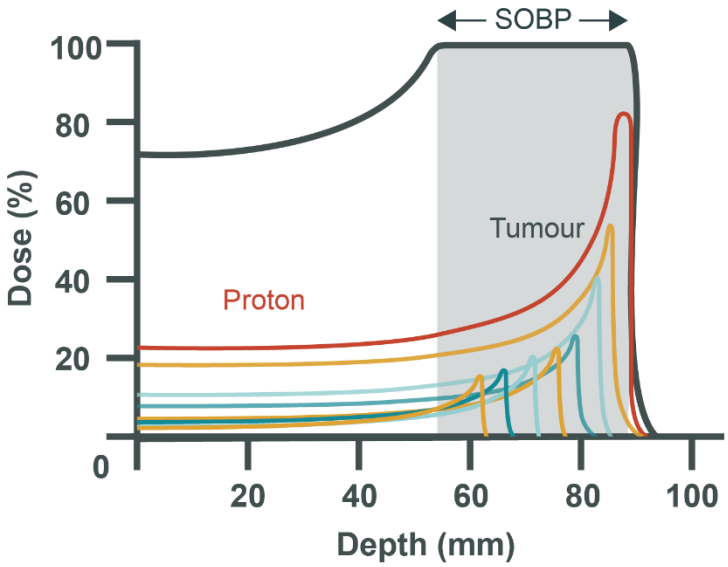

Figure 1.13 shows the Spread-Out Bragg Peak at 20mm depth

Since the energy of the proton beam determines the depth at which the BP will appear, multiple proton beams of different energy are irradiated to obtain the SOBP. A total of 7.2×10^{10} protons are approximately equal to $2Gy$ of dose[31]. Figure 1.14 shows proton beam energy ranging from 71.3 MeV to 228.8 MeV, approximately at a range of 4 cm to $32cm$. The range of the proton beam is at the distal end of the Bragg peak where 90% (d_{90}) of the dose is being deposited[24]. The width of the SOBP is the distance between the proximal and distal end of SOBP where 90% (p_{90} and d_{90}) of the dose is being deposited. However, other definitions of range and width are not uncommon.

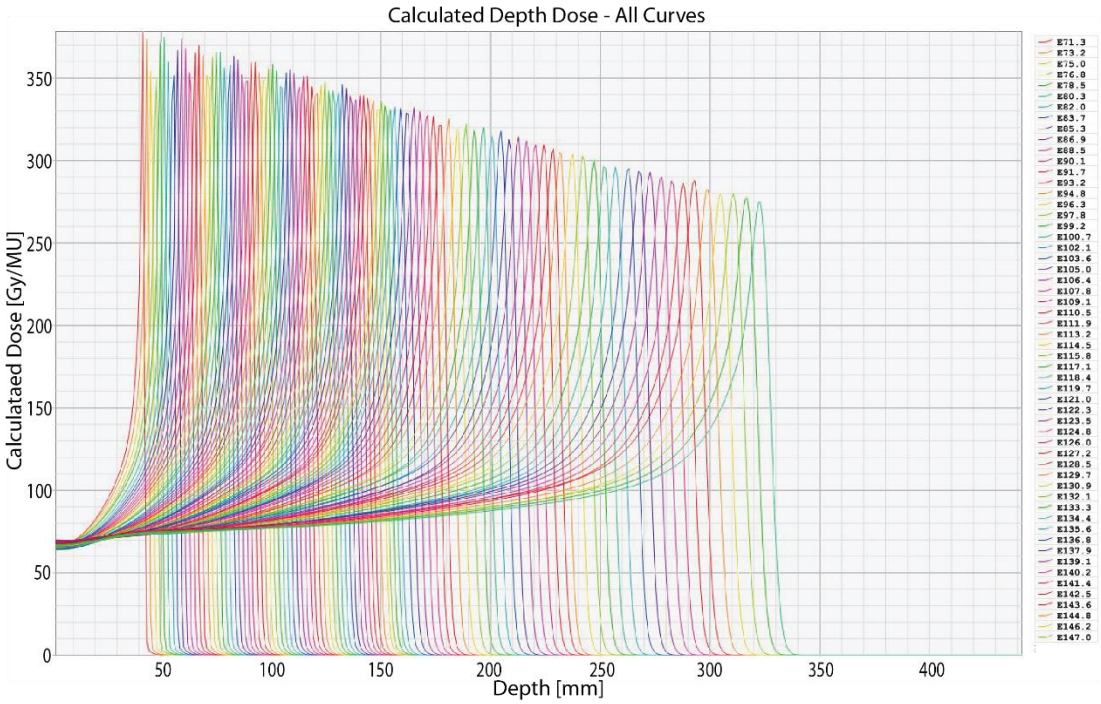

Figure 1.14 shows the Depth Dose curves simulated in water for mono-energetic proton beam from 71.3 MeV to 228.8 MeV.

1.3.5 Dose Calculation

In this section, one clinical PBT Treatment Planning System (TPS) will be described which is related to this project. In PBT, different TPS are used by different clinics, each with a different type of dose calculation algorithm. This project is conducted using the Eclipse Treatment Planning System (Varian Medical System, Inc. USA). The Proton Convolution Superposition (PCS) algorithm will be described. This algorithm determines the dose at any point by summing the dose from the point kernels located on the calculation grid as shown in Figure 1.15.

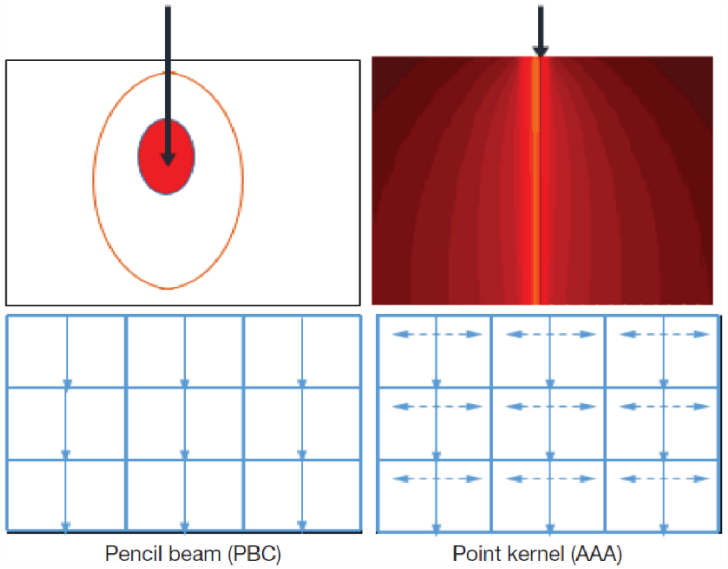

Figure 1.15 shows the calculation grid and Point Kernel[32]

When a proton Pencil Beam enters the body, protons would interact with the matter as they travel. When a proton stops in a voxel, the three types of proton interactions with the medium as previously discussed occurs. Thus, energy is released within a voxel or passed on to another voxel. This event stops until all the energy has been absorbed or released. Point kernel, as described by a Gaussian curve, represents the sum of the spread of energy at a particular point $P(x, y, z)$ in Figure 1.16. The calculation grid is referred to as a voxel

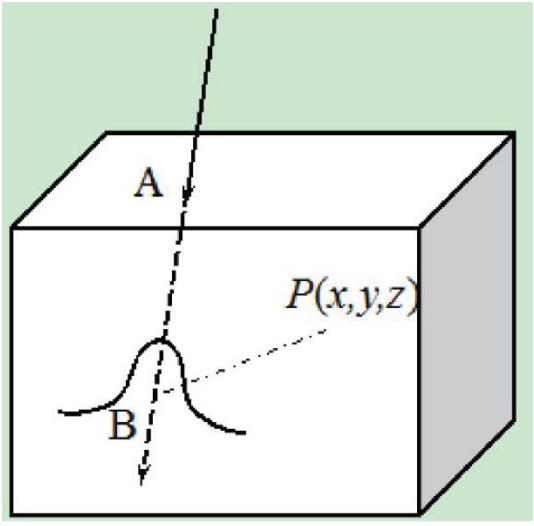

Figure 1.16 shows a Proton Convolution/Superposition Algorithm[33] voxel

The dose at point P is the summation of the energy released from the voxel given by [33]

$$D(x,y,z) = \iint_{\Sigma} dx'dy'T(x',y')K(x-x',y-y',z) \qquad (1.9)$$

The dose is the integral over an area Σ on which all the proton pencil beams pass through, $T(x,y)$ is the pencil beam intensity and $K(x,y,z)$ is given by [33]

$$K(x,y,z) = p(d_{eff})\left(\frac{SSD+d_{eff}}{z}\right)^2 G(x,y,z) \qquad (1.10)$$

where $p(d_{eff})$ is the depth dose distribution of a proton pencil beam in water equivalent length, $\left(\frac{SSD+d_{eff}}{z}\right)^2$ is the inverse square correction and $G(x,y,z)$ is given by[33]

$$G(x,y,z) = \frac{1}{2\pi\sigma(z)}\exp\left[-\frac{x^2+y^2}{2\sigma^{2(z)}}\right] \qquad (1.11)$$

$\sigma(z)$ represents the amount of beam spread which increases linearly with depth (z) due to MCS. From Equation 1.10, the dose depends on the water equivalent length of the material that the proton passes through. Therefore, knowing the density of the material and the stopping power of the proton through each material would be able to provide more accurate information on the dose deposited[34].

1.4 Radiobiology in PT

Deoxyribonucleic Acid (DNA) contains genetic information related to cell development and functionality. It is surrounded by mostly water and it is the largest target with a diameter of $\sim 2\ nm$ and a length of $\sim 2\ m$ in a cell nucleus.

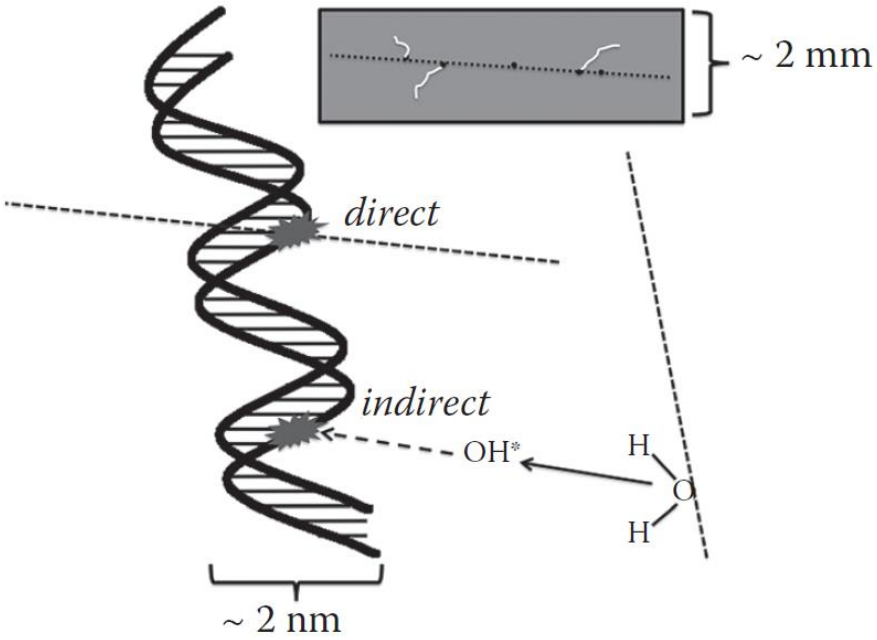

Figure 1.17 shows the Direct and Indirect actions of radiation on the structure of DNA[24]

When proton radiation interacts in a biological medium, it can cause excitation or ionization. The ionizing radiation thus damages the DNA by causing pyrimidine lesions, purine lesions, single-strand breaks (SSB) and double-strand breaks (DSB)[35]. These damages are done through a dominant process called direct action of radiation[36]. However, in RT, DSB is the main radiobiological mechanism for tumor control.

When damages to DNA occur, naturally, it will tend to repair itself with its own repair mechanism. However, unrepaired DNA may cause a loss of genetic information and become dysfunctional. Mutation, secondary cancers, or chromosomal aberrations might occur when broken DNA strands join together abnormally. This may result in cell death[24].

1.4.1 The Cell Survival Curve and $(\frac{\alpha}{\beta})$ ratio in RT

A cell survival curve shows the relationship between the fraction of cells that survive relatively to the dose of radiation being delivered. One way is via in vitro experiments using different types of cell lines typically with x-ray radiation. It is usually described by the Linear-Quadratic Model (LQM)[37] as shown,

$$S(D) = e^{(-\alpha D - \beta D^2)} \tag{1.12}$$

S refers to the surviving fraction of the cells and D is the dose. α (Gy^{-1}) describes the initial slope of the curve while β (Gy^{-2}) describes the quadratic component. An example of a mammalian cell survival curve is shown in Figure 1.18.

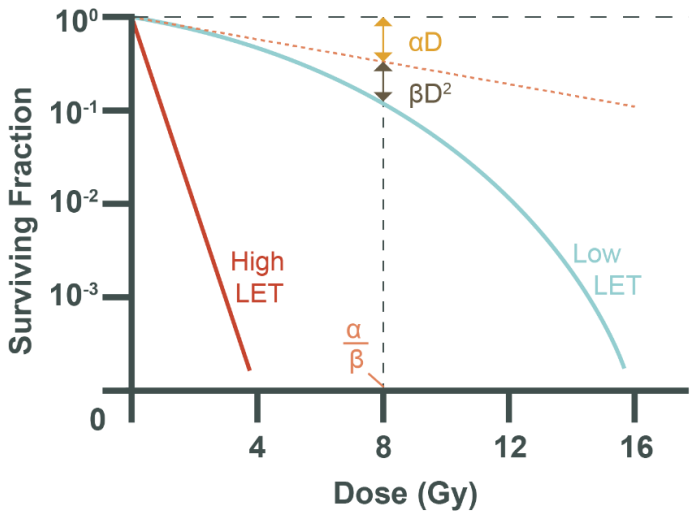

Figure 1.18 shows the Cell Survival Curve of mammalian cells exposed to radiation of different LET

The position where $\alpha D = \beta D^2$ refers to the term $\frac{\alpha}{\beta}$ (Gy) ratio of the tissue. With regards to response time, late responding tissues (lower (α/β)) shows the radiation effects damage over months to years compared to early responding tissues (higher (α/β)) as shown in Figure 1.19. The (α/β) of tumors varies from $\sim 2\,Gy$ (e.g. Prostate) to $\sim 10Gy$ (e.g. Central Nervous System) depending on tumor site as shown by a review study by Leeuwen *et al.*[38]

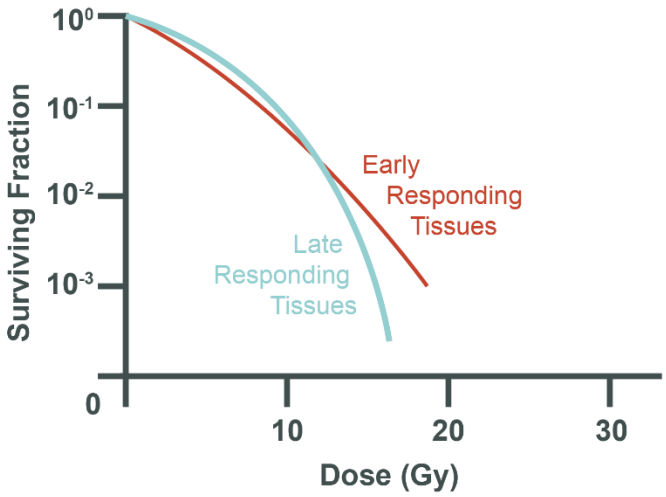

Figure 1.19 shows the surviving Fraction of Early vs Late Responding Tissue

1.4.2 Radiobiological Effectiveness (RBE)

To fully leverage the advantages of Proton in PT, the potential difference in radiobiological effectiveness can be considered to provide a higher tumor control probability. Although PBT has existed for more than 60 years, it is still limited by insufficient in vivo and clinical data[1,39,40] especially in the area of Relative Biological Effectiveness (RBE) which will be the subject of this project.

RBE refers to the ratio of which the radiobiological effect of proton absorbed dose is similar to a reference radiation dose of x-ray. Currently, a single factor of 1.1 is in clinical use where a given proton dose (D_p) is assumed to produce the same biological effect as a 10% higher than x-ray dose (D_x) as given in Equation 1.13. This is an average value deduced in the 1970s from in-vivo studies of proton therapy[1] where it was extracted from the center of a Spread-Out Bragg Peak (SOBP) at 2Gy fraction size.

$$D_x = 1.1 \times D_p \tag{1.13}$$

A constant RBE value that relates x-ray to proton dose and vice versa makes the conversion convenient. This value is however simplistic and might not truly reflect the

advantages of proton beam RBE which may lead to sub-optimal treatment plans and clinical plan evaluations and plan quality. A constant RBE of 1.1 has been discussed to be inaccurate[40,41] and in-vitro data indicates that it is a complex function where it depends on parameters such as dose, linear energy transfer (LET), the response of tissue type (α/β) and biological endpoint[42,43].

Studies have shown that there is an increase in RBE value towards the distal end of the proton range [44–46]. This might cause an underestimation of potential adverse effects with the current use of constant RBE 1.1, especially in low doses and low $\frac{\alpha}{\beta}$ tissue regions[40,42].

Till date, many RBE models have been developed to address the issue of RBE variations in patients[39,47–55]. These models are mainly based on the concepts of either Linear Quadratic Model (LQM), Local Effect Model (LEM)[56] or Microdosimetric-Kinetic Model (MKM)[57]. The main difference among these three concepts is that LQM is an experimental data-driven model while LEM and MKM are simulation data-driven. In this work, the LQM-based RBE model is adopted with the assumption that the use of experimental data to derive the model would be more accurate. This model suggests that RBE is based on three parameters, namely D_p, Dose-averaged LET (LET_D) and $(\alpha/\beta)_x$, which will be discussed in the following sections. The RBE formalism is given as,

$$RBE\left[D_p, \left(\frac{\alpha}{\beta}\right)_x, LET_D\right] = \frac{1}{2D_p}\left(\sqrt{\left(\frac{\alpha}{\beta}\right)_x^2 + 4D_p\left(\frac{\alpha}{\beta}\right)_x RBE_{max} + 4D_p^2 RBE_{min}^2} - \left(\frac{\alpha}{\beta}\right)_x\right) \qquad (1.14)$$

RBE_{max} and RBE_{min} refers to the RBE when D_p is ∞ and 0, respectively. Equation 1.14 is derived using Equations 1.12 (linear-quadratic model) and 1.13 (definition of RBE) as shown in Appendix A[1]. The majority of the RBE models assume RBE_{min} to be 1 and some with dependence on LET_D. Majority of RBE_{max} is assumed to be dependent on LET_D. The dependence on LET_D is motivated by the experimental studies

from Folkard *et al.*[58], Coutrakon *et al.*[59] and Wouters *et al.*[60] which suggest a strong correlation between LET_D and RBE. These LQM RBE models are shown in Table 1.1. These RBE models have assumed that LET_d has a linear relationship with RBE[52–55,61,62], while others assumed that there is a non-linearity between them[48,63].

Table 1.1 RBE models developed by different research groups based on the LQM concept

RBE Models	RBE_{max}	RBE_{min}
Carabe [61]	$0.843 + 0.413644\frac{LET_d}{(\alpha/\beta)_x}$	$1.09 + 0.01612\frac{LET_d}{(\alpha/\beta)_x}$
Chen [62]	$\frac{0.1}{\alpha_x} + \frac{1 - e^{-0.0013LET_d^2}}{0.045\alpha_x LET_d}$	1.0
McNamara [52]	$0.99064 + 0.35605\frac{LET_d}{(\alpha/\beta)_x}$	$1.1012 - 0.0039\sqrt{(\alpha/\beta)_x}LET_d$
Wedenberg [54]	$1 + 0.434\frac{LET_d}{(\alpha/\beta)_x}$	1.0
Wilkens [55]	$\frac{0.1 + 0.02LET_d}{\alpha_x}$	1.0
Rorviks [53]	$1.0 + 0.645\frac{LET_d}{(\alpha/\beta)_x}$	1.0

1.4.2.1 Linear Energy Transfer (LET) and RBE

Linear Energy Transfer (LET) of a material for charged particles of a given type and energy is given by,

$$LET_\Delta = S_{el} - \frac{dE_{\mathrm{KE},\Delta}}{dl}\ keV/\mu m \qquad (1.15)$$

where Δ is the energy cut-off value of secondary electrons, S_{el} is the linear electronic stopping power and $dE_{\mathrm{KE},\Delta}$ is the mean sum of the kinetic energy larger than Δ of all electrons released by the charged particle per unit path length dl[27]. It is important to quantify the LET that is lost by the charged particles and therefore be able to calculate the dose absorbed by the material.

LET can be categorised into either *Restricted* LET or *Unrestricted* LET. *Restricted* LET only accounts for the transfer energy that is greater than Δ whereas *Unrestricted* LET

accounts for transfer energy where $\Delta = \infty$ resulting in no secondary electrons being produced. LET is an important quantity that RBE is strongly dependent on[64] and the relationship between RBE and LET is as shown in Figure 1.20.

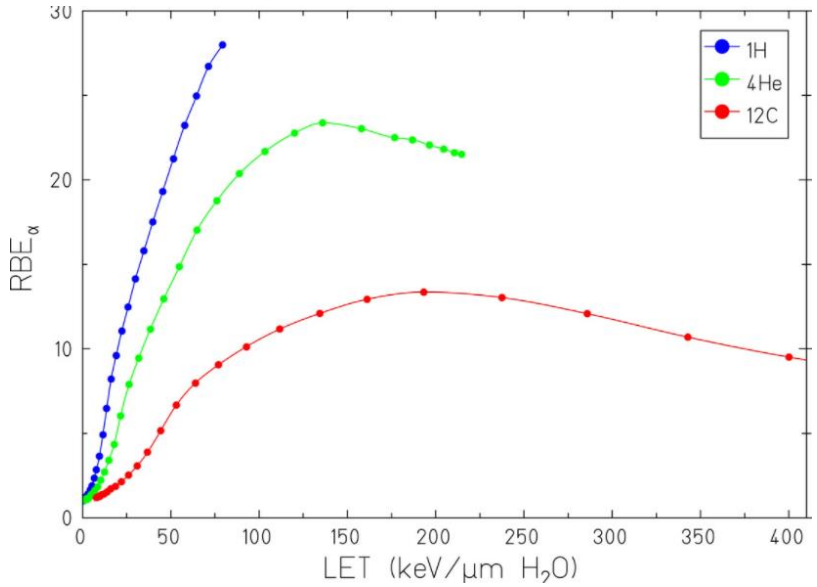

Figure 1.20 shows the RBE vs LET for Proton, Helium and Carbon[65]

As LET increases, the biological effect of the radiation beam increases. However, upon reaching the maxima of LET, RBE decreases due to Overkilling Effect of the radiation. Overkilling Effect is caused by a single particle depositing more energy than required to kill a cell, leading to lesser cells killed per absorbed dose[66,67].

There were three main definitions used for LET – (1) *pure* – LET, (2) Track-averaged LET (LET_t) and (3) Dose-averaged LET (LET_D). *Pure* – LET is used in mono-energetic proton experiments and it is extracted from the stopping power of proton in water. However, it fails to account for the composition of myriad particles which are slowed down by various degrees stochastically in the medium leading to energy straggling. LET_t and LET_D are macroscopic quantities representing mean LET for a proton beam with energy distribution at any spatial point. They are as described by

$$LET_t(\vec{r}) = \frac{\int \Phi(E,\vec{r})LET(E)dE}{\int \Phi(E,\vec{r})dE} \tag{1.16}$$

and

$$LET_D(\vec{r}) = \frac{\int D(E,\vec{r})LET(E)dE}{\int D(E,\vec{r})dE} \tag{1.17}$$

where $\Phi(E,\vec{r})$ is the fluence of a proton with energy E at location $\vec{r}$ while $D(E,\vec{r})$ is the dose deposited by a proton with energy E at location $\vec{r}$. Equations 1.16 and 1.17 are shown to be different especially when using small step sizes of less than $100\mu m$ [68], and at the plateau region of the proton depth-dose curve. Despite the differences in the LET definitions, $LET \approx LET_D \approx LET_t$ for high energy proton and very thin material. This is due to two conditions, energy straggling effect on the primary proton is minimal and $\Phi(E) \approx \delta(E - E_0)$, where $\delta(E)$ is the Dirac delta function and E_0 is the energy of primary proton.

Usually, LET values are often determined analytically[69] or via Monte Carlo simulation[66,70] as they are difficult to measure experimentally[68,71]. In this work, only LET_D is used due to its correlation with RBE and it can be determined via Monte Carlo simulation (see Chapter 2). In GEANT4, LET_D can be easily extracted for specific particle type depending on user preference. In order to calculate LET_D for each voxel, we can output the energy, ϵ, deposited by the particle and ϵ^2/l, where l is the step size of each interaction. Thereafter, we can compute LET_D for each voxel, j, given the following:

$$LET_{D,j} = \frac{\sum_{i=1}^{n} \frac{\epsilon_i^2}{l_i}}{\sum_{i=1}^{n} \epsilon_i} \tag{1}$$

where n is the total number of particles interacted in the voxel, j. This method will be used in Chapter 4.

1.4.2.2 Dose and RBE

RBE is dependent on the absorbed dose and because of this dependency, the fraction of cell survival must be specific. Since RBE is the dose of photon divided by the dose of the proton to cause a similar biological effect, it is necessary to keep the surviving fraction of cells constant when obtaining the dose using both photons and protons. This is often labelled as RBE_1, RBE_{10} and RBE_{80} for 1%, 10% and 80% respectively as shown in Figure 1.21. The RBE values are determined using the dose that was measured in correspondence to the surviving fraction of the cells as mentioned.

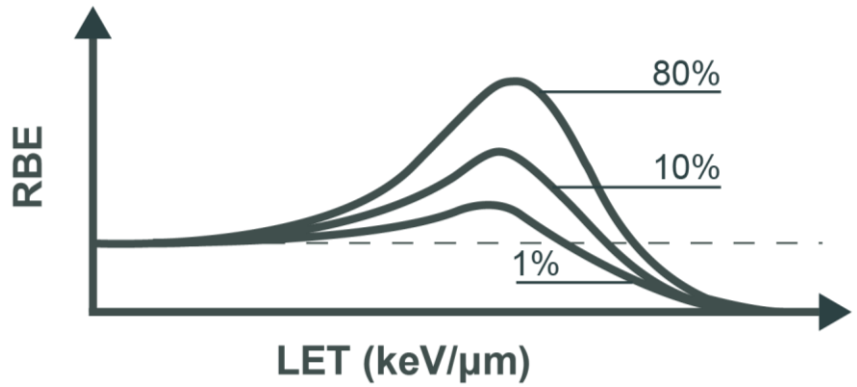

Figure 1.21 shows the RBE vs LET for 1%, 10%, 80% surviving fraction of cells[72].

1.4.2.3 Tissue Type and RBE

RBE is also dependent on the repair capability of the tissue in response to radiation. As shown in Figure 1.22, tissues with better repair capability have a higher RBE maximum as compared to those with no repair capabilities. Therefore, it is important to know the $(\alpha/\beta)_x$ ratio of individual tissue types to obtain a more accurate RBE value for dose calculation in Proton Therapy.

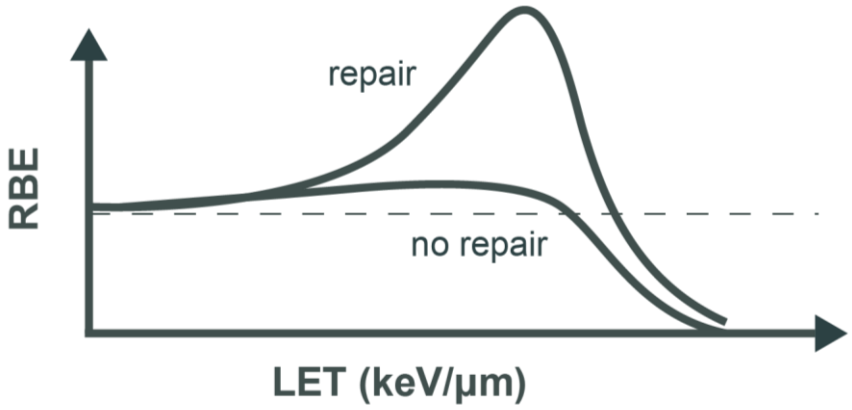

Figure 1.22 shows the RBE vs LET with Non-Repair and Repair Capability Tissue Curve[72].

Table 1.2 shows the mean $(\alpha/\beta)_x$ values for different tumour sites derived from a comprehensive study by Leeuwen *et al.*[38]. This is based on the summary of 149 different analyses of $(\alpha/\beta)_x$, where an extensive study of 1177 articles was reviewed and 64 were chosen. Despite the intensive review, the uncertainties in $(\alpha/\beta)_x$ are large for certain tumor types. In the head and neck case of Glioma, the $(\alpha/\beta)_x$ can range from 3.1 to 12.5. This would, thus, greatly affect and challenge the calculation of RBE.

Table 1.2 Summary from 149 different analyses of α/β based on 81 distinct sets of clinical data.

$(\alpha/\beta)_x$	Type of Tumor				
$\sim 3\ Gy$	Prostate	Breast	Rhabdomyosarcoma	Liposarcoma	
$\sim 10\ Gy$	Head and Neck	Cervix	Bladder	Liver	
Mixture	Oesophagus	Rectum	Central Nervous System	Skin	Lung

1.4.3 RBE Modelling Review

Despite the long history of RBE studies, the adoption of variable RBE models has been modest in the clinic due to large uncertainties in values[73]. As suggested by AAPM TG-256[1], there is a need to understand the spatial variations of RBE within and outside the target volume on a voxel-wise basis. A voxel refers to a volume of a few mm^3 which stores the data (e.g. dose, LET and HU value) depending on the resolution the user defined in the DICOM (Digital Imaging and Communications in Medicine) files. HU

value, also known as Hounsfield Unit, is a relative quantitative scale to measure the radio density of a CT image. This can be inferred from the evidence of experiments showing RBE exceeding 1.1 at the end of range[45,46,74].

Research has shown clearly that RBE 1.1 is not a good representation of the biological effect in proton therapy especially at the distal end of an SOBP despite being a conservative estimate. In a work reported by McNamara *et al.*[52], their RBE model (linear relationship between LET and RBE) was compared with RBE 1.1 in a treatment planning system for different tumour sites as shown in Figure 1.23.

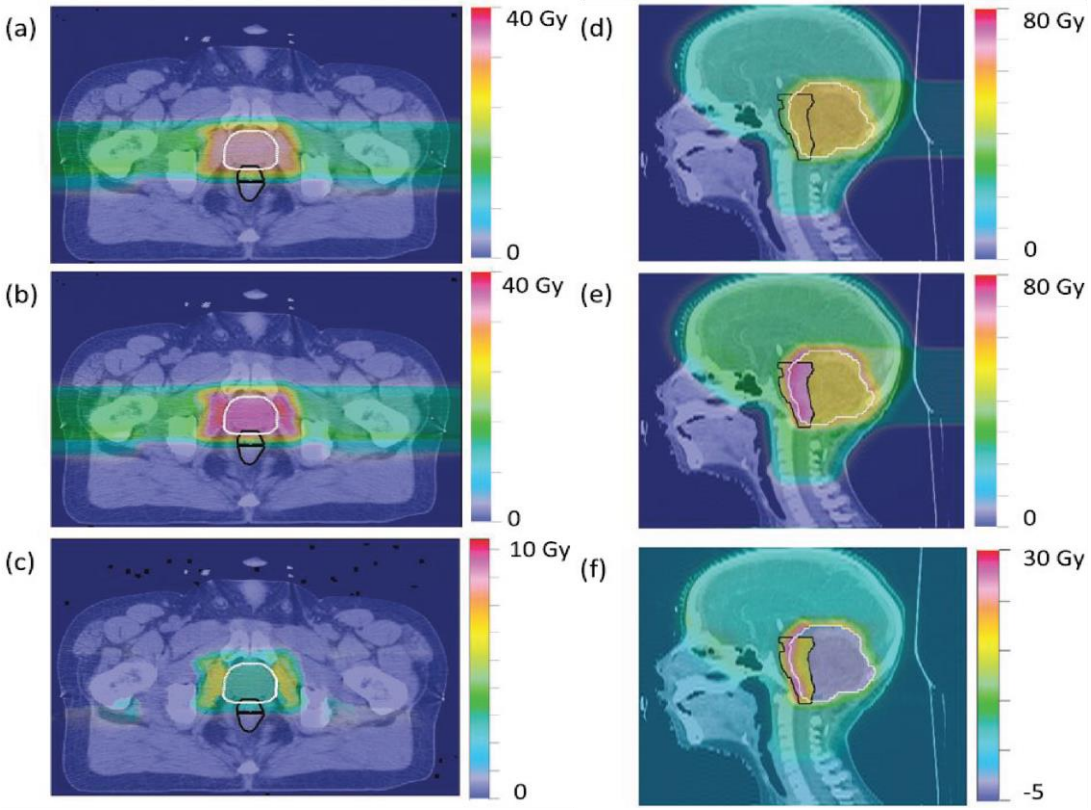

Figure 1.23 shows the patient simulation of prostate and head and neck proton treatment comparison of RBE 1.1 and RBE model[52]

In Figure 1.23, (a) and (d) exemplify patient biological dose distribution simulation of a prostate and a head and neck tumour using RBE 1.1 respectively. (b) and (e) are simulated with their own RBE model and lastly, (c) and (f) show the difference in

biological dose distribution for both tumour sites. As seen from (c) and (f), there is a higher biological dose in the target region when using their RBE model compared to RBE 1.1. Hence, this relates to having more doses being delivered to the target when using variable RBE models. Moreover, for the head and neck case, doses were delivered to a critical organ, the brainstem, and this might lead to brainstem toxicity.

Another example is illustrated in Figure 1.24, where Resch *et al.*[75] used Wedenberg *et al.'s*[54] RBE model to compare with RBE 1.1 using a nasopharyngeal cancer patient plan. It shows more doses being deposited using their variable RBE model (Figure 1.24b) at the optic nerves (orange and green) and brainstem region as compared to RBE 1.1 (Figure 1.24a).

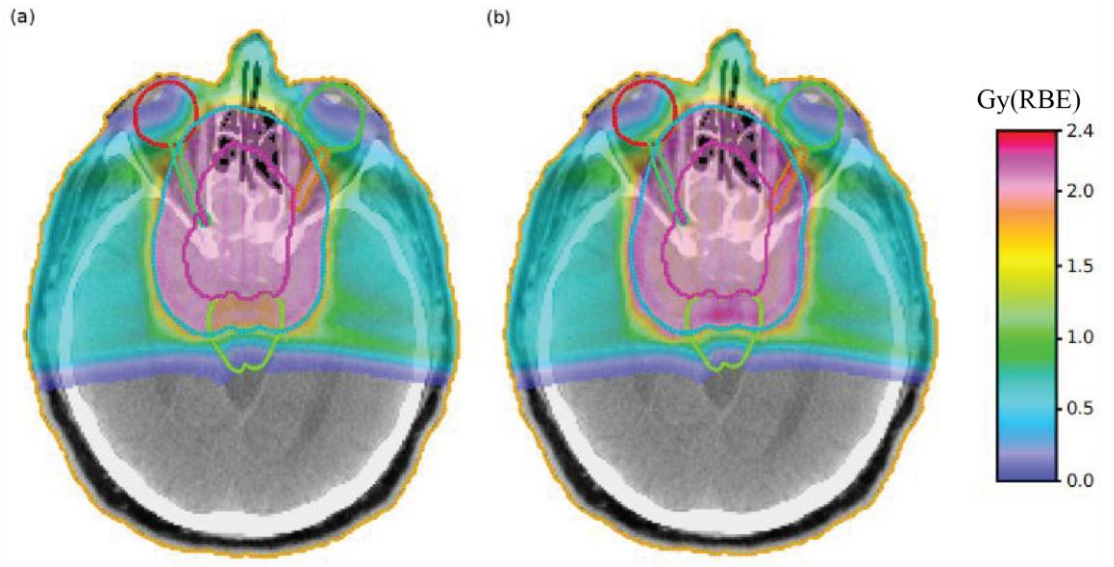

Figure 1.24 shows the patient simulation of nasopharyngeal cancer proton treatment dose comparison of RBE 1.1 and RBE model[75]

As shown in Figure 1.25, Rovik *et al.*[53] compared different RBE models contributed by other groups analysing the SOBP of different RBE models using simulated in a water phantom (sliced into voxels) along the central axis. Solid lines show the depth-dose distribution (left axis) of the physical dose and biological dose of a modulated proton

beam in the water. The dashed lines (right axis) showed the calculated RBE from different models.

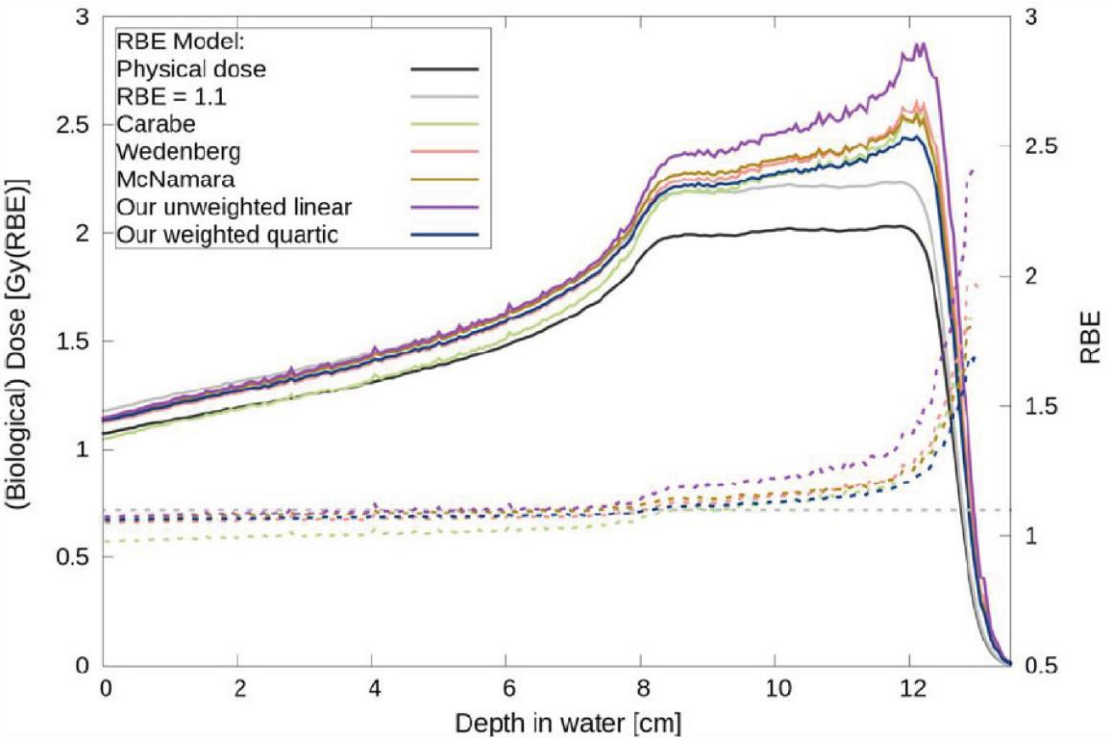

Figure 1.25 shows the RBE weighted dose and RBE plot of different RBE models. Solid lines refer to the comparison of depth dose distribution of different RBE Models. Dotted lines refer to the RBE values of the respective RBE models[53].

A single RBE value to each voxel was calculated along the beam axis, based on each RBE model discussed. The calculated RBE values were then multiplied with the physical dose to obtain the RBE-weighted dose (solid lines). Based on the results, there is a large variation between models especially towards the distal end of the SOBP. There is a significant rise in the RBE curves (dotted lines) towards the end of the range. These RBE models show a linear relationship between LET_D and RBE, where LET_D increases as proton come to a stop. This peak at the distal end of the SOBP is due to the RBE values resulting from the increase of LET_D.

In addition to the linear relationship between RBE and LET_D, some groups also presented that LET is non-linear to RBE. Chen *et al.*[48] had used in-vitro experimental data to measure the surviving fraction of one type of cell line. The result in Figure 1.26(a) shows that LET has a non-linear trend with RBE. This is also supported by Guan *et al.*[63] as shown in Figure 1.26(b), where they conducted in vitro experiments of two cell lines and the measurement of proton beam LET.

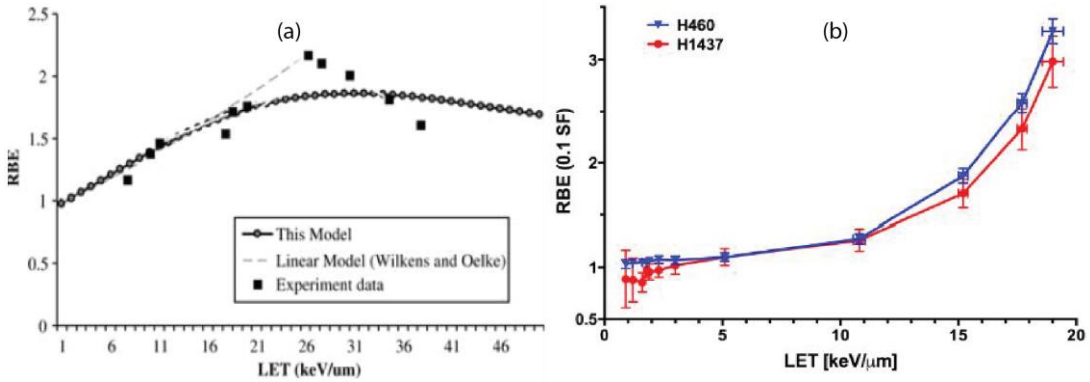

Figure 1.26 (a) shows the experimental RBE values for V79 CHO cells. Linear RBE model by Wilkens *et al.*[55] (Dashed line) and their model[48]. (b) shows the experimental RBE values for H460 and H1437 cells. RBE vs LET relationship of their model[48].

From these evidences, RBE or biological uncertainties in dose calculation might be magnified when the physical uncertainties (e.g. range uncertainty) are being reduced. Thus, it is still unclear if patients should be treated with RBE 1.1 or with a variable RBE model. If patients were to be treated with a variable RBE model, the choice of model that should be used clinically for the treatment planning remains questionable. Currently, there were no researches found in applying an RBE model-agnostic approach that will guide the clinical decision for PBT biological treatment planning. Therefore, this work aims to study the uncertainties contributed by each factor in the RBE model to, subsequently, reduce the RBE-weighted dose uncertainties. Focusing on LET_D, which drives the RBE curve, the current method to obtain LET_D is not clearly defined.

This thesis will examine whether the simulation of LET_D in water medium is a representation of simulating LET_D in different mediums (e.g. Cytoplasm and Nucleus). In addition, we aim to standardize the definition of LET_D and simulation parameters of Monte Carlo simulation to obtain LET_D. Thereafter, by incorporating the result achieved from the LET_D studies, we can apply them to calculate the different RBE models using different planning techniques and determine the RBE-weighted dose uncertainties distribution. By achieving this RBE model-agnostic approach, one need not rely heavily on any particular RBE models to guide the clinical decision for PBT biological treatment planning.

1.5 References

1. Paganetti H, Blakely E, Carabe-Fernandez A, et al. Report of the AAPM TG-256 on the relative biological effectiveness of proton beams in radiation therapy. *Med Phys*. 2019;46(3):e53-e78. doi:10.1002/mp.13390

2. Ling A, Foo LL, Lee E, et al. Singapore Cancer Registry Annual Report 2018. 2021:1-47.

3. Sung H, Ferlay J, Siegel RL, et al. Global Cancer Statistics 2020: GLOBOCAN Estimates of Incidence and Mortality Worldwide for 36 Cancers in 185 Countries. *CA Cancer J Clin*. 2021;71(3):209-249. doi:10.3322/caac.21660

4. Mould RF. Centennial of röntgen's discovery of X-rays. *J JASTRO*. 1996;8(1):1-7. doi:10.11182/jastro1989.8.1

5. Grubbé EH. Priority in the Therapeutic Use of X-rays. *Radiology*. 1933;21(2):156-162. doi:10.1148/21.2.156

6. Lauber K, Ernst A, Orth M, Herrmann M, Belka C. Dying cell clearance and its impact on the outcome of tumor radiotherapy. 2012;2(September):1-14. doi:10.3389/fonc.2012.00116

7. Baltas D, Sakelliou L, Zamboglou N. The physics of modern brachytherapy for oncology. *Phys Mod Brachytherapy Oncol*. 2006:1-648. doi:10.1201/9781420012422

8. Lawrence JH. Proton irradiation. *Am Cancer Soc*. 1957. doi:10.1002/1097-0142(195707/08)10:4<795::AID-CNCR2820100426>3.0.CO;2-B

9. Lin R, Hug EB, Schaefer RA, Miller DW, Slater JM, Slater JD. Conformal proton radiation therapy of the posterior fossa: A study comparing protons with three-dimensional planned photons in limiting dose to auditory structures. *Int J Radiat Oncol Biol Phys*. 2000;48(4):1219-1226. doi:10.1016/S0360-3016(00)00741-0

10. Lin LL, Vennarini S, Dimofte A, et al. Proton beam versus photon beam dose to the heart and left anterior descending artery for left-sided breast cancer. *Acta Oncol (Madr)*. 2015;54(7):1032-1039. doi:10.3109/0284186X.2015.1011756

11. Leiser D, Calaminus G, Malyapa R, et al. Tumour control and Quality of Life in children with rhabdomyosarcoma treated with pencil beam scanning proton therapy. *Radiother Oncol*. 2016;120(1):163-168. doi:10.1016/j.radonc.2016.05.013

12. Ventura LM, Grieco JA, Evans CL, et al. Executive functioning, academic skills, and quality of life in pediatric patients with brain tumors post-proton radiation therapy. *J Neurooncol*. 2018;137(1):119-126. doi:10.1007/s11060-017-2703-6

13. Arjomandy B, Taylor P, Ainsley C, et al. AAPM task group 224: Comprehensive proton therapy machine quality assurance. *Med Phys*. 2019;46(8):e678-e705. doi:10.1002/mp.13622

14. Brenner DJ, Elliston CD, Hall EJ, Paganetti H. Reduction of the secondary neutron dose in passively scattered proton radiotherapy, using an optimized pre-collimator/collimator. *Phys Med Biol*. 2009;54(20):6065-6078. doi:10.1088/0031-9155/54/20/003

15. Trinkl, S., Mares V, Englbrecht, F.S., et al. Systematic Out-of-Field Secondary

Neutron Spectrometry and Dosimetry in Pencil Beam Scanning Proton Therapy. *Med Phys*. 2017;44(5):1912-1920. doi:https://doi.org/10.1002/mp.12206

16. Newhauser WD, Durante M. Assessing the risk of second malignancies after modern radiotherapy. *Nat Rev Cancer*. 2011;11(6):438-448. doi:10.1038/nrc3069

17. Schneider U, Lomax A, Besserer J, Pemler P, Lombriser N, Kaser-Hotz B. The Impact of Dose Escalation on Secondary Cancer Risk After Radiotherapy of Prostate Cancer. *Int J Radiat Oncol Biol Phys*. 2007;68(3):892-897. doi:10.1016/j.ijrobp.2007.02.029

18. Hälg RA, Schneider U. Neutron dose and its measurement in proton therapy- current State of Knowledge. *Br J Radiol*. 2020;93(1107). doi:10.1259/bjr.20190412

19. Pedroni E. *Latest Developments in Proton Therapy*. Vienna, Austria; 2000. doi:10.1016/s0151-9107(99)80030-0

20. Kooy HM, Clasie BM, Lu HM, et al. A Case Study in Proton Pencil-Beam Scanning Delivery. *Int J Radiat Oncol Biol Phys*. 2010;76(2):624-630. doi:10.1016/j.ijrobp.2009.06.065

21. Chuong M, Badiyan SN, Yam M, et al. Pencil beam scanning versus passively scattered proton therapy for unresectable pancreatic cancer. *J Gastrointest Oncol*. 2018;9(4):687-693. doi:10.21037/jgo.2018.03.14

22. DE. B. Current developments in proton therapy: a review. *Phys Med Biol*. 1993. doi:10.1088/0031-9155/38/10/001

23. ICRP. *The 2007 Recommendations of the International Commission on Radiological Protection*.; 2007. doi:10.1017/CBO9781107415324.004

24. Paganetti H. *Proton Therapy Physics (Series in Medical Physics and Biomedical Engineering)*. First Edit. CRC Press; 2012. doi:10.1201/9780367803551

25. Berger MJ, Inokuti M, Andersen HH, et al. *ICRU Report 49*. Vol os25.; 1993. doi:10.1093/jicru/os25.2.Report49

26. Bethe H. Zur Theorie des Durchgangs schneller Korpuskularstrahlen durch Materie. *Ann Phys*. 1930;397(3):325-400. doi:10.1002/andp.19303970303

27. Seltzer SM. ICRU Report 85 FUNDAMENTAL QUANTITIES AND UNITS FOR IONIZING RADIATION. *Jicru*. 2011;11(1). doi:10.1093/jicru/nd

28. Seltzer SM, Berger MJ. Bremsstrahlung energy spectra from electrons with kinetic energy 1 keV-10 GeV incident on screened nuclei and orbital electrons of neutral atoms with Z = 1-100. *At Data Nucl Data Tables*. 1986;35(3):345-418. doi:10.1016/0092-640X(86)90014-8

29. Tufan MÇ, Namdar T, Gümüş H. Stopping power and CSDA range calculations for incident electrons and positrons in breast and brain tissues. *Radiat Environ Biophys*. 2013;52(2):245-253. doi:10.1007/s00411-013-0457-x

30. Elizabeth McGowan S, Burnet Simon J Thomas NG. Incorporating Range Uncertainty into Proton Therapy Treatment Planning. 2015.

31. Sulistya E, Hermanto A. Determination of Proton Energy and Dosage to Obtain SOBP Curve in the Proton Beam Radiotherapy Treatment Planning. *Int J Eng Res Appl*. 2016;6(8):28-30.

32. Chaikh A, Docquière N, Bondiau P-Y, Balosso J. Impact of dose calculation models on radiotherapy outcomes and quality adjusted life years for lung cancer treatment: Do we need to measure radiotherapy outcomes to tune the radiobiological parameters of a normal tissue complication probability model? *Transl Lung Cancer Res*. 2016;5(6):673-680. doi:10.21037/tlcr.2016.11.04

33. Jia X, Pawlicki T, Murphy KT, Mundt AJ. Proton therapy dose calculations on GPU: advances and challenges. *Transl Cancer Res*. 2012;1(3):207-216. doi:10.3978/j.issn.2218-676X.2012.10.03

34. Zhang R, Newhauser WD. Calculation of water equivalent thickness of materials of arbitrary density, elemental composition and thickness in proton beam irradiation Rui. *Phys Med Biol*. 2009;54(6):1383–1395. doi:10.1038/jid.2014.371

35. Lomax ME, Folkes LK, O'Neill P. Biological consequences of radiation-induced DNA damage: Relevance to radiotherapy. *Clin Oncol*. 2013;25(10):578-585. doi:10.1016/j.clon.2013.06.007

36. Hall EJ, Giaccia AJ. *Radiobiology for the Radiologist: 7th Edition*. Lippincott Williams and Wilkins Publishing; 2012.

37. Kellerer AM, Rossi HH. A Generalized Formulation of Dual Radiation Action. *Radiat Res*. 2006;75(3):471. doi:10.2307/3574835

38. van Leeuwen CM, Oei AL, Crezee J, et al. The alfa and beta of tumours: A review of parameters of the linear-quadratic model, derived from clinical radiotherapy studies. *Radiat Oncol*. 2018;13(1):1-11. doi:10.1186/s13014-018-1040-z

39. Giovannini G, Böhlen T, Cabal G, et al. Variable RBE in proton therapy: Comparison of different model predictions and their influence on clinical-like scenarios. *Radiat Oncol*. 2016;11(1):1-16. doi:10.1186/s13014-016-0642-6

40. Jones B. Why RBE must be a variable and not a constant in proton therapy. *Br J Radiol*. 2016;89(1063):1-10. doi:10.1259/bjr.20160116

41. Ödén J, DeLuca PM, Orton CG. The use of a constant RBE=1.1 for proton radiotherapy is no longer appropriate: *Med Phys*. 2018;45(2):502-505. doi:10.1002/mp.12646

42. Paganetti H. Relative biological effectiveness (RBE) values for proton beam therapy. Variations as a function of biological endpoint, dose, and linear energy transfer. *Phys Med Biol*. 2014;59(22):R419-R472. doi:10.1088/0031-9155/59/22/R419

43. Paganetti H, Niemierko A, Ancukiewicz M, et al. Relative biological effectiveness (RBE) values for proton beam therapy. *Int J Radiat Oncol Biol Phys*. 2002;53(2):407-421. doi:10.1016/S0360-3016(02)02754-2

44. Matsumoto Y, Matsuura T, Wada M, Egashira Y, Nishio T, Furusawa Y. Enhanced radiobiological effects at the distal end of a clinical proton beam: In vitro study. *J Radiat Res*. 2014;55(4):816-822. doi:10.1093/jrr/rrt230

45. Sørensen BS, Bassler N, Nielsen S, et al. Relative biological effectiveness (RBE) and distal edge effects of proton radiation on early damage in vivo. *Acta Oncol (Madr)*. 2017;56(11):1387-1391. doi:10.1080/0284186X.2017.1351621

46. Ilicic K, Combs SE, Schmid TE. New insights in the relative radiobiological

effectiveness of proton irradiation. *Radiat Oncol*. 2018;13(1):4-11. doi:10.1186/s13014-018-0954-9

47. Carabe-Fernandez A, Dale RG, Jones B. The incorporation of the concept of minimum RBE (RbEmin) into the linear-quadratic model and the potential for improved radiobiological analysis of high-LET treatments. *Int J Radiat Biol*. 2007;83(1):27-39. doi:10.1080/09553000601087176

48. Chen Y, Ahmad S. Empirical model estimation of relative biological effectiveness for proton beam therapy. *Radiat Prot Dosimetry*. 2012;149(2):116-123. doi:10.1093/rpd/ncr218

49. Chen Y, Li J, Li C, Qiu R, Wu Z. A modified microdosimetric kinetic model for relative biological effectiveness calculation. *Phys Med Biol*. 2018;63(1). doi:10.1088/1361-6560/aa9a68

50. Frese MC, Wilkens JJ, Huber PE, Jensen AD, Oelfke U, Taheri-Kadkhoda Z. Application of constant vs. variable relative biological effectiveness in treatment planning of intensity-modulated proton therapy. *Int J Radiat Oncol Biol Phys*. 2011;79(1):80-88. doi:10.1016/j.ijrobp.2009.10.022

51. Grün R, Friedrich T, Krämer M, et al. Physical and biological factors determining the effective proton range. *Med Phys*. 2013;40(11). doi:10.1118/1.4824321

52. McNamara AL, Schuemann J, Paganetti H. A phenomenological relative biological effectiveness (RBE) model for proton therapy based on all published in vitro cell survival data. *Phys Med Biol*. 2015;60(21):8399-8416. doi:10.1088/0031-9155/60/21/8399

53. Rørvik E, Thornqvist S, Stokkevag CH, Dahle TJ, Fjæra LF, Ytre-Hauge KS. A phenomenological biological dose model for proton therapy based on linear energy transfer spectra. *Med Phys*. 2017;44(6):2586-2594. doi:10.1002/mp.12216

54. Wedenberg M, Lind BK, Hårdemark B. A model for the relative biological effectiveness of protons: The tissue specific parameter α/β of photons is a predictor for the sensitivity to LET changes. *Acta Oncol (Madr)*. 2013;52(3):580-588. doi:10.3109/0284186X.2012.705892

55. Wilkens JJ, Oelfke U. A phenomenological model for the relative biological effectiveness in therapeutic proton beams. *Phys Med Biol*. 2004;49(13):2811-2825. doi:10.1088/0031-9155/49/13/004

56. Harding C. Religious Transformation in South Asia: The Meanings of Conversion in Colonial Punjab. *Relig Transform South Asia Meanings Convers Colon Punjab*. 2009;(36):1-320. doi:10.1093/acprof:oso/9780199548224.001.0001

57. Hawkins RB. A microdosimetric-kinetic model of cell death from exposure to ionizing radiation of any LET, with experimental and clinical applications. *Int J Radiat Biol*. 1996;69(6):739-755. doi:10.1080/095530096145481

58. Folkard M, Prise KM, Vojnovic B, Newman HC, Roper MJ, Michael BD. Inactivation of V79 cells by low-energy protons, deuterons and helium-3 ions. *Int J Radiat Biol*. 1996;69(6):729-738. doi:10.1080/095530096145472

59. Coutrakon G, Cortese J, Ghebremedhin A, et al. Microdosimetry spectra of the Loma Linda proton beam and relative biological effectiveness comparisons. *Med Phys*.

1997;24(9):1499-1506. doi:10.1118/1.598038

60. Wouters BG, Sy AM, Skarsgard LD. Low-dose hypersensitivity and increased radioresistance in a panel of human tumor cell lines with different radiosensitivity. *Radiat Res*. 1997;146:399.

61. Carabe A, Moteabbed M, Depauw N, Schuemann J, Paganetti H. Range uncertainty in proton therapy due to variable biological effectiveness. *Phys Med Biol*. 2012;57:1159.

62. Chen Y, Ahmad S. Empirical model estimation of relative biological effectiveness for proton beam therapy. *Radiat Prot Dosimetry*. 2012;149(2):116-123. doi:10.1093/rpd/ncr218

63. Guan F, Bronk L, Titt U, et al. Spatial mapping of the biologic effectiveness of scanned particle beams: Towards biologically optimized particle therapy. *Sci Rep*. 2015;5:1-10. doi:10.1038/srep09850

64. Jones B. Towards achieving the full clinical potential of proton therapy by inclusion of LET and RBE models. *Cancers (Basel)*. 2015;7(1):460-480. doi:10.3390/cancers7010460

65. Grün R, Friedrich T, Traneus E, Scholz M. Is the dose-averaged LET a reliable predictor for the relative biological effectiveness? *Med Phys*. 2019;46(2):1064-1074. doi:10.1002/mp.13347

66. Grassberger C, Paganetti H. Elevated LET components in clinical proton beams. *Phys Med Biol*. 2011;56(20):6677-6691. doi:10.1088/0031-9155/56/20/011

67. Mendonca MS, Chang DS, Lasley FD, Das IJ, Dynlacht JR. *Basic Radiotherapy Physics and Biology*.; 2014. doi:10.1007/978-3-319-06841-1

68. Guan F, Peeler C, Bronk L, et al. Analysis of the track- and dose-averaged LET and LET spectra in proton therapy using the geant 4 Monte Carlo code. *Med Phys*. 2015;42(11):6234-6247. doi:10.1118/1.4932217

69. Wilkens JJ, Oelfke U. Analytical linear energy transfer calculations for proton therapy. *Med Phys*. 2003;30(5):806-815. doi:10.1118/1.1567852

70. Romano F, Cirrone GAP, Cuttone G, et al. A Monte Carlo study for the calculation of the average linear energy transfer (LET) distributions for a clinical proton beam line and a radiobiological carbon ion beam line. *Phys Med Biol*. 2014;59(12):2863-2882. doi:10.1088/0031-9155/59/12/2863

71. Granville DA, Sawakuchi GO. Comparison of linear energy transfer scoring techniques in Monte Carlo simulations of proton beams. *Phys Med Biol*. 2015;60(14). doi:10.1088/0031-9155/60/14/N283

72. Kraft G. Tumor therapy with heavy charged particles. *Prog Part Nucl Phys*. 2003;46(2):I. doi:10.1016/s0146-6410(01)00151-x

73. Paganetti H. Relating proton treatments to photon treatments via the relative biological effectiveness - Should we revise current clinical practice? *Int J Radiat Oncol Biol Phys*. 2015;91(5):892-894. doi:10.1016/j.ijrobp.2014.11.021

74. Matsumoto Y, T. Matsuura MW, Egashira Y, Nishio T, Furusawa F. Enhanced radiobiological effects at the distal end of a clinical proton beam: in vitro study. *J*

Radiat Res. 2014;55:816.

75. Resch AF, Landry G, Kamp F, et al. Quantification of the uncertainties of a biological model and their impact on variable RBE proton treatment plan optimization. *Phys Medica*. 2017;36:91-102. doi:10.1016/j.ejmp.2017.03.013

Chapter 2 Configuration of Monte Carlo Simulation Toolkit

Monte Carlo (MC) Simulation is the gold standard for dose calculation in radiotherapy[1]. This thesis uses GEANT4[2–4] and TOPAS[5,6] MC simulation extensively for RBE and LET dose calculation studies. In this chapter, we will discuss the implementation of the MC Simulation toolkit of GEANT4 and TOPAS. GEANT4 is the acronym for Geometry and Tracking and TOPAS is the acronym for Tool for Particle Simulation. They provide the functionalities required for simulation in various applications such as Medical, Space and Radiation Protection. To achieve the primary aim of the thesis, MC simulation plays an important role for all studies in this work. Therefore the workflow and structure of the system will be presented and validated in order to obtain accurate results.

2.1 The Monte Carlo Method

As described by Alex Bielajew, "The Monte Carlo method is a numerical solution to a problem that models objects interacting with other objects or their environment based upon simple object-object or object-environment relationships. It represents an attempt to model nature through direct simulation of the essential dynamics of the system in question."[7]

The MC method is used in numerous physics disciplines to approximate a solution of differential or integro-differential equation in the case of transport. In radiation transport, the main transport equation to be solved is the Boltzmann equation[8].

$$\left(\vec{\Omega}\cdot\vec{\nabla}\right)\Phi\left(\vec{r},\vec{\Omega},E\right)+\sigma(\vec{r},E)\Phi\left(\vec{r},\vec{\Omega},E\right)=S\left(\vec{r},\vec{\Omega},E\right)+\int dE'\int d\vec{\Omega}'\,\sigma_s\left(\vec{r},\overrightarrow{\Omega'},E'\rightarrow\vec{\Omega},E\right)\Phi\left(\vec{r},\overrightarrow{\Omega'},E'\right) \quad (2.1)$$

The first term on the left-hand side of the equation is the streaming operator $\left(\vec{\Omega}\cdot\vec{\nabla}\right)$ multiply the fluence ($\Phi\left(\vec{r},\vec{\Omega},E\right)$) by the which accounts for the particle travel derived

from accounting for particles entering and leaving the volume ΔV through the surface. The second term on the left-hand side of the equation represents the collision density (average number of collisions) which accounts for the loss of particles from the interactions that result in a change of momentum of the particle. $\sigma(\vec{r}, E)$ is the probability of interaction per unit path length. The first term on the right-hand side of the equation is the *Source Function* which characterizes the spatial, angular and energy distribution of the radiation source. The second term on the right-hand side of the equation is the collision integral where $\int dE' \int d\vec{\Omega}' \, \sigma_s \left(\vec{r}, \overrightarrow{\Omega'}, E' \rightarrow \vec{\Omega}, E\right)$ is the total cross-section.

MC uses a statistical approach where it is an excellent technique to study the random process of radiation transport. This approach will however mean that there will be statistical and systematic uncertainties. Statistical uncertainties arise from the lack of simulated histories while systematic uncertainties are caused by any approximations in the physics models. Nonetheless, the MC simulation is still used for this purpose as it is regarded as the gold standard in radiation transport simulation[1], better than other Type 'a' and 'b' dose calculation algorithms.

Type 'a' and 'b' dose calculation algorithms are proposed by Knöös *et al.*[9] and Type 'c' dose calculation algorithm is proposed by Ojala *et al.*[10]. Type 'a' is a correction-based algorithm (semi-empirical). It is based on measurement data where a water phantom is irradiated with a standard source skin distance ($SSD = 100\, cm$) setup. Doses are collected at multiple points. In the patient set up, the dose is then corrected based on beam modifiers (e.g. wedges), patient contours and tissue heterogeneities. Subsequently, this is replaced by Type 'b' dose calculation algorithm. Type 'b' is a model-based dose calculation algorithm where it uses superposition and convolution

techniques. Measurements (fewer than Type ‘a’) in water phantom is done and the measured data is used a finger print to characterize the beam. When the identity of the beam is determine, dose is calculated based on first principle of attentuation and scatter. The treatment planning system by Varian used in this work is a type ‘b’ dose calculation algorithm (Proton Convolution Superposition, PCS) and has been discussed in Chapter 1. Type ‘c’ is a grid-based linear Boltzmann transport equation solver. It provides better accuracy in modelling secondary electron transport which is important for accurate heterogeneity correction. It has the ability to calculate accurate dose deposition in high-Z materials. The Monte Carlo system is classified as a Type ‘c’ dose calculation algorithm.

In this work, GEANT4 and TOPAS are used for all the simulation experiments. GEANT4 is an object-oriented computing toolkit, and TOPAS wraps and extends the GEANT4 classes. The physics model and transport implementation are the same as GEANT4.

We started off using GEANT4 by understanding the workflow and the GEANT4 classes to simulate a proton beam. TOPAS is then used to configure geometries like treatment head and patient CT due to the simplicity of the text-based parameter files where C++ coding is not necessary. This is widely used in medical physics research due to its flexibility to configure the physics model and input different types of geometries for dose calculation. MC simulation allows greater detail in the modelling of secondary electron transport.

The algorithm used in GEANT4 is the condensed history algorithm; this is in contrast to the track structure algorithm which is employed in GEANT4-DNA. Track structure algorithm is only efficient if the geometry is small as all interactions by the particle are

simulated. In a condensed history algorithm, all interactions are classified as “hard” or “soft” collisions[8]. The condensed history algorithm is dependent on the energy loss (ΔE) of the charged particle during collision. If energy loss exceeds a particular threshold energy (E_c), the collision is considered a hard collision, otherwise, it would result in a soft collision. This threshold is set by the user and the smaller the threshold is, the more accurate the result will be. However, this would come at the cost of simulation time. Usually, all hard collisions are simulated explicitly while soft collisions are accounted for by approximation through the multiple scattering theory[1]. The theory gives a probability distribution of the charged particle parameters and that is based on the azimuthal and polar multiple scattering angles. *Continuous Slowing Down Approximation* (CSDA) is to account for energy loss in a soft collision as shown in Equation 1.8. This avoids modelling explicitly for all the secondary electrons.

The subsequent sections will discuss the concept and pipeline of GEANT4 and TOPAS including a discussion on how the commissioning of the MC system has been done for the specific machine that NCCS has installed. Commissioning the MC system will thus allow for the proper comparison of clinical treatment plans between a commercial clinical TPS and MC simulation. The MC simulation can be used as a secondary check for the clinical treatment plans.

2.2 GEANT4/TOPAS Simulation Tool

In this section, we will discuss the workflow and concepts behind the GEANT4 simulation system. The basic concept of GEANT4 is categorized into five parts – *Run*, *Event*, *Track*, *Step* and *Processes*.

1. *Run* – It refers to the start of the MC simulation and as an analogy of the real experiment, “Beam on”. It is a collection of events where there can be no changes to the geometry of the detector and physics processes.
2. *Event* – In an event, primary particle tracks are generated and are pushed into a stack. The tracks are then processed individually, and secondary tracks are produced and pushed in the stack. One event ends when the stack is empty upon repeating the cycle as mentioned above.
3. *Track* – A track is a snapshot of a particle containing the position and the physical quantities of the *current instance*. The track is deleted once it is ended. The tracks end based on the following conditions; when the particle exits the world volume, disappear, is defined by the user to be killed or when it reaches zero kinetic energy.

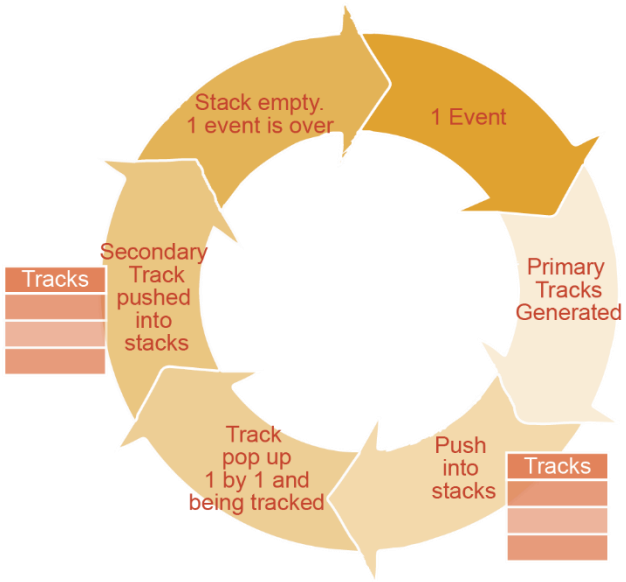

Figure 2.1 shows the flowchart of a Condensed History Algorithm where a single *Run* consists of N_E number of *Events* and each *Event* consists of N_t number of *Tracks*

4. *Step* - A step has two points – The beginning of a step point and the End of the step point as shown in Figure 2.2. It contains the information of the particle such as energy loss on the step and the time of flight spent on the step. Each point knows

the volume and material it is in. In the case where the step is limited by the volume boundary, the endpoint will be on the boundary and considered to be part of the next volume.

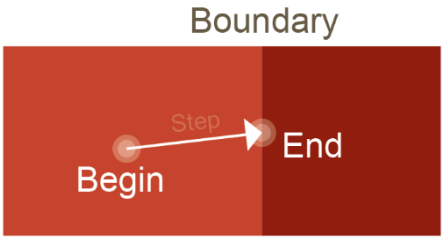

Figure 2.2 shows the concept of a Step in Monte Carlo Simulation. *Begin* shows the start of a stepping point while *End* shows the end of the particular step. The step will stop upon reaching the boundary as defined by the difference in color.

The step length is randomly sampled using the mean free path of the interaction using the cross-section of the physics process and density of the atoms given by the following equation

$$\lambda(E) = \left(\sum_i \left[\frac{N_A \rho w_i}{A_i} \times \sigma(Z_i, E) \right] \right)^{-1} \tag{2.2}$$

where N_A is the Avogadro's constant, ρ is the density of the medium, A_i is the mass of a mole of the *ith* element, w_i is the proportion by mass of the *ith* element and $\sigma(Z_i, E)$ is the total cross-section per atom of the process with Z_i being the atomic number of the *ith* element.

5. *Processes* – Each particle possesses its own set of applicable processes. It describes how particles interact with the material or the volume. Every step the particle takes, all processes listed (e.g. physics processes) will be invoked to obtain the proposed physical interaction length. The step is then limited by the process which requires the shortest interaction length.

Every simulation will go through these procedures and different outputs (dose, linear energy transfer, step size, etc.) can be scored depending on the user's needs. After a brief overview of the underlying concepts of GEANT4, we will detail the process of configuring the MC system according to the physical properties of the proton machine. The workflow and the details of some important MC simulation parameters will also be discussed in the following section.

2.3 Configuring MC System

Three important simulation parameters are crucial for configuring a successful Proton Therapy MC simulation system – (1) Physics Model, (2) Twiss Parameters and (3) Cut-off Energy (setCut) and step size (*stepMax*)[11]. The results depend heavily on the physics models (e.g., electromagnetic and nuclear models) and these parameters incorporated in the simulation. In this work, we will model a Pencil Beam Scanning (PBS) Proton Therapy system which follows the specification of NCCS's PT system from Hitachi Ltd (Hitachi, Ltd. Healthcare Business Unit) as shown in Figure 2.3. The following figure is drawn using AutoCAD software for easier visualization.

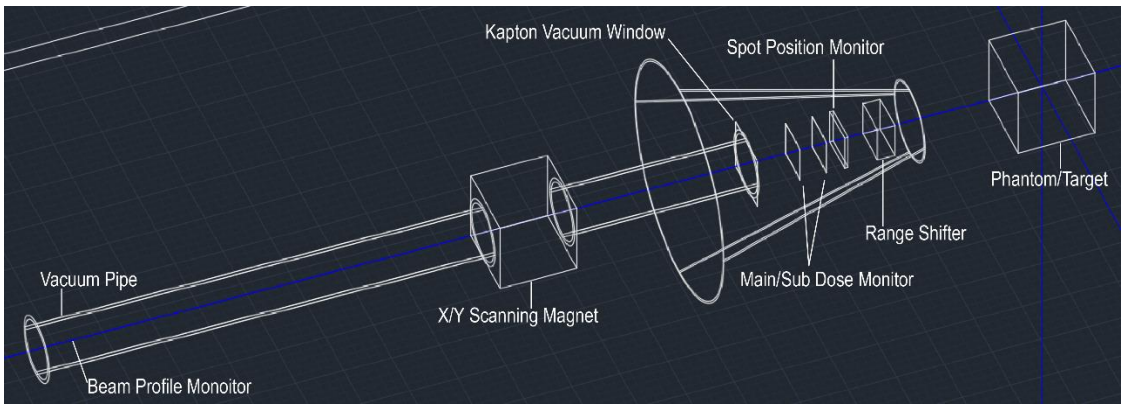

Figure 2.3 shows the beamline of a PBS PT system consisting of a few main components – Vacuum Pipe, X and Y direction Scanning Magnet, Main and Sub Dose monitor, Spot Position Monitor (SPM) and Range Shifter.

Figure 2.3 shows the geometry of the nozzle of a PBS PT system. The proton will start at the Beam Profile Monitor (BPM) where the phase space parameters of the beam are provided by the manufacturer at this position. The proton will travel down the vacuum pipe passing through the X and Y Direction Scanning Magnet, Main and Sub dose Monitor, Spot Position Monitor (SPM) and Range Shifter. The BPM, together with the Main and Sub Dose Monitor are used to monitor different aspects of the beam. Meanwhile, X and Y Direction Scanning Magnets as well as the Range Shifter are used to shape or modify the beam characteristics. The target is the position where the user can place the desired phantoms or CT images for dose scoring.

Dose scoring is heavily dependent on the three simulation protocols mention before. The physics model is the most important feature of Monte Carlo Simulation. It affects the spatial dose distribution of the proton beam such as the range and the beam spot size. The three main physical interactions of protons that are of clinical relevance (<250 MeV) have been discussed in Chapter 1.3, namely inelastic and elastic Coulomb scattering, and non-elastic nuclear reactions. Inelastic coulomb scattering contributes significantly to the dose distribution and the range of the proton beam. Elastic Coulomb scattering affects the lateral straggling of the proton beam which thus affects the beam spot size. The non-elastic nuclear reaction has a lower interaction cross-section which contributes less than the above two interactions.

2.3.1 Physics Model

In GEANT4, there is a list of physics models available depending on the application used. In medical physics for proton therapy, there have been studies done on which model is best suited for the application. In our study, we followed the recommendations where G4EmStandardPhysics_option4 is used for electromagnetic physics processes[11], and g4h-phy_FTFP_BERT (FRITIOF model[12] (FTFP) and Bertini-style cascade[13]

(BERT)) are used when hadrons energy are below $6\,GeV$ and above $3\,GeV$ respectively[14].

Electromagnetic process

In general, G4EmStandardPhysics_option4 consists of multiple models to account for electromagnetic interactions at different energy range. It is also considered the most accurate electromagnetic physics model for use in Medical Physics.

For instance, Compton scattering (CS) above and below $20\ MeV$ is governed by Klein-Nishina and Monash University Model[15] respectively. Photoelectric Effect (PE) and Rayleigh use the Livermore database where total cross sections for PE, CS, Rayleigh, pair production and Bremsstrahlung are interpolated from the data for the recommended energy range between $250\ eV - 100\ GeV$. Below $250\ eV$ can be evaluated however at the expense of reduced accuracy. *PENetration and Energy LOss of Positrons and Electrons* (PENELOPE) database is used for gamma conversion below $1\ GeV$.

Multiple Coulomb Scattering (MSC) uses *Goudsmit-Saunderson* model[16] for e^+ and e^- with energy between $0 - 100\,MeV$ and *WentzelVI* model[17] for any particle of energy between $100\ MeV - 100\ TeV$.

The extensive explanations of the physics processes have been discussed in the *Physics Reference Manual*[18] of GEANT4

Nuclear process

FTFP and BERT models are nonelastic models used for the inelastic hadron-nucleus processes in our application. FTFP model is first used for particles with energy below

6 GeV. In the overlapping region of energy and particle type between FTFP and BERT, a probability of a linear decrease from 1 to 0 is sampled to determine the choice of model used for the particular particle. As discussed in Chapter 1, the main secondary particles from the nuclear interactions are protons, neutrons, helium and gamma. These particles interaction are accounted for by the FTFP and BERT model.

2.3.2 Twiss Parameters

The other simulation parameter is the Twiss Parameter. This parameter characterises the phase space in TOPAS. The phase space information describes the initial beam profile which is influential to the final beam profile at the isocentre. Isocenter is defined at a point in space where the radiation beams intersect during the rotation of the gantry. The ellipse shows a typical phase space of particles in a synchrotron. This ellipse is defined by the 3 Twiss parameters, α, β, γ, and beam emittance, ε[19].

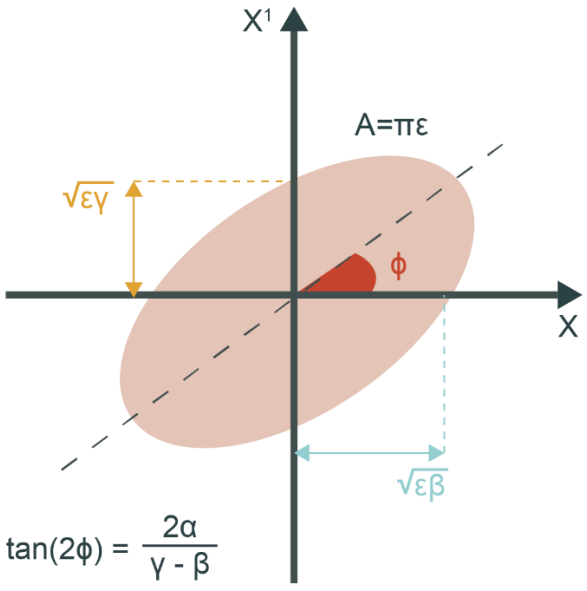

Figure 2.4 shows the beam ellipse in phase space and the relationship of the Twiss parameters. X and X' describe the position and the transverse momenta, respectively.

α, β and ε are independent variables whereas γ is dependent on both α and β. α determines if the beam is converging or diverging while β is related to the beam spot size. The beam emittance, ε, is the phase space area of the beam which defines the beam quality. The Twiss parameters and emittance are defined by Equations 2.3 and 2.4.

$$\gamma = \frac{1 + \alpha^2}{\beta} \tag{2.3}$$

$$\varepsilon = \gamma x^2 + 2\alpha x x' + \beta x'^2 \tag{2.4}$$

In this work, α, β and ε parameters at the BPM are given by the manufacturer for both vertical (Y) and horizontal (X) beam profiles. The phase space information of the proton beam used to generate the SOBP and pristine Bragg Peak in the simulation follows the spot scanning Proton Therapy System from Hitachi Ltd[11].

2.3.3 Cut-off Energy (*setCut*) and step size (*stepMax*)

The last important parameter of MC simulation is the cut-off energy (*setCut* value) and step size of the particle (*stepMax* value). The cut-off energy is the production threshold of secondary particles resulting from the interaction between the primary particle and the medium. The step size is the maximum length the particle can travel, but limited by the energy loss, cross-section of the medium and the boundary conditions such as voxel size or different medium. These two parameters are chosen such that the MC system is optimized to balance the computing speed and accuracy. Ideally, the lower the values are, the more accurate the result will be. However, this will come at the expense of computing speed. In addition, if the voxel size of the detector is larger than the *setCut* and *stepMax* value, the accuracy will not improve. Therefore, these parameters must be set reasonably to produce an accurate result while not compromising the computation speed.

2.4 Validating MC Simulation System for our work

In this section, we will discuss the procedures of validating the TOPAS-based MC simulation system. Due to the limitation of this work where the physical proton beam is absent, we are validating the MC Simulation system against the TPS. Since the gantry in NCCS is similar to Mayo Clinic (Rochester, Minnesota, United States), our TPS has been configured with their beam data. However, it is important to note that the MC Simulation system and TPS should eventually be validated against the experimental result. Due to the limitation of not having the Proton therapy system ready, we will only be validating TOPAS against TPS. The calculation algorithm used by TPS (Proton Convolution Superposition PCS), although sufficient, is not as accurate as MC Simulation. Therefore, differences in the dose calculated are expected. We follow the AAPM TG224 Report[20] closely such that the validation of spot position, range, beam width and gamma analysis are within the tolerance stated in the report. This report is established by the American Association of Physicists in Medicine's Science Council under the Radiation Therapy Committee and Work Group on Particle Beams. They developed comprehensive quality assurance guidelines and recommendations to ensure the safe, accurate, and consistent delivery of radiation therapy dose distributions to patients.

In the very first step of configuring the TOPAS, the schematic diagram of the proton beam nozzle as shown in Figure 2.3 would need to be translated into TOPAS by placing the components at the respective position and assigning the materials to each component. Figure 2.5 shows a zoomed-out schematic of the proton beam nozzle placed in the "World" we have created in TOPAS. The smaller zoomed-in schematic shows the phantom we have created, and it is placed at the isocentre of the gantry defined by the intersection point of the yellow axes.

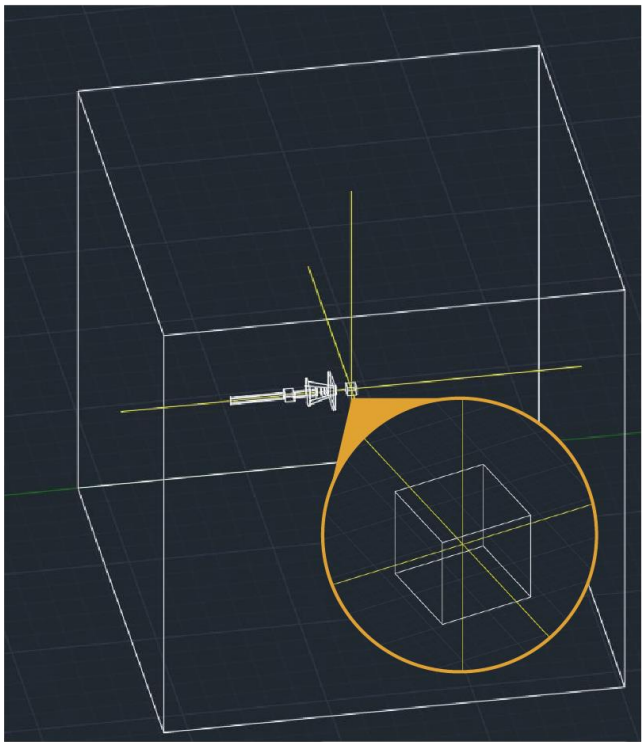

Figure 2.5 shows the "World" of the MC Simulation where we placed the proton beam nozzle. The zoomed-in diagram shows the target placed at the isocentre defined by the yellow axes.

After the proton beam line "installation", the following procedures are crucial in validating the MC simulation system - *Nozzle and Couch Rotation*, *Spot Position, Range*, *Beam Width* and *Gamma Analysis*.

Coordinate System

It can be confusing in obtaining the correct rotation angle for nozzle and couch when the axes in TOPAS and TPS are different. In TPS, both the nozzle and couch rotation can be accounted for by rotating the individual components themselves. The axis of the TPS following the IEC coordinate system is as shown in Figure 2.6.

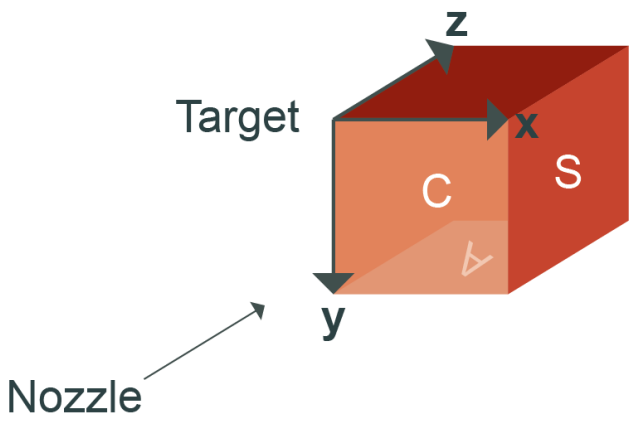

Figure 2.6 shows the axes of the TPS coordinate system where C, A and S refer to the Coronal, Axial and Sagittal planes of the patient.

However, when a patient file (DICOM – Digital Imaging and Communication in Medicine) is imported from TPS into TOPAS, the target will require a passive rotation ($-90°$) along the x-axis with respect to the Target axis to obtain the coordinate system as shown in Figure 2.7 (A) to (B). This is to match the coordinate system of the patient to TPS. The coordinate system is shown in Figure 2.7 (B) is with respect to the "World". Thereafter, TOPAS will take in the nozzle and couch rotation values and perform an active rotation to the Target axis accordingly. The nozzle rotation angle is then applied along the y-axis with respect to the "World" coordinate while the couch rotation is applied along the z-axis with respect to the "World" coordinate.

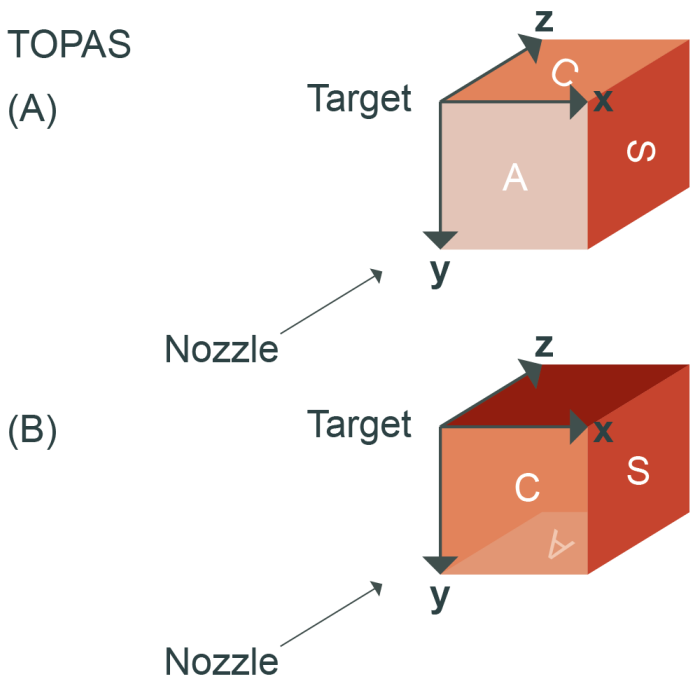

Figure 2.7 shows the axes of the TOPAS coordinate system where C, A and S refer to the Coronal, Axial and Sagittal planes of the patient. (A) shows the original coordinate system before any rotation is applied to the target. (B) shows the corrected coordinate system with respect to TPS.

Spot Position

After matching the coordinate system between TPS and TOPAS, we will compare the spot position of the beam in a water phantom at isocentre. We created a $40 \times 40 \times 40\ cm$ water phantom in TPS with a target size of $3 \times 3 \times 3\ cm$ at isocentre. Three different pristine BP of energies ($71.3\ MeV$, $150.3\ MeV$ and $228.8\ MeV$) were simulated at the yellow spot as shown in Figure 2.8.

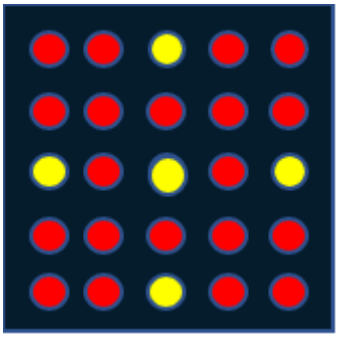

Figure 2.8 shows the target board created at isocentre. The yellow spot represents the position of the proton beam that we are measuring.

These energies are specifically chosen as it represents the lowest, middle, and highest energy that the synchrotron can generate, respectively. The commissioning verification with HITACHI will only focus on the lowest and highest energy with the highest energy being the most important due to the largest magnetic field present. Thereafter, a water phantom of the same size is created in TOPAS and the same plan from TPS is loaded into TOPAS. The lateral profile of the beam spot was then compared at different depths using in-house scripts.

Furthermore, the beam spot position can be affected by how we place the patient in the TOPAS "World". It is important to account for the DICOM shift due to the position coordinate of the DICOM files. This can be done by subtracting the *Image Position* of the CT DICOM from the TPS isocentre to determine the TOPAS isocentre. Thereafter, using the DICOM *Origin* Coordinate from TPS, subtract the isocentre shift from the DICOM *Origin*. This information can be found in the metadata of the DICOM file.

Range

Upon configuring the geometry and the beam spot position, we must ensure the *range* of the proton beam energies matches between the MC Simulation system and TPS. This can be done by simulating pristine BP of three different energies ($71.3\ MeV$,

150.3 MeV and 228.8 MeV) in the water phantom. Integrated Depth Dose (IDD) can then be plotted using MATLAB. IDD can be calculated using Equation 2.5.

$$\frac{\sum(D_i \times \rho \times abc)}{\rho \times abcn^2} \times abn^2 = \sum D_i \times ab \qquad (2.5)$$

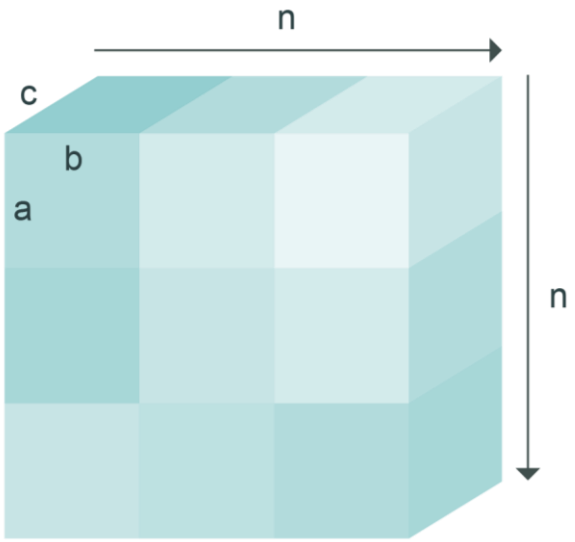

Figure 2.9 shows a simplified version of a plane of voxelized geometry. It is a representation of the DICOM file where information is stored in each voxel. a, b and c refers to the voxel dimension, ρ is the density of the voxel, n refers to the total number of voxels in each row and column. D_i refers to the dose stored in each voxel.

As the water phantom of $40 \times 40 \times 40$ cm was divided into planes of 1 mm, the dose was sum across each plane using Equation 2.5 and plotted in the direction of the beam (z-axis). Normalization to the global maximum dose was done after the total dose of each plane was then multiplied by the area of each voxel. The normalized dose was then plotted (similar to Figure 2.9) and the D_{90} was compared. The differences between TPS and MC system was kept to smaller than 0.1 mm.

However, there were some energies where the D_{90} did not match. One of the solutions at this point was to use a straightforward approach. We will simulate all energies in

TPS and determine the D_{90}. Thereafter, energies in the step of 10 MeV were simulated in TOPAS and D_{90} is determined. A polynomial fit was done to the TOPAS result between Energy and Range and a lookup table for TPS to TOPAS energy conversion is done.

Beam Width

In the fourth component of the proton beam line "installation", we will match the beamwidth of the proton beam between TPS and TOPAS. Firstly, we will extract the spot fluence Full-Width Half-Maximum (FWHM) from TPS to determine σ_x and σ_y at 8 different depths in air. A good choice of depth would consist of the beam entrance and exit of the pristine BP. A linear fit is then done to both σ_x and σ_y to obtain σ_x' and σ_y'. These values were then entered into TOPAS and a pristine proton beam was simulated for energies in the step of 10 MeV from 71.3 MeV to 228.8 MeV. A Gaussian fit was done on the simulated result and the FWHM was calculated. The FWHM difference between TPS and TOPAS will only be accepted if it is lesser than 2 mm and the comparison was done for both the Axial and Sagittal plane of the proton beam. An example of comparison was done in MATLAB as shown in Figure 2.10.

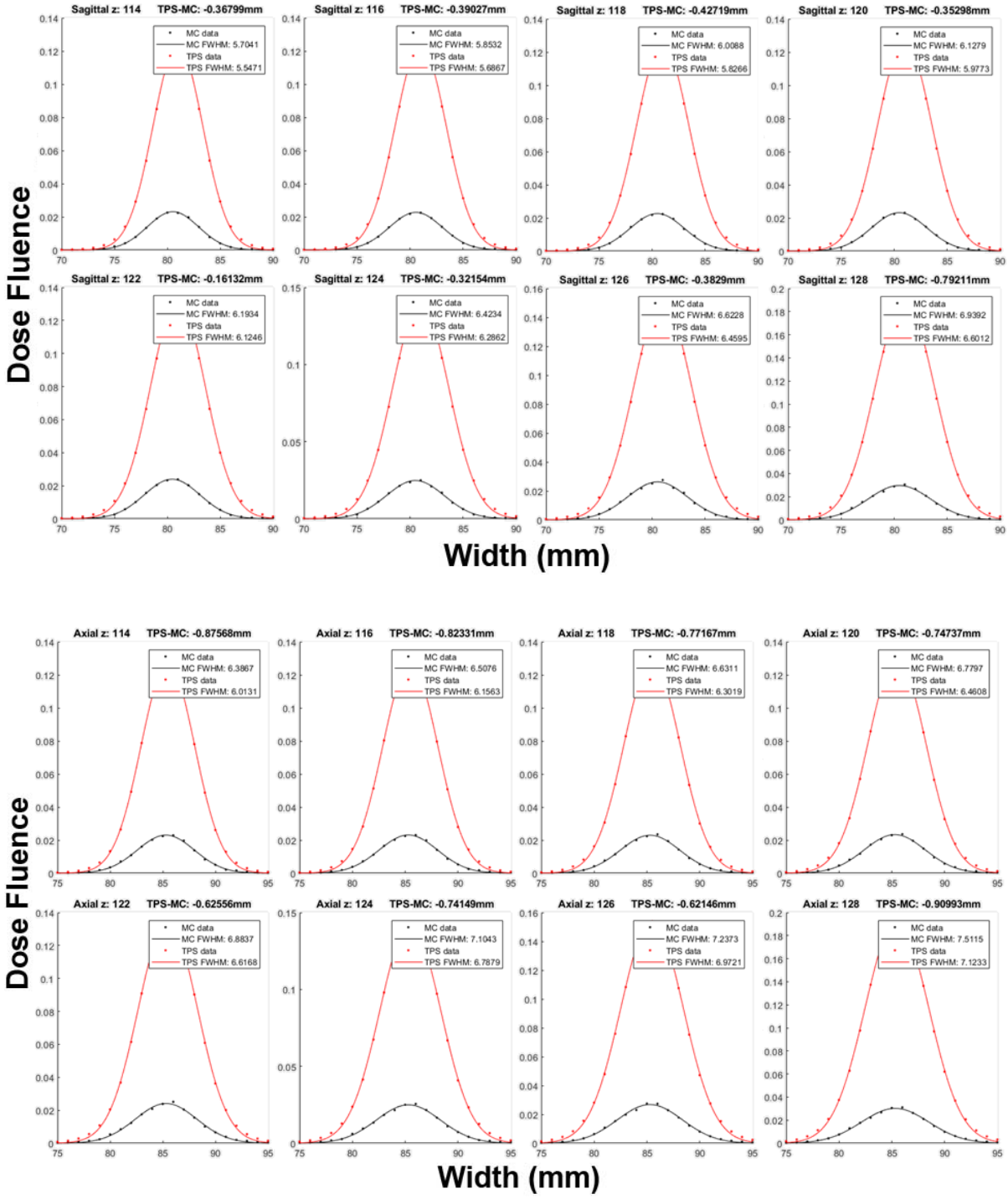

Figure 2.10 shows the comparison of beam width of 221.3 MeV proton beam at 8 different depths for both Sagittal and Axial planes. The Gaussian fit was fitted on the data point and FWHM was determined. The red curve represents the data from TPS while the black curve represents the data from Monte Carlo.

Generally, applying the σ_x, σ_y, σ_x' and σ_y' into TOPAS after obtaining from TPS, the beam width in the TOPAS will not match closely to TPS. Therefore, a trial and error method must be done to these variables to match the beamwidth of TOPAS to TPS. This step is repeated until the FWHM differences are lesser than 1 mm. Since only energies in the step of 10 MeV were done, a polynomial fit was done between energy and σ_x, σ_y, σ_x' and σ_y' to obtain the value across the whole energy range.

Gamma Analysis

Gamma analysis (γ) is a verification metric proposed by Low *et al.*[21] and it is commonly used in radiotherapy to compare the planned dose distribution (evaluated) and measured dose distribution (reference). It encompasses two criteria – Distance to Agreement (DTA in mm) and Dose difference (%) and can be used for point, 1D, 2D and 3D measurement. These constraints are determined by the user to create an acceptance circle around the reference point as shown in Figure 2.11. It is usually expressed as $\delta D(\%)/\delta r(mm)$ – 3%/3mm, 2%/2mm, 3%/2mm etc.

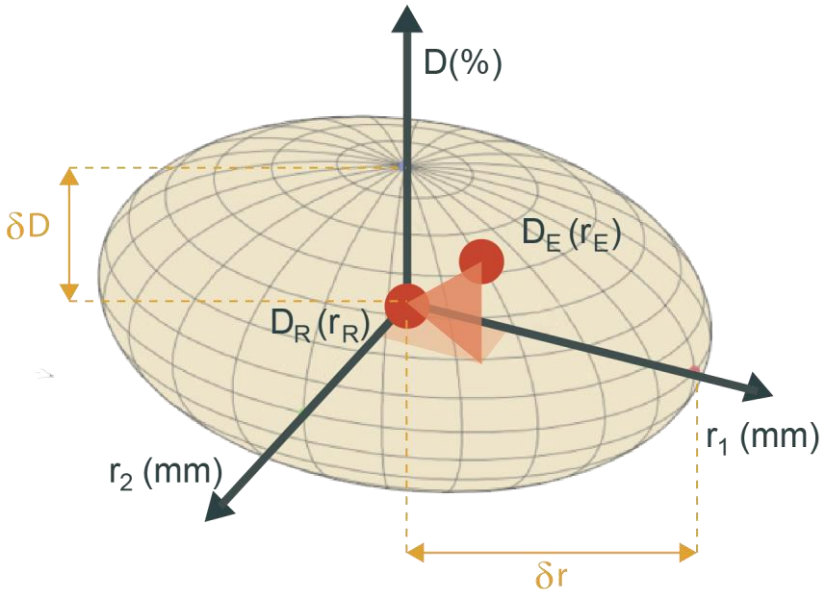

Figure 2.11 shows the schematic diagram of a gamma index in 2D. The circle represents the acceptance criteria boundary. *D* and *r* represent the dose and distance. Subscript R and E refer to the reference and the evaluated point.

Each point in the reference dose distribution has a corresponding γ value where the ellipse is established based on the user preference. Thereafter, each point in the reference dose distribution can be coupled with any point in the evaluated dose distribution. The dose difference is calculated using Equation 2.6[22]

$$\Delta D(r_R, r_E) = D_E(r_E) - D_R(r_R) \tag{2.6}$$

where D_E and D_R is the evaluated reference dose. The Γ is then calculated for each evaluated point using Equation 2.7[22]

$$\Gamma(r_R, r_E) = \sqrt{\frac{\Delta r^2(r_R, r_E)}{\delta r^2} + \frac{\Delta D^2(r_R, r_E)}{\delta D^2}} \tag{2.7}$$

where δr and δD is the distance difference and dose difference criteria. γ is then taken as the minimum value from Γ, defined overall evaluated point. $\Gamma^2 = 1$ describes the

acceptance boundary. When $\gamma \leq 1$, the evaluated distribution passes the comparison as it is within the acceptance criteria. Whereas $\gamma > 1$, the evaluated distribution fails the comparison as no evaluated point falls within the acceptance circle. These two criteria are designed to check for variations in patient setup uncertainties and machine uncertainties. In addition, a low-dose threshold of 10% is used to exclude dose points below 10% and clinically insignificant regions during the calculation of the gamma index. When low dose regions are excluded in the gamma analysis, the analysis result will provide us with meaningful information and therefore, assist us in the decision making process.

In the last part of TOPAS commissioning, gamma analysis is done in a water phantom and patient plan. Multiple targets consisting of two different sizes ($3 \times 3 \times 3\ cm^3$ and $5 \times 5 \times 5\ cm^3$) are created along the central axis (CAX). Multiple targets at different depths are created to test for the range of energy spectrum from $71.3\ MeV$ to $228.8\ MeV$. The TPS dose matrix distribution for the z-axis is set at a resolution of $0.1\ cm$ as shown in Figure 2.12.

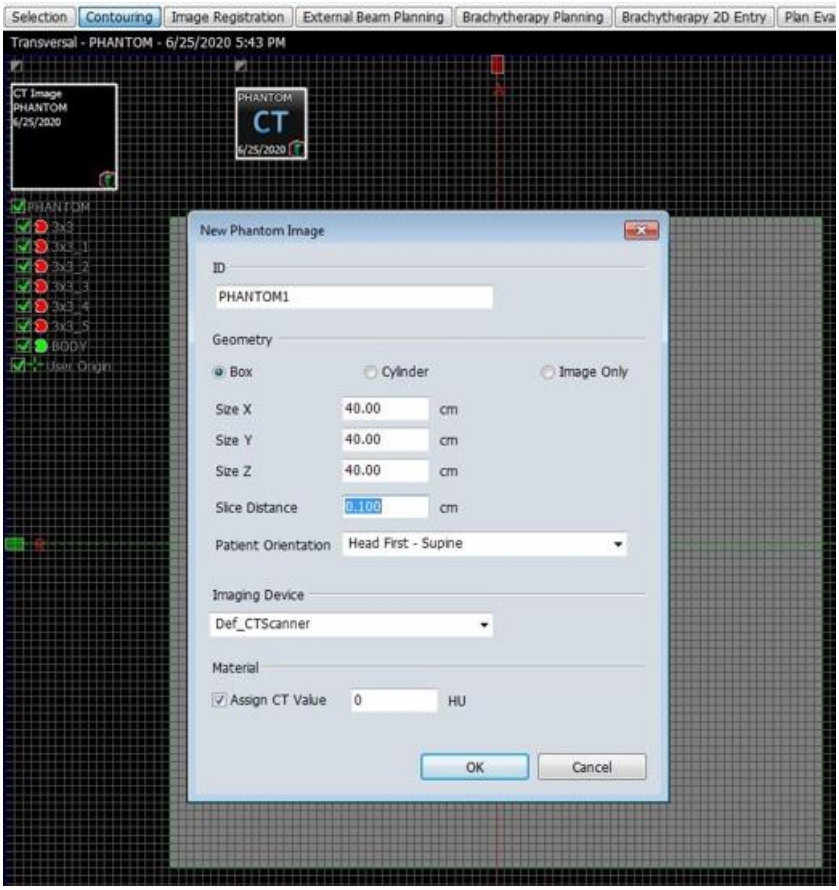

Figure 2.12 shows the dimension of the water phantom created in the TPS and the z-axis resolution determine by the slice distance.

The resolution for the x and y-axis is dependent on the size of the phantom created if the PCS algorithm is used. The larger the dimension of the phantom, the poorer the resolution gets. The resolution for a $20\,cm$ and $40\,cm$ length cube possesses a resolution of $0.1172\,cm$ and $0.2344\,cm$ respectively. However, this can be overcome by using a different dose calculation algorithm such as AcurosPT. It is a Monte Carlo algorithm created by Varian and it allows users to set the resolution they desired. Nonetheless, AcurosPT is usually not used clinically as the computational time is much longer than the PCS algorithm.

In the PCS algorithm, we can set the calculation resolution to $0.1\,cm$ as shown in Figure 2.13. This means that the calculation of dose deposition will be recorded in a

$1 \times 1 \times 1\ mm$ grid volume. But the output of the dose distribution will follow the resolution of the CT images.

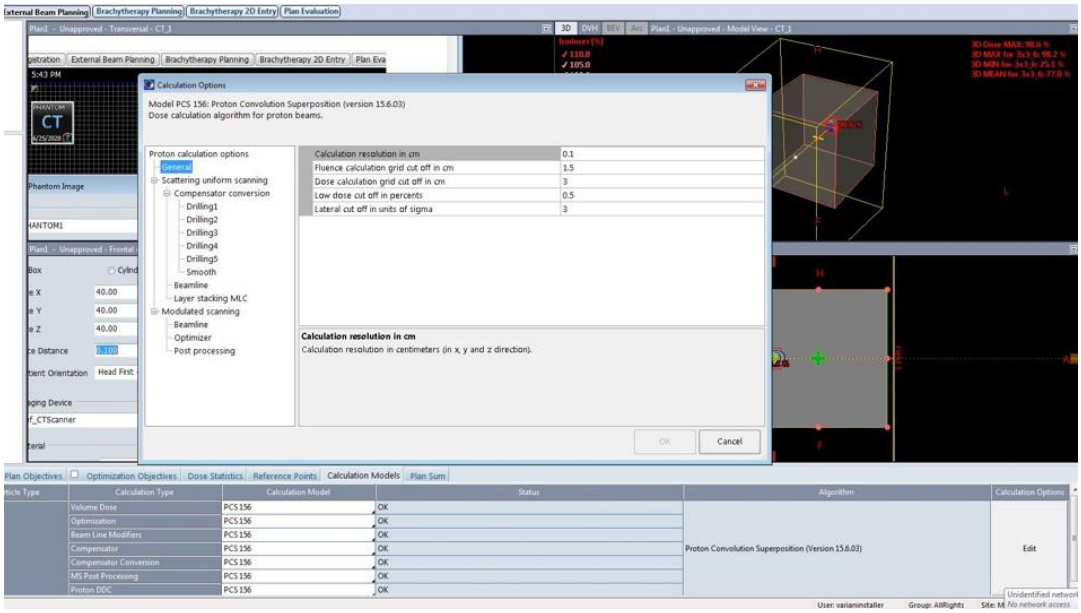

Figure 2.13 shows the calculation options of the PCS algorithm in the TPS. We have set the calculation resolution to be 0.1 cm.

As gamma analysis is the check of dose distribution between simulated and experimented results, absolute dose calculation is very important. Firstly, a monoenergetic proton beam is simulated in the water phantom in TPS the plan is extracted to TOPAS for recalculation. The information obtained from TPS output is the number of Monitor Unit (MU) to achieve the dose distribution. The MU is then converted in TOPAS to the number of protons (fluence) depending on the energy. The relationship between the number of protons per MU and energy is derived through a linear interpolation from experimental results expressed in a cubic equation.

An integrated depth dose (IDD) is plotted and compared at the 2 cm depth along the BP as shown in Figure 2.14. Being the flattest region of the BP for all energy range[23] and this made the measurements reliable even in the presence of small positioning

errors, 2 cm is specifically chosen. The equation in TOPAS is then modified by a specific factor for each energy such that the IDD at 2 cm matches the TPS result, producing a Look-Up Table (LUP) between energy and factor for modification.

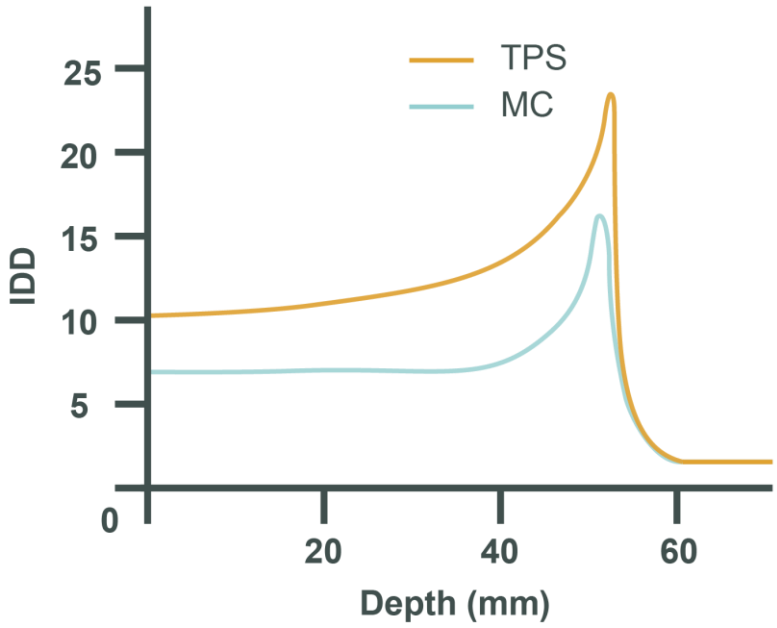

Figure 2.14 shows the exaggerated version of the IDD curve obtained from TPS and TOPAS. The difference in dose is determined at the 2 cm depth for each energy to form an LUP.

Once the IDD of TOPAS and TPS matches closely, gamma analysis is done on a cube target using Slicer[24] software as shown in Figure 2.15. We can achieve a passing rate of 99% for $3\%/3\ mm$ gamma for small target ($3 \times 3 \times 3\ cm^3$) to $> 90\%$ passing rate for larger target ($5 \times 5 \times 5\ cm^3$) at high energy. As we are not comparing to the experimental results, we believe that MC calculation is more accurate than analytical model calculation. In addition, the difference in resolution used in TPS and TOPAS affects the passing rate of gamma as well. Therefore, leading to a decrease in the passing rate of gamma when compared between TPS and TOPAS results.

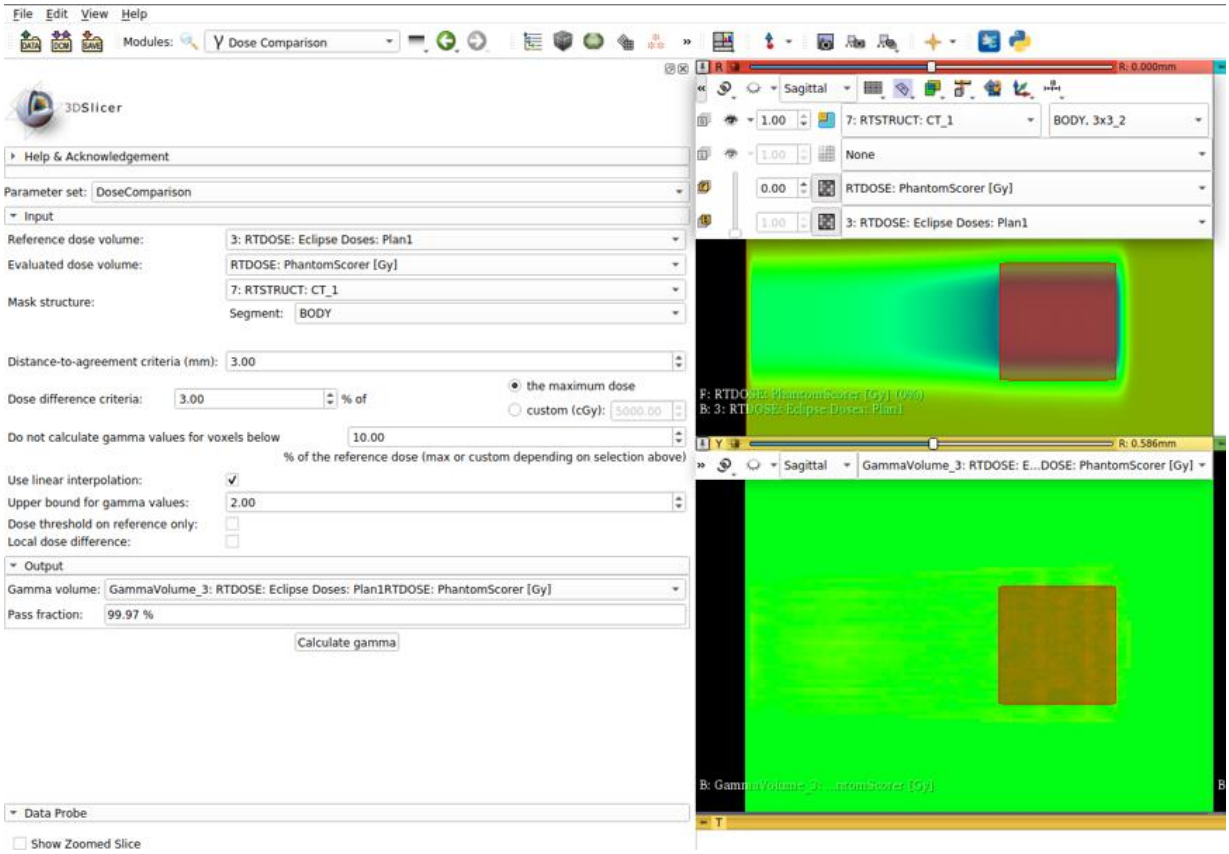

Figure 2.15 shows the slicer software and the gamma passing rate of 99.97% in a $3 \times 3 \times 3\ cm^3$ target in water based on 3%/3mm criteria.

Thereafter, patient plans are compared between TPS and TOPAS using gamma criteria as shown in Figure 2.16. For a prostate case, the gamma passing rate is 85.53% for a $3\%/3\ mm$ criteria. In a Head and Neck case, the gamma passing rate is 96% for a $3\%/3\ mm$ criteria. Although the passing rate is fairly low, the DVH of both cases (Prostate and Head and Neck) shows comparable results. We had also expected a low passing rate for the actual patient plan as a different dose algorithm was used. However, there is good agreement in the gamma passing rate in the water phantom.

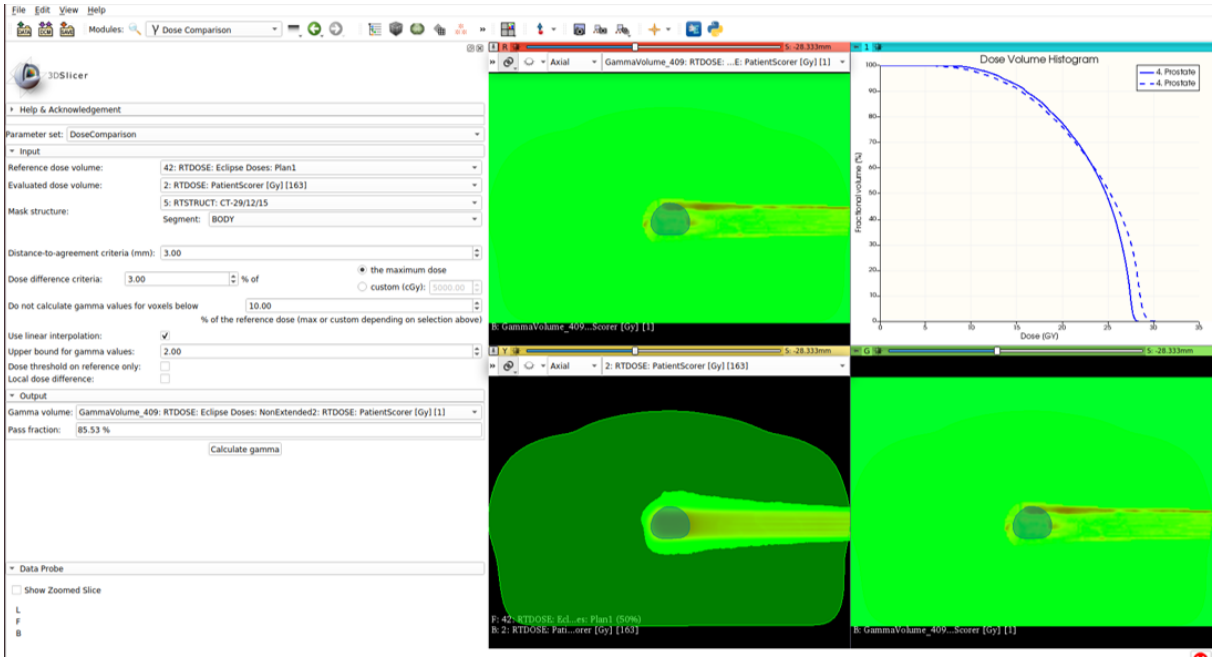

Figure 2.16 shows the gamma passing rate of 85.53% for a prostate case. The DVH is shown in the top right of the figure. The target coverage at D95 is almost similar. The solid line refers to the TPS calculated DVH while the dotted line refers to the Monte Carlo simulated DVH.

Once the DVH and the gamma analysis are within the acceptable range, this concludes the validation of the TOPAS with TPS. Further work needs to be done when we acquire the proton beamline. Physical measurements are made during the commissioning of the physical proton machine. The MC system should then be re-validated with the experimental results during machine commissioning. Fine-tuning must be made to spot size in air, proton per MU conversion factor, twiss parameters and finally, gamma analysis to successfully replicate the physical proton beamline into the MC system.

The MC statistical uncertainty is calculated at the isocentre dose of a Head and Neck patient plan using 2×10^7 proton particles averaged over 10 simulation runs. The statistical uncertainty is obtained to be $< 0.34\%$.

Using TOPAS, we can recalculate plans extracted from TPS for further exploration such as implementing variations to the calculation (RBE modelling) and generating

LET distribution for specific studies. It also allows for the customization of target material for further study. In the subsequent chapters, the configured MC system is used to determine LET and Dose distribution in different scenarios and RBE modelling is then further implemented in the final aim of this thesis. A snippet of the code for this chapter is shown in Appendix B1.

2.5 References

1. Seco J, Verhaegen F. *Monte Carlo Techniques in Radiation Therapy*. Vol 42. CRC/Taylor & Francis; 2013. doi:10.1118/1.4922694

2. Allison J, Amako K, Apostolakis J, et al. Recent developments in GEANT4. *Nucl Instruments Methods Phys Res Sect A Accel Spectrometers, Detect Assoc Equip*. 2016;835:186-225. doi:10.1016/j.nima.2016.06.125

3. Allison J. Geant4–a simulation toolkit. *Int J Phytoremediation*. 2007;17(2):20-24. doi:10.1080/10506890701404297

4. Agostinelli S, Allison J, Amako K, et al. GEANT4 - A simulation toolkit. *Nucl Instruments Methods Phys Res Sect A Accel Spectrometers, Detect Assoc Equip*. 2003;506(3):250-303. doi:10.1016/S0168-9002(03)01368-8

5. Perl J, Shin J, Schümann J, Faddegon B, Paganetti H. TOPAS: An innovative proton Monte Carlo platform for research and clinical applications. *Med Phys*. 2012;39(11):6818-6837. doi:10.1118/1.4758060

6. Faddegon B, Ramos-Méndez J, Schuemann J, et al. The TOPAS tool for particle simulation, a Monte Carlo simulation tool for physics, biology and clinical research. *Phys Medica*. 2020;72(February):114-121. doi:10.1016/j.ejmp.2020.03.019

7. Bielajew AF. Fundamentals of the Monte Carlo method for neutral and charged particle transport. *Sci York*. 2000.

8. Vassiliev ON. *Monte Carlo Methods for Radiation Transport*.; 2017. http://link.springer.com/10.1007/978-3-319-44141-2.

9. Knöös T, Wieslander E, Cozzi L, et al. Comparison of dose calculation algorithms for treatment planning in external photon beam therapy for clinical situations. *Phys Med Biol*. 2006;51(22):5785-5807. doi:10.1088/0031-9155/51/22/005

10. Ojala JJ, Kapanen MK, Hyödynmaa SJ, Wigren TK, Pitkänen MA. Performance of dose calculation algorithms from three generations in lung SBRT: Comparison with full Monte Carlo-based dose distributions. *J Appl Clin Med Phys*. 2014;15(2):4-18. doi:10.1120/jacmp.v15i2.4662

11. Tan HQ, Phua JH, Tan L, Ang KW, Lee J, Bettiol AA. *Geant4 Simulation for Commissioning of Proton Therapy Centre*. Springer Singapore; 2019. doi:10.1007/978-981-10-9035-6

12. Yarba J. Recent developments and validation of Geant4 hadronic physics. *J Phys Conf Ser*. 2012;396(PART 2). doi:10.1088/1742-6596/396/2/022060

13. Heikkinen A, Stepanov N, Wellisch JP. Bertini intra-nuclear cascade implementation in Geant4. *Comput High Energy Nucl Phys*. 2003;(March). http://arxiv.org/abs/nucl-th/0306008.

14. Guan F, Peeler C, Bronk L, et al. Analysis of the track- and dose-averaged LET and LET spectra in proton therapy using the geant 4 Monte Carlo code. *Med Phys*. 2015;42(11):6234-6247. doi:10.1118/1.4932217

15. Brown JMC, Dimmock MR, Gillam JE, Paganin DM. A low energy bound atomic electron Compton scattering model for Geant4. *Nucl Instruments Methods Phys Res*

Sect B Beam Interact with Mater Atoms. 2014;338:77-88. doi:10.1016/j.nimb.2014.07.042

16. Kadri O, Ivanchenko V, Gharbi F, Trabelsi A. Incorporation of the Goudsmit-Saunderson electron transport theory in the Geant4 Monte Carlo code. *Nucl Instruments Methods Phys Res Sect B Beam Interact with Mater Atoms*. 2009;267(23-24):3624-3632. doi:10.1016/j.nimb.2009.09.015

17. Wentzel G. Zwei Bemerkungen über die Zerstreuung korpuskularer Strahlen als Beugungserscheinung. *Zeitschrift für Phys*. 1926;40(8):590-593. doi:10.1007/BF01390457

18. Collaboration G. Physics Reference Manual Documentation. 2017:1-280. https://geant4-userdoc.web.cern.ch/UsersGuides/PhysicsReferenceManual/BackupVersions/V10.6c/html/index.html.

19. Krinsky S. *Particle Accelerator Physics*. Vol 7.; 1994. doi:10.1080/08940889408261288

20. Arjomandy B, Taylor P, Ainsley C, et al. AAPM task group 224: Comprehensive proton therapy machine quality assurance. *Med Phys*. 2019;46(8):e678-e705. doi:10.1002/mp.13622

21. Low DA, Harms WB, Mutic S, Purdy JA. A technique for the quantitative evaluation of dose distributions. *Med Phys*. 1998;25(5):656-661. doi:10.1118/1.598248

22. Hussein M, Clark CH, Nisbet A. Physica Medica Challenges in calculation of the gamma index in radiotherapy – Towards good practice. *Phys Medica*. 2017;36:1-11. doi:10.1016/j.ejmp.2017.03.001

23. Fracchiolla F, Lorentini S, Widesott L, Schwarz M. Characterization and validation of a Monte Carlo code for independent dose calculation in proton therapy treatments with pencil beam scanning. *Phys Med Biol*. 2015;60(21):8601-8619. doi:10.1088/0031-9155/60/21/8601

24. Fedorov A, Beichel R, Kalpathy-Cramer J, et al. 3D Slicer as an image computing platform for the Quantitative Imaging Network. *Magn Reson Imaging*. 2012;30(9):1323-1341. doi:10.1016/j.mri.2012.05.001

Chapter 3 Dependence of LET on materials and its impact on current RBE model

In this chapter, we aim to re-derive the LQ-based RBE model by comparing it with the previous models, using the correct LET_D values. The comparison is achieved by using the GEANT4 as discussed in the previous chapter. RBE models are then compared using clinical examples to evaluate the potential dosimetric errors when the LET_D is not calculated accurately in experiments. This allows us to understand the importance of the need for consistency in the study of LET_D. Therefore, the objective of this study is to determine if the simulation of LET_D in water medium is representative of simulating LET_D in different mediums such as Nucleus and Cytoplasm. This work has been published in *Physics in Medicine and Biology*[1].

3.1 Introduction

Variable RBE models are recently gaining attention because of the attempt to optimize proton therapy clinical outcomes and to allow a better comprehension of clinical (and experimental) results originating from proton therapy[2–11]. However, there is insufficient evidence to show the credibility of the models. Thus, it is extremely crucial to establish a well-validated variable RBE model to be applied for proton therapy. Most of the LET_D-dependent models as shown in Table 1.1 can be easily implemented due to the existence of a single parametric form. The exact parametric form is taken by performing regression analysis on radiobiological data for various biological endpoints (such as clonogenic cell survival, double-strand breaks or chromosome aberrations) and cell lines.

All the related work so far has assumed that the composition of the cell or tissue in the experiment is entirely water. Based on such assumption, the fitting of the LQ-based

models as well as the calculation of the LET_D are performed. This could cause the actual LET_D values in the experiment to be underestimated and give rise to an inaccurate RBE model. Previously, there are no conclusive reports on the impact of types of cellular materials on LET_D and this will be analysed in-depth in this work.

Therefore, this chapter serves to bring out the point that the assumptions made to determine LET_D might affect the RBE-weighted dose calculation if implemented into clinical practice.

3.2 Methods

3.2.1 RBE Models

In this work, three RBE models (Wedenberg *et al.*[10], Carabe *et al.*[12] and McNamara *et al.*[8]) are used. The constants as shown in Table 1.1 and the p_i in Equations 3.1-3.3 for RBE_{min} and RBE_{max} are determined by performing regression analysis on the experimental data with reported values on $\alpha[LET_D]$, $\beta[LET_D]$, $(\alpha/\beta)_x$ and LET_D. The parameterisations for the three RBE models are as shown in Equations 3.1-3.3. The Wedenberg *et al.* model assumed

$$RBE_{min} = 1, \;\; RBE_{max} = p_0 + p_1 \frac{LET_D}{(\alpha/\beta)_x}. \tag{3.1}$$

The Carabe *et al.* model assumed

$$RBE_{min} = p_0 + p_1 \frac{LET_D}{(\alpha/\beta)_x}, \;\; RBE_{max} = p_2 + p_3 \frac{LET_D}{(\alpha/\beta)_x}. \tag{3.2}$$

Lastly, the McNamara *et al.* model assumed

$$RBE_{min} = p_0 + p_1 \sqrt{\left(\frac{\alpha}{\beta}\right)_x} LET_D, \;\; RBE_{max} = p_2 + p_3 \frac{LET_D}{(\alpha/\beta)_x}. \tag{3.3}$$

The insufficiency of experimental data in the entire $(D_p, (\alpha/\beta)_x, LET_D)$ hyperspace may present difficulty in obtaining an accurate RBE model based on current knowledge.

Thus, the above three RBE models are fitted to the revised data in this work to examine the influence of LET_D on RBE models.

3.2.2 LET_D dependence on biologic materials

Currently, all the LET_D data in Paganetti[13] are calculated using water as the surrogate material. Therefore, this brings about the novelty of this work, where we will calculate LET_D with different cellular materials. Two different cellular materials are chosen and the elemental composition of both materials - cytoplasm and nucleus from Incerti *et al.*[14] and Byrne *et al.*[15] are as shown in Table 3.1. These materials are specifically chosen as they should be the relevant material of consideration during *in vitro* or *in vivo* irradiation.

From the knowledge of proton and its stopping power relationship with the composition of the material it travels, two types of Cytoplasm and Nucleus are used for comparison. The elemental composition of water is also included for comparison purposes. The difference in cellular composition in Table 3.1 arises from the separate methods of determining the compositions. The cellular composition in Incerti *et al.*[14] is obtained by Ion Beam Analysis Techniques with Rutherford Backscattering (RBS) and Proton-Induced X-ray Emission (PIXE) of a human keratinocyte cell line, whereas the composition in Byrne *et al.*[15] is obtained from the estimation of the data published in ICRU report 44 and soft tissue data in White *et al.*[16].

Table 3.1 A table showing the elemental mass composition of cellular materials – cytoplasm and nucleus, Incerti *et al.*[14] and Byrne *et al.*[15]. The composition of water is included for comparison.

Elemental Mass Composition (%)

	Cytoplasm-1 Incerti *et al*[14]	Cytoplasm-2 Byrne *et al*[15]	Nucleus-1 Incerti *et al*[14]	Nucleus-2 Byrne *et al*[15]	Water
Carbon	13.01	29.88	12.25	9.00	0.00
Hydrogen	21.86	10.55	21.77	10.6	11.11
Oxygen	62.34	56.3	62.35	74.2	88.89
Nitrogen	1.29	2.51	2.13	3.20	0.00
Sodium	0.00	0.11	0.04	0.00	0.00
Magnesium	0.00	0.00	0.03	0.00	0.00
Silicon	0.06	0.00	0.01	0.00	0.00
Phosphorus	0.48	0.00	0.60	0.00	0.00
Sulphur	0.11	0.24	0.12	0.40	0.00
Chlorine	0.29	0.16	0.10	0.00	0.00
Potassium	0.57	0.21	0.60	0.00	0.00
Total	100.00	100.00	100.00	100.00	100.00

3.2.3 Simulation parameters and LET_D irradiation configurations

Both the dose and LET_D are computed using an GEANT4[17–19]. The MC system is first tested again by simulating the LET_D distribution in water and our LET_D results agree with the LET_D data provided by Paganetti[13]. The resulting LET_D values range from $2-3\ keV/\mu m$ at the center of SOBP and rises sharply at the distal fall-off to below $20\ keV/\mu m$.

The physics model used in this simulation is FTFP_BERT with standard EM model which is the recommended physical model for clinical proton beam below $5\ GeV$[20]. The maximum step size and the length cut-off to be $0.5\ mm$ and $0.7\ mm$ respectively. Due to the nature of this work, these simulation parameters are sufficient to achieve a balance between computational time and the accuracy of the LET_D result. However, a

smaller cut-off length and step size of $0.1\,mm$ is used in calculating the dose distribution for a more accurate distribution. Lastly, the scoring of dose and LET_D quantities are done in 1 mm voxel. A snippet of the code used for this chapter is shown in Appendix B2, B3 and B4.

It is of paramount importance to replicate the most realistic Monte Carlo simulation to improve the accuracy of LET_D obtained for each data set. This demands scrutiny of the experimental set-up and biological protocol. Therefore, each article referenced from Paganetti[13] data were revisited to categorize the experimental set-up. The two main pieces of information we looked out for in the literature for this assignment are the type of proton beams (monoenergetic or modulated) and the design of the cell irradiation target.

Figures 3.1 depicts four scenarios of geometry setup of the simulation which are applicable in simulation. Configuration P1 is used when the whole Bragg Peak is located within the cell sample either due to the use of low energy proton or a cell suspension (not a monolayer cell) in a flask. Configuration P2 is used in the case that a monoenergetic proton beam is irradiated through a *monolayer* cell culture and the proton beam has sufficient energy to cross the entire cell. In this context, the cell thickness is assumed to be 10 μm and the LET_D is calculated within this small volume. Configuration S1 is used for the experimental technique developed by Skarsgard *et al.*[21] which is adopted by Wouters *et al.*[22,23] and Raju *et al.*[24,25] to acquire their data sets. In a long tube, the cell and medium are combined with gelatine that solidifies under low temperature. This tube is then irradiated with the SOBP span fully within it and subsequently sampled at different spatial intervals for analysis and assay. Under such a configuration, the entire irradiated volume will be homogenous and take on the same cellular composition. Configuration S2 is used when a *monolayer* cell culture is

irradiated with an energy-modulated proton beam or SOBP. The cells are often irradiated either at the plateau or the SOBP region of the depth dose in experiments. The thickness of the monolayer cells is assumed to be 10 μm unless otherwise stated in the journal. Out of the configurations, one is selected and assigned to each data point based on the information given in the journal. This is indicated in the fifth column of the data Table C1 – C4 in Appendix C.

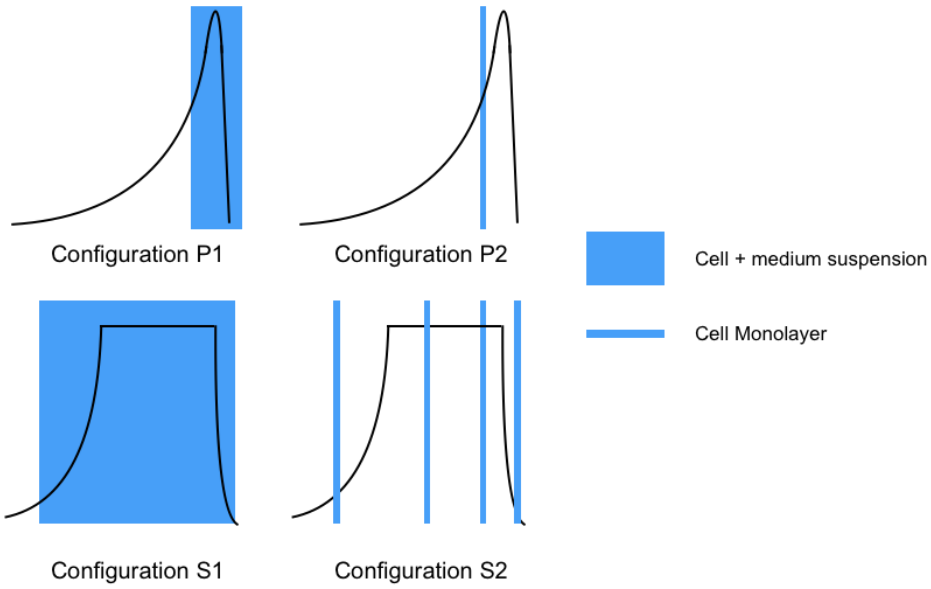

Figure 3.1 shows the classification of the configurations of the irradiation set-up. (Top Left) A mono-energetic proton with Bragg Peak lying entirely within the cells. (Top Right) A mono-energetic proton with sufficient energy to exit the cells. (Bottom Left) Irradiation using SOBP with the cells lying throughout the proton beam. (Bottom Right) Irradiation using SOBP with thin layers of cells lying at the specific location of SOBP.

3.2.4 Omission of Data

Some data points from the original compilation by Paganetti[13] were removed and hence absent in the data table in Appendix C. This removal is on the account of the following restrictions:

(i) To ensure clinical relevance in proton therapy, only data points with $\left(\frac{\alpha}{\beta}\right)_x < 30\ Gy$ and $LET_D < 20\ keV/\mu m$ were considered for later analysis. This specification was also agreed upon from the work by McNamara *et al.*[26]. No calculation of LET_D was performed for monoenergetic proton experimental studies involving *pure* - $LET_D > 50\ keV/\mu m$ (these data points will not appear in Appendix C).

(ii) Data points obtained from *microbeam experiments* with *several microns* beam spots were eliminated as it was recently proven that tumors showed differential response upon irradiation with microbeam and clinical beam[27–30]. This factors out data from Folkard *et al.*[31] and Schettino *et al.*[32].

(iii) Experiments involving high dose rates are clinically irrelevant and impractical. One such instance is the work by Doria *et al.*[33], thus entailing the omission of its corresponding data points

3.3 Results

3.3.1 LET dependence on simulation materials

The effect of cellular materials on Depth-Dose and LET_D profile is investigated using GEANT4 and the results are shown in Figure 3.2. The simulation is implemented using an SOBP with a range of $20\ cm$ and SOBP width of $5\ cm$ in water. Cellular materials of $5\ mm$ thickness are placed at $17\ cm$ depth, close to the centre of SOBP. This consist of energy ranges from $150\ MeV$ to $170\ MeV$ protons. The resulting dose and LET_D in Figure 3.2 are quantities obtained along the central axis (CAX) of the beam at different depths.

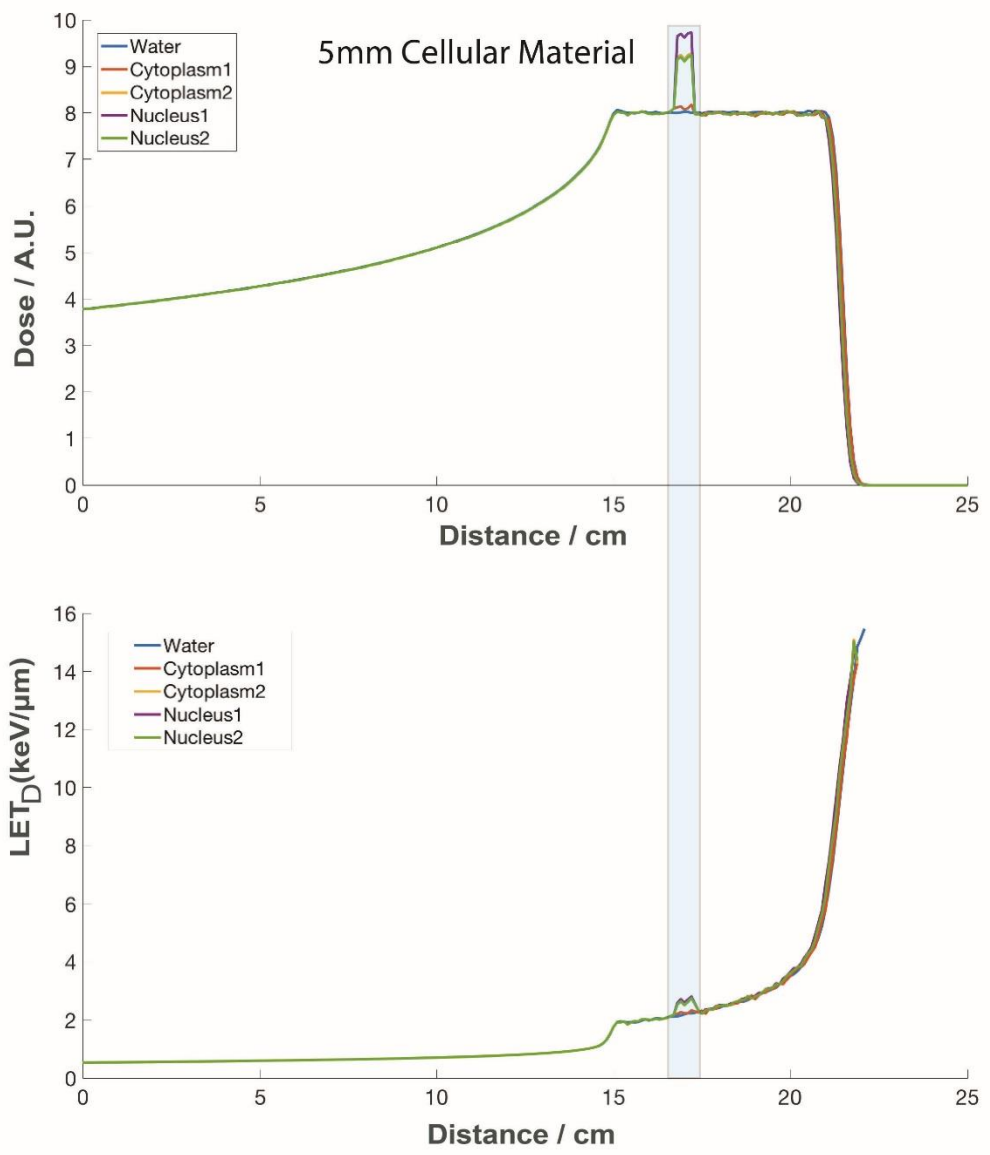

Figure 3.2 shows the effect of cellular materials stated in Table 3.1 on the dose (top) and LET_D (bottom) values of a proton SOBP. The cellular materials of 5 mm thickness are placed at 17 cm depth indicated by the blue band in the figure. Non-negligible increase in dose and LET_D values are observed at the positions where the cellular materials are located.

The LET_D values were calculated for all data points used in this study using 3 different materials - water, cytoplasm-1[14] and cytoplasm-2[15]. In terms of cellular effects, the nucleus is the most important as it is the primary target in radiotherapy and it directly affects the clonogenic survival of the cells. However, in the calculation of LET_D,

cytoplasm makes up most of the material in the cell and the stopping power will be determined by the cytoplasm than the nucleus. Therefore, the nucleus material is neglected as cytoplasm is more relevant as compared to the nucleus for the subsequent sections. These values are compiled and presented in the 6th to 8th columns in the appendix (The tables in Appendix C are sorted according to the type of cell lines. Table C1, C2, C3 and C4 corresponds to the Chinese Hamster, rat or mouse, human cancer and human fibroblasts and epithelial cell lines, respectively). The classification of tables C1, C2, C3 and C4 in Appendix C follows from Paganetti[13] and should be referred to for further information on the origin of the data.

3.3.2 Fitting Results

From the previous section, it proves the point that LET_D indeed is dependent on the cellular material it is simulated in. Therefore, in this section, our data points will be incorporated into this study.

The plot of $\mathrm{RBE_{max}}$ and $\mathrm{RBE_{min}}$ against $\mathrm{LET_D}/(\alpha/\beta)_x$ (due to the parameterisation used in Equations 3.1-3.3) are displayed in Figure 3.3. The original data points from Paganetti[13] as well as the corrected data points in our work with 3 different materials are shown. The regression lines are fitted using our data points represented by the solid blue circles. The fitting is done using the Least Absolute Residuals (LAR) algorithm[34] to lessen the effect of anomalies.

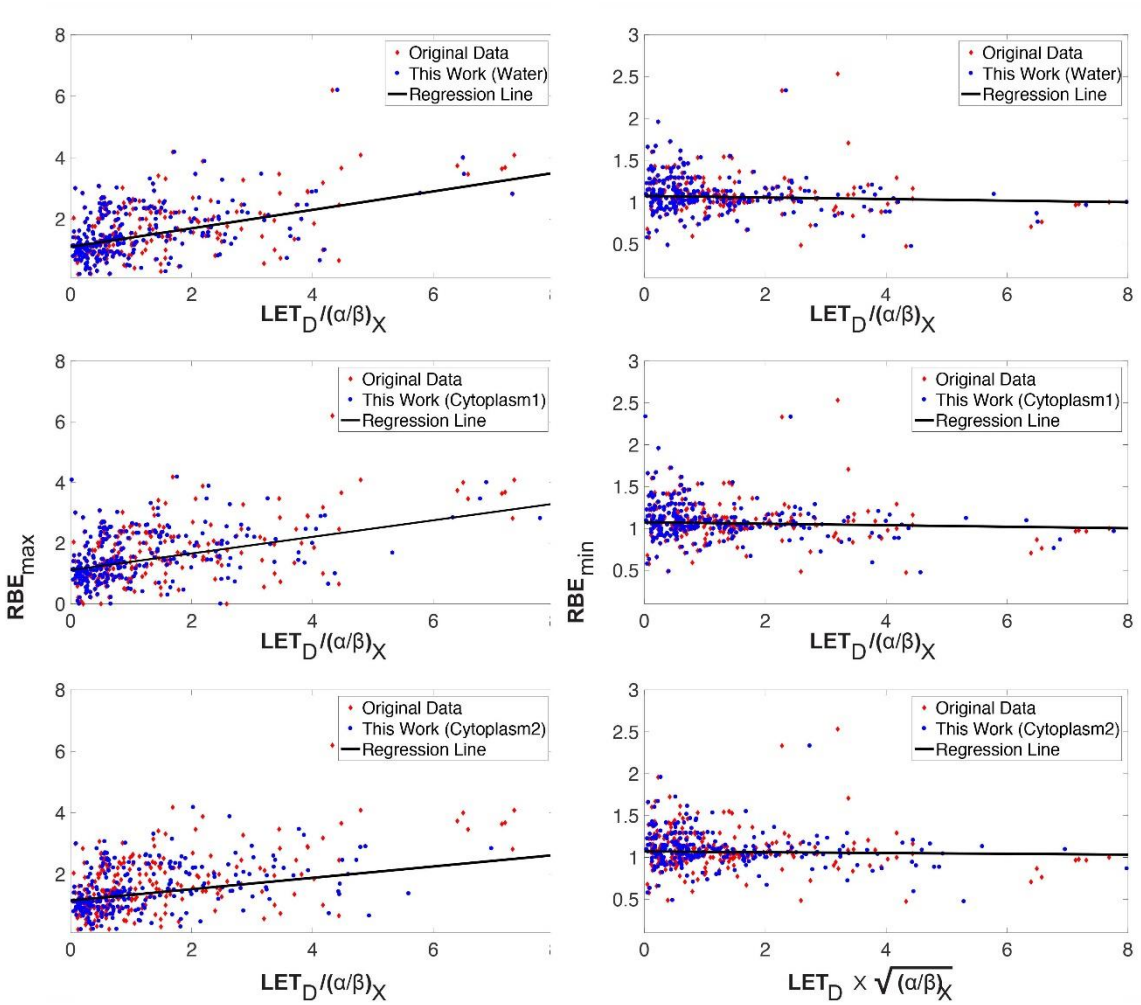

Figure 3.3 All the red solid diamond in the 6 plots represent the data points from Paganetti[13] and the blue solid circles represent simulation data from this work. The regression lines are fitted to our simulation data. (Top Left) RBE_{max} against $LET_D/(\alpha/\beta)_x$ with red diamond representing water data. (Middle Left) RBE_{max} against $LET_D/(\alpha/\beta)_x$ with red diamond representing cytoplasm from Incerti *et al.*[14]. (Bottom Left) RBE_{max} against $LET_D/(\alpha/\beta)_x$ with red diamond representing cytoplasm from Byrne *et al.*[15]. (Top Right) RBE_{min} against $LET_D/(\alpha/\beta)_x$ with red diamond representing water data. (Middle Right) RBE_{min} against $LET_D/(\alpha/\beta)_x$ with red diamond representing cytoplasm from Incerti *et al.*[14]. (Bottom Right) RBE_{min} against $LET_D\sqrt{(\alpha/\beta)_x}$ with red diamond representing cytoplasm from Byrne *et al.*[15]

The regression lines for RBE_{max} and RBE_{min} using the three different materials are plotted together as shown in Figure 3.4. Three published models from Wedenberg *et al.*[10], Carabe *et al.*[12] and McNamara *et al.*[8] are also plotted for comparison. The bottom subfigure of Figure 3.4 shows the plot of RBE_{min} against $LET_D\sqrt{(\alpha/\beta)_x}$ due to the parameterisation used by McNamara *et al.*[8].

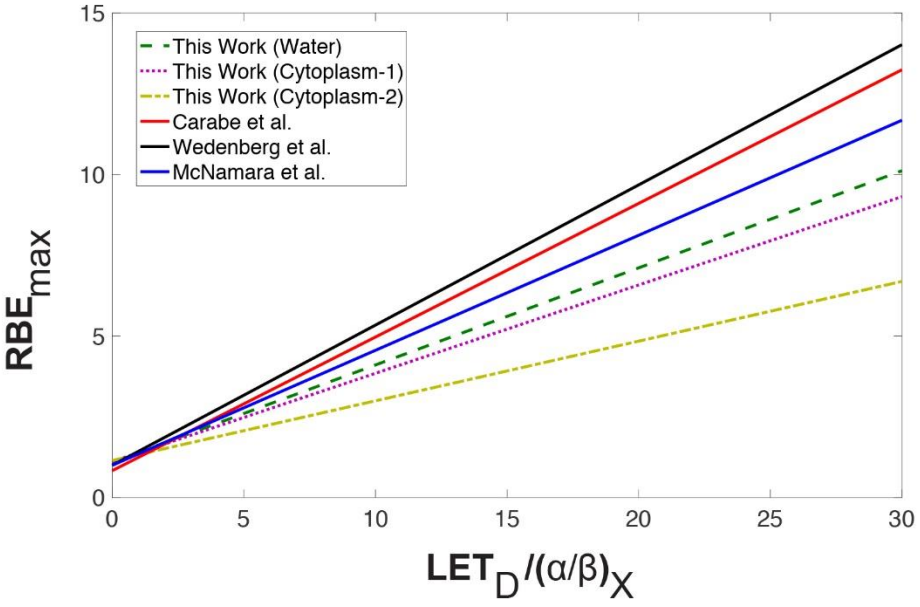
This Work (Water)
This Work (Cytoplasm-1)
This Work (Cytoplasm-2)
Carabe et al.
Wedenberg et al.
McNamara et al.
RBE_max
LET_D/(α/β)_X

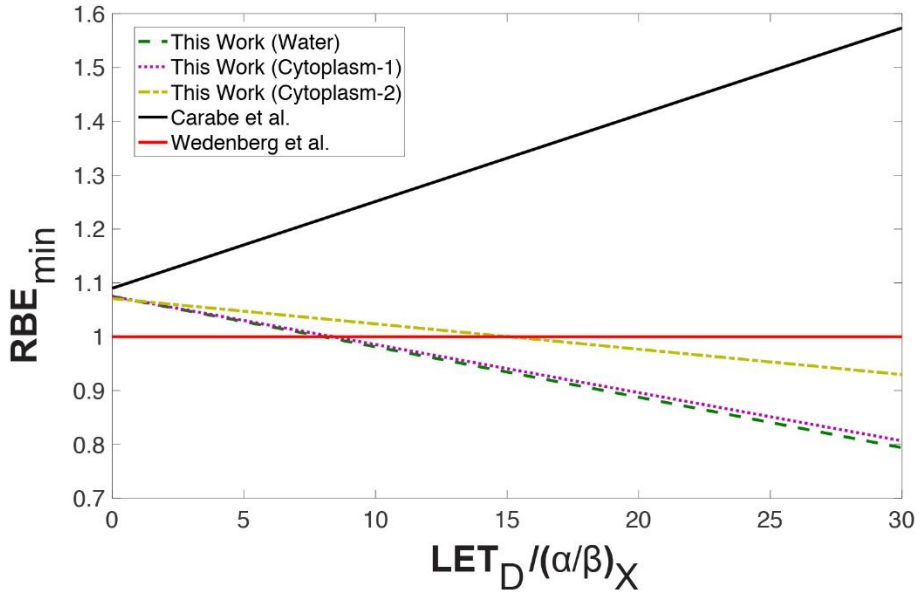
This Work (Water)
This Work (Cytoplasm-1)
This Work (Cytoplasm-2)
Carabe et al.
Wedenberg et al.
RBE_min
LET_D/(α/β)_X

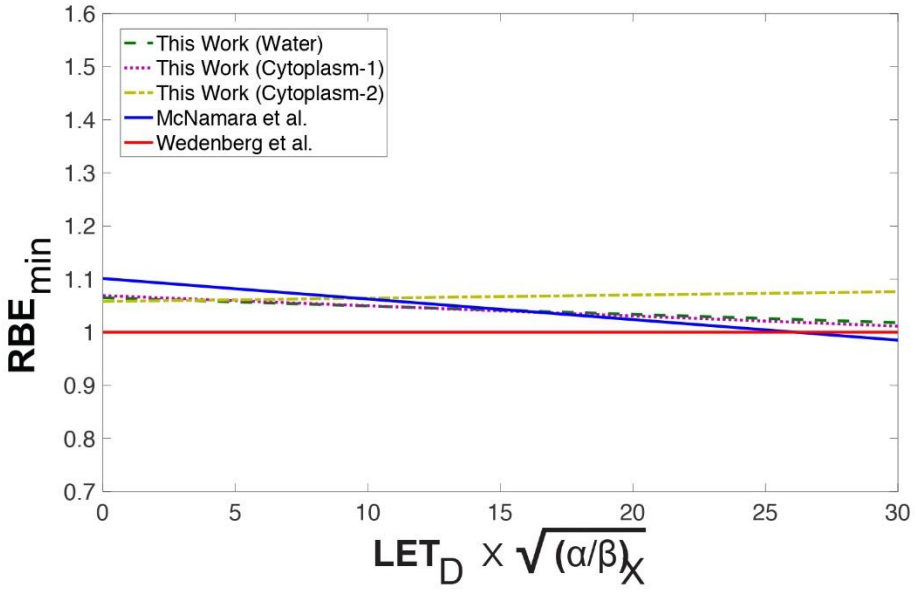
This Work (Water)
This Work (Cytoplasm-1)
This Work (Cytoplasm-2)
McNamara et al.
Wedenberg et al.
RBE_min
LET_D x √(α/β)_X

Figure 3.4 The solid lines represent the models obtained from Wedenberg *et al.*[10], Carabe *et al.*[12] and McNamara *et al.*[8] and the dashed, dotted and dashed-dotted lines are obtained from data assuming water, cytoplasm-1 and cytoplasm-2 materials respectively. (Top) A plot of RBE_{max} against $LET_D/(\alpha/\beta)_x$. (Middle) A plot of RBE_{min} against $LET_D/(\alpha/\beta)_x$. (Bottom) A plot of RBE_{min} against $LET_D\sqrt{(\alpha/\beta)_x}$.

Using the parameterisation given in Equation 3.2, the RBE corresponding to different LET_D values are determined for different cellular materials in Figure 3.5. Two values of $\left(\frac{\alpha}{\beta}\right)_x$ are used, as depicted in the top and bottom plots for $\left(\frac{\alpha}{\beta}\right)_x = 3$ and $\left(\frac{\alpha}{\beta}\right)_x = 10$ respectively. Looking at this figure, we find that the RBE models calculated with LET_D re-calculation and with cellular materials addition differs from a current published version, be it for normal tissue (low $\left(\frac{\alpha}{\beta}\right)_x$) or tumor tissues (high $\left(\frac{\alpha}{\beta}\right)_x$).

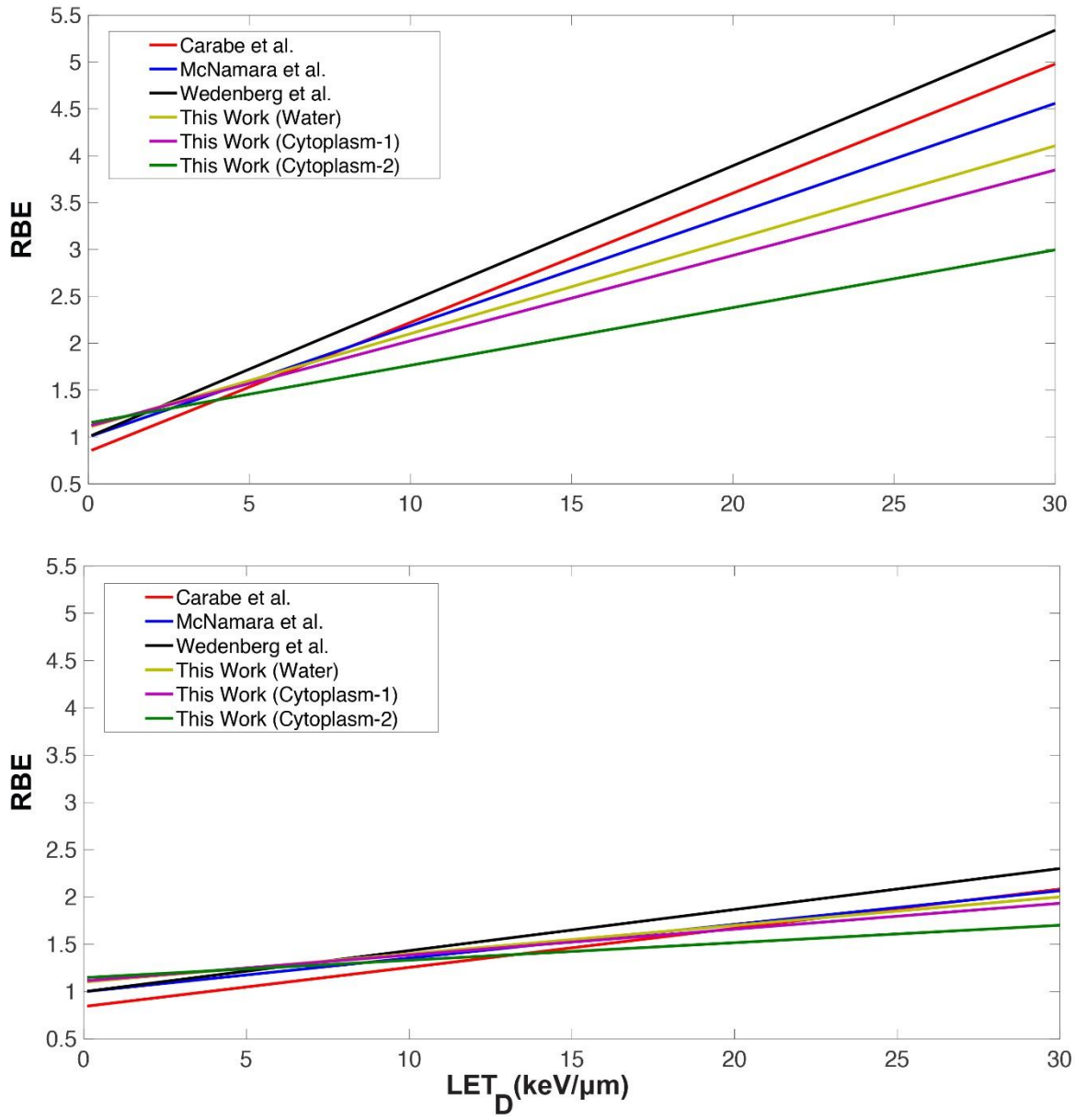

Figure 3.5 (Top) RBE plotted against LET_D for $\left(\frac{\alpha}{\beta}\right)_x = 3$. (Bottom) RBE plotted against LET_D for $\left(\frac{\alpha}{\beta}\right)_x = 10$.

3.3.3 Effects on RBE models

This section examines how RBE models derived from different cellular materials affect a clinical-like SOBP. They are evaluated on the dose distributions (RBE-weighted dose). The results are shown in Figure 3.6 and Figure 3.7 which uses different RBE

parametrisation according to Equations 3.2 and 3.3 respectively. The dosimetric difference between RBE models of different materials are evaluated based on mean dose (D_{mean}) and maximum dose (D_{max}) at the SOBP region.

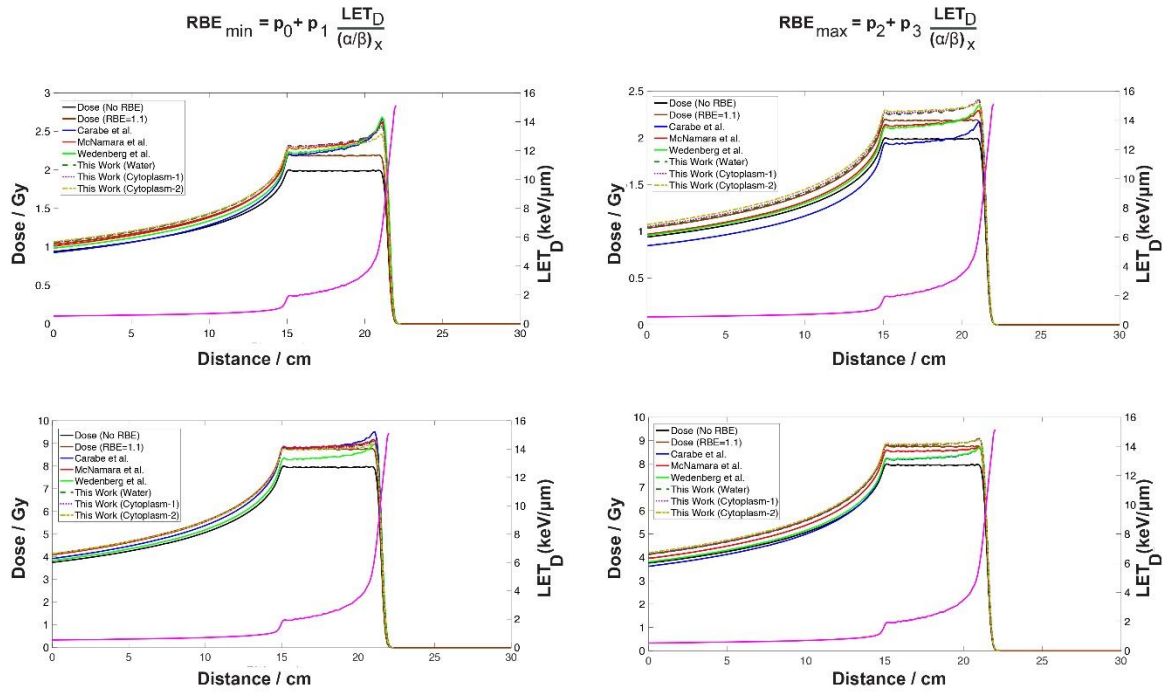

Figure 3.6 This figure shows the RBE weighted doses of an SOBP calculated using parameterization from Equation 3.2 for (Top Left) $\left(\frac{\alpha}{\beta}\right)_x = 3, D = 2\ Gy$, (Top Right) $\left(\frac{\alpha}{\beta}\right)_x = 10, D = 2\ Gy$, (Bottom Left) $\left(\frac{\alpha}{\beta}\right)_x = 3, D = 8\ Gy$, (Bottom Right) $\left(\frac{\alpha}{\beta}\right)_x = 10, D = 8\ Gy$. The RBE-weighted dose are calculated for RBE models derived from 3 different cellular materials (shown in dotted, dashed, and dashed-dotted lines) and RBE models that are derived from Wedenberg *et al.*[10], Carabe *et al.*[12] and McNamara *et al.*[8](shown in solid lines). A constant $RBE = 1.1$ calculation is also included in the graphs for comparison. The magenta line represents the LET_D with values shown on the right vertical axis.

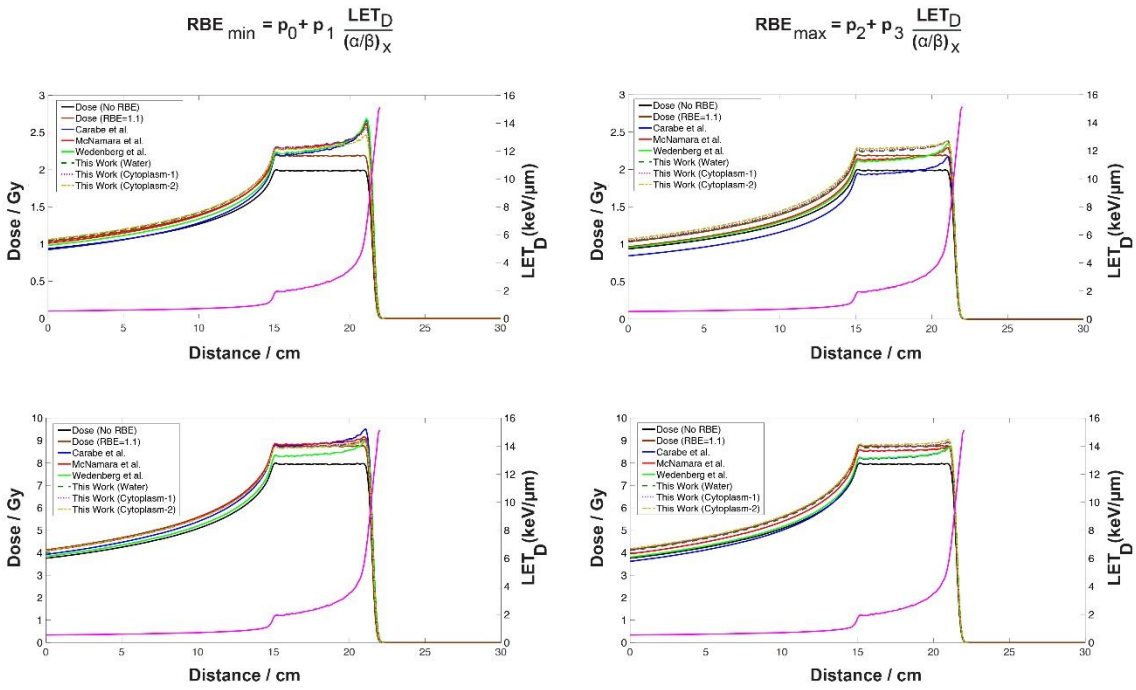

Figure 3.7 This figure shows the RBE weighted doses of an SOBP calculated using parameterization from Equation 3.3 for (Top Left) $\left(\frac{\alpha}{\beta}\right)_x = 3, D = 2\ Gy$, (Top Right) $\left(\frac{\alpha}{\beta}\right)_x = 10, D = 2\ Gy$, (Bottom Left) $\left(\frac{\alpha}{\beta}\right)_x = 3, D = 8\ Gy$, (Bottom Right) $\left(\frac{\alpha}{\beta}\right)_x = 10, D = 8\ Gy$. The RBE-weighted dose are calculated for RBE models derived from 3 different cellular materials (shown in dotted, dashed, and dashed-dotted lines) and RBE models that are derived from Wedenberg *et al.*[10], Carabe *et al.*[12] and McNamara *et al.*[8](shown in solid lines). A constant $RBE = 1.1$ calculation is also included in the graphs for comparison. The magenta line represents the LET_D with values shown on the right vertical axis.

The LET_D of the SOBP is also shown in every plot with its values denoted by the right axis. The RBE-weighted SOBPs in Figure 3.6 and Figure 3.7 are calculated for $\left(\frac{\alpha}{\beta}\right)_x = 3$ and $\left(\frac{\alpha}{\beta}\right)_x = 10$, and for two different doses of 8 Gy and 2 Gy. Different RBE models from Wedenberg *et* al.[10], Carabe *et al.*[12] and McNamara *et al.*[8] *are* also plotted in both

figures to allow comparison of the *inter-model variation* with errors resulting from LET_D uncertainties. The summary of this comparison is shown in Table 3.2.

Table 3.2 shows the summary of the results from Figure 3.6 and Figure 3.7. The percentage difference of D_{mean} and D_{max} are calculated from the SOBP between water and cytoplasm-1 and cytoplasm-2.

	RBE Model from Eq. (7)				RBE Model from Eq. (8)			
	Cytoplasm-1		Cytoplasm-2		Cytoplasm-1		Cytoplasm-2	
	ΔD_{mean} (%)	ΔD_{max} (%)	ΔD_{mean} (%)	ΔD_{max} (%)	ΔD_{mean} (%)	ΔD_{max} (%)	ΔD_{mean} (%)	ΔD_{max} (%)
$(\alpha/\beta)_x = 3, D = 2Gy$	0.32	0.94	1.83	4.35	0.23	0.95	1.71	4.02
$(\alpha/\beta)_x = 10, D = 8Gy$	-0.22	0.00	0.00	0.48	-0.27	0.11	-1.19	-1.15
$(\alpha/\beta)_x = 3, D = 8Gy$	0.11	0.36	0.72	1.63	-0.04	0.37	0.51	1.04
$(\alpha/\beta)_x = 10, D = 2Gy$	-0.40	0.01	-0.93	0.76	-0.42	0.06	-1.30	0.03

3.3.4 Effects on Clinical Study

This section explores the effect of the RBE models derived from different cellular materials on a prostate clinical case. The prostate is irradiated with two opposing lateral proton fields. The spot weights are determined from optimization in our Varian Eclipse (ver. 13.7) TPS and are imported into our GEANT4 simulation. The tumor is contoured and shown as a white circle at the centre of Figure 3.8. The dose and LET_D values are scored for each voxel for further calculation of RBE and RBE-weighted dose and are shown in Figure 3.8(a) and Figure *3.8*(b) respectively.

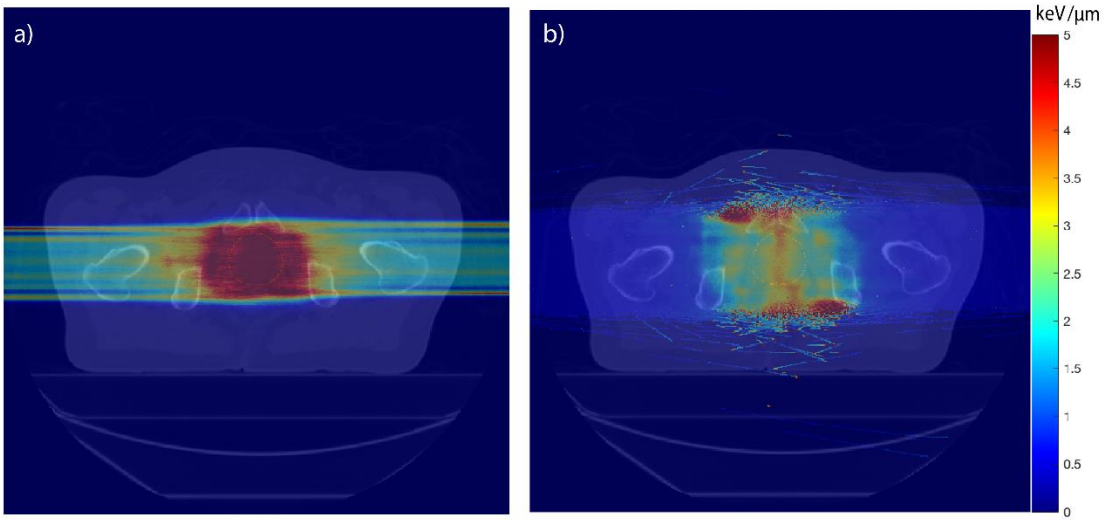

Figure 3.8 (a) shows the dose calculation in a clinical prostate case with two opposing proton fields. The calculation is carried out using GEANT4 with HU to stopping power conversion following Schneider *et al.*[35]. b) This figure shows the scoring of LET_D in the same clinical prostate case with two opposing fields.

The analysis outcome is shown in the histograms in Figure 3.9. The top two figures are results obtained using cytoplasm-1 and the bottom two figures are those using cytoplasm-2 materials. The left two figures use the RBE model from Equation 3.2 and the right two figures use the RBE model from Equation 3.3.

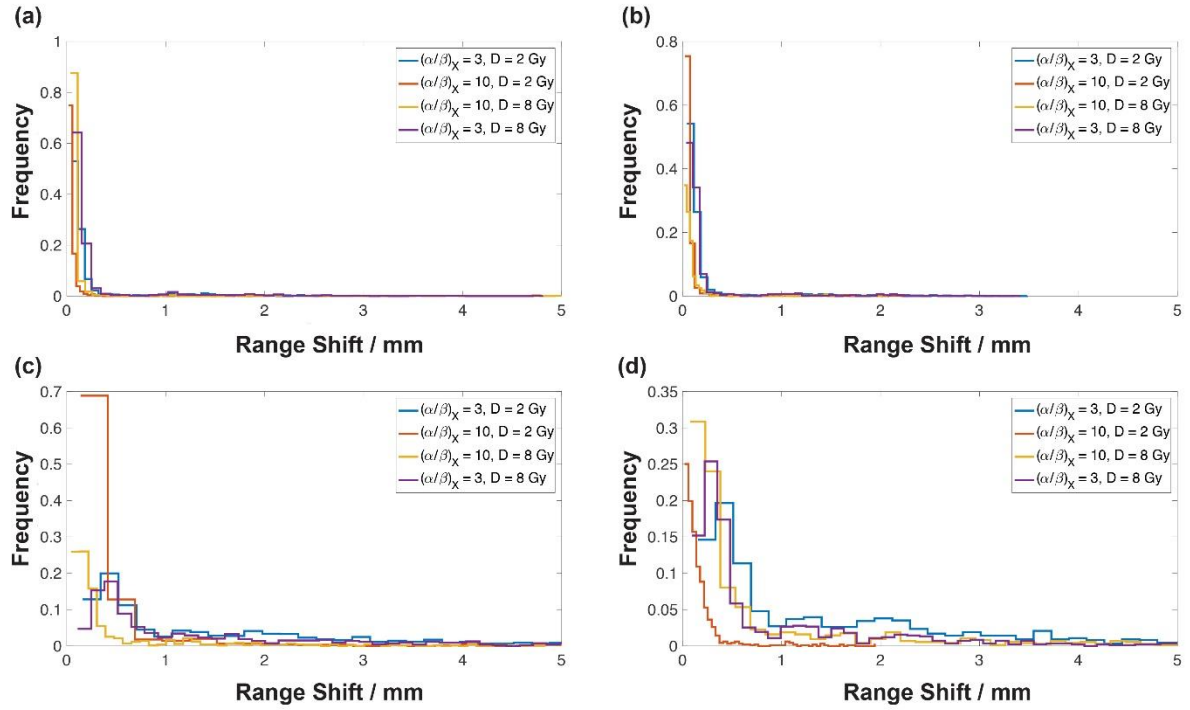

Figure 3.9 shows the histograms of the range shifts of the 90% isodose contour between RBE-weighted dose of cytoplasmic materials and water under different model parameterisations. Graphs (a) and (b) corresponds to RBE models derived from cytoplasm-1 and graphs (c) and (d) correspond to that from cytoplasm-2. Graph (a) and (c) use $RBE_{min} = p_0 + p_1 \frac{LET_D}{(\alpha/\beta)_x}$, $RBE_{max} = p_2 + p_3 \frac{LET_D}{(\alpha/\beta)_x}$, and graph (b) and (d) use $RBE_{min} = p_0 + p_1 LET_D \sqrt{(\alpha/\beta)_x}$, $RBE_{max} = p_2 + p_3 \frac{LET_D}{(\alpha/\beta)_x}$.

3.4 Discussion

LET Dependence on Simulations

In this section, the results prove that LET_D is dependent on the cellular material it is simulated in. As shown in Figure 3.2, it is found that the dose deposition and LET_D values are higher at the regions where the cellular materials are located, implying that the choice of water as surrogate material will result in an underestimation of the local dose and LET_D. This suggests that the RBE model based on calculated LET_D may be

refined after taking the actual composition of the cellular materials into account. Cytoplasm[14,15] will be used as the substitute for cellular material seeing that it constitutes a major part of the cell for the subsequent parts of this study. Moreover, studies have shown the desirability of having a similar elemental composition for the cell-culture medium and the biological material[36]. Hence, the cell medium is assumed to be made up of the same elements as the cellular composition in this simulation.

Generally, the LET_D values for cytoplasm-2 are larger than those for cytoplasm-1, which are in turn larger than those for water. Comparing different irradiation configurations as shown in, the greatest disagreement between our calculated LET_D for water (4th column in Appendix C1) and the LET_D stated by Paganetti[13] (6th column in Appendix C1) is most remarkable for experiments involving low energy monoenergetic protons (configurations P1 and P2). Our calculated LET_D values is higher than Paganetti[13] with a difference of approximately 17%. This finding stems from an elevated energy straggling effect due to the use of low energy proton (resulting in a distribution of primary protons energies) which is not accounted for when the journal reported the $pure - LET$ values. In contrast, the difference in LET_D values for water at the SOBP region for configurations S1 and S2 is minimal at 5% as average LET in terms of LET_D or LET_t (instead of $pure - LET$) are often reported in the journals or calculated by Paganetti[13].

Impacts on RBE models

With the addition of our data points, greater rightward shifts ensue from higher LET_D data as they normally originate from mono-energetic proton experiments which quote the $pure - LET$ instead of LET_D values in Figure 3.3. This rightward shift is greatest for cytoplasm-2[15] data followed by cytoplasm-1[14] data and lastly water data.

A discrepancy was perceived between different *models* and between different assumed cellular materials for the RBE_{min} and RBE_{max} functions. In general, the recalculation of LET_D in this work caused the regression lines to produce a smaller gradient in Figure 3.4, due to an increase in LET_D for most of the data points. Cytoplasm-2 displayed the most pronounced effect as the LET_D is considerably larger than water. Hence, this result confirmed that a non-negligible correction to LET_D and the resulting RBE models could be brought about by including cellular materials in the simulation of irradiation experiment introduces.

Furthermore, we fitted the RBE_{max} and RBE_{min} functions into the RBE models. The result shows a maximal deviation for cytoplasm-2 due to the greatest difference of LET_D when compared with water. Therefore, Figure 3.5 imply that the RBE values may in fact be *lower* than what is previously published. If that is the case, it can have an impact on treatment planning during proton therapy when RBE modelling are included in dose calculation.

To verify the impact it has on treatment planning when RBE modelling is incorporated, RBE models derived from different cellular materials are compared. The difference in D_{mean} decreases when the $\left(\frac{\alpha}{\beta}\right)_x$ and dose becomes higher, for all materials and parameterisations. There is no obvious variation pattern observed for the difference in D_{max} with dose, but it declines with higher $\left(\frac{\alpha}{\beta}\right)_x$ for both parameterisations is clear. Another point worth mentioning is that the RBE-weighted doses are not equivalent if different RBE model parameterisations are employed for all cellular materials. Consequently, the choice of parameterisation will in practice contribute to additional uncertainty other than the LET_D uncertainties from cellular materials. The investigation in this section reveals that the LET_D uncertainties due to cytoplasmic cellular materials

can induce uncertainties of up to 1.83% in ΔD_{mean} and 4.35% in ΔD_{max} for low $\left(\frac{\alpha}{\beta}\right)_x$ target under low dose (per fraction) such as in prostate cancer[37]. In all other cases, the uncertainties are trivial with ΔD_{mean} and ΔD_{max} of about 1% or less.

Impact on prostate case

In addition, we have compared the dose and LET_D distribution in a clinical prostate case. The differences in HU to stopping power conversion methodology and dose calculation algorithm (less than 3 mm biological range shift for 90% isodose line) give rise to a slight deviation of the dose calculated using GEANT4 from TPS calculation. However, this issue is insignificant for the relative comparison between RBE models in this work. The metric for comparison is the *biological dose shift* which is the spatial change in the isodose line of the RBE-weighted dose. The isodose level selected is 90%. Considering all the four histograms, the range shifts are higher for $\left(\frac{\alpha}{\beta}\right)_x = 3$ and $D = 2\ Gy$ data, giving it a maximal *average* range shift of 1.6 mm. Meanwhile, the *average* range shifts turn out to be smaller than 1 mm for the rest of the data. This result agrees well with the SOBP study from the previous section and once again, it verifies that uncertainty in LET_Dcan result in a significant dosimetric impact for low $\left(\frac{\alpha}{\beta}\right)_x$ and low dose values.

3.5 Conclusion

In this chapter, we managed to show that cellular composition knowledge is critical despite using only two generic intracellular components (nucleus and cytoplasm), especially in cases with low $\left(\frac{\alpha}{\beta}\right)_x$ and low dose ($D = 2\ Gy$). Under such circumstances, the mean and maximum dose uncertainties in SOBP can go as high as 1.83% and 4.35% respectively, and the maximal range uncertainties in 90% isodose level can be up to

1.67 mm for our prostate clinical study. Conversely, for high $\left(\frac{\alpha}{\beta}\right)_x$ target, the dose uncertainties are minor, and it is still feasible to use water as a surrogate material for LET_D computation in this scenario. All in all, there is a need to adopt (developed) better dosimetry and precise instrumentation in future radiobiological experiments to enhance the accuracy of dose and LET_D values on biological targets such that a clinically robust RBE modelling could be made possible. In the next chapter, we will investigate the methods in obtaining accurate information of LET_D values to further improve the RBE modelling during treatment planning.

3.6 References

1. Qi Tan H, Yang Calvin Koh W, Kuan Rui Tan L, et al. Dependence of LET on material and its impact on current RBE model. *Phys Med Biol*. 2019;64(13):135022. doi:10.1088/1361-6560/ab1c90

2. Carabe-Fernandez A, Dale RG, Jones B. The incorporation of the concept of minimum RBE (RbEmin) into the linear-quadratic model and the potential for improved radiobiological analysis of high-LET treatments. *Int J Radiat Biol*. 2007;83(1):27-39. doi:10.1080/09553000601087176

3. Chen Y, Ahmad S. Empirical model estimation of relative biological effectiveness for proton beam therapy. *Radiat Prot Dosimetry*. 2012;149(2):116-123. doi:10.1093/rpd/ncr218

4. Chen Y, Li J, Li C, Qiu R, Wu Z. A modified microdosimetric kinetic model for relative biological effectiveness calculation. *Phys Med Biol*. 2018;63(1). doi:10.1088/1361-6560/aa9a68

5. Frese MC, Wilkens JJ, Huber PE, Jensen AD, Oelfke U, Taheri-Kadkhoda Z. Application of constant vs. variable relative biological effectiveness in treatment planning of intensity-modulated proton therapy. *Int J Radiat Oncol Biol Phys*. 2011;79(1):80-88. doi:10.1016/j.ijrobp.2009.10.022

6. Giovannini G, Böhlen T, Cabal G, et al. Variable RBE in proton therapy: Comparison of different model predictions and their influence on clinical-like scenarios. *Radiat Oncol*. 2016;11(1):1-16. doi:10.1186/s13014-016-0642-6

7. Grün R, Friedrich T, Krämer M, et al. Physical and biological factors determining the effective proton range. *Med Phys*. 2013;40(11). doi:10.1118/1.4824321

8. McNamara AL, Schuemann J, Paganetti H. A phenomenological relative biological effectiveness (RBE) model for proton therapy based on all published in vitro cell survival data. *Phys Med Biol*. 2015;60(21):8399-8416. doi:10.1088/0031-9155/60/21/8399

9. Rørvik E, Thornqvist S, Stokkevag CH, Dahle TJ, Fjæra LF, Ytre-Hauge KS. A phenomenological biological dose model for proton therapy based on linear energy transfer spectra. *Med Phys*. 2017;44(6):2586-2594. doi:10.1002/mp.12216

10. Wedenberg M, Lind BK, Hårdemark B. A model for the relative biological effectiveness of protons: The tissue specific parameter α/β of photons is a predictor for the sensitivity to LET changes. *Acta Oncol (Madr)*. 2013;52(3):580-588. doi:10.3109/0284186X.2012.705892

11. Wilkens JJ, Oelfke U. A phenomenological model for the relative biological effectiveness in therapeutic proton beams. *Phys Med Biol*. 2004;49(13):2811-2825. doi:10.1088/0031-9155/49/13/004

12. Carabe A, Moteabbed M, Depauw N, Schuemann J, Paganetti H. Range uncertainty in proton therapy due to variable biological effectiveness. *Phys Med Biol*. 2012;57:1159.

13. Paganetti H. Relative biological effectiveness (RBE) values for proton beam therapy. Variations as a function of biological endpoint, dose, and linear energy transfer. *Phys Med Biol*. 2014;59(22):R419-R472. doi:10.1088/0031-9155/59/22/R419

14. Incerti S, Barberet P, Moretto P, Habchi C, Simon M, Seznec H. Monte Carlo dosimetry for targeted irradiation of individual cells using a microbeam facility. *Radiat Prot Dosimetry*. 2009;133(1):2-11. doi:10.1093/rpd/ncp003

15. Byrne HL, McNamara AL, Domanova W, Guatelli S, Kuncic Z. Radiation damage on sub-cellular scales: beyond DNA. *Phys Med Biol*. 2013;58(5):1251-1267. doi:10.1088/0031-9155/58/5/1251

16. White D, Woodard H, Hammond S. Average soft-tissue and bone models for use in radiation-dosimetry. *Br J Radiol*. 1987;60:907.

17. Allison J. Geant4–a simulation toolkit. *Int J Phytoremediation*. 2007;17(2):20-24. doi:10.1080/10506890701404297

18. Agostinelli S, Amako K, Apostalakis J, Araujo H, others. Geant4 developments and applications. *IEEE Trans Nucl Sci*. 2006;53:270-278.

19. Allison J, Amako K, Apostolakis J, et al. Recent developments in GEANT4. *Nucl Instruments Methods Phys Res Sect A Accel Spectrometers, Detect Assoc Equip*. 2016;835:186-225. doi:10.1016/j.nima.2016.06.125

20. Guan F, Peeler C, Bronk L, et al. Analysis of the track- and dose-averaged LET and LET spectra in proton therapy using the geant 4 Monte Carlo code. *Med Phys*. 2015;42(11):6234-6247. doi:10.1118/1.4932217

21. Skarsgard LD, Palcic B, Douglas BG, Lam GKY. Radiobiology of pions at TRIUMF. In: *International Journal of Radiation Oncology, Biology, Physics*. Vol 8. ; 1982:2127-2132. doi:10.1016/0360-3016(82)90556-9

22. Wouters BG, Sy AM, Skarsgard LD. Low-Dose Hypersensitivity and Increased Radioresistance in a Panel of Human Tumor Cell Lines with Different Radiosensitivity. *Radiat Res*. 2006;146(4):399. doi:10.2307/3579302

23. Wouters BG, others. Radiobiological intercomparison of the 160 MeV and 230 MeV proton therapy beams at the Harvard Cyclotron Laboratory and the Massachusetts General Hospital. *Radiat Res*. 2015;(183)(2):174.

24. Raju MR, Amols HI, Bain E, Carpenter SG, Cox RA, Robertson JB. A heavy particle comparative study. Part III: OER and RBE. *Br J Radiol*. 1978;51:712.

25. Raju MR, Bain E, Carpenter SG, Cox RA, Robertson JB. A heavy particle comparative study. Part II: cell survival versus depth. *Br J Radiol*. 1978;51:704.

26. McNamara AL, Schuemann J, Paganetti H. A phenomenological relative biological effectiveness (RBE) model for proton therapy based on all published in vitro cell survival data. *Phys Med Biol*. 2015;60:8399.

27. Grotzer MA, Schultke E, Brauer-Krisch E, Laissue JA. Microbeam radiation therapy: Clinical perspectives. *Phys Medica*. 2015;31(6):564.

28. Girst S, Greubel C, Reindl J, Siebenwirth C, others. Proton Minibeam Radiation Therapy Reduces Side Effects in an In Vivo Mouse Ear Model. *Int J Radiat Oncol Biol Phys*. 2016;95(1):234.

29. Prezado Y, Jouvion G, Hardy D, Patriarca A, others. Proton minibeam radiation therapy spares normal rat brain: Long-Term Clinical, Radiological and

Histopathological Analysis. *Sci Rep*. 2017;7:14403.

30. Friedrich T, Ilicic K, Greubel C, Girst S, Reindl J, others. DNA damage interactions on both nanometer and micrometer scale determine overall cellular damage. *Sci Rep*. 2018;8:16063.

31. Folkard M, Prise KM, Vojnovic B, Newman HC, Roper MJ, Michael BD. Inactivation of V79 cells by low-energy protons, deuterons and helium-3 ions. *Int J Radiat Biol*. 1996;69(6):729-738. doi:10.1080/095530096145472

32. Schettino G, Folkard M, Prise KM, Vojnovic B, Boweyand AG, Michael BD. Low-dose hypersensitivity in Chinese hamster V79 cells targeted with counted protons using a charged particle microbeam. *Radiat Res*. 2001;156:526.

33. Doria D, Kakolee KF, Kar S, et al. Biological effectiveness on live cells of laser driven protons at dose rates exceeding 109 Gy/s. *AIP Adv*. 2012;2(1). doi:10.1063/1.3699063

34. Dodge Y. *The Concise Encyclopedia of Statistics*. Springer; 2008. doi:10.1007/978-0-387-32833-1

35. Schneider W, Bortfeld T, Schlegel W. Correlation between CT numbers and tissue parameters needed for the Monte Carlo simulations of clinical dose distributions. *Phys Med Biol*. 2000;45:459.

36. Spaargaren DH. The design of culture media based on the elemental composition of biological material. *J Biotechnol*. 1996;45:97.

37. van Leeuwen CM, Oei AL, Crezee J, et al. The alfa and beta of tumours: A review of parameters of the linear-quadratic model, derived from clinical radiotherapy studies. *Radiat Oncol*. 2018;13(1):1-11. doi:10.1186/s13014-018-1040-z

38. Hall EJ, Kellerer AM, others. The relative biological effectiveness of 160 MeV protons. II. Biological data and their interpretation in terms of microdosimetry. *Int J Radiat Oncol Biol Phys*. 1978;4:1009.

39. Britten RA, Nazaryan V, Davis LK, others. Variations in the {RBE} for cell killing along the depth-dose profile of a modulated proton therapy beam. *Radiat Res*. 1978;179:21.

40. Grosse N, Fontana A, Hug EB, Lomax A, Coray A, others. Deficiency in homologous recombination renders mammalian cells more sensitive to proton versus photon irradiation. *Int J Radiat Oncol Biol Phys*. 2014;88:175.

41. Gueulette J, Gregoire V, Octave-Prignot M, Wambersie A. Measurements of radiobiological effectiveness in the 85 MeV proton beam produced at the cyclotron CYCLONE of Louvain-la-Neuve, Belgium. *Radiat Res*. 1996;145:70.

42. Coutrakon G, Cortese J, Ghebremedhin A, et al. Microdosimetry spectra of the Loma Linda proton beam and relative biological effectiveness comparisons. *Med Phys*. 1997;24(9):1499-1506. doi:10.1118/1.598038

43. Wouters BG, Sy AM, Skarsgard LD. Low-dose hypersensitivity and increased radioresistance in a panel of human tumor cell lines with different radiosensitivity. *Radiat Res*. 1997;146:399.

44. Belli M, Cera F, Cherubini R, Haque AMI, Ianzini F, others. Inactivation and mutation

induction in V79 cells by low energy protons: re-evaluation of the results at the LNL facility. *Int J Radiat Oncol Biol Phys*. 1993;63:331.

45. Ogheri S, Bruna V, Cera F, Favaretto S, Cherubini R, Celotti L. Mutant frequency at the HPRT locus and in minisatellite sequences in Chinese hamster V79 cells irradiated with low-energy protons (31 $keV/μm$) and ultraviolet light (254 nm). *Radiat Res*. 1997;148:203.

46. Belli M, others. RBE-LET relationships for cell inactivation and mutation induced by low energy protons in V79 cells: further results at the LNL facility. *Int J Radiat Oncol Biol Phys*. 1998;74:501.

47. Goodhead DT, others. Direct comparison between protons and alpha-particles of the same LET: I. Irradiation methods and inactivation of asynchronous V79, HeLa and C3H 10T1/2 cells. *Int J Radiat Biol*. 1992;61:611.

48. Doria D, others. Biological effectiveness on live cells of laser driven protons at dose rates exceeding $109 Gy s^{-1}$. *AIP Adv*. 1996;2:11209. doi:10.1063/1.3699063

49. Yashkin PN, others. Relative biological effectiveness of proton medical beam at Moscow synchrotron determined by the chinese hamster cells assay. *Int J Radiat Biol*. 1995;31:535.

50. Matsumura S, others. Differences in the biological effects of in vitro irradiation by 65 {MeV} protons and 137 cesium gamma-rays. *Anticancer Res*. 1999;19:477.

51. Blomquist E, Russell KR, Stenerlow B, Montelius A, Grusell E, Carlsson J. Relative biological effectiveness of intermediate energy protons. Comparisons with 60Co gamma-radiation using two cell lines. *Radiother Oncol*. 1993;28:44.

52. Wainson AA, Lomanov MF, Shmakova NL, Blokhin SI, Jarmonenko SP. The {RBE} of accelerated protons in different parts of the Bragg curve. *Br J Radiol*. 1972;45:525.

53. Bird RP, Rohrig N, Colvett RD, Geard CR, Marino SA. Inactivation of synchronized Chinese hamster V79 cells with charged-particle track segments. *Radiat Res*. 1980;82:277.

54. Folkard M, Prise KM, Vojnovic B, Davies S, Roper MJ, others. The irradiation of V79 mammalian cells by protons with energies below 2 MeV. Part I: experimental arrangement and measurement of cell survival. *Int J Radiat Biol*. 1989;56:221.

55. Prise KM, Folkard M, Davies S, Michael BD. The irradiation of V79 mammalian cells by protons with energies below 2 MeV. Part II. Measurement of oxygen enhancement ratios and DNA damage. *Int J Radiat Biol*. 1990;58:261.

56. Robertson JB, Eaddy JM, Archambeau JO, Coutrakon GB, others. *Variation of Measured Proton Relative Biological Effectiveness (RBE) as a Function of Initial Proton Energy Hadrontherapy and Oncology: Proceedings of the First International Symposium on Hadrontherapy*. Amsterdam: Elsevier; 1994.

57. Schuff JA, others. Relative biological effectiveness measurements of low energy proton and lithium beams on tumor cells. *Nucl Instrum Methods Phys Res B*. 2002;187:345.

58. Jeynes JCG, others. Broadbeam irradiation of mammalian cells using a vertical microbeam facility. *Radiat Environ Biophys*. 2012;52:513.

59. Moertel H, Georgi JC, Distel L, et al. Effects of low energy protons on clonogenic survival, DSB repair and cell cycle in human glioblastoma cells and B14 fibroblasts. *Radiother Oncol*. 2004;73:S115.

60. Tang JT, Inoue T, Yamazaki H, Fukushima S, others. Comparison of radiobiological effective depths in 65 {MeV} modulated proton beams. *Br J Cancer*. 1997;76:220.

61. Sgura A, Antoccia A, Cherubini R, et al. Micronuclei, CREST-positive micronuclei and cell inactivation induced in Chinese hamster cells by radiation with different quality. *Int J Radiat Biol*. 2000;76:367.

62. Ando K, others. Relative biological effectiveness of the 235 MeV proton beams at the National Cancer Center Hospital East. *J Radiat Res*. 2001;42:79.

63. Perris A, Pialoglou P, Katsanos AA, Sideris EG. Biological effectiveness of low energy protons. I. Survival of Chinese hamster cells. *Int J Radiat Biol*. 1986;50:1093.

64. Green LM, Murray DK, Tran DT, et al. Response of thyroid follicular cells to gamma irradiation compared to proton irradiation. I. Initial characterization of DNA damage, micronucleus formation, apoptosis, cell survival, and cell cycle phase redistribution. *Radiat Res*. 2001;155:32.

65. Williams JR, Gould RG, Flynn D, Robertson JB, Little JB. Relative survival of hybrid x-ray resistant, and normally sensitive mammalian cells exposed to x rays and protons under aerobic and hypoxic conditions. *Radiat Res*. 1978;73:585.

66. Ibanez IL, others. Induction and rejoining of DNA double strand breaks assessed by H2AX phosporylation in melanoma cells irradiated with proton and lithium beams. *Int J Radiat Oncol Biol Phys*. 2009;74:1226.

67. Hei TK, Komatsu K, Hall EJ, Zaider M. Oncogenic transformation by charged particles of defined {LET}. *Carcinogenesis*. 1988;9:747.

68. Green LM, Tran DT, Murray DK, Rightnar SS, Todd S, Nelson GA. Response of thyroid follicular cells to gamma irradiation compared to proton irradiation: II. The role of connexin 32. *Radiat Res*. 2002;158:475.

69. Robertson JB, Williams JR, Schmidt RA, Little JB, Flynn DF, Suit HD. Radiobiological studies of a high-energy modulated proton beam utilizing cultured mammalian cells. *Cancer*. 1975;35:1664.

70. Urano M, Goitein M, Verhey L, Mediondo O, Suit HD, Koehler A. Relative biological effectiveness of a high energy modulated proton beam using a spontaneous murine tumor in vivo. *Int J Radiat Oncol Biol Phys*. 1980;6:1187.

71. Bettega D, others. Inactivation of C3H10T1/2 cells by low energy protons and deuterons. *Int J Radiat Biol*. 1998;73:303.

72. Satoh S, Inada T, Eguchi K, Tatsuzaki H, Kitagawa T, Hirokawa Y. Studies on relative biological effectiveness and therapeutic gain factor of high energy protons modulated for radiotherapy (in Japanese). *Nippon Igaku Hoshasen Gakkai Zasshi*. 1986;46:714.

73. Sakamoto K, Takai T, Ito A, Hasegawa T, Sugai I, Takaku S. Survival of clonogenic murine epithelioma cells exposed to 52 MeV proton beam produced from the cyclotron at INS. *J Radiat Res*. 1980;21:271.

74. Aoki-Nakano M. Relative biological effectiveness of therapeutic proton beams for {HSG} cells at Japanese proton therapy facilities. *J Radiat Res*. 2014;55:812.

75. Gerelchuluun A, Hong Z, Sun L, et al. Induction of in situ DNA double-strand breaks and apoptosis by 200 MeV protons and 10 MV x-rays in human tumour cell lines. *Int J Radiat Biol*. 2011;87:57.

76. Chaudhary P, others. Relative biological effectiveness variation along monoenergetic and modulated Bragg peaks of a 62 {MeV} therapeutic proton beam: a preclinical assessment. *Int J Radiat Oncol Biol Phys*. 2014;90:27.

77. Calugaru V, Nauraye C, Noel G, Giocanti N, Favaudon V, Megnin-Chanet F. Radiobiological characterization of two therapeutic proton beams with different initial energy spectra used at the Institut Curie Proton Therapy Center in Orsay. *Int J Radiat Oncol Biol Phys*. 2011;81:1136.

78. Courdi A, Brassart N, Herault J, Chauvel P. The depth-dependent radiation response of human melanoma cells exposed to 65 {MeV} protons. *Br J Radiol*. 1994;67:800.

79. Zhang X, Lin SH, Fang B, Gillin M, Mohan R, Chang JY. Therapy-resistant cancer stem cells have differing sensitivity to photon versus proton beam radiation. *J Thorac Oncol Off Publ Int Assoc Study Lung Cancer*. 2013;8:1484.

80. Baggio L, Cavinato M, Cherubini R, Conzato M, Cucinotta F, others. Relative biological effectiveness of light ions in human tumoural cell lines: role of protein p53. *Radiat Prot Dosim*. 2002;99:211.

81. Inada T, Kawachi K, Kanai T, Nojiri I. Inactivation of cultured human tumor cells irradiated by cyclotron neutrons and protons. *J Radiat Res*. 1981;22:143.

82. Kagawa K, Murakami M, Hishikawa Y, Abe M, Akagi T, Yanou T, Kagiya G, Furusawa Y, Ando K, Nojima K, Aoki M KT. Preclinical biological assessment of proton and carbon ion beams at Hyogo Ion Beam Medical Center. *Int J Radiat Oncol Biol Phys*. 2002;54:928. doi:10.1016/s0360-3016(02)02949-8

83. Kase Y, Yamashita W, Matsufuji N, Takada K, Sakae T, Furusawa Y, Yamashita H MS. Microdosimetric calculation of relative biological effectiveness for design of therapeutic proton beams. *J Radiat Res*. 2013;54(3):485-493. doi:10.1093/jrr/rrs110

84. Matsuura T, others. Apparent absence of a proton beam dose rate effect and possible differences in {RBE} between Bragg peak and plateau. *Med Phys*. 2010;37:5376.

85. Baek HJ, Kim TH, Shin D, Kwak JW, others. Radiobiological characterization of proton beam at the National Cancer Center in Korea. *J Radiat Res*. 2008;49:509.

86. Butterworth KT. Relative biological effectiveness {(RBE)} and out-of-field cell survival responses to passive scattering and pencil beam scanning proton beam deliveries. *Phys Med Biol*. 2013;57:6671.

87. Matsumoto Y, T. Matsuura MW, Egashira Y, Nishio T, Furusawa F. Enhanced radiobiological effects at the distal end of a clinical proton beam: in vitro study. *J Radiat Res*. 2014;55:816.

88. Ogata T, Teshima T, Kagawa K, Hishikawa Y, others. Particle irradiation suppresses metastatic potential of cancer cells. *Cancer Res*. 2005;65:113.

89. Belli M, others. Inactivation of human normal and tumour cells irradiated with low energy proton. *Int J Radiat Biol*. 2000;76:831.

90. Yogo A, others. Measurement of relative biological effectiveness of protons in human cancer cells using a laser-driven quasimonoenergetic proton beamline. *Appl Phys Lett*. 2011;98:53701.

91. Bettega D, Calzolari P, Chauvel P, Courdi A, Herault J, others. Radiobiological studies on the 65 {MeV} therapeutic proton beam at {Nice} using human tumour cells. *Int J Radiat Biol*. 2000;76:1297.

92. Pertrovic I, Ristic-fira A, Todorovic D, Valastro L, Cirrone P, Cuttone G. Radiobiological analysis of human melanoma cells on the 62 {MeV CATANA} proton beam. *Int J Radiat Biol*. 2006;82:251.

93. Ristic-Fira AM, Pertrovic IM, Koricanac LB, Valastro LM, Privitera G, Cuttone G. Assessment of the inhibitory effects of different radiation qualities or chemotherapeutic agents on a human melanoma cell line. *Phys Med*. 2008;24:187.

94. Wera AC, Heuskin AC, Requier H, Michiels C, Lucas S. Low-LET proton irradiation of A549 nonsmall cell lung adenocarcinoma cells: dose response and RBE determination. *Radiat Res*. 2013;179:273.

95. Wera AC, Requier H, Heuskin AC, Michiels C, Lucas S. In vitro irradiation station for broad beam radiobiological experiments. *Nucl Instrum Methods Phys Res B*. 2011;269:3120.

96. Ristic-Fira AM, Todorovic T, Zakula J, Keta O, Cirrone P, Cuttone G. Response of human {HTB140} melanoma cells to conventional radiation and hadrons. *Physiol Res/Academia Sci Bohemoslov*. 2010;60:S129.

97. Pertrovic I, Ristic-fira A, Todorovic D, et al. Response of a radioresistant human melanoma cell line along the proton spread-out Bragg peak. *Int J Radiat Biol*. 2010;86:742.

98. Keta O, Todorovic D, Popovic N, et al. Radiosensitivity of human ovarian carcinoma and melanoma cells to gamma-rays and protons. *Arch Med Sci*. 2014;10:578.

99. Hei TK, Chen DJ, Brenner DJ, Hall EJ. Mutation induction by charged particles of defined linear energy transfer. *Carcinogenesis*. 2014;9:1233.

100. Yang H, Anzenberg V, Held KD. Effects of heavy ions and energetic protons on normal human fibroblasts. *Radiats Biol Radioecol*. 2007;47:302.

101. Slonina D, Biesaga B, Swakon J, et al. Relative biological effectiveness of the 60 MeV therapeutic proton beam at the Institute of Nuclear Physics (IFJ PAN) in Krakow, Poland. *Radiat Environ Biophys*. 2014;53:745.

102. Conti AMF, Francone G, Volonte M, Gallini RE. Induction of 8-azaguanine resistant mutants in human cultured cells exposed to 31 {MeV} protons. *Int J Radiat Biol*. 1988;53:467.

103. Antoccia A, Sgura A, Berardinelli F, Cavinato M, Cherubini R, others. Cell cycle perturbations and genotoxic effects in human primary fibroblasts induced by low-energy protons and x/gamma-rays. *J Radiat Res*. 2009;50:457.

104. Bettega D, Birattari C, Bombana M, et al. Relative biological effectiveness for protons of energies up to 31 {MeV}. *Radiat Res*. 1979;77:85.

Chapter 4 Standardizing Monte Carlo Simulation parameters for a reproducible Dose-averaged Linear Energy Transfer

In the previous chapter, we understand how different experimental assumptions impact the LET_D values and its effect on the RBE model. Therefore, it is important to reduce the uncertainty in obtaining LET_D values. In this chapter, we will determine how different combinations of MC simulation parameters in GEANT4 will affect the result in the sampling of LET_D using different MC scoring methods and established a set of protocols to obtain accurate LET_D values that complement the previous study. Therefore the objective of this study is to standardize the definition of LET_D and simulation parameters of Monte Carlo simulation to obtain LET_D. This work has been published in the *British Institute of Radiology*[1]

4.1 Introduction

LET values are difficult to be measured experimentally[2,3] and they are often determined by analytical means[4] or via simulation[5,6]. Even though the importance of LET values and their effect on cell killing are well known[7,8], there are still inadequate studies investigating the credibility of the methods employed to obtain LET values from MC simulation. Moreover, there had not been a standardized simulation protocol despite the extensive use of MC simulation in proton therapy. As a result, comparing LET_D results across institutions proves a challenge, with each work adopting its own set of simulation protocols.

The reproducibility of LET values will depend on the definition of LET - (a) LET_t and (b) LET_D as represented by analytical equations discussed in Wilkens and Oelfke[4]. In MC simulation, parameters such as the choice of physics model, maximum step length (upper limit of a particle's tracking step length), range cut limits (minimum energy of

secondary particles in inelastic interaction) and voxel dimensions can also cause a variation in the scoring of LET. Since LET_D is used for the calculation of RBE[9–11], it will be the main focus of this work and the analytical equation is calculated using Equation 1.17. However, in MC simulation, LET_D is generally expressed as

$$LET_D = \frac{\sum_{i=1}^{n} \frac{\epsilon_i^2}{l_i}}{\sum_{i=1}^{n} \epsilon_i} \tag{4.1}$$

where ϵ_i is the energy deposition by the *i*th charged particle, l_i is the step length and *n* is the total number of steps in each voxel[2,3,12]. According to ICRU Report No. 85[13], LET is defined as the *average energy transfer* by the charged particle per unit length due to electronic interactions at a spatial point. This definition of LET is limited to one specified type of charged particles (proton, electron and other heavy ions) at any one point in time. However, LET_D is used in this work as it accounts for not just one type of particle but an ensemble of charged particles in a particular voxel and this has a higher correlation to biological damage. Since primary protons and secondary electrons both contribute to biological damage in a real-life situation, they should be included in the LET_D calculation. Therefore, LET_D is simplified to the *total energy deposited* by the charged particles in MC simulation[2] as described by Equation 1.17.

Several studies which made use of MC simulation to sample LET_D have been done. Due to the longer computational time for explicit electron tracking, a large range cut for secondary electrons is often used in a typical MC simulation for Proton Therapy application[14,15]. This poses a problem in a real-life situation of a lung patient where the electrons do travel over a higher range due to the low density of the lung and secondary electrons need to be factored in for greater dose accuracy. In the study by Guan *et al.*[2], GEANT4[16–18] was used to simulate a proton beam with a high range cut (no explicit secondary electron production) and only electronic inelastic interactions were

considered (nuclear interactions were neglected) to compare LET_D and LET_t values. Cortes-Giraldo *et al.*[19] showed that the different LET_D scoring methods, range cut and voxel dimensions used in the simulation resulted in different calculated LET_D values. However, their work was done using MC simulation with a cylindrical volume rather than a voxelised geometry which is used clinically.

In addition to the variation of parameters in MC simulation, the scoring methods for LET_D differ with different studies. Both Guan *et al.*[2] analysis of LET_D and Granville *et al.*[3] comparison of LET_D scoring techniques uses Equation 1.17 for their LET_D calculations. Similarly, Cortes-Giraldo *et al.*[19] also used similar equations to Equation 4.2, except that they had included a weighting factor to each equation to account for only primary protons in their LET_D calculation. They had recommended a scoring method that provided a stable unrestricted LET_D with different voxel sizes and production cuts. However, this method simplifies the LET_D scoring method to unrestricted LET_D and is similar to the *Unrestricted* method in Section 4.2. Thus, their method is excluded in our comparison. All these indicated that the LET_D scoring method is not clearly defined in MC and there is no strong physical basis on which scoring methods should be used in scoring LET_D especially when both primary protons and secondary electrons are present in the simulation.

$$LET_D = \frac{\frac{(\sum_{i=1}^{n} \epsilon_i)^2}{\sum_{i=1}^{n} l_i}}{\sum_{i=1}^{n} \epsilon_i} \tag{4.2}$$

In this work, we are interested in the scoring of both primary protons and secondary electrons due to the aforementioned problem in a real-life situation. We examine the best step length (*stepMax*), range cut (*setCut*) value and LET_D scoring methods (

Table ***4.***) that should be implemented in MC simulation to achieve a reproducible LET_D value in a clinically relevant voxelized geometry. Supposedly, LET_D values must not be affected by changes in the hyperparameters used in the simulation. Yet, the fact that hyperparameters indeed influenced the LET_D results could not be overlooked. Therefore, we aim to propose and standardize a step length, range cut and LET_D scoring method for MC simulation to obtain the most reproducible LET_D result.

4.2 MC Simulation Setting

The irradiation of a mono-energetic proton beam with three different energies (80 MeV, 150 MeV and 200 MeV) at the central axis of a 30 x 30 x 30 cm^3 water phantom is simulated using GEANT4. The water phantom is resolved into voxels constituted of a 1 mm^3 cube and the z-coordinate (depth) of the phantom ranges from 0 mm to 300 mm. The number of particle histories is set to 100000 and the dose errors are less than 2% across the central axis of the dose. G4EmStandardPhysics_option4 is used for the physics model as it is the recommended physical model for clinical proton beams below 5 GeV^2. A snippet of the code used for this chapter is shown in Appendix B2, B3 and B4.

Energy deposition and step length are scored individually for every particle in the selected voxels at *Position 1, 2, 3* and *4* for each proton beam energy as shown in Figure 4.1 **(**A), (B) and (C).

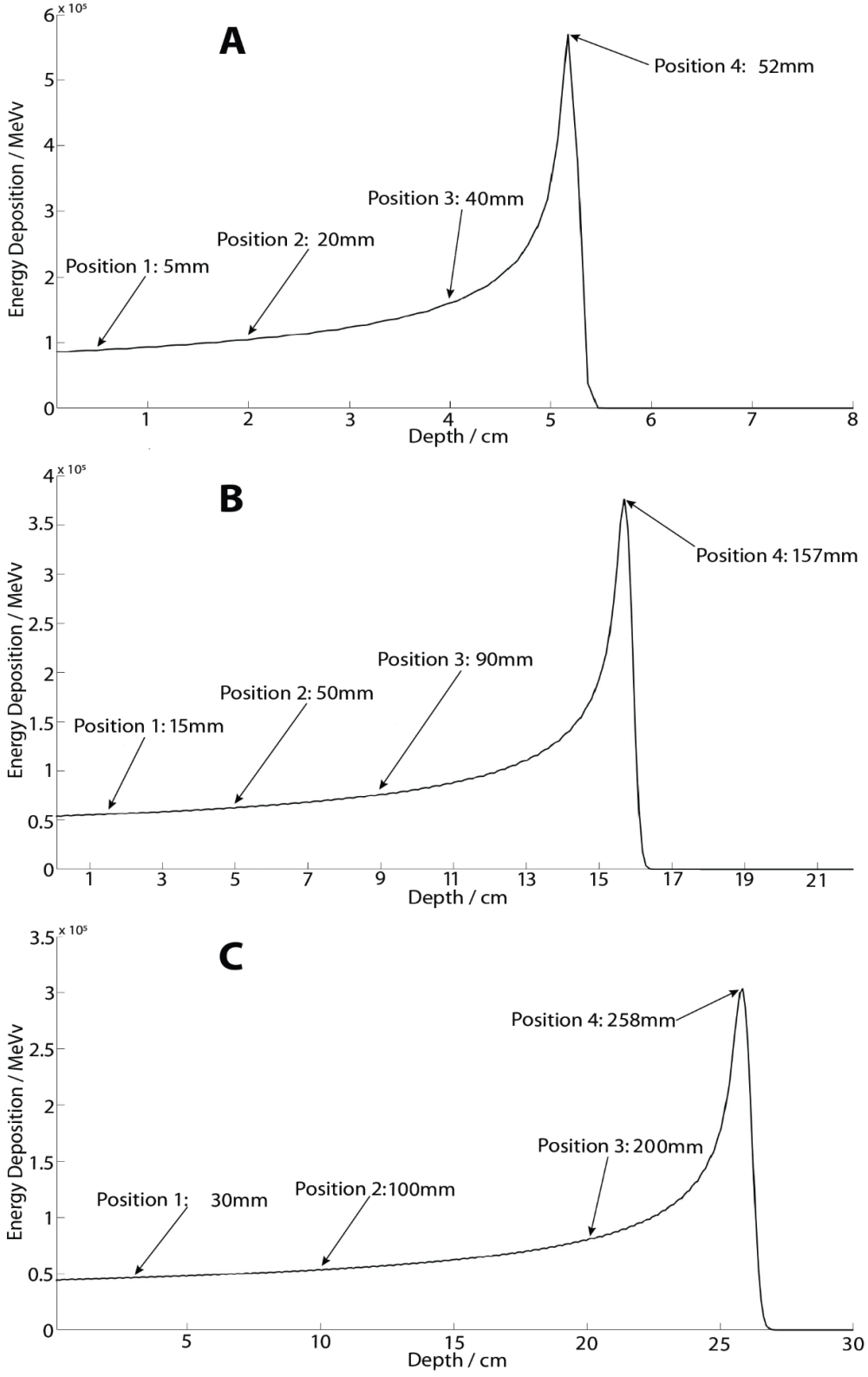

Figure 4.1 (A), (B) and (C) shows the Bragg peak of 80 MeV, 150 MeV and 200 MeV respectively. Energy deposition and step length are scored individually for every particle in the selected voxels at Position 1, 2, 3 and 4 of each proton beam energy.

Positions beyond the Bragg peak were not chosen due to the absence of secondary electrons. There is no difference in the LET_D calculated using the five scoring methods as most of the energies of the secondary electrons are below the range cut value, thus all calculation converges. The positions are described by the depth from the water phantom range as mentioned above. The parameters used to calculate the LET_D values are summarized in Table 4.1.

Table 4.1 This table shows the MC simulation parameters of 3 proton beam energies, 3 step length and 4 range cut that are used in this work. Unrestricted refers to a range cut of 10^6 mm.

Energy/MeV	**stepMax/mm**	**setCut/mm**
80.00	0.01	0.01
150.00	0.05	0.05
200.00	0.50	0.10
		Unrestricted: 10^6

4.3 LET_D variations

The plots depicting how LET_D values vary with different energy cut for 80 MeV and 200 MeV beams are shown in Figure 4.2. *Proton - Unrestricted* refers to the result obtained using a range cut of 1000 m. *Proton – Restricted* and *Proton/Electron - Restricted* refer to the results acquired using a range cut of 0.01 mm and by applying *Method 1*. The former LET_D calculation factors in only primary proton while the latter accounts for both primary protons and secondary electrons. Figure 4.2 shows the dependence of LET_D values on the range cut value set for MC simulation. A discrepancy is observed between *Unrestricted* and *Restricted* LET_D, particularly at the plateau region. This is due to the presence of secondary electrons as limited by the range

cut. Notwithstanding the exclusion of secondary electrons from the calculations, *Unrestricted* LET_D turns out to be higher than *Restricted* LET_D. This observation further corroborated the importance of choosing the appropriate range cut value during simulation.

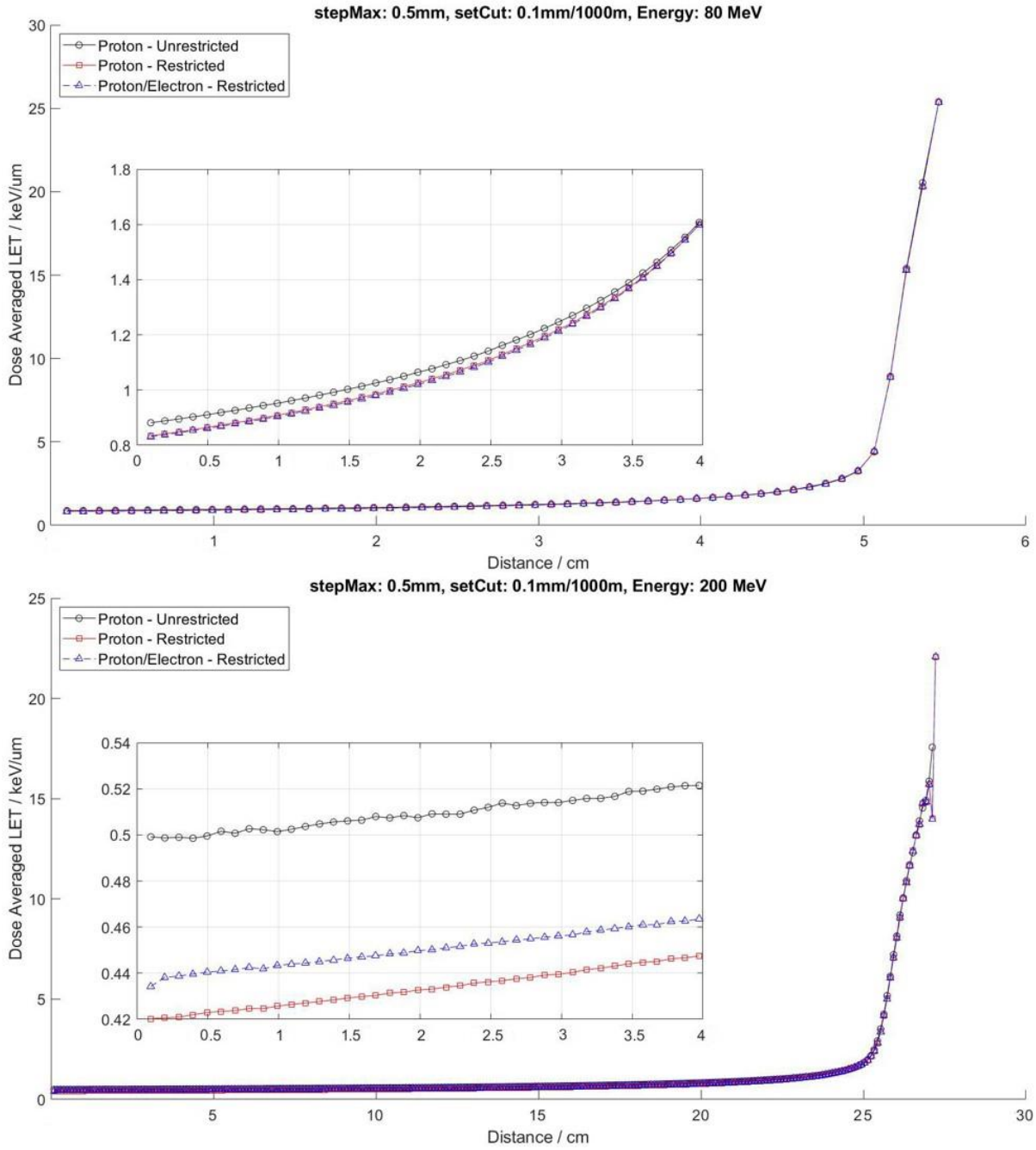

Figure 4.2 shows LET_D vs Depth for 80 MeV (top) and 200 MeV (bottom) proton beam with a step length of 0.5 mm and a comparison of Unrestricted and 0.1 mm range cut. The additional plot focuses on the plateau region of the main graph. The ○ represents LET_D values for Unrestricted setCut, Δ and □ represent LET_D values for 0.1 mm range cut, considering only protons and protons + secondary electrons, respectively.

4.4 Correlation between LET_D Scoring Methods

In this work, we used the concept of correlation to understand differences between LET_D scoring methods. Most of the differences in LET definition arises from the inequality of $\mathrm{E}\left(\frac{\epsilon_i^2}{l}\right)$ and $\frac{\mathrm{E}(\epsilon_i^2)}{\mathrm{E}(l)}$. $\mathrm{E}\left(\frac{\epsilon_i^2}{l}\right)$ can be approximated by Equation 4.3[20,21] from doing a bivariate second-order Taylor expansion. Assuming random variables with finite means are $E(X) = \mu_x$ and $E(Y) = \mu_y$, the first-order Taylor expansion on $f(X,Y)$ was done at an expansion point ($\theta = (\mu_x, \mu_y)$). We will arrive at Equation 4.3.

$$\mathrm{E}\big(f(X,Y)\big) \approx f\big(E(X), E(Y)\big) = f(\mu_x, \mu_y) \tag{4.3}$$

In the case where $f(X,Y) = \frac{X}{Y}$, Equation 4.34.34.3 can be approximated as $f\big(\mu_x, \mu_y\big) = \frac{\mu_x}{\mu_y}$. By doing the second-order Taylor expansion at the same expansion point θ, we can simplify to Equation 4.4.

$$\mathrm{E}\big(f(X,Y)\big) \approx f(\theta) + \frac{1}{2}\{f''_{xx}(\theta)Var(X) + 2f''_{xy}(\theta)Cov(X,Y) + f''_{yy}(\theta)Var(Y)\} \tag{4.4}$$

Since we know that $f(\theta) = \frac{\mu_x}{\mu_y}$, we can determine the second derivative of function $f(\theta) = \frac{\mu_x}{u_y}$ with respect to xx, yy and xy as shown in Table 4.2.

Table 4.2 This table shows the MC simulation parameters of 3 proton beam energies, 3 step length and 4 range cut that are used in this work. Unrestricted refers to a range cut of 10^6 mm.

First Derivative	$f'_x(\theta) = \frac{1}{\mu_y}$	$f'_y(\theta) = -\frac{\mu_x}{(\mu_y)^2}$	$f'_x(\theta) = \frac{1}{\mu_y}$
Second Derivative	$f''_{xx}(\theta) = 0$	$f''_{yy}(\theta) = \frac{2}{(\mu_y)^3}$	$f''_{xy}(\theta) = -\frac{1}{(\mu_y)^2}$

By substituting (x, y) with (ϵ_i^2, l_i), we will arrive at Equation 4.3.

$$\mathrm{E}\left(\frac{\epsilon_i^2}{l}\right) \approx \frac{\mathrm{E}(\epsilon_i^2)}{\mathrm{E}(l)} - \frac{Cov(\epsilon_i^2, l)}{\big(\mathrm{E}(l)\big)^2} + \frac{Var(l)\mathrm{E}(\epsilon_i^2)}{\big(\mathrm{E}(l)\big)^3} \tag{4.5}$$

The difference depends on the covariance of energy deposition and step length. Hence, if the distribution of ϵ^2 against l for all steps in a voxel is linearly correlated, it implies that the covariance will be high and the values of the LET_D will be affected significantly by the definition.

4.4.1 Correlation Analysis

The covariance between energy deposition per step and step length at the plateau region (*Position 1*, *2* and *3*) for 200 MeV of the proton beam is shown in Figure 4.3. Individual particle track was scored at selected voxels and the energy deposition per step were plotted for each permutation of energy, step length and range cut. Plot A, B and C represent range cut of 0.01 mm at Position 1; Plot D, E and F represent range cut of 0.05 mm at Position 2; and Plot G, H and I represent range cut of 0.1 mm at Position 3. Plot A, D and G represent step length of 0.01 mm; Plot B, E and H represent step length of 0.05 mm; and Plot C, F and I represent step length of 0.5 mm. Only 200 MeV data were presented as both 80 MeV and 150 MeV data display a similar pattern at *Position 1*, *2* and *3*. Comparing across all simulation parameters, the linear and non-linear correlation for both protons and secondary electrons were observed. The *Pearson r-squared* values showed up to 0.99.

Unlike at the plateau region**,** certain simulation parameters do not show any secondary electrons due to the range cut parameter at the Bragg peak region. Upon closer inspection of the plots, the distribution of the data points suggested that the difference between $\mathrm{E}\left(\frac{\epsilon_i^2}{l}\right)$ and $\frac{\mathrm{E}(\epsilon_i^2)}{\mathrm{E}(l)}$ could be subtle with an r-squared value of 0.96 (Figure 4.3C,

F and I) or significant with an r-squared value of 9×10^{-5} (Figure 4.3 A, B, D, E, G and H). This points to the need to carefully selecting the scoring methods and simulation parameters for LET_D calculation since higher r-squared values relate to higher covariance.

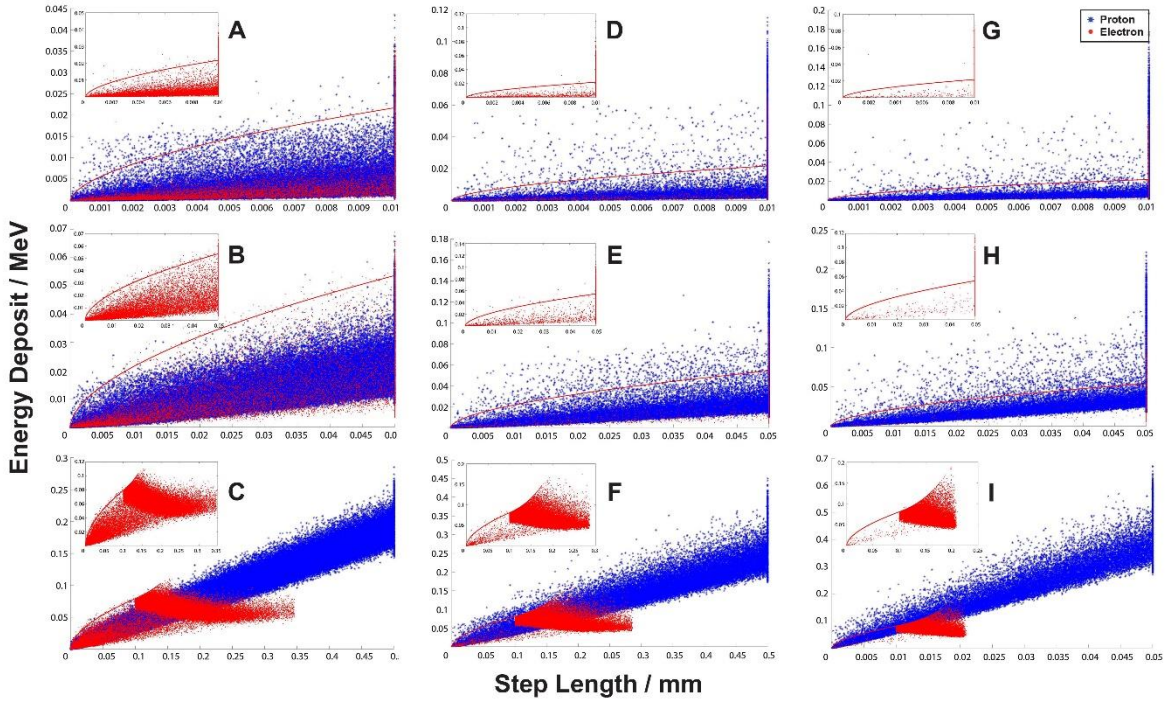

Figure 4.3 shows the plots of Energy Deposition Vs Step Length of both protons and secondary electrons of 200 MeV proton beam at the plateau region. Plot A, B and C represent range cut of 0.01 mm at Position 1; Plot D, E and F represent range cut of 0.05 mm at Position 2; and Plot G, H and I represent range cut of 0.1 mm at Position 3. Plot A, D and G represent step length of 0.01 mm; Plot B, E and H represent step length of 0.05 mm; and Plot C, F and I represent step length of 0.5 mm. The zoomed-in plot shows only secondary electrons (red) while the actual plot shows protons (blue) and secondary electrons (red).

Table 4.3 indicates the presence of secondary electrons in different simulation parameters.

Table 4.3 shows the simulation parameters at Position 4. ✔ represent the presence of secondary electrons while ✘ representing the absence of secondary electrons.

stepMax (mm)	0.50			0.05			0.01		
setCut (mm)	0.01	0.05	0.10	0.01	0.05	0.10	0.01	0.05	0.10
80 MeV	✔	✘	✘	✔	✘	✘	✔	✘	✘
150 MeV	✔	✘	✘	✔	✔	✘	✔	✔	✘
200 MeV	✔	✔	✘	✔	✔	✘	✔	✔	✘

Only data from range cut of 0.01 mm at *Position 4* is shown in Figure 4.4 as secondary electrons are present, and it follows a similar trend for other range cut and step length values. Plot A, B and C represent step length of 0.01 mm; Plot D, E and F represent step length of 0.05 mm; and Plot G, H and I represent step length of 0.5 mm. Plot A, D and G represent proton beam energy of 80 MeV; Plot B, E and H represent proton beam energy of 150 MeV; and Plot C, F and I represent proton beam energy of 200 MeV.

At the Bragg peak region (*Position 4)*, the number of secondary electrons decreases as most of the primary protons' energy fall below the cut-off energy. Accordingly, the percentage difference at *Position 4* is found to be much lower (35%) than that at *Position 1*. At all positions, an *Unrestricted* range cut resulted in a 0% difference since secondary electrons were absent. We aim to achieve better dose accuracy by accounting for secondary electrons during dose calculation. However, all positions see a rise in the percentage difference between $\mathrm{E}\left(\frac{\epsilon_i^2}{l}\right)$ and $\frac{\mathrm{E}(\epsilon_i^2)}{\mathrm{E}(l)}$ as the range cut decreases.

A low covariance between Energy Deposition and Step Length was found with the same set of simulation parameters as Figure 4.3. This implies that the choice of scoring

method could be randomly done as it will not have a significant impact on the exact values of LET_D. Therefore, to achieve a reproducible LET_D value, we had calculated and compared the percentage difference between $\mathrm{E}\left(\frac{\epsilon_i^2}{l}\right)$ and $\frac{\mathrm{E}(\epsilon_i^2)}{\mathrm{E}(l)}$ as shown in Table D1 for each permutation for the simulation parameters.

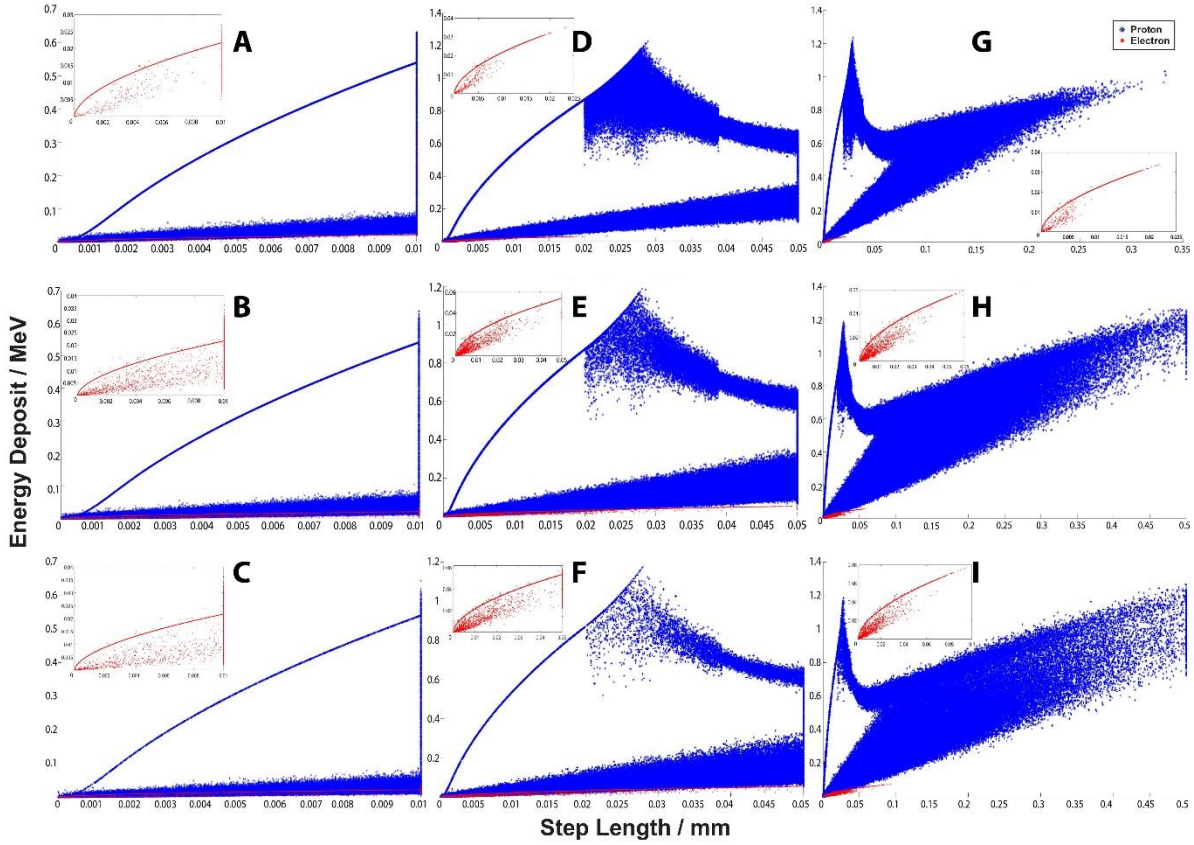

Figure 4.4 shows the plots of Energy Deposition Vs Step Length of both protons and secondary electrons of 0.01 mm range cut at Position 4. Plot A, B and C represent step length of 0.01 mm; Plot D, E and F represent step length of 0.05 mm; and Plot G, H and I represent step length of 0.5 mm. Plot A, D and G represent proton beam energy of 80 MeV; Plot B, E and H represent proton beam energy of 150 MeV; and Plot C, F and I represent proton beam energy of 200 MeV. The zoomed-in plot shows only secondary electrons (red) while the actual plot shows protons (blue) and secondary electrons (red).

Table D1 in Appendix D shows the calculated values of the individual terms of Equation 4.3 at *Position 1*. Data from *Position 2* and *3* was not shown as it follows a similar trend to the data from *Position 1*. The percentage difference accounting for both primary protons and secondary electrons was calculated with respect to $\mathrm{E}\left(\frac{\epsilon_i^2}{l}\right)$. It has been noted that as range cut decreases, the difference between $\mathrm{E}\left(\frac{\epsilon_i^2}{l}\right)$ and $\frac{\mathrm{E}(\epsilon_i^2)}{\mathrm{E}(l)}$ increases by up to 43%. A step length of 0.05 mm gave rise to the smallest percentage difference while a step length of 0.5 mm produced the largest percentage difference.

4.5 Evaluation of LET_D Scoring Methods in Different Simulation Parameters

There are various approaches to calculate the average LET in an ensemble of ϵ_p and $\mathrm{l_p}(\epsilon_e$ and $l_e)$ pair.

Table ***4.***4 shows the five different scoring methods to calculate LET_D for each voxel and their respective mathematical expectation form.

Table 4.4 shows the LET_D Scoring Methods where n_p (n_e) refers to the number of protons (electrons), ϵ_p (ϵ_e) is the energy deposition of protons (electrons) and l_p (l_e) is the step length of protons (electrons). The last row shows the mathematical expectation form of each corresponding LET_D scoring methods where $i \in p, e$.

Unrestricted	**Method 1**	**Method 2**	**Method 3**	**Method 4**
$\frac{\sum_{p=1}^{n_p} \frac{\epsilon_p^2}{l_p}}{\sum_{p=1}^{n_p} \epsilon_p}$	$\frac{\sum_{p=1}^{n_p} \frac{\epsilon_p^2}{l_p} + \sum_{e=1}^{n_e} \frac{\epsilon_e^2}{l_e}}{\sum_{p,e=1}^{n_p,n_e} \epsilon_p + \epsilon_e}$	$\frac{\frac{\sum_{p,e=1}^{n_p,n_e} \epsilon_p^2 + \epsilon_e^2}{\sum_{p,e=1}^{n_p,n_e} l_p + l_e}}{\frac{\sum_{p,e=1}^{n_p,n_e} \epsilon_p + \epsilon_e}{n_p + n_e}}$	$\frac{\frac{\sum_{p=1}^{n_p} \epsilon_p^2}{\sum_{p=1}^{n_p} l_p} + \frac{\sum_{e=1}^{n_e} \epsilon_e^2}{\sum_{e=1}^{n_e} l_e}}{\frac{\sum_{p,e=1}^{n_p,n_e} \epsilon_p + \epsilon_e}{n_p + n_e}}$	$\frac{\frac{\left(\sum_{p=1}^{n_p} \epsilon_p\right)^2}{\sum_{p=1}^{n_p} l_p} + \frac{\left(\sum_{e=1}^{n_e} \epsilon_e\right)^2}{\sum_{e=1}^{n_e} l_e}}{\sum_{p,e=1}^{n_p,n_e} \epsilon_p + \epsilon_e}$
$\frac{\mathrm{E}\left(\frac{\epsilon_p^2}{l_p}\right)}{\mathrm{E}(\epsilon_p)}$	$\frac{\mathrm{E}\left(\frac{\epsilon_i^2}{l_i}\right)}{\mathrm{E}(\epsilon_i)}$	$\frac{\frac{\mathrm{E}(\epsilon_i^2)}{\mathrm{E}(l_i)}}{\mathrm{E}(\epsilon_i)}$	$\frac{\frac{\mathrm{E}(\epsilon_p^2)}{\mathrm{E}(l_p)} + \frac{\mathrm{E}(\epsilon_e^2)}{\mathrm{E}(l_e)}}{\mathrm{E}(\epsilon_i)}$	$\frac{\frac{[\mathrm{E}(\epsilon_p)]^2}{\mathrm{E}(l_p)} + \frac{[\mathrm{E}(\epsilon_e)]^2}{\mathrm{E}(l_e)}}{\mathrm{E}(\epsilon_i)}$

The LET_D scoring methods are the possible ways to calculate LET_D in MC simulation and the mathematical expectation form can be approximated by Equation 4.6. The expectation takes into account all the steps and events in the particular voxel and assumes the same form for all five methods. *The Unrestricted* method is similar to the LET_D scoring methods suggested by both Cortes-Giraldo *et al.*[19] and Granville *et al.*[3]It is the only one among all which does not include secondary electrons in the scoring of LET_D.

$$\frac{E\left(\frac{\epsilon_i^2}{l_i}\right)}{E(\epsilon_i)} \approx \frac{\sum_{i=1}^{n_i} \frac{\epsilon_i^2}{l_i}}{\sum_{i=1}^{n_i} \epsilon_i} \times \frac{\frac{1}{n_i}}{\frac{1}{n_i}} \tag{4.6}$$

Looking at

Table ***4.***4, we see that *Unrestricted* and *Method 1* are similar to each other. The difference merely arises from the absence of n_e, ϵ_e and l_e for *Unrestricted, as it* uses a high range cut value which translates into a zero output of secondary electron. *Method 1* and *4* are based on a concept similar to that used in the work by Cortes-Giraldo *et al.*[19], except that energy deposition from secondary electrons was left out in the previous work. Another point worth mentioning is that the energy depositions for every single particle are added up before dividing by the sum of step length in *Method 2*, *3* and *4*. On the other hand, the sum is taken following the division of the energy deposition for each particle by its corresponding step length in *Unrestricted* and *Method 1*.

Besides, a closer examination of Equation 4.3 would help to elucidate why different scoring methods yield different LET_D results. Thus,

Table ***4.***4 shows the numerator of each scoring method expressed in exact mathematical form. Ultimately, an optimal set of MC simulation parameters could be proposed through an analysis of the reproducibility of LET_D values at *Position* 1 to *4* (as defined in Section 4.2.1) when different scoring methods are used.

4.6 LET_D Scoring Methods Analysis

In this section, LET_D values at the four *Positions* were determined using five scoring methods for all permutations of simulation parameters introduced in Section 4.2.1. Every *Position* for each *Energy* has three step length values (x-axis) and each step length value further corresponds to three range cut values of 0.01 mm, 0.05 mm and 0.1 mm as represented by *(i)*, *(ii)* and *(iii)* respectively in Figure 4.5**.** It was found that the disagreement among the LET_D values obtained from different scoring methods increases as step length and range cut decrease at all positions. For example, at *Position 1* of 80 MeV, the LET_D values calculated using the five different scoring methods have a larger variation for range cut of 0.01 mm as compared to range cut of 0.1 mm. The same pattern was observed for all positions and step lengths. The percentage difference of LET_D, with respect to the *Unrestricted* scoring method, is up to 200% (LET_D values at step length of 0.5 mm and range cut of 0.01 mm at *Position 3* of 80 MeV) depending on which simulation parameters and scoring methods were used.

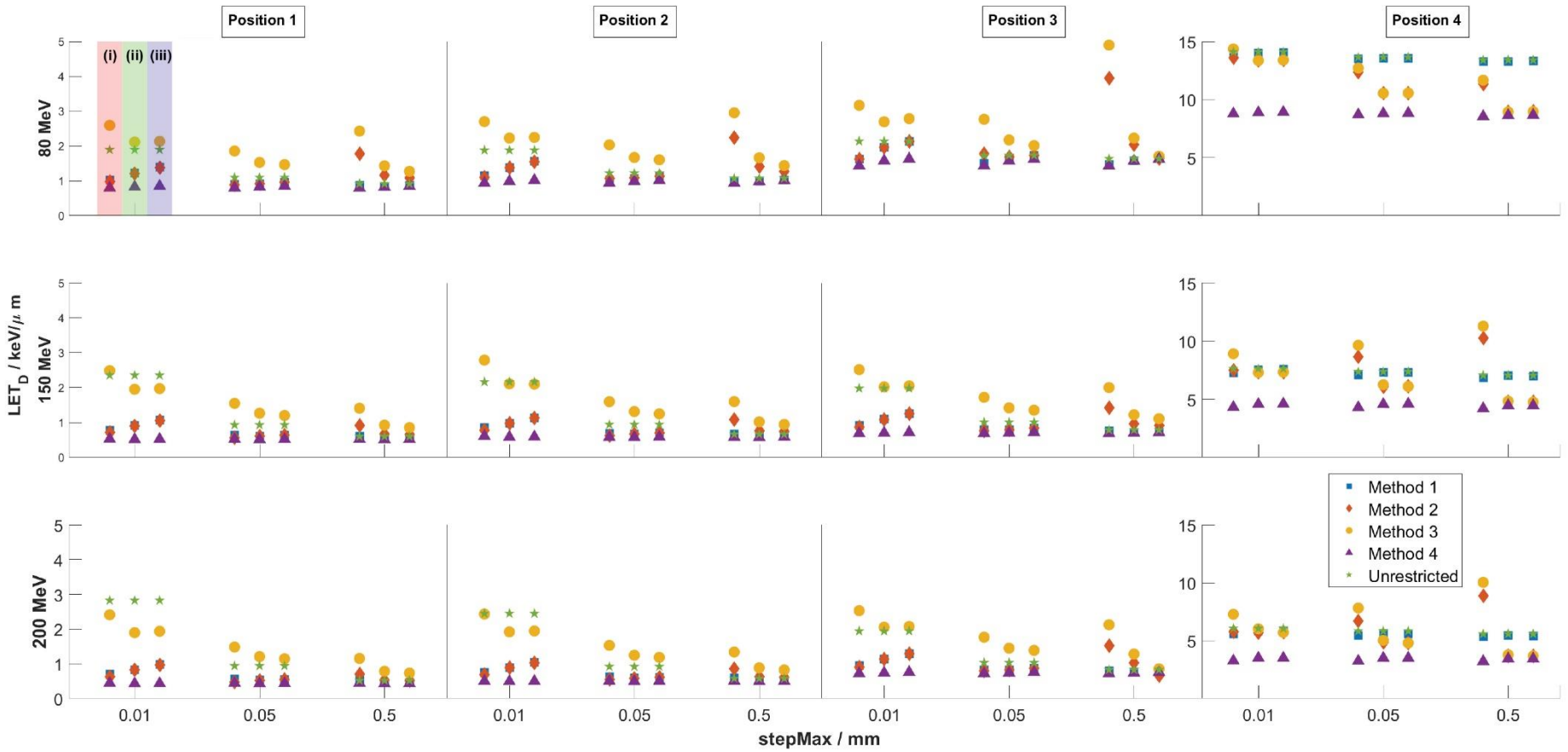

Figure 4.5 shows the LET_D values calculated using each scoring methods as represented by different symbols for all simulation parameters at Positions 1, 2, 3 and 4. Range cut of 0.01 mm, 0.05 mm and 0.1 mm is represented by (i), (ii) and (iii) respectively and it is similar for all subsequent step length. Position 1, 2 and 3 share the same y-axis while Position 4 uses its own y-axis due to higher LET_D values at the Bragg peak region.

LET_D value determined by the *Unrestricted* scoring method is plotted for all step length. For a 200 MeV proton beam, range cut of 1000 m and step length of 0.5 mm, approximately 1100 protons/second are simulated on a single core of an Intel Xeon Gold CPU running at 2.10 GHz. The results of CPU time taken for all simulation parameters using a 200 MeV proton beam and particle histories of 100000 are displayed in Table 4.5.

Table 4.5 CPU time (in protons/second) used for 200 MeV proton beam with different range cut and step size using 100000 particles.

200 MeV	**Range Cut**			
Step length	**0.01 mm**	**0.05 mm**	**0.10 mm**	**1000 m**
0.01 mm	20	22	23	25
0.05 mm	83	106	111	120
0.50 mm	200	666	714	1111

Taking the LET_D values corresponding to the *Unrestricted* scoring method as a reference point, the percentage difference between scoring methods was determined for each set of simulation protocols. The largest difference of 200% occurs at *Position 3* of 80 MeV, step length of 0.5 mm and range cut of 0.01 mm using *Method 3*. At the Bragg peak region of 200 MeV proton beam, the largest percentage difference (81%) occurs at step length of 0.5 mm and range cut of 0.01 mm using *Method 3*. The percentage difference compared across all energies using *Method 1* is up to 8% regardless of simulation parameters chosen at the Bragg peak region. Furthermore, the percentage difference at the Bragg peak region with a range cut of 0.01 mm turns out to be the lowest for step length of 0.05mm (up to 45%) as compared to step length of 0.5 mm

(up to 81%) and 0.01 mm (up to 47%). Scoring *Method* 1 has one of the lowest percentage differences compared across all simulation parameters. Hence, this analysis once again highlighted the necessity of exercising prudence while choosing simulation parameters and scoring methods in MC simulation.

4.7 Discussion

In this chapter, we have shown that a step length of 0.05 mm produced the highest consistency for all range cut and scoring methods at all positions. The other two step length values have their drawbacks which will be discussed in the rest of the paragraph. Comparing the percentage difference between $\mathrm{E}\left(\frac{\epsilon_i^2}{l}\right)$ and $\frac{\mathrm{E}(\epsilon_i^2)}{\mathrm{E}(l)}$ throughout the Bragg peak curve, a step length of 0.5 mm is not advisable due to its highest percentage difference. On top of that, the difference of LET_D values compared among different scoring methods could go as high as 200%. As for step length of 0.01 mm, Figure 4.5 shows an initial decrease in LET_D at the plateau region before increasing towards the Bragg peak and this is physically incorrect due to small step size artefacts [2]. Thus, it is not recommended due to the large variance from different scoring methods. Following that, 0.05 mm is proposed to be the most suitable step length for use in MC simulation.

Subsequently, a range cut of 0.01 mm is chosen since the priority is to obtain a better dose accuracy by including explicit electron transports in the medium. When a high range cut is chosen, there will be fewer or even an absence of secondary electrons, especially at the Bragg peak region. In that case, LET_D scoring methods as shown in

Table ***4.***4 would converge to Table 4.6. *Method 1* would be identical to *Unrestricted* while *Method 2* and *3* are equal.

Table 4.6 LET_D Scoring methods when there is an absence of secondary electrons.

Unrestricted	**Method 1**	**Method 2**	**Method 3**	**Method 4**
$\frac{\sum_{p=1}^{n_p} \frac{\epsilon_p^2}{l_p}}{\sum_{p=1}^{n_p} \epsilon_p}$	$\frac{\sum_{p=1}^{n_p} \frac{\epsilon_p^2}{l_p}}{\sum_{p=1}^{n_p} \epsilon_p}$	$\frac{\frac{\sum_{p=1}^{n_p} \epsilon_p^2}{\sum_{p=1}^{n_p} l_p}}{\frac{\sum_{p=1}^{n_p} \epsilon_p}{n_p}}$	$\frac{\frac{\sum_{p=1}^{n_p} \epsilon_p^2}{\sum_{p=1}^{n_p} l_p}}{\frac{\sum_{p=1}^{n_p} \epsilon_p}{n_p}}$	$\frac{\left(\sum_{p=1}^{n_p} \epsilon_p\right)^2}{\frac{\sum_{p=1}^{n_p} l_p}{\sum_{p=1}^{n_p} \epsilon_p}}$

We expect the percentage difference arising from different LET_D scoring methods to decrease nearer to the Bragg peak. This is deduced from the low covariance (Figure 4.4) and the convergence of scoring methods (Table 4.6) at the Bragg peak region. However, a converse situation is observed. At low energy with a range cut of 0.1 mm or 0.05 mm, the percentage difference decreases along the plateau and increases as it approaches the Bragg peak. The percentage difference rises to 65% (plateau region) and 41% (Bragg peak region) for these range cut (0.1 mm and 0.05 mm). Despite having a larger percentage difference of up to 72% (plateau region) and 59% (Bragg peak region) at 200 MeV, the results using a range cut of 0.01 mm manifest the greatest consistency throughout all energies. Thus, step length of 0.05 mm and range cut of 0.01 mm constitute the optimal set of simulation parameters for proton therapy.

With regards to the LET_D scoring methods, we could observe that LET_D values calculated from *Method 3* deviate the most from other scoring methods at step length of 0.05 mm and range cut of 0.01 mm along the plateau region (*Position 1*, *2* and *3*) in Figure 4.5. At the Bragg peak region (*Position 4*), it is predicted that the LET_D values

calculated using *Method 2* and *Method 3* would be close to each other and likewise for *Method 1* and *Unrestricted* due to the reduction of the secondary electron. Meanwhile, LET_D values calculated using *Method 4* disagree with other scoring methods at *Position 4*. Given all these findings, it is more appropriate to use *Method 1* since the LET_D values are approximately the average of other scoring methods.

4.8 Conclusion

From what we have discussed above, a set of simulation parameters and scoring method that would result in a most reproducible LET_D could be put forward. We recommend using a step length of 0.05 mm and a range cut of 0.01 mm for all range of energies and scoring *Method 1* for LET_D calculation. This method can be generalized for a clinically relevant spread-out-Bragg peak (SOBP) by introducing a weighting factor to the equations in

Table ***4.***4. The expectation form of each method will need to include the weighted sum of the individual expectation for the mono-energetic proton beam as shown in Equation 4.7. The weight (w_j) corresponds to the relative contribution of each mono-energetic proton beam (denoted by *j*) required to make up the SOBP.

$$\sum_{j=1}^{n} w_j \frac{\mathrm{E}\left(\frac{\epsilon_i^2}{l_i}\right)}{\mathrm{E}(\epsilon_i)} \tag{4.7}$$

Furthermore, this recommendation can be applied for other ions which are used clinically such as Carbon or Helium. Yet, the caveat regarding the difficulty of tracking a large number of secondary electrons and the inclusion of huge species of nuclear secondary products is inevitable. By establishing these MC simulation protocols, better dose calculation accuracy and LET_D consistency could be achieved. Hopefully, this would benefit future work in obtaining a more precise biological dose calculation by including a more standardised LET_D value in the RBE formula.

4.9 References

1. Koh WYC, Tan HQ, Ang KW, Park SY, Lew WS, Lee JCL. Standardizing Monte Carlo simulation parameters for a reproducible dose-averaged linear energy transfer. *Br J Radiol*. 2020;93(1112):20200122. doi:10.1259/bjr.20200122

2. Guan F, Peeler C, Bronk L, et al. Analysis of the track- and dose-averaged LET and LET spectra in proton therapy using the geant 4 Monte Carlo code. *Med Phys*. 2015;42(11):6234-6247. doi:10.1118/1.4932217

3. Granville DA, Sawakuchi GO. Comparison of linear energy transfer scoring techniques in Monte Carlo simulations of proton beams. *Phys Med Biol*. 2015;60(14). doi:10.1088/0031-9155/60/14/N283

4. Wilkens JJ, Oelfke U. Analytical linear energy transfer calculations for proton therapy. *Med Phys*. 2003;30(5):806-815. doi:10.1118/1.1567852

5. Grassberger C, Paganetti H. Elevated LET components in clinical proton beams. *Phys Med Biol*. 2011;56(20):6677-6691. doi:10.1088/0031-9155/56/20/011

6. Romano F, Cirrone GAP, Cuttone G, et al. A Monte Carlo study for the calculation of the average linear energy transfer (LET) distributions for a clinical proton beam line and a radiobiological carbon ion beam line. *Phys Med Biol*. 2014;59(12):2863-2882. doi:10.1088/0031-9155/59/12/2863

7. Ray S, Cekanaviciute E, Lima IP, Sørensen BS, Costes S V. Comparing Photon and Charged Particle Therapy Using DNA Damage Biomarkers. *Int J Part Ther*. 2018;5(1):15-24. doi:10.14338/ijpt-18-00018.1

8. Wang W, Li C, Qiu R, Chen Y, Wu Z, Zhang H. Modelling of Cellular Survival Following Radiation-Induced DNA Double-Strand Breaks. *Sci Rep*. 2018;(July):1-12. doi:10.1038/s41598-018-34159-3

9. McMahon SJ, Paganetti H, Prise KM. LET-weighted doses effectively reduce biological variability in proton radiotherapy planning. *Phys Med Biol*. 2018;63(22). doi:10.1088/1361-6560/aae8a5

10. Paganetti H. Relative biological effectiveness (RBE) values for proton beam therapy. Variations as a function of biological endpoint, dose, and linear energy transfer. *Phys Med Biol*. 2014;59(22):R419-R472. doi:10.1088/0031-9155/59/22/R419

11. Wilkens JJ, Oelfke U. A phenomenological model for the relative biological effectiveness in therapeutic proton beams. *Phys Med Biol*. 2004;49(13):2811-2825. doi:10.1088/0031-9155/49/13/004

12. Cortés-Giraldo MA, Carabe A. A critical study of different Monte Carlo scoring methods of dose average linear-energy-transfer maps calculated in voxelized geometries irradiated with clinical proton beams. *Phys Med Biol*. 2015;60(7):2645-2669. doi:10.1088/0031-9155/60/7/2645

13. Seltzer SM. ICRU Report 85 FUNDAMENTAL QUANTITIES AND UNITS FOR IONIZING RADIATION. *Jicru*. 2011;11(1). doi:10.1093/jicru/nd

14. Fippel M, Soukup M. A Monte Carlo dose calculation algorithm for proton therapy. *Med Phys*. 2004;31(8):2263-2273. doi:10.1118/1.1769631

15. Schümann J, Paganetti H, Shin J, Faddegon B, Perl J. Efficient voxel navigation for proton therapy dose calculation in TOPAS and Geant4. *Phys Med Biol*. 2012;57(11):3281-3293. doi:10.1088/0031-9155/57/11/3281

16. Allison J. Geant4–a simulation toolkit. *Int J Phytoremediation*. 2007;17(2):20-24. doi:10.1080/10506890701404297

17. Yoshida H, Cuttone G, Sasaki T, et al. Geant4 developments and applications. *IEEE Trans Nucl Sci*. 2006;53(1):270-278. doi:10.1109/tns.2006.869826

18. Allison J, Amako K, Apostolakis J, et al. Recent developments in GEANT4. *Nucl Instruments Methods Phys Res Sect A Accel Spectrometers, Detect Assoc Equip*. 2016;835:186-225. doi:10.1016/j.nima.2016.06.125

19. Cortés-Giraldo MA, Carabe A. A critical study of different Monte Carlo scoring methods of dose average linear-energy-transfer maps calculated in voxelized geometries irradiated with clinical proton beams. *Phys Med Biol*. 2015;60(7):2645-2669. doi:10.1088/0031-9155/60/7/2645

20. Elandt-Johnson RC, Johnson NL. *Survival Models and Data Analysis*. New York : Wiley; 1980. doi:10.1002/9781119011040

21. Kendall MG, Stuart A, Ord JK, Arnold SF, O'Hagan A. *Kendall's Advanced Theory of Statistics*. 6th Editio. London : Edward Arnold ; New York : Halsted Press; 1998.

Chapter 5 Quantifying RBE-weighted dose uncertainty arising from multiple variable RBE models in Organ-At-Risk

From the previous chapters, we were able to understand the importance of LET_D and $\left(\frac{\alpha}{\beta}\right)_x$ as the significant contributing factors towards RBE modelling. We know that is challenging to *select* a single RBE model based on the uncertainties unravelled from these experimental data. In this last chapter, we will focus on arriving at an RBE model-agnostic treatment planning approach to minimize the systematic dose variation between six different RBE models, especially in the case where the tumor overlaps with the OARs. This will be achieved using TOPAS for RBE dose calculation. Therefore, the objective of this study is to quantify the systematic RBE-weighted dose uncertainties arising from multiple variable RBE models. This work has been published in the *Advances in Radiation Oncology*[1].

5.1 Introduction

Currently, a constant RBE of 1.1 is used clinically to include the differential biological effect of protons as compared to photons during treatment planning. It is a conservative estimate based on in-vivo RBE experimental results in the Spread-Out Bragg Peak (SOBP). The need for variable RBE models are also eliminated as the effect in RBE at the end of the range may be mitigated by range uncertainties [2].

However, the counter-argument against the use of a constant RBE of 1.1stems from the possibility of under - or over - dosing in the target volume. As suggested by AAPM TG-256 [2], there is a need to understand the spatial variations of RBE within and outside the target volume on a voxel-wise basis. This can be inferred from the evidence of

experiments that showed RBE exceeding 1.1 at the end of range [3–5]. Hence, RBE-weighted dose is especially important when the target volume is extremely close to the OARs.

Numerous variable RBE models have been proposed [6–11] with the more prominent ones being Local Effect Model (LEM) and Microdosimetric Kinetic Model (MKM). Despite the long history of variable RBE models, the adoption of the variable RBE models has been modest in the clinic due to the large uncertainties in RBE values [12]. These uncertainties arise from uncertainties in the Alpha-Beta ratio $\left(\frac{\alpha}{\beta}\right)_x$ (patient sensitivity), Dose-Averaged Linear Energy Transfer (LET_d), cell-lines used in the experiments and the experimental set-up [13]. Apart from the variable RBE model approach, another approach using a combination of dose and LET was also established [14–19]. This approach is motivated by the correlation between LET and RBE, where RBE increases with LET along the proton beam path. Presently, there are no commercial and *clinical* Treatment Planning Systems (TPS) that can provide LET-guided optimization during treatment planning or calculate variable RBE-weighted dose.

Following the TG-256 report, variable RBE models are recommended for certain clinical situations (OARs close to the target). However, it does not provide recommendations on the exact RBE models to be used. This motivates this study, where the dose difference arising from the use of various variable Linear Quadratic (LQ) - based RBE models was examined. Clinical sites where OARs were situated close to or overlapping the target volume were chosen as these were the clinical cases where variable RBE models would be highly relevant. Multi-Field Optimization (MFO) or

Single-Field Optimization (SFO) treatment planning was then used on these clinical cases.

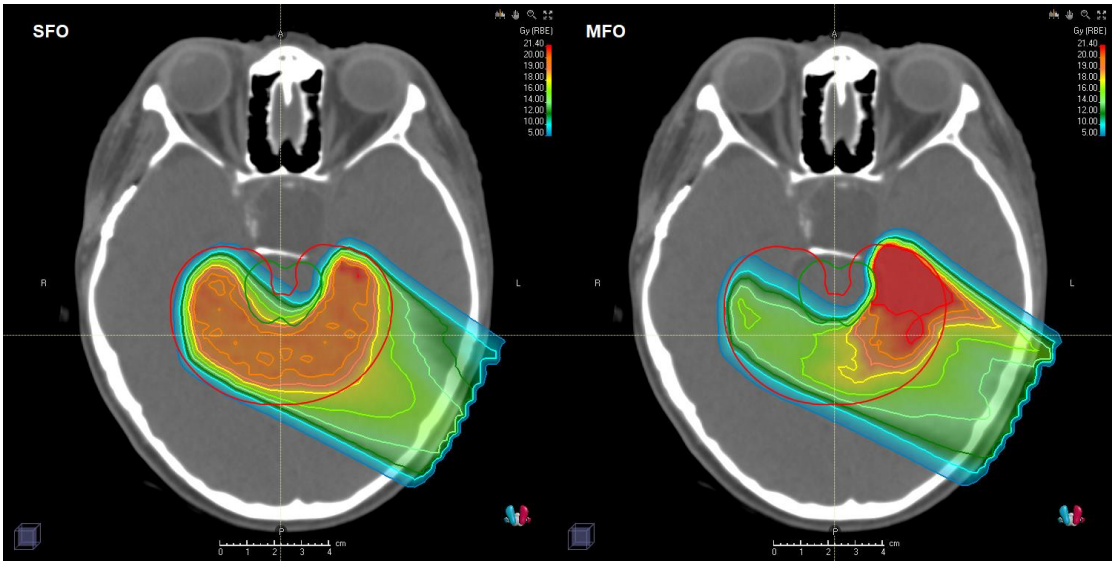

Figure 5.1 shows the dose distribution of a single field of MFO plan and a single field of SFO plan. The red contour defines the target region while the green contour defines the brainstem.

In SFO planning, the beam spot position and weightage of individual fields are optimized individually to fulfil the dose coverage. Whereas in MFO planning, all beam spots of all fields are optimized simultaneously where different fields can be used to cover a different part of the tumor to achieve a highly conformal dose distribution. There is more flexibility with more degrees of freedom during MFO planning since the missing doses from one field can be compensated by the other fields. However, this leads to complex dose distribution for each field as shown in Figure 5.1. The dose in each field in a SFO plan covers the target fully. MFO plans are more complex as each field contributes an inhomogeneous dose to the target with the summation of all fields producing a homogeneous and conformal dose to the target. This concerns the

robustness of the MFO plan as the dose coverage in MFO planning is dependent on each field and any displacement in the tumor may result in an underdose to the tumor or overdose to the healthy tissues [20].

Currently, MFO planning is known to yield a better plan quality as compared to SFO planning. [21–23]. Tommasino et al. [23] stated that there were no statistically significant differences in RBE-weighted dose increase between MFO and SFO planning based on McNamara's RBE model [9]. However, Giantsoudi et al. [15] revealed that MFO planning has a higher RBE-variable dose as compared to SFO planning. To the best of our knowledge, there is no literature on whether MFO or SFO planning can lead to a model-agnostic RBE dose distribution.

In this study, the area of interest lies in the brain tumor where the Clinical Target Volume (CTV) overlaps with the brainstem (CTV-BS) and optic chiasm (CTV-CH). In these overlapping regions, RBE-weighted dose uncertainties were analysed based on the 6 RBE models in the overlapping regions (CTV-BS and CTV-CH) and OARs (brainstem and optic chiasm). Different $\left(\frac{\alpha}{\beta}\right)_x$ were also applied to the RBE models. Subsequently, the RBE models were implemented on both MFO and SFO planning to determine if there was any difference in RBE-weighted dose uncertainties distribution.

This enabled the determination of which planning technique (MFO vs SFO) was more suitable for arriving at an RBE model-agnostic dose distribution.

5.2 Methods and Materials

5.2.1 Patient Characteristics

In this study, 15 retrospective patients with brain tumors of specific features were selected. The types of brain tumors involve in this study are Glioblastoma (GBM), Astrocytoma and Oligodendroglioma. The CTV of each patient overlapped with OARs (brainstem and optic chiasm) as shown in Table 5.1. All patients were treated with photon radiotherapy treatment before 2017. They were re-planned by a trained and experienced dosimetrist (Y.Y. Ng) and all plans were clinically approved for proton therapy treatment.

Table 5.1 shows the overlap volume in cc between Target and OARs.

Patient	CTV (cc)	CTV - Brainstem Intersect (cc)	CTV - Chiasm Intersect (cc)	Tumor Type
1	65.82	1.40	3.92	Meningioma
2	48.26	3.88	0.23	Meningioma
3	48.23	2.47	4.30	Chordoma
4	338.57	0.36	0.05	Glioblastoma Multiforme
5	107.33	0.15	0.37	Ependymoma
6	164.44	0.82	1.78	Astrocytoma
7	426.85	1.54	1.58	Glioblastoma Multiforme

8	397.11	1.13	1.12	Astrocytoma
9	151.53	2.16	0.58	Astrocytoma
10	262.83	0.27	0.69	Astrocytoma
11	316.43	0.04	0.47	Glioblastoma Multiforme
12	396.18	0.78	1.24	Oligodendroglioma
13	441.78	0.35	4.74	Glioblastoma Multiforme
14	264.47	0.08	0.47	Anaplatic Astrocytoma
15	254.50	3.39	1.10	Brain Metastases

5.2.2 TPS and MC Simulation

CTVs were created using a 2 cm uniform expansion from Gross Tumor Volume (GTV). The dose prescription was 60 Gy was over 30 fractions. These plans were optimized to achieve D_{95} > 60 Gy, D_{10} < 63 Gy and D0.03cc < 63.6 Gy for the CTV. The dose constraint for brainstem and optic chiasm is D0.03cc < 60 Gy.

Each plan consisted of either two or three proton beams. Gantry angles varied between 0-300° for the first beam, 40-270° for the second beam and 90-160° for the third beam. The rotation of the couch ranged from 0-300°. A range shifter of 4.5 cm Water Equivalent Thickness (WET) was used, depending on the distance of the CTV from the skin.

Robust Optimization (RO) was used on CTV, brainstem and optic chiasm with 3% range uncertainties and 1 mm setup uncertainties resulting in a total of 12 scenarios.

As the patient is set up using the ExacTrac system (BrainLAB AG, Feldkirchen, Germany), less than $1\ mm$ setup uncertainty is expected.

The calculation grid size was set to $0.25\ cm$ and the beam spot FWHM in the air was $4.56\ mm$ (228.8 MeV) to 12.70 mm (71.3 MeV) measured at isocentre. Proton Convolution Superposition (PCS) algorithm was used to calculate the dose in the TPS. Both MFO and SFO techniques followed the same treatment planning protocols. These plans were clinically approved and planned using Eclipse TPS version 15.6 (Varian, Palo Alto, USA).

All plans were then extracted from TPS and recalculated using TOPAS Monte Carlo System (MCS). The TOPAS has been validated against TPS in both water phantom and the patient, specifically for proton therapy. The number of particle histories was set to a minimum of 10^7 particles, resulting in a statistical uncertainty in isocentre dose of less than 0.34 %. The physics models used in this study include g4em-standard_opt4, g4h-phy_QGSP_BERT_HP, g4h-elastic and g4stopping as these are the recommended physical models for clinical proton beam below 5 GeV[24]. An 80 cores Intel Xeon Gold CPU running at 2.10 GHz was used for this study. The simulation run time was 4700 protons/s at 150 MeV and each patient's plan took approximately 2-13 hours, depending on the target size. Dose (to medium) and proton LET were then exported as DICOM files from the simulation. Nuclear particles are considered in both dose and LET scoring and the range cut for secondary electron was set to 1 m. A snippet of the code used for this chapter is shown in Appendix B5 and B6.

5.2.3 Variable RBE Models

In this study, the dose obtained from TPS and MCS represents the constant RBE of 1.1. Six variable RBE models were applied to the physical dose output from MCS to obtain an RBE-weighted dose. These variable RBE models are based on the LQ model and are shown in Table 5.1. $\left(\frac{\alpha}{\beta}\right)_x$ for the brain tumor is set at 3 and 8 Gy to study the variations of RBE-weighted doses when low and high $\left(\frac{\alpha}{\beta}\right)_x$ values are considered[25]. Both 3 and 8 Gy are used due to the uncertainties in $\left(\frac{\alpha}{\beta}\right)_x$ as shown in Leeuwen *et al.* review[25]

5.2.4 Statistical Analysis

A voxel-wise calculation of RBE-weighted dose standard deviation (SD) is calculated from the six RBE models, thus obtaining a spatial RBE-weighted dose SD map for each planning technique of each patient. Statistical analysis was performed on the overlapping region between both $\left(\frac{\alpha}{\beta}\right)_x$ values for CTV-BS and CTV-CH as these were the regions receiving high RBE-weighted doses while trying to satisfy the dose coverage for CTV. Kruskal-Wallis H-test was first used to test for the significant difference in the RBE-weighted dose SD between the two planning techniques across all patients. A posthoc test was then used to determine significant differences of RBE-weighted dose SD between the MFO and SFO planning techniques of each patient. Bonferroni correction was applied for multiple comparisons. A two-sided p-value < 0.05 was considered significant.

5.3 Results

5.3.1 CTV coverage and OARs Dose Constraint

Figure 5.2 shows the dose distribution of a patient for MFO and SFO planning. There were no distinct visual differences in conformality. For all patients, target coverage in TPS was similar where it fulfilled the criteria for D_{95}. D_{10} for CTV and D0.03cc for both CTV and OARs were within constraints. Figure 5.3 to Figure 5.5 show the boxplot of CTV D_{95}, brainstem D0.03cc and optic chiasm D0.03cc, respectively. These were calculated for all patients based on RBE 1.1 and the RBE models with different $\left(\frac{\alpha}{\beta}\right)_x$ Assuming a $\left(\frac{\alpha}{\beta}\right)_x$ of 8 Gy will lead to an increase in median RBE-weighted dose for CTV D_{95} and OAR D0.03cc as compared to $\left(\frac{\alpha}{\beta}\right)_x$ of 3 Gy.

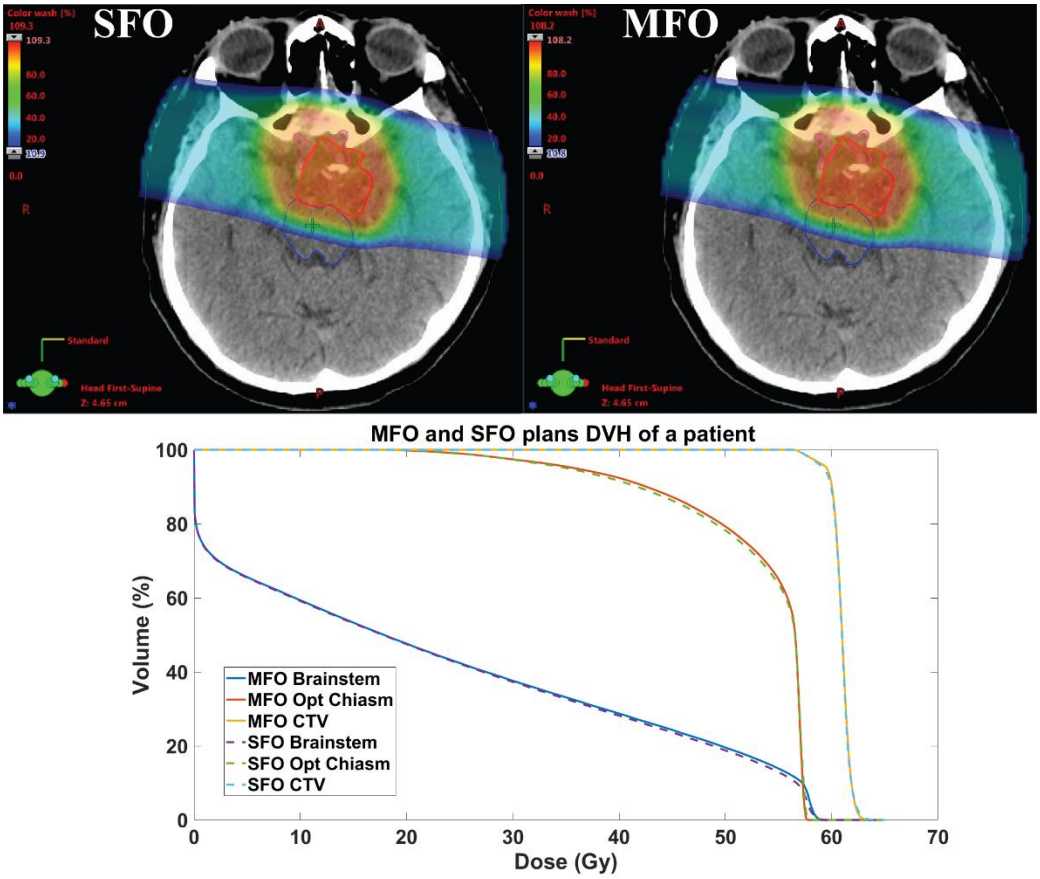

Figure 5.2 shows the dose distribution and the dose volume histogram of SFO and MFO plans of the same patient, both techniques used the same planning protocols and beam angles.

In Figure 5.3, the SFO planning technique is observed to have a slight edge over MFO in terms of CTV coverage. The difference between the median RBE-weighted dose and 60 Gy is lesser for SFO as compared to MFO.

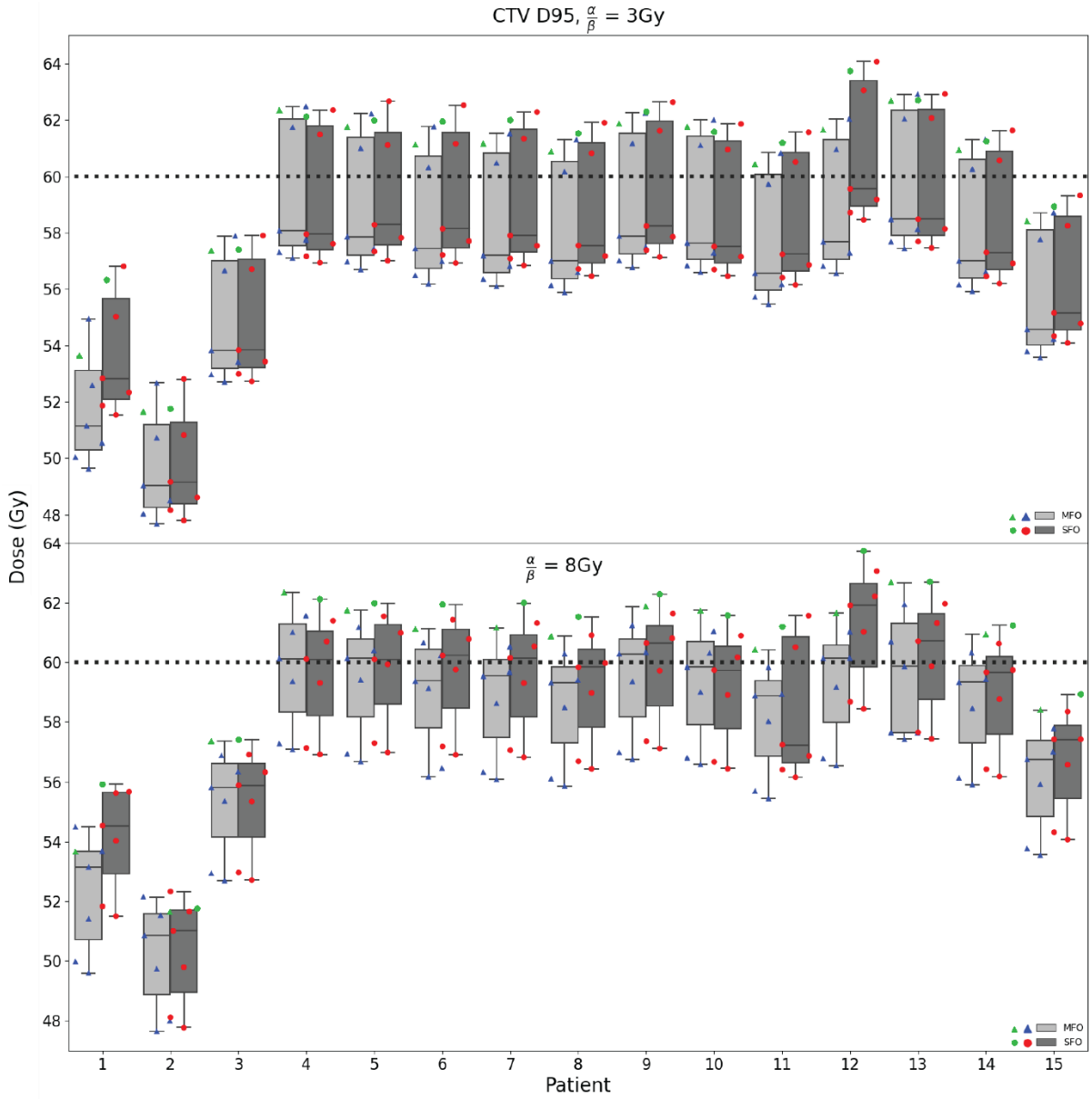

Figure 5.3 shows the CTV D95 of both $\left(\frac{\alpha}{\beta}\right)_x$. Six RBE models were applied to both MFO and SFO planning. Δ/○ shows the dose of each RBE model. The green Δ/○ represent RBE 1.1. The dotted line refers to the dose prescribed to the tumor.

In Figure 5.4 and Figure 5.5, the difference between the median dose of D0.03cc and 60 Gy (dose constraint) is lesser for both OARs in SFO as compared to MFO plans.

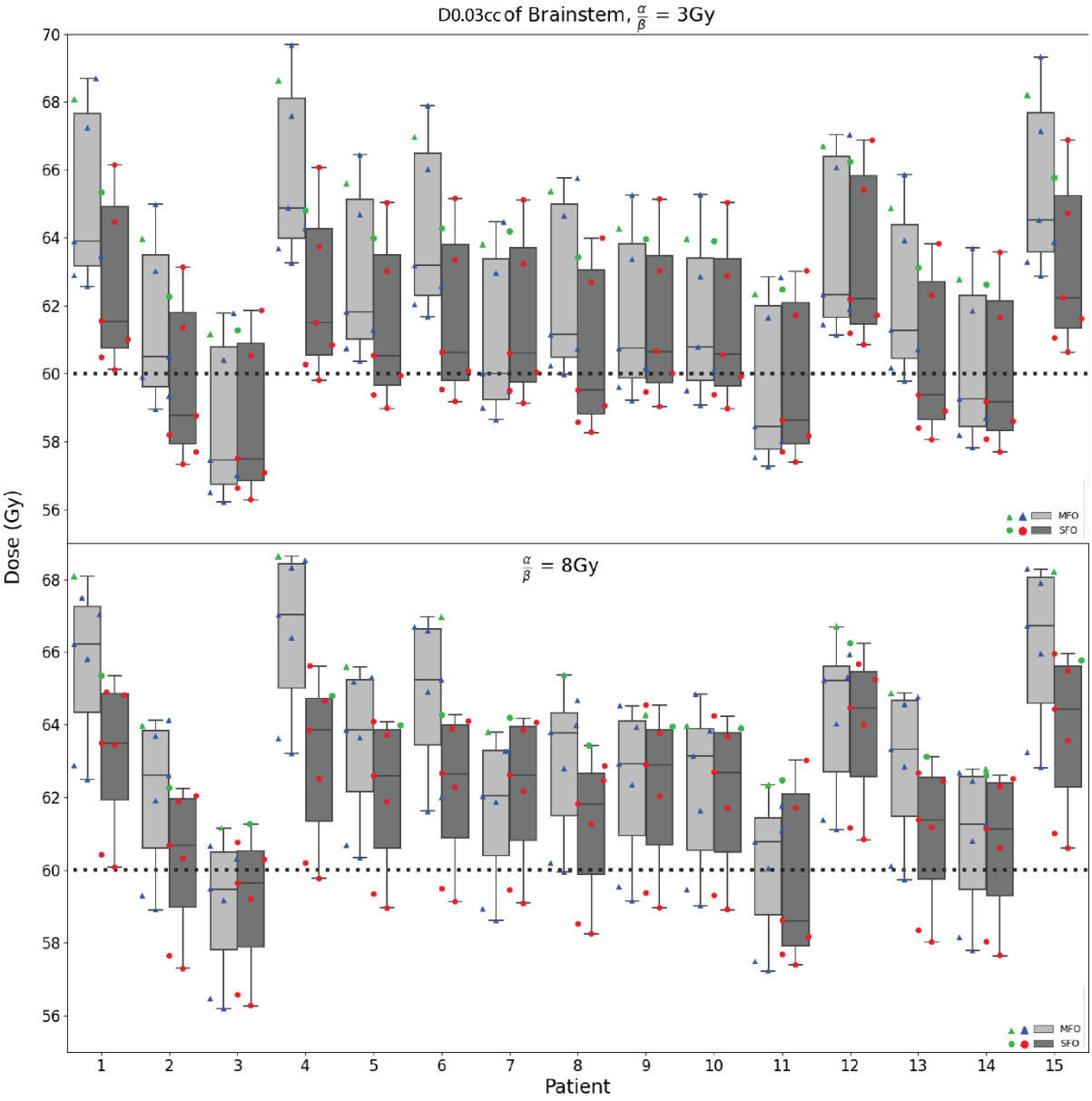

Figure 5.4 shows the D0.03cc of Brainstem for both $\left(\frac{\alpha}{\beta}\right)_x$. Six RBE models were applied to both MFO and SFO planning. Δ/○ shows the dose of each RBE model. The green Δ/○ represent RBE 1.1. The dotted line refers to the tumor dose constraint of 60Gy.

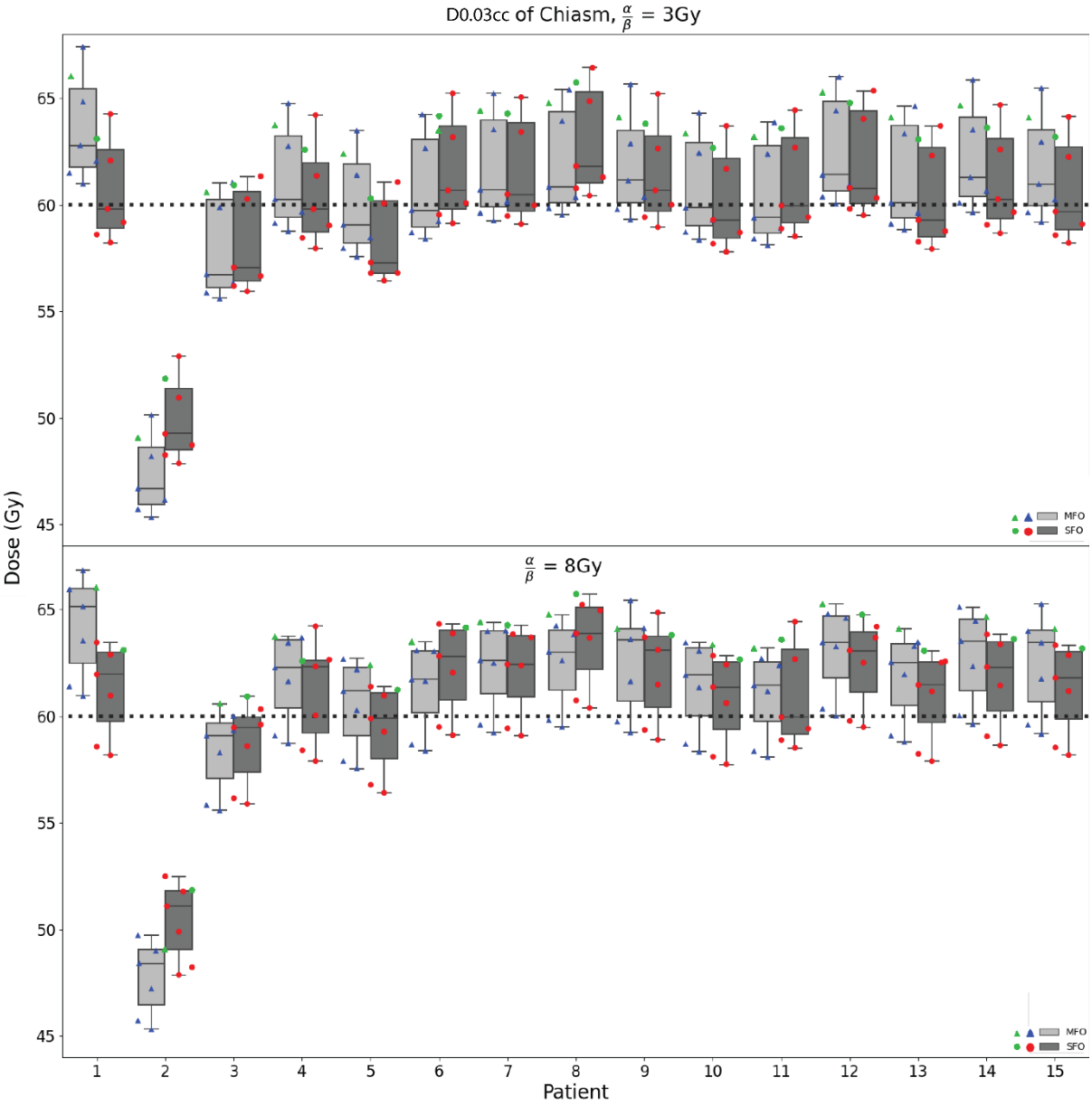

Figure 5.5 shows the D0.03cc of Optic Chiasm for both $\left(\frac{\alpha}{\beta}\right)_x$. Six RBE models were applied to both MFO and SFO planning. Δ/○ shows the dose of each RBE model. The green Δ/○ represent RBE 1.1. The dotted line refers to the tumor dose constraint of 60 Gy.

5.3.2 Dose uncertainties in CTV-OAR overlapping regions

When considering the RBE-weighted dose uncertainties between models, the regions of interest are the OARs and the overlapping region between the CTV and OAR. Figure 5.6 and Figure 5.7 show the violin plot of the RBE-weighted dose SD in the overlapping region between CTV-BS and CTV-CH with different $\left(\frac{\alpha}{\beta}\right)_x$ values, respectively. In the CTV-BS overlap region, 10 out of 15 patients have lower median RBE-weighted dose SD when using MFO planning as compared to when using SFO planning. The median RBE-weighted dose SD ranges from 1.6-1.9 Gy for high $\left(\frac{\alpha}{\beta}\right)_x$ and 1.9-2.2 Gy for low $\left(\frac{\alpha}{\beta}\right)_x$.

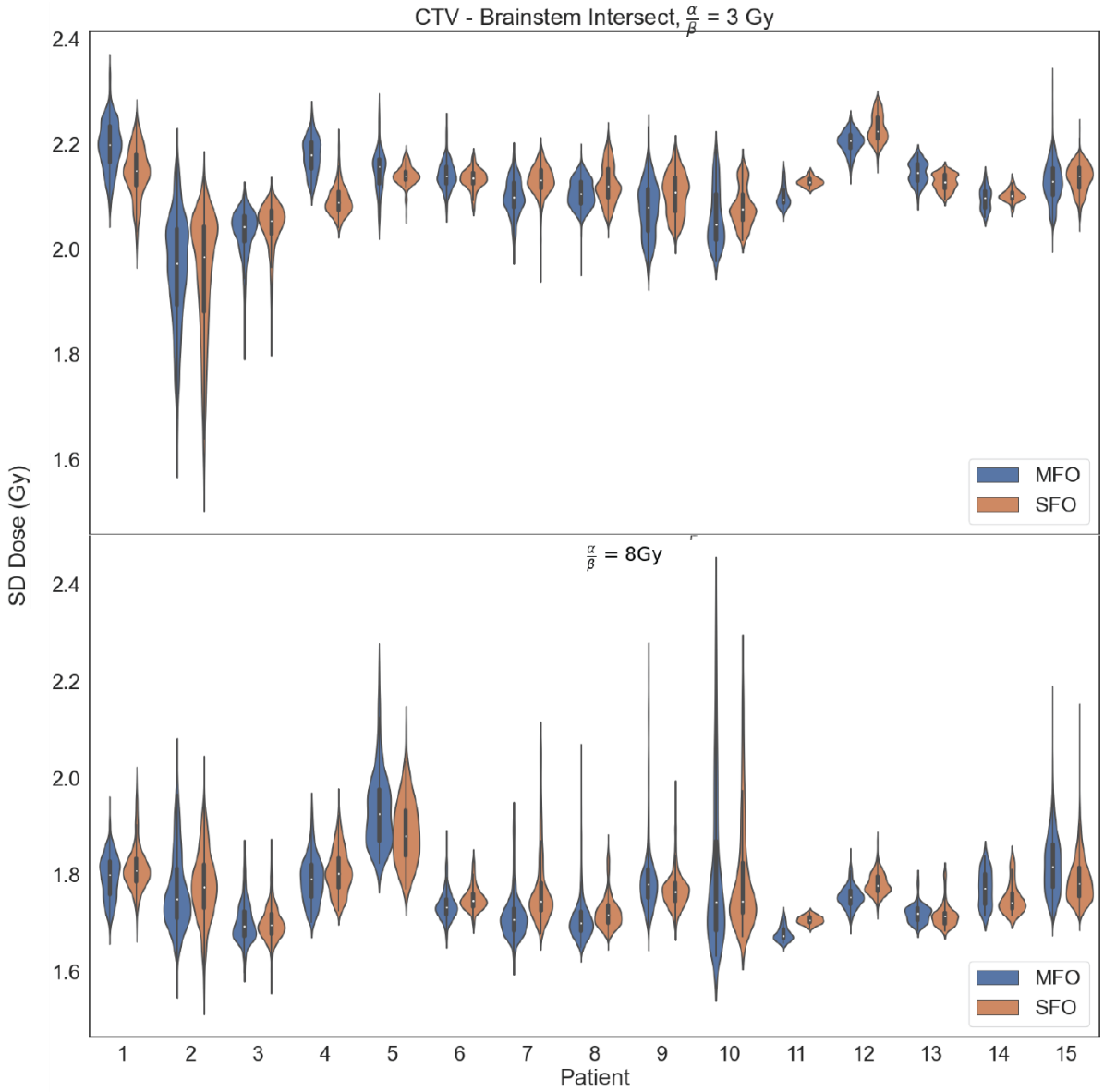

Figure 5.6 shows the violin plot of RBE-weighted dose uncertainties based on the six RBE models in the CTV-BS intersecting regions for both $\left(\frac{\alpha}{\beta}\right)_x$.

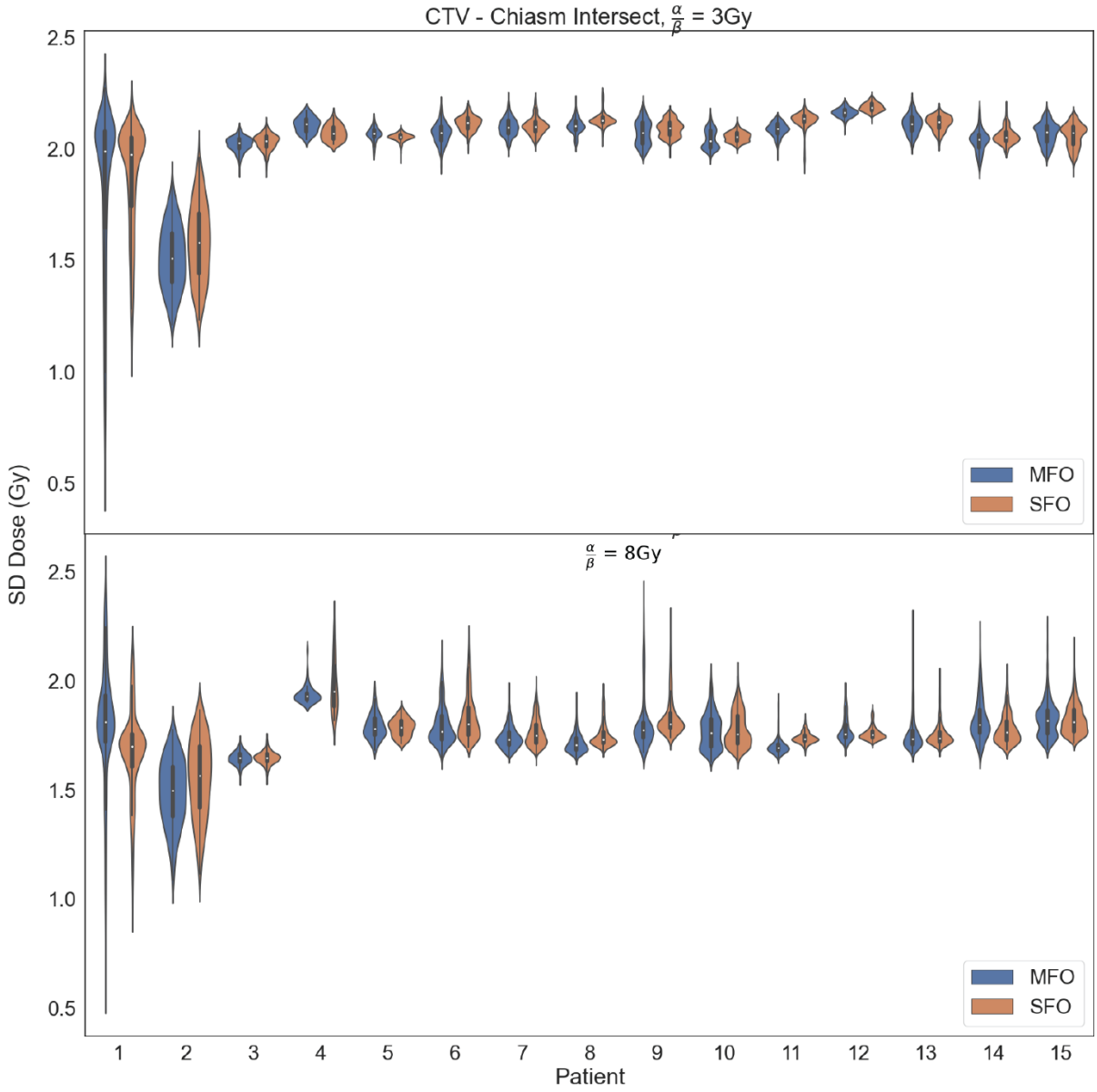

Figure 5.7 shows the violin plot of RBE-weighted dose uncertainties based on six RBE models in the CTV-CH intersecting regions for both $\left(\frac{\alpha}{\beta}\right)_x$.

CTV-CH follows a similar trend as CTV-BS, where 10 out of 15 patients have lower median RBE-weighted dose SD in MFO planning as compared to SFO planning. The median RBE-weighted dose SD ranges from 1.5-2 Gy for high $\left(\frac{\alpha}{\beta}\right)_x$ and 1.5-2.2 Gy

for low $\left(\frac{\alpha}{\beta}\right)_x$. There is a statistically significant difference (P-value < 0.01), between MFO and SFO planning in terms of RBE-weighted dose SD.

5.3.3 LET in OARs

Figure 5.8 shows the LET distribution in the axial plane between MFO and SFO planning of a patient where the beam angles are set at 290° and 180°. Figure 5.9 shows the LET distribution difference between MFO and SFO planning in the overlapping region of CTV and OARs (brainstem and optic chiasm).

There is no clear trend on which planning technique results in a higher LET distribution. In the non-overlapping region of OARs, lower median LET in MFO planning was observed as compared to SFO planning for optic chiasm (8 patients) and brainstem (13 patients).

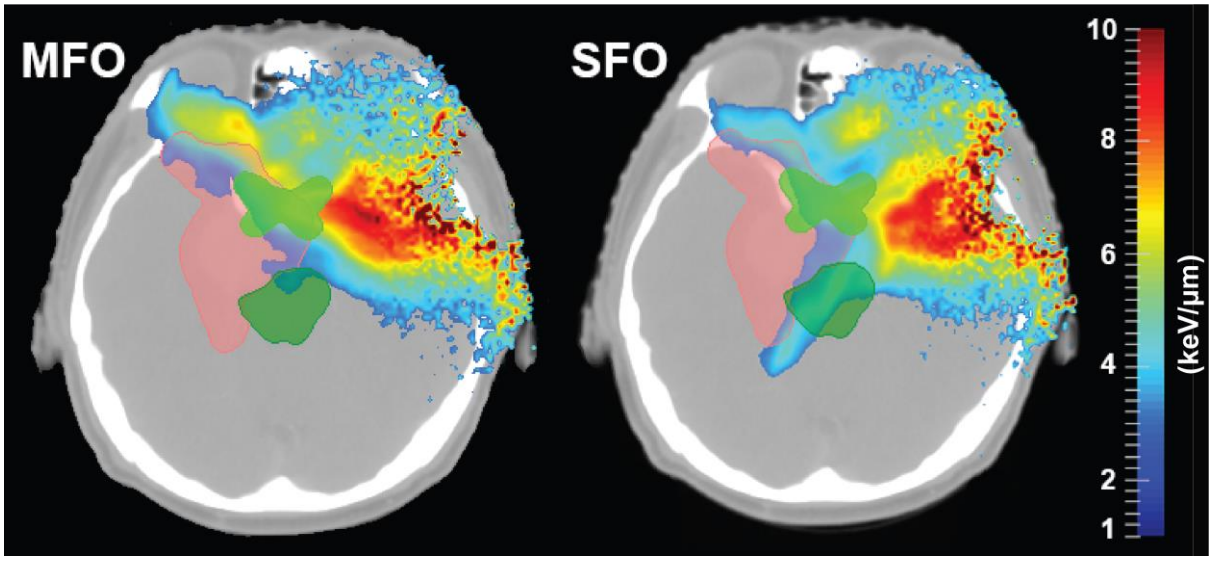

Figure 5.8 shows the LET distribution of SFO and MFO plans of the same patient, where both techniques used the same planning protocols and beam angles.

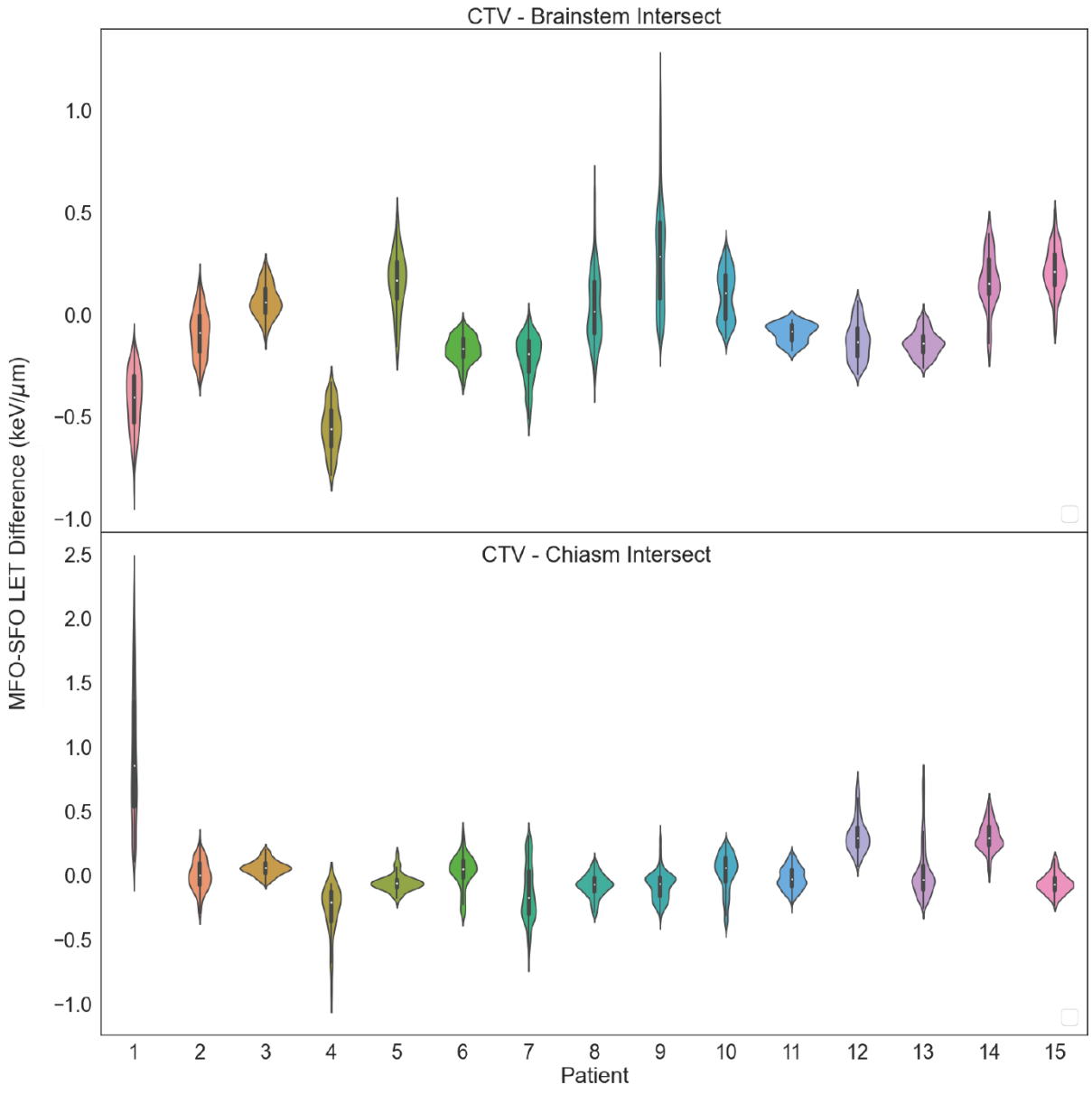

Figure 5.9 shows the LET distribution for both the MFO and SFO plans of each patient in the CTV-BS and CTV-CH intersecting regions.

Figure 5.10 shows the voxel-wise difference in LET between MFO and SFO planning for both brainstem and optic chiasm. In the entire brainstem, 14 patients have a lower

mean LET in MFO planning as compared to SFO planning; in the entire optic chiasm, 9 patients have lower mean LET in MFO planning as compared to SFO planning. The majority of MFO planned patients showed lower LET values as compared to SFO planned patients in this study.

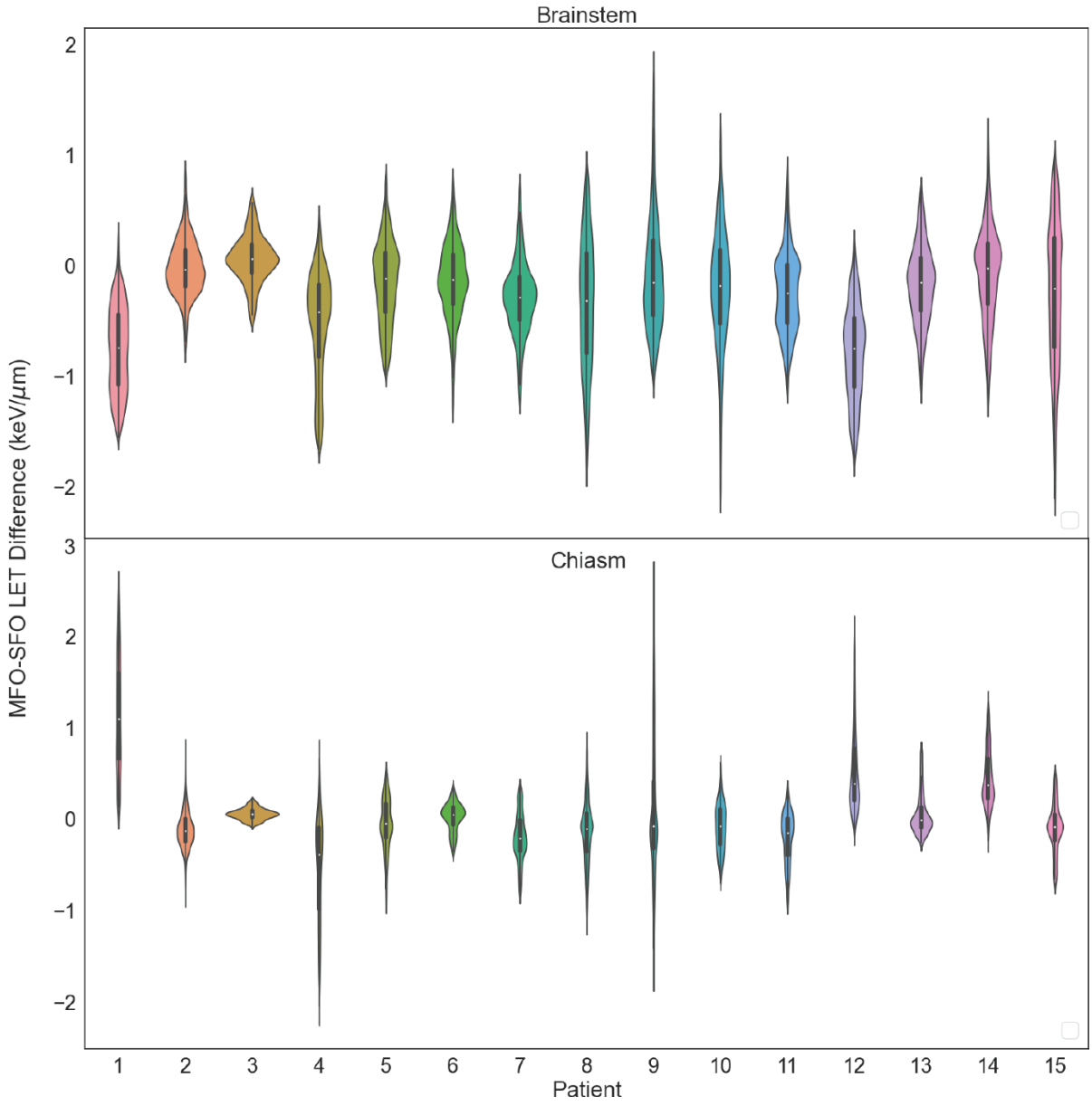

Figure 5.10 shows the voxel-wise difference between MFO and SFO LET distribution in the brainstem and optic chiasm.

5.4 Discussion

In RBE modelling, the majority of the models are phenomenological where it is based on the LQ concept, using empirical data from clonogenic cell survival for curve fitting. There are other types of RBE models that are implemented clinically such as the MKM [26,27] and LEM [28] models. However, only the LQ-based RBE model is used in this study. Many studies have been done on the comparison between the different RBE models [10,29–31], and the novelty of our work lies in achieving a model agnostic in RBE-weighted dose calculation with two different treatment planning techniques.

Dose uncertainties in CTV-OARs overlapping regions

MFO and SFO planning was performed on 15 patients to study the RBE-weighted dose differences in the OAR resulting from six representative variable LQ-based RBE models (including the constant 1.1 RBE model). MFO planning shows a better target coverage[21–23] as compared to SFO planning. In this study, all RBE models and RBE 1.1 are compared. Looking at the RBE 1.1 data points alone, the majority of the patients exhibited better target coverage with MFO planning as compared to SFO planning. Nonetheless, SFO planning has a slight advantage over MFO planning in relation to dose coverage. This is due to the smaller difference between the median RBE-weighted dose and 60 Gy at D95 for both high and low $\left(\frac{\alpha}{\beta}\right)_x$ when all RBE models are considered. Based on the RBE formalism, an increase in $\left(\frac{\alpha}{\beta}\right)_x$ value will lead to an increase in RBE-weighted dose, and this is as shown in Figure 5.3. Additionally, SFO plans have a lower median D0.03cc for both brainstem and optic chiasm as shown in Figure 5.4 and Figure 5.5, thus revealing better control of hotspots in the OARs.

Overall, it is inconclusive which planning technique would be better for the plan to achieve the dose constraint with the inclusion of RBE models.

The largest contribution of uncertainty to proton therapy lies in the range uncertainty. Many works regarding the range uncertainties in proton therapy have been done, especially in the area of MFO and SFO [23,32,33]. In addition to range uncertainty, RBE-weighted dose is also a concern. As shown by Carabe *et al.*[34], the biological dose uncertainties will translate to a displacement of the distal end of the RBE-weighted SOBP curve. Considering the overlap between the OARs and CTV, an increase in RBE might lead to a larger depth of the SOBP curve. Thus, it is important to consider the RBE-weighted dose uncertainties between models in the event where the end of the range of the proton beam might fall in the OARs. The first observation in the result is the distinct difference in RBE-weighted dose SD, where low $\left(\frac{\alpha}{\beta}\right)_x$ leads to higher median RBE-weighted dose SD as compared to high $\left(\frac{\alpha}{\beta}\right)_x$ in the OARs. This can be explained by the RBE formalism. When $\left(\frac{\alpha}{\beta}\right)_x$ increases, the RBE-weighted dose decreases for four of the RBE models, while the models by Chen [7] and Wilkens [8] return an increase in RBE-weighted dose, assuming a constant α_x and LET. Thus, this reduces the RBE-weighted dose SD in the OARs. Similarly, Marteinsdottir *et al.* [35] had also demonstrated that the impact of a variable RBE is larger in low $\left(\frac{\alpha}{\beta}\right)_x$ as compared to high $\left(\frac{\alpha}{\beta}\right)_x$. Therefore, it is advised to be cautious during treatment planning for low $\left(\frac{\alpha}{\beta}\right)_x$ CTV overlaps with OARs.

In the overlapping region between CTV and brainstem, 5 patients have higher median RBE-weighted dose SD in MFO planning as compared to SFO planning regardless of $\left(\frac{\alpha}{\beta}\right)_x$. Similarly, in the overlapping region between CTV and Chiasm, 4 patients in low $\left(\frac{\alpha}{\beta}\right)_x$ and 5 patients with high $\left(\frac{\alpha}{\beta}\right)_x$ have a higher median RBE-weighted dose SD in MFO planning as compared to SFO. There is a significant difference (P<0.01) in RBE-weighted dose SD between SFO and MFO for all patients. Comparing the kurtosis and skewness of the RBE-weighted dose SD distribution in these regions for each patient, there is no significant difference between MFO and SFO planning. However, 12-14 patients have RBE-weighted dose SD negatively skewed when assuming a higher $\left(\frac{\alpha}{\beta}\right)_x$ in both overlapping regions. From the above results, MFO plans show lower RBE-weighted dose SD distribution. Hence, there is a higher probability of having lesser RBE-weighted dose uncertainties when RBE models are considered during dose calculation. Therefore, MFO planning can be a better choice in eliminating RBE-weighted dose variations in patients. In other works, MFO plans have also been shown to be superior to SFO plans in terms of plan quality and dose sparing in OAR [21,23]. This supplements the fact that MFO planning might be a better choice in the situation where CTV and OAR overlaps.

LET in OARs

The LET distribution of each plan is further studied to examine any LET difference between MFO and SFO plans. As seen in Figure 5.8, there is no visually detectable difference in the LET distribution of the patients between the two techniques. Figure 5.9 shows that more patients possess lower median LET values in the intersecting

region between CTV and OAR by MFO planning as compared to SFO planning. The LET distributions in the OARs and overlapping areas are more inhomogeneous and have higher maximum LET as compare to the CTV in SFO plans and this is consistent with the findings from Hahn *et al*. [33]. Also, having higher LET might lead to an increase in RBE-weighted dose and range uncertainties. Therefore, it will be advantageous to choose MFO plans where the max LET is lower. Considering the results for the entire brainstem and chiasm in Figure 5.10, MFO planning results were observed to have a lower median LET in the OAR as compared to SFO planning. A lower median LET leads to a decrease in RBE dose SD at high $\left(\frac{\alpha}{\beta}\right)_x$ but an increase in RBE-weighted dose SD at low $\left(\frac{\alpha}{\beta}\right)_x$. This further explains why the MFO techniques are more effective in reducing RBE-weighted dose uncertainty arising from different RBE models.

Limitations

LEM and MKM models were not used, this limits the study to only LQ-based RBE models. Further analysis can be done by factoring in LEM and MKM models, to obtain the RBE-weighted dose uncertainties. This methodology can easily be extended to other clinical sites to determine which planning technique is better at reducing RBE-weighted dose uncertainties arising from different RBE models when the OARs are situated close or overlapping with the CTV. In addition, LET optimization can be considered for it has proven to be able to redistribute high LET out of OARs into CTV [16,19,36]. A reduced LET in the OARs will lead to a decrease in RBE-weighted dose uncertainties as shown in the results. RBE-weighted dose uncertainties can then be examined in the OAR

between MFO and SFO planning to determine if there are any differences between the application of these two techniques.

5.5 Conclusion

In conclusion, there is no indication of which planning technique would be better in achieving the planning constraint of the brain tumor. In situations where OARs are extremely close or where they overlap with the target volume, the results present the case that there is lesser RBE-weighted dose SD in the region of overlap in MFO planning. The median LET in the OAR is lower in most of the patients using MFO planning as compared to using SFO planning. Therefore, MFO is the preferred technique for reducing RBE-weighted dose uncertainties which arise from RBE models and this is important for OARs near to target volume during treatment planning.

5.6 References

1. Koh WYC, Tan HQ, Ng YY, et al. Quantifying systematic RBE-weighted dose uncertainty arising from multiple variable RBE models in Organ-At-Risk. *Adv Radiat Oncol*. 2021:100844. doi:10.1016/j.adro.2021.100844

2. Paganetti H, Blakely E, Carabe-Fernandez A, et al. Report of the AAPM TG-256 on the relative biological effectiveness of proton beams in radiation therapy. *Med Phys*. 2019;46(3):e53-e78. doi:10.1002/mp.13390

3. Matsumoto Y, Matsuura T, Wada M, Egashira Y, Nishio T, Furusawa Y. Enhanced radiobiological effects at the distal end of a clinical proton beam: In vitro study. *J Radiat Res*. 2014;55(4):816-822. doi:10.1093/jrr/rrt230

4. Sørensen BS, Bassler N, Nielsen S, et al. Relative biological effectiveness (RBE) and distal edge effects of proton radiation on early damage in vivo. *Acta Oncol (Madr)*. 2017;56(11):1387-1391. doi:10.1080/0284186X.2017.1351621

5. Ilicic K, Combs SE, Schmid TE. New insights in the relative radiobiological effectiveness of proton irradiation. *Radiat Oncol*. 2018;13(1):4-11. doi:10.1186/s13014-018-0954-9

6. Carabe-fernandez A, Moteabbed M, Depauw N, Paganetti H. SU-E-T-648: Range Uncertainty in Proton Therapy Due to Variable Biological Effectiveness. *Med Phys*. 2011;38(6):3639. doi:10.1118/1.3612611

7. Chen Y, Ahmad S. Empirical model estimation of relative biological effectiveness for proton beam therapy. *Radiat Prot Dosimetry*. 2012;149(2):116-123. doi:10.1093/rpd/ncr218

8. Wilkens JJ, Oelfke U. A phenomenological model for the relative biological effectiveness in therapeutic proton beams. *Phys Med Biol*. 2004;49(13):2811-2825. doi:10.1088/0031-9155/49/13/004

9. McNamara AL, Schuemann J, Paganetti H. A phenomenological relative biological effectiveness (RBE) model for proton therapy based on all published in vitro cell survival data. *Phys Med Biol*. 2015;60(21):8399-8416. doi:10.1088/0031-9155/60/21/8399

10. Rørvik E, Thornqvist S, Stokkevag CH, Dahle TJ, Fjæra LF, Ytre-Hauge KS. A phenomenological biological dose model for proton therapy based on linear energy transfer spectra. *Med Phys*. 2017;44(6):2586-2594. doi:10.1002/mp.12216

11. Wedenberg M, Lind BK, Hårdemark B. A model for the relative biological effectiveness of protons: The tissue specific parameter α/β of photons is a predictor for the sensitivity to LET changes. *Acta Oncol (Madr)*. 2013;52(3):580-588. doi:10.3109/0284186X.2012.705892

12. Paganetti H. Relating proton treatments to photon treatments via the relative biological effectiveness - Should we revise current clinical practice? *Int J Radiat Oncol Biol*

Phys. 2015;91(5):892-894. doi:10.1016/j.ijrobp.2014.11.021

13. Tan HQ, Koh, Wei Yang C, Tan LKR, et al. Dependence of LET on material and its impact on current RBE model. *Phys Med Biol*. 2019. doi:10.1088/1361-6560/ab1c90

14. Drosoula Giantsoudi PD., Clemens Grassberger M, David Craft PD, Andrzej Niemierko PD, Alexei Trofimov PD, Harald Paganetti PD. Linear energy transfer (LET)-Guided Optimization in intensity modulated proton therapy (IMPT): feasibility study and clinical potential. 2015;73(4):389-400. doi:10.1016/j.ijrobp.2013.05.013

15. Unkelbach J, Hospital MG, Botas P, et al. HHS Public Access. 2017;96(5):1097-1106. doi:10.1016/j.ijrobp.2016.08.038.Reoptimization

16. Cao W, Khabazian A, Yepes P, et al. Reply to Comment on "Linear energy transfer incorporated intensity modulated proton therapy optimization." *Phys Med Biol*. 2019;64(5):0-10. doi:10.1088/1361-6560/aaff72

17. Fjæra LF, Li Z, Ytre-Hauge KS, et al. Linear energy transfer distributions in the brainstem depending on tumour location in intensity-modulated proton therapy of paediatric cancer. *Acta Oncol (Madr)*. 2017;56(6):763-768. doi:10.1080/0284186X.2017.1314007

18. Toussaint L, Indelicato DJ, Holgersen KS, et al. Towards proton arc therapy: physical and biologically equivalent doses with increasing number of beams in pediatric brain irradiation. *Acta Oncol (Madr)*. 2019;58(10):1451-1456. doi:10.1080/0284186X.2019.1639823

19. Liu C, Patel SH, Shan J, et al. Robust Optimization for Intensity Modulated Proton Therapy to Redistribute High Linear Energy Transfer from Nearby Critical Organs to Tumors in Head and Neck Cancer. *Int J Radiat Oncol Biol Phys*. 2020;107(1):181-193. doi:10.1016/j.ijrobp.2020.01.013

20. Paganetti H. *Proton Therapy Physics(Series in Medical Physics and Biomedical Engineering)*.; 2012. http://www.lavoisier.fr/livre/notice.asp?id=RK2W6SA2XKKOWQ.

21. Quan EM, Liu W, Wu R, et al. Preliminary evaluation of multifield and single-field optimization for the treatment planning of spot-scanning proton therapy of head and neck cancer. *Med Phys*. 2013;40(8). doi:10.1118/1.4813900

22. Barten DLJ, Tol JP, Dahele M, Slotman BJ, Verbakel WFAR. Comparison of organ-at-risk sparing and plan robustness for spot-scanning proton therapy and volumetric modulated arc photon therapy in head-and-neck cancer. *Med Phys*. 2015;42(11). doi:10.1118/1.4933245

23. Tommasino F, Widesott L, Fracchiolla F, et al. Clinical implementation in proton therapy of multi-field optimization by a hybrid method combining conventional PTV with robust optimization. *Phys Med Biol*. 2020;65(4):0-14. doi:10.1088/1361-6560/ab63b9

24. Guan F, Peeler C, Bronk L, et al. Analysis of the track- and dose-averaged LET and

LET spectra in proton therapy using the geant 4 Monte Carlo code. *Med Phys*. 2015;42(11):6234-6247. doi:10.1118/1.4932217

25. van Leeuwen CM, Oei AL, Crezee J, et al. The alfa and beta of tumours: A review of parameters of the linear-quadratic model, derived from clinical radiotherapy studies. *Radiat Oncol*. 2018;13(1):1-11. doi:10.1186/s13014-018-1040-z

26. Inaniwa T, Furukawa T, Kase Y, et al. Treatment planning for a scanned carbon beam with a modified microdosimetric kinetic model. *Phys Med Biol*. 2010;55(22):6721-6737. doi:10.1088/0031-9155/55/22/008

27. Kamada T, Tsujii H, Blakely EA, et al. Carbon ion radiotherapy in Japan: An assessment of 20 years of clinical experience. *Lancet Oncol*. 2015;16(2):e93-e100. doi:10.1016/S1470-2045(14)70412-7

28. Scholz M, Kellerer AM, Kraft-Weyrather W, Kraft G. Computation of cell survival in heavy ion beams for therapy. *Radiat Environ Biophys*. 1997;36(1):59-66. doi:10.1007/s004110050055

29. McNamara AL, Schuemann J, Paganetti H. A phenomenological relative biological effectiveness (RBE) model for proton therapy based on all published in vitro cell survival data. *Phys Med Biol*. 2015;60:8399.

30. Giovannini G, Böhlen T, Cabal G, et al. Variable RBE in proton therapy: Comparison of different model predictions and their influence on clinical-like scenarios. *Radiat Oncol*. 2016;11(1):1-16. doi:10.1186/s13014-016-0642-6

31. McNamara A, Willers H, Paganetti H. Proton Therapy special feature : Review Article Modelling variable proton relative biological effectiveness for treatment planning. *Br J Radiol*. 2019;92(April):20190334.

32. Cubillos-Mesías M, Baumann M, Troost EGC, et al. Impact of robust treatment planning on single- and multi-field optimized plans for proton beam therapy of unilateral head and neck target volumes. *Radiat Oncol*. 2017;12(1):1-10. doi:10.1186/s13014-017-0931-8

33. Hahn C, Eulitz J, Peters N, et al. Impact of range uncertainty on clinical distributions of linear energy transfer and biological effectiveness in proton therapy. *Med Phys*. 2020;47(12):6151-6162. doi:10.1002/mp.14560

34. Carabe A, Moteabbed M, Depauw N, Schuemann J, Paganetti H. Range uncertainty in proton therapy due to variable biological effectiveness. *Phys Med Biol*. 2012;57:1159.

35. Marteinsdottir M, Schuemann J, Paganetti H. Impact of uncertainties in range and RBE on small field proton therapy. *Phys Med Biol*. 2019;64(20):1-10. doi:10.1088/1361-6560/ab448f

36. Giantsoudi D, Grassberger C, Craft D, Niemierko A, Trofimov A, Paganetti H. Linear energy transfer-guided optimization in intensity modulated proton therapy: Feasibility study and clinical potential. *Int J Radiat Oncol Biol Phys*. 2013;87(1):216-222. doi:10.1016/j.ijrobp.2013.05.013

Chapter 6 Conclusion and Future Works

6.1 Summary

For proton therapy treatment planning to include RBE, a reliable RBE model needs to be established. In this thesis, only empirical LQ-based RBE models are used and the highly dependent factors such as LET_D and $\left(\frac{\alpha}{\beta}\right)_x$ contributing to the RBE model are further investigated theoretically and via MC simulation. Due to current data limitations, $\left(\frac{\alpha}{\beta}\right)_x$ is varied between low (3 Gy) and high (8 and 10 Gy) values. In conjunction with the variations in $\left(\frac{\alpha}{\beta}\right)_x$ values, a comprehensive study was conducted on the process of defining and calculating LET_D to reduce the uncertainties in the RBE model. In Chapter 3, LET_D values are simulated for Cytoplasm and the results are compared with data provided by Paganetti[1]. Thereafter, the RBE models are re-derived by using the corrected LET_D values and compared with the original RBE models. The corrected RBE model is then implemented for a clinical prostate case and the dose distributions were evaluated against the other RBE models. These results showed that there were dosimetric differences especially in the low dose (2Gy) and low $\left(\frac{\alpha}{\beta}\right)_x$ values. To improve RBE modelling further, better dosimetry and more precise instrumentation needs to be developed in the radiobiological experiments to reduce the uncertainties in dose and LET_D values.

In Chapter 4, the effects on LET_D by the hyperparameters (step length and range cut) in the MC simulation system (TOPAS) was investigated. It is known that the LET_D values should not change when the simulation protocols are modified. This is based on the

definition of LET_D in ICRU Report No. 85[2], which by definition is a macroscopic average quantity that depends on the particle kinetic energy and the material it traversed. However, it should be noted that LET_D results are indeed affected by the variations of these hyperparameters. Therefore, we recommended an optimal set of MC simulation parameters ($step\ length = 0.05\ mm, range\ cut = 0.01\ mm$) for the community to follow to obtain a reproducible LET_D. This method balances between the accuracy of LET_D values and the simulation time. In addition, the definition provided by ICRU Report No. 85[2] on the calculation method of LET_D was evaluated. From the definition of LET_D, Equation 6.1 is the recommended calculation method to determine LET_D where secondary electrons are included to obtain an accurate LET_D value. The reason to account for both proton and electron particles is that electrons tend to travel over a higher range in low density medium (e.g. lung) and incorporating it into the calculation will provide a more accurate LET_D value.

$$\frac{\sum_{p=1}^{n_p} \frac{\epsilon_p^2}{l_p} + \sum_{e=1}^{n_e} \frac{\epsilon_e^2}{l_e}}{\sum_{p,e=1}^{n_p,n_e} \epsilon_p + \epsilon_e} \tag{6.1}$$

n_p (n_e) refers to the number of protons (electrons), ϵ_p (ϵ_e) is the energy deposition of protons (electrons) and l_p (l_e) is the step length of protons (electrons).

In Chapter 5, the study was focused on a RBE model-agnostic treatment planning approach. This case study involved a brain tumor. We investigated the systematic dose variation from different RBE models using TOPAS. MFO and SFO planning techniques were used in the clinical brain case where OARs overlapped with the tumor. In implementing this new approach towards radiobiological studies, we would be able

to disregard the need to select any RBE model. The results supported MFO over SFO planning technique in reducing uncertainties contributed by RBE models in the case of brain tumors. This would be important during treatment planning where the OARs overlap or are near the target volume for brain cases.

In this thesis, systematic and comprehensive studies were done on LET_D and $\left(\frac{\alpha}{\beta}\right)_x$ for a robust RBE-modelling for proton therapy treatment planning. These studies provide a novel approach towards RBE-based treatment planning. In addition, the standardization of simulating LET_D would result in a more accurate RBE-weighted dose calculation and will also facilitate multiple cross-institutional studies in the future.

6.2 Future works

In preparation for our PT treatment at National Cancer Centre Singapore, the MC simulation treatment planning system (TOPAS) can be established according to the specific proton machine by performing physical beam measurements and matching the simulation results to measurement. This system can be used as a quality assurance tool for clinical treatment plans and further RBE research purposes. The work presented in Chapter 5 can be expanded to other tumor sites that are especially beneficial to be treated with PT such as paediatric oncology and local recurrent cases. Patient selection where OARs overlap with target volume must be taken into account on the biological uncertainties that depend on the planning techniques like MFO and SFO. Different treatment planning systems may also be included to further validate the results.

Despite the work done in reducing uncertainties in RBE models and the ongoing efforts in implementing the models, the largest biological uncertainty is still due to the inherent variation in individual sensitivity of the tumor type to radiation[3]. With the lack of accurate RBE knowledge, these models may not be ready for use in plan optimization for clinical practice. Therefore, LET based optimization has become an area of interest as it can influence the LET distribution without significantly varying the dose constraints in a treatment plan[4,5]. With LET optimization, one can determine the LET distribution such that high LET falls in the target instead of the OAR. In the OAR, any decrease in LET will reduce the RBE value. This results in smaller RBE uncertainties. In parallel with robust optimization and LET optimization for PT treatment planning, the possibility of mitigating the biological uncertainties using these two optimization techniques can be explored further.

For example, a patient case of 20 fractions PT treatment, a base plan and a LET optimized plan can be generated. In the base plan, a specific randomised error based on the robustness criteria can be introduced into each fraction. The randomised errors consist of the range uncertainty (i.e., $\pm x\%$) and positioning uncertainty (i.e., $\pm y\ mm$). Thereafter, a robust optimal base plan (composition of all fractions of randomize errors) can be compared to a robust LET optimized plan. Hypothetically, if the difference between these plans is minimal and knowing the fact that LET optimization can reduce high RBE in OARs, an RBE model-agnostic dose distribution might be achievable just by having robust optimization and LET optimization to mitigate biological uncertainties. A more in-depth study is needed to examine the difference between these plans.

6.3 References

1. Paganetti H. Relative biological effectiveness (RBE) values for proton beam therapy. Variations as a function of biological endpoint, dose, and linear energy transfer. *Phys Med Biol*. 2014;59(22):R419-R472. doi:10.1088/0031-9155/59/22/R419

2. *ICRU Report 85*. Vol 11.; 2011. doi:10.1093/jicru/ndr012

3. Paganetti H, Beltran C, Both S, et al. Roadmap: Proton therapy physics and biology. *Phys Med Biol*. 2021;66(5). doi:10.1088/1361-6560/abcd16

4. Giantsoudi D, Grassberger C, Craft D, Niemierko A, Trofimov A, Paganetti H. Linear energy transfer-guided optimization in intensity modulated proton therapy: Feasibility study and clinical potential. *Int J Radiat Oncol Biol Phys*. 2013;87(1):216-222. doi:10.1016/j.ijrobp.2013.05.013

5. Liu C, Patel SH, Shan J, et al. Robust Optimization for Intensity Modulated Proton Therapy to Redistribute High Linear Energy Transfer from Nearby Critical Organs to Tumors in Head and Neck Cancer. *Int J Radiat Oncol Biol Phys*. 2020;107(1):181-193. doi:10.1016/j.ijrobp.2020.01.013

Appendix A

$$S(D) = e^{(-\alpha D - \beta D^2)} \quad (1.12)$$

$$D_x = RBE \times D_p \quad (1.13)$$

To obtain the same surviving fraction from photon and proton,

$$SF_x = SF_p$$

$$e^{(-\alpha_x D_x - \beta_x D_x^2)} = e^{(-\alpha_p D_p - \beta_p D_p^2)}$$

we can ln on both sides of the equation,

$$\alpha_x D_x + \beta_x D_x^2 = \alpha_p D_p + \beta_p D_p^2.$$

Thereafter we can divide D_p^2 and β_x on both sides,

$$\frac{\alpha_x}{\beta_x}\frac{D_x}{D_p}\frac{1}{D_p} + (\frac{D_x}{D_P})^2 = \frac{\alpha_p}{\beta_x}\frac{1}{D_p} + \frac{\beta_p}{\beta_x}.$$

Since $RBE = \frac{D_x}{D_p}$, it can be rewritten as

$$\frac{\alpha_x}{\beta_x}\frac{1}{D_p}RBE + RBE^2 - \frac{\alpha_p}{\beta_x}\frac{1}{D_p} - \frac{\beta_p}{\beta_x} = 0.$$

By solving the quadratic formula with $RBE \geq 0$,

$$RBE = \frac{1}{2D_p}(\sqrt{\left(\frac{\alpha_x}{\beta_x}\right)^2 + 4D_p\frac{\alpha_p}{\beta_x} + 4D_p^2\frac{\beta_p}{\beta_x}} - \frac{\alpha_x}{\beta_x}.$$

Therefore,

$$RBE\left(D_p,\ \left[\frac{\alpha}{\beta}\right]_x, LET_d\right) = \frac{1}{D_p}(\sqrt{\frac{1}{4}\left[\frac{\alpha}{\beta}\right]_x^2 + \left[\frac{\alpha}{\beta}\right]_x RBE_{max}D_p + RBE_{min}D_p^2} - \frac{1}{2}\left[\frac{\alpha}{\beta}\right]_x)$$

$$RBE_{max} = \lim_{D\to 0} RBE = \frac{\alpha_p}{\alpha_x}$$

$$RBE_{min} = \lim_{D\to \infty} RBE = \sqrt{\frac{\beta_p}{\beta_x}}$$

Appendix B

B1. This section shows samples of the code during the commissioning of the proton beamline that is required to be fine-tuned.

Scanning Nozzle

```
# Calculate Distance for Vacuum Window
d:VacuumWindow_thickness = 0.1 mm
d:VacuumWindow_pos_z = -770.0 mm
# Create Vacuum Window
s:Ge/vacuumWindow/Parent = "NozzleGroup"
s:Ge/vacuumWindow/Type     = "TsBox"
s:Ge/vacuumWindow/Material = "Titanium"
d:Ge/vacuumWindow/HLX  = 75. mm
d:Ge/vacuumWindow/HLY  = 75. mm
d:Ge/vacuumWindow/HLZ  = VacuumWindow_thickness mm * 0.5
d:Ge/vacuumWindow/RotX     = 0.0 deg
d:Ge/vacuumWindow/RotY     = 0.0 deg
d:Ge/vacuumWindow/RotZ     = 0.0 deg
d:Ge/vacuumWindow/TransX   = 0.0 mm
d:Ge/vacuumWindow/TransY   = 0.0 mm
d:Ge/vacuumWindow/TransZ   = VacuumWindow_pos_z mm
s:Ge/vacuumWindow/Color = "green"
s:Ge/vacuumWindow/DrawingStyle = "Solid"
b:Ge/VacuumWindow/Include  = "True"
```

Basic Control Parameters

```
# Use Time Features for Scanning
d:Tf/TimelineStart              = 0. s
d:Tf/TimelineEnd                = 0.269 s
i:Tf/NumberOfSequentialTimes = 269

# Define the World
s:Ge/World/Material  = "G4_AIR"
d:Ge/World/HLX       = 500.0 cm
d:Ge/World/HLY       = 500.0 cm
d:Ge/World/HLZ       = 500.0 cm

# Define Gantry Control
b:use_bpm          = "True"
b:use_spm          = "True"

##### Gantry Rotation
s:Ge/NozzleGroup/Parent = "World"
s:Ge/NozzleGroup/Type = "Group"
d:Ge/NozzleGroup/RotY = 270 deg

##### Couch Rotation
s:Ge/CouchGroup/Parent = "World"
s:Ge/CouchGroup/Type = "Group"
d:Ge/CouchGroup/RotZ = 30 deg
```

```
#Particle Numbers
i:So/particleSource/NumberOfHistoriesInRun = Tf/nbParticle/Value
s:So/particleSource/BeamParticle = "proton"
d:So/particleSource/BeamEnergy = Tf/energy/Value MeV
```

Patient Scorer

```
##### Dicom to Couch group
s:Ge/Dicom_to_Couch/Parent = "CouchGroup"
s:Ge/Dicom_to_Couch/Type = "Group"
d:Ge/Dicom_to_Couch/RotX = -90 deg
d:Ge/Dicom_to_Couch/RotY = 0 deg
d:Ge/Dicom_to_Couch/RotZ = 0 deg
d:Ge/Dicom_to_Couch/TransX = 0.0 mm
d:Ge/Dicom_to_Couch/TransY = 0.0 mm
d:Ge/Dicom_to_Couch/TransZ = 0.0 mm

# Patient
s:Ge/Patient/Parent = "Dicom_to_Couch"
s:Ge/Patient/Type     = "TsDicomPatient"
iv:Gr/Patient/ShowSpecificSlicesZ = 1 -2
s:Ge/Patient/DicomDirectory = "Patient1"
sv:Ge/Patient/DicomModalityTags = 1 "CT"
d:Ge/Patient/TransX = 7.2712595796813 mm
d:Ge/Patient/TransY = -26.1010114574833 mm
d:Ge/Patient/TransZ = 12.603944296645999 mm
d:Ge/Patient/RotX = 0 deg
d:Ge/Patient/RotY = 0 deg
d:Ge/Patient/RotZ = 0 deg
b:Ge/Patient/FakeStructures = "True"
b:Ge/Patient/Include = "True"
s:Ge/Patient/CloneRTDoseGridFrom = Ge/Patient/DicomDirectory +
"/RD.Patient1.dcm"
b:Ge/Patient/IgnoreInconsistentFrameOfReferenceUID = "True"

s:Sc/PatientScorer/Quantity = "DoseToMedium"
s:Sc/PatientScorer/Component = "Patient/RTDoseGrid"
s:Sc/PatientScorer/IfOutputFileAlreadyExists = "Overwrite"
s:Sc/PatientScorer/OutputType = "DICOM"
b:Sc/PatientScorer/Active = "True"
s:Sc/PatientScorer/OutputFile = "PatientDose"
s:Sc/PatientScorer/ReferencedDicomPatient = "Patient"

#-- shared sub-scorers
s:Sc/PhysDose/Quantity   = "DoseToWater"
s:Sc/PhysDose/Component  = "Patient"
b:Sc/PhysDose/PreCalculateStoppingPowerRatios = "True"
s:Sc/PhysDose/IfOutputFileAlreadyExists = "Overwrite"
s:Sc/PhysDose/OutputType = "csv"
s:Sc/PhysDose/OutputFile = "PhysicalDose"

s:Sc/ProtonLET/Quantity   = "ProtonLET"
s:Sc/ProtonLET/Component  = "Patient"
s:Sc/ProtonLET/IfOutputFileAlreadyExists = "Overwrite"
s:Sc/ProtonLET/OutputType = "csv"
s:Sc/ProtonLET/OutputFile = "LET"
```

B2. This section shows part of the code for the post-processing of the output from the simulation to calculate LET_D and graph plotting.

```
import os
import numpy as np
import matplotlib.pyplot as plt

def Unravel_index(index):

class ImportData:
    def __init__(self,fname1,fname2,fname3):
    def _Get_3D_Array(self,data):

if __name__=="__main__":
    data_proton = ImportData('proton_h3_7.csv','proton_h3_8.csv','proton_h3_9.csv')
    data_electron = ImportData('proton_h3_10.csv','proton_h3_11.csv','proton_h3_12.csv')

    #Ground truth
    data_proton_unrestricted =
ImportData('proton_h3_7_unrestricted.csv','proton_h3_8_unrestricted.csv','proton_h3_9_unre
stricted.csv')

    #Plotting results
    distance = np.linspace(-15.0, 15.0, dimZ-2)
    distance = np.linspace(-15.0, 15.0, dimZ-2)
    centroid_x = int((dimX-2) / 2.)+1
    centroid_y = int((dimY-2) / 2.)+1
    letd_proton_unrestricted = data_proton_unrestricted.data3d_E2_L /
data_proton_unrestricted.data3d_E
    letd_proton = data_proton.data3d_E2_L / data_proton.data3d_E
    letd_electron = data_electron.data3d_E2_L / data_electron.data3d_E
    letd_total = (data_electron.data3d_E2_L + data_proton.data3d_E2_L) /
(data_electron.data3d_E + data_proton.data3d_E)

    plt.plot(distance,letd_proton_unrestricted[centroid_x,centroid_y,1:-1],'ko-',label='Proton-
unrestricted')
    plt.plot(distance,letd_proton[centroid_x,centroid_y,1:-1],'bo-',label='Proton-restricted')
    plt.plot(distance,letd_total[centroid_x,centroid_y,1:-1],'mo-',label='Total')
    plt.yscale('log')
    plt.xlabel('Distance / cm')
    plt.ylabel('Dose Averaged LET / keV/um')
    plt.legend()
    plt.figure()
    plt.plot(distance,letd_electron[centroid_x,centroid_y,1:-1],'ro-',label='Electron')
    plt.plot(distance,letd_proton[centroid_x,centroid_y,1:-1],'bo-',label='Proton-restricted')
    plt.xlabel('Distance / cm')
```

```
plt.ylabel('Dose Averaged LET / keV/um')
plt.legend()
plt.show()
```

B3. This section of the code shows an example that is added into the *DetectorConstruction* source file of the GEANT4 library to create the geometry (e.g. water phantom and cell culture) for tracking.

```
G4Box* SolidWorld =
      new G4Box("World",
        0.5*WorldSize, 0.5*WorldSize, 0.5*WorldSize);

  G4LogicalVolume* LogicWorld =
      new G4LogicalVolume(SolidWorld,
                    WorldMat,
                    "World");

  G4VPhysicalVolume* PhysWorld =
      new G4PVPlacement(0,
                    G4ThreeVector(),
                    LogicWorld,
                    "World",
                    0,
                    false,
                    0,
                    checkOverlaps);

 // Create the cell culture region
 if (1) {
    G4double cellSize = 5.*mm;
    G4Material* CellMat = nist->FindOrBuildMaterial("G4_WATER");
    //G4Material* CellMat = fMaterial;

    G4Box* SolidCell =
        new G4Box("Cell",
          0.5*cellSize, 0.5*cellSize, 0.5*cellSize);

    G4LogicalVolume* LogicCell =
        new G4LogicalVolume(SolidCell,
                      CellMat,
                      "Cell");G4Box* SolidWorld =
      new G4Box("World",
        0.5*WorldSize, 0.5*WorldSize, 0.5*WorldSize);

  G4LogicalVolume* LogicWorld =
      new G4LogicalVolume(SolidWorld,
                    WorldMat,
                    "World");

  G4VPhysicalVolume* PhysWorld =
```

```
new G4PVPlacement(0,
                  G4ThreeVector(),
                  LogicWorld,
                  "World",
                  0,
                  false,
                  0,
                  checkOverlaps);
```

B4. This section of the code is added into *SteppingAction* source file of the GEANT4 library to calculate LET_D.

```
void SteppingAction::UserSteppingAction(const G4Step* step)
{
 //continuous energy deposit per event
 fEventaction->AddEnergyDeposit (step->GetTotalEnergyDeposit());
 //step size
 G4AnalysisManager* analysisManager = G4AnalysisManager::Instance();
 G4double parentID = step->GetTrack()->GetParentID();
 G4double stepSize = step->GetStepLength();
 G4double eDep     = (step->GetTotalEnergyDeposit());
 G4double eDep1    = eDep / stepSize;
 G4double eDep2    = eDep * eDep / stepSize; // For computing Dose-averaged LET
fRunaction->AddTrackLength(stepSize);

 // Get position of LET computation
 G4ThreeVector pos1 = step->GetPreStepPoint()->GetPosition();
 G4ThreeVector pos2 = step->GetPostStepPoint()->GetPosition();
 G4double zPos = (pos1[2] + pos2[2]) / 2.;
 G4double yPos = (pos1[1] + pos2[1]) / 2.;
 G4double xPos = (pos1[0] + pos2[0]) / 2.;

 G4String particleName = step->GetTrack()->GetParticleDefinition()->GetParticleName();

 // Output File for post processing
 if (particleName=="proton") {
   analysisManager->FillH3(0,xPos,yPos,zPos,eDep2);
   analysisManager->FillH3(1,xPos,yPos,zPos,eDep);
   analysisManager->FillH3(2,xPos,yPos,zPos,eDep1);
 }
 if (particleName == "e-") {
   analysisManager->FillH3(3,xPos,yPos,zPos,eDep2);
   analysisManager->FillH3(4,xPos,yPos,zPos,eDep);
   analysisManager->FillH3(5,xPos,yPos,zPos,eDep1);
 }
```

B5. This section shows part of the code of the in-house script to calculate the dose of a patient plan by reading in actual patient plans and CT images.

```
import os
import glob
import pydicom
import copy
import math
import subprocess
import numpy as np

### ----------------------------------------------------
### File I/O and Options
### ----------------------------------------------------

option = 'dss' # ddcs or dss
errorShift = [0.0, 0.0, 0.0]
### Directory Name ###
dirName = 'Patient1'
### Define Gy per Fraction ###
GyPerFrac = 2.025
##### Set Patient Dose filename for cloning dose grid
rtdoseName = 'RD.Patient1.dcm'
##### Set Dicom Origin
dicomOrigin = [0.0, 0.0, 0.0]
uniqueName = None
dirName_out = dirName + '_MC'
##### Change here to change the scaling of the particle
constantScale = 10**-3

### ----------------------------------------------------
### Utility Functions
### ----------------------------------------------------

### Define Global Function ###
def ReplaceStringInFile(fname, ref_string, change_string):

### Error Checking class
class ErrorChecking:

### ----------------------------------------------------
### Main Code
### ----------------------------------------------------

class ReadDicomPlan:
    def __init__(self, planName):
```

```
    def _ReadPlan(self, name):

class ProtonBeamConfiguration:
    def __init__(self):
    def _ConvertMU2NbParticles(self, energy, GyPerFrac):

class CalculateDose_DSS(ProtonBeamConfiguration):
    def __init__(self, plan):
    def _SetPatientDirectory(self):
    def _RunMonteCarlo(self, planDict, gantryAngle, isocenter, patientSupportAngle):
    def _RunTOPAS(self):
        subprocess.call(["../bin/topas", "PT_main.txt"])
    def _ConvertDicomPlan2TimeFeatures(self, planDict):
    ##### Set Gantry, Couch Rotation
    def _SetPatientRotationVector(self, gantryAngle, patientSupportAngle):
    ##### Set Isocenter
    def _SetPatientPosition(self, isocenter, gantryAngle, patientSupportAngle):
    def _CalculateBeamAngle(self, oneSpotArray):
    def _CalculateNbSpots(self, planDict):
    def _ChangeFileNames(self):
    def _CalculateDicomShifts(self):

class CalculateDose_DDCS(ProtonBeamConfiguration):

if __name__ == '__main__':
    ErrorCheck = ErrorChecking()
    plan = ReadDicomPlan(ErrorCheck.planName)
    if option == 'ddcs':
        pass
    elif option == 'dss':
        doseCalculator = CalculateDose_DSS(plan)
    else:
        raise Exception('Wrong options....')
```

B6. This section of the code is the main text file called by the above in-house python script to run TOPAS.

```
# Define overall program control
b:Ts/DumpNonDefaultParameters = "False"
i:Ts/NumberOfThreads = 35
i:Ts/Seed = 1
i:Ts/ShowHistoryCountAtInterval = 50
b:Ts/PauseBeforeQuit = "False"
Ge/CheckForOverlaps = "True"
Ge/QuitIfOverlapDetected = "True"
Ge/CheckForUnusedComponents = "False"

# Define Physics Interaction
s:Ph/ListName = "PhysicsList1"
s:Ph/PhysicsList1/Type = "Geant4_Modular"
sv:Ph/PhysicsList1/Modules = 4 "g4em-standard_opt4" "g4h-phy_QGSP_BERT_HP" "g4h-elastic" "g4stopping"
d:Ph/PhysicsList1/CutForElectron = 1 m
i:Ph/PhysicsList1/Verbosity = 1

# Particle Sources
s:Ge/BeamPosition/Parent = "NozzleGroup"
s:Ge/BeamPosition/Type = "Group"
d:Ge/BeamPosition/TransX = 0.0 mm
d:Ge/BeamPosition/TransY = Tf/yPosition/Value mm
d:Ge/BeamPosition/TransZ = -1350. mm
d:Ge/BeamPosition/RotX = Tf/xAngle/Value deg
d:Ge/BeamPosition/RotY = Tf/yAngle/Value deg
d:Ge/BeamPosition/RotZ = 0.0 deg

s:So/particleSource/Component = "BeamPosition"
s:So/particleSource/Type = "emittance"
u:So/particleSource/BeamEnergySpread = 0.0

s:So/particleSource/Distribution   = "BiGaussian"
d:So/particleSource/SigmaX         = Tf/twissX/Value mm
u:So/particleSource/SigmaXprime    = Tf/twissXprime/Value
u:So/particleSource/CorrelationX   = -0.9261
d:So/particleSource/SigmaY         = Tf/twissY/Value mm
u:So/particleSource/SigmaYPrime    = Tf/twissYprime/Value
u:So/particleSource/CorrelationY   = -0.9231


#Include Files
includeFile = ./PT_ScanningNozzle.txt
```

```
includeFile = ./PT_RangeShifter.txt
includeFile = ./PT_Patient.txt      # Change here to control options
```

Appendix C

Table C1 Calculated LET_D for Chinese hamster cell lines. The dashed line in the first column means $\beta_x = 0.000$.

$(\alpha/\beta)_x$ (Gy)	α (Gy^{-1})	β (Gy^{-2})	LET_D Original $(keV\mu m^{-1})$	Config.	LET_D Water $(keV\mu m^{-1})$	LET_D Cytoplasm-1 $(keV\mu m^{-1})$	LET_D Cytoplasm-2 $(keV\mu m^{-1})$	References
0.000	0.028	0.041	2.050	S2	1.940	1.990	2.310	[38]
0.500	0.024	0.033	4.300	S2	4.970	5.160	5.890	[39]
0.500	0.018	0.048	6.350	S2	7.340	7.710	9.930	[39]
0.500	0.016	0.033	8.220	S2	12.200	12.890	15.990	[39]
0.969	0.042	0.030	2.050	S2	1.940	1.990	2.310	[38]
0.969	0.038	0.029	1.110	S2	1.140	1.150	1.230	[38]
1.431	0.102	0.052	1.110	S1	1.140	1.150	1.230	[23]
1.431	0.105	0.050	1.190	S1	1.190	1.200	1.290	[23]
1.431	0.087	0.056	1.450	S1	1.260	1.280	1.380	[23]
1.431	0.072	0.059	1.770	S1	1.500	1.540	1.720	[23]
1.431	0.120	0.052	1.940	S1	1.870	1.920	2.340	[23]
1.431	0.108	0.054	2.090	S1	2.020	2.200	2.450	[23]
1.431	0.104	0.055	2.280	S1	2.320	2.370	2.840	[23]
1.431	0.122	0.054	2.530	S1	2.490	2.700	3.170	[23]
1.431	0.113	0.056	2.900	S1	2.850	2.950	3.600	[23]
1.431	0.113	0.059	3.460	S1	3.260	3.530	4.630	[23]
1.431	0.141	0.059	4.820	S1	4.590	4.730	5.280	[23]
1.431	0.533	0.050	11.000	S1	11.420	12.000	21.280	[23]
1.431	0.098	0.052	1.080	S1	1.040	1.050	1.120	[23]
1.431	0.103	0.049	1.050	S1	1.080	1.090	1.160	[23]
1.431	0.091	0.052	1.110	S1	1.120	1.130	1.200	[23]
1.431	0.086	0.050	1.130	S1	1.170	1.180	1.270	[23]
1.431	0.099	0.052	1.410	S1	1.250	1.270	1.380	[23]
1.431	0.089	0.054	1.800	S1	1.530	1.750	1.990	[23]
1.431	0.094	0.055	1.910	S1	1.730	1.800	2.120	[23]
1.431	0.110	0.054	2.030	S1	1.880	1.990	2.310	[23]
1.431	0.103	0.055	2.170	S1	2.090	2.230	2.640	[23]
1.431	0.106	0.057	2.360	S1	2.310	2.450	2.980	[23]
1.431	0.086	0.062	2.640	S1	2.650	2.860	3.500	[23]
1.431	0.141	0.054	2.990	S1	3.190	3.580	4.650	[23]
1.431	0.099	0.064	3.480	S1	3.900	4.830	8.000	[23]
1.431	0.121	0.063	4.040	S1	5.200	7.620	13.330	[23]
1.431	0.294	0.273	10.500	S1	14.200	0.030	0.000	[23]

1.725	0.152	0.034	2.530	S2	2.690	2.770	3.170	[40]
1.833	0.103	0.095	1.290	S2	1.280	1.300	1.490	[41]
1.833	0.192	0.077	4.100	S2	4.000	4.150	4.910	[41]
1.833	0.071	0.085	2.730	S2	2.980	3.030	3.350	[41]
1.833	0.198	0.073	4.530	S2	4.690	4.850	5.950	[41]
2.040	0.128	0.033	1.090	S2	0.980	0.990	1.050	[42]
2.040	0.115	0.035	0.990	S2	1.000	1.010	1.070	[42]
2.040	0.120	0.035	1.130	S2	1.020	1.030	1.100	[42]
2.040	0.136	0.033	1.020	S2	1.050	1.060	1.130	[42]
2.040	0.138	0.031	1.140	S2	1.080	1.090	1.170	[42]
2.040	0.137	0.029	1.030	S2	1.130	1.140	1.230	[42]
2.040	0.125	0.031	1.120	S2	1.190	1.240	1.300	[42]
2.040	0.129	0.030	1.160	S2	1.310	1.330	1.490	[42]
2.040	0.154	0.027	1.750	S2	1.560	1.580	1.850	[42]
2.040	0.135	0.030	2.100	S2	1.970	2.080	2.550	[42]
2.040	0.113	0.032	2.710	S2	2.920	3.040	4.210	[42]
2.040	0.145	0.030	7.060	S2	11.800	12.900	14.200	[42]
2.040	0.103	0.033	0.990	S2	1.080	1.090	1.170	[42]
2.040	0.126	0.029	1.230	S2	1.130	1.140	1.220	[42]
2.040	0.108	0.032	1.110	S2	1.190	1.200	1.290	[42]
2.040	0.113	0.030	1.280	S2	1.300	1.310	1.440	[42]
2.040	0.119	0.031	1.700	S2	1.690	2.230	2.600	[42]
2.040	0.133	0.030	2.080	S2	2.010	2.600	2.990	[42]
2.040	0.120	0.032	2.630	S2	2.480	3.080	3.690	[42]
2.040	0.167	0.027	5.820	S2	5.120	5.380	7.880	[42]
2.040	0.128	0.027	1.160	S2	1.150	1.150	1.240	[42]
2.040	0.118	0.027	1.200	S2	1.210	1.220	1.320	[42]
2.040	0.129	0.026	1.790	S2	1.350	1.370	1.500	[42]
2.040	0.132	0.025	2.320	S2	2.470	2.550	2.690	[42]
2.040	0.169	0.025	3.200	S2	2.680	2.710	2.800	[42]
2.232	0.161	0.027	2.300	S2	2.410	2.510	2.890	[43]
2.232	0.162	0.029	2.800	S2	3.100	3.160	3.660	[43]
2.232	0.154	0.030	2.950	S2	3.210	3.270	3.690	[43]
2.232	0.163	0.028	3.120	S2	3.360	3.400	3.870	[43]
2.232	0.156	0.030	3.270	S2	3.500	3.570	4.040	[43]
2.232	0.142	0.033	3.480	S2	3.700	3.770	4.270	[43]
2.232	0.152	0.031	3.700	S2	3.900	3.980	4.520	[43]
2.232	0.154	0.032	4.000	S2	4.190	4.270	4.860	[43]
2.232	0.139	0.035	4.400	S2	4.570	4.660	5.310	[43]
2.232	0.143	0.035	5.280	S2	5.470	5.600	6.390	[43]
2.232	0.170	0.034	6.300	S2	6.410	6.570	7.560	[43]

2.626	0.213	0.040	1.180	S1	1.231	1.242	1.354	[25]
2.626	0.091	0.049	2.120	S1	2.160	2.230	2.950	[25]
0.027	0.320	0.039	10.100	P2	10.180	10.540	12.180	[31]
0.027	0.450	0.028	17.800	P2	17.630	18.350	21.560	[31]
0.027	0.740	0.011	27.600	P2	27.460	28.400	34.530	[31]
0.027	0.733	0.000	25.400	-	0.000	0.000	0.000	[32]
0.027	0.241	0.046	10.900	-	0.000	0.000	0.000	[32]
0.028	0.171	0.000	88.800	P2	0.000	0.000	0.000	[44]
0.028	0.367	0.000	63.700	P2	0.000	0.000	0.000	[44]
2.783	0.744	0.000	30.500	P2	38.250	39.960	53.100	[44]
2.783	0.471	0.044	20.000	P2	21.730	22.540	26.810	[44]
2.783	0.372	0.036	10.900	P2	11.310	11.720	13.580	[44]
0.028	0.744	0.000	31.000		0.000	0.000	0.000	[45]
0.028	0.580	0.000	37.800	P2	0.000	44.650	0.000	[46]
2.804	0.653	0.000	34.600	P2	37.700	39.330	51.820	[46]
2.804	0.721	0.000	30.500	P2	32.880	34.040	42.680	[46]
2.804	0.469	0.043	20.000	P2	20.780	21.570	25.570	[46]
2.804	0.372	0.036	11.000	P2	11.200	11.610	13.450	[46]
2.804	0.289	0.024	7.700	P2	7.960	8.190	9.430	[46]
2.804	0.300	0.052	22.910	P2	24.330	25.230	30.290	[47]
2.804	0.420	0.019	20.270	P2	21.360	22.170	26.330	[47]
3.018	0.115	0.049	2.530	S2	2.690	2.770	3.170	[40]
0.031	0.059	0.218	10.000	-	0.000	0.000	0.000	[48]
0.031	0.388	0.000	14.000	-	0.000	0.000	0.000	[48]
0.031	0.433	0.000	15.000	-	0.000	0.000	0.000	[48]
0.031	0.396	0.017	20.000	-	0.000	0.000	0.000	[48]
0.031	0.263	0.045	28.000	-	0.000	0.000	0.000	[48]
3.305	0.100	0.025	5.220	S1	5.250	5.290	5.670	[49]
3.305	0.071	0.030	1.090	S2	1.015	1.020	1.089	[49]
3.429	0.204	0.021	11.000	P2	11.230	11.640	13.480	[50]
3.429	0.226	0.020	4.250	P2	4.420	4.520	5.140	[50]
3.429	0.151	0.025	1.250	P2	1.270	1.300	1.480	[50]
3.652	0.329	0.024	3.710	S2	3.910	3.990	4.530	[51]
3.905	0.109	0.016	0.790	P2	0.810	0.820	0.926	[52]
3.905	0.243	0.013	3.100	P2	14.170	14.740	17.400	[52]
4.045	0.085	0.040	2.530	S2	2.690	2.770	3.170	[40]
4.056	0.399	0.272	9.230	P2	9.510	9.830	11.100	[53]
4.074	1.030	0.000	32.000	P2	38.250	40.000	53.100	[54]
4.074	0.330	0.066	24.000	P2	25.790	26.690	32.220	[54]
4.074	0.110	0.027	17.000	P2	17.120	17.820	20.900	[54]
4.074	0.350	0.045	17.000	P1	31.800	33.800	38.990	[55]

4.074	0.330	0.066	24.000	P1	39.700	42.630	49.580	[55]
4.074	1.030	0.000	32.000	P1	46.600	50.090	61.800	[55]
4.338	0.062	0.023	1.220	P2	1.240	1.260	1.430	[56]
4.338	0.071	0.025	1.120	P2	1.130	1.150	1.310	[56]
4.338	0.053	0.037	1.910	P2	1.940	1.980	2.250	[56]
4.338	0.062	0.040	2.410	P2	2.470	2.520	2.870	[56]
4.338	0.044	0.047	3.830	P2	4.070	4.150	4.900	[56]
4.338	0.090	0.019	1.170	P2	1.190	1.210	1.370	[56]
4.338	0.096	0.019	1.120	P2	1.130	1.150	1.310	[56]
4.338	0.068	0.023	1.070	P2	1.090	1.100	1.250	[56]
4.338	0.083	0.024	1.190	P2	1.210	1.230	1.390	[56]
4.338	0.079	0.033	1.690	P2	1.720	1.740	1.990	[56]
4.338	0.081	0.040	2.060	P2	2.100	2.140	2.440	[56]
4.338	0.050	0.046	2.540	P2	2.610	2.660	3.030	[56]
4.338	0.060	0.048	6.080	P2	6.190	6.350	7.300	[56]
4.338	0.099	0.019	1.070	P2	1.090	1.100	1.250	[56]
4.338	0.099	0.020	1.080	P2	1.100	1.110	1.260	[56]
4.338	0.073	0.022	0.990	P2	1.010	1.020	1.160	[56]
4.338	0.087	0.020	1.080	P2	1.100	1.110	1.260	[56]
4.338	0.070	0.021	1.050	P2	1.070	1.080	1.220	[56]
4.338	0.047	0.024	1.090	P2	1.100	1.110	1.260	[56]
4.338	0.040	0.024	1.160	P2	1.190	1.210	1.370	[56]
4.338	0.037	0.025	1.130	P2	1.130	1.150	1.310	[56]
4.338	0.042	0.028	1.720	P2	1.750	1.780	2.020	[56]
4.338	0.027	0.039	1.880	P2	1.910	1.950	2.220	[56]
4.338	0.019	0.043	2.760	P2	2.840	2.890	3.300	[56]
4.338	0.040	0.037	7.750	P2	7.880	8.110	9.330	[56]
4.522	0.142	0.032	2.530	S2	2.690	2.770	3.170	[40]
5.000	0.140	0.045	3.440	S2	3.840	4.030	4.620	[57]
5.054	0.122	0.149	9.230	P2	9.510	9.830	11.100	[53]
5.217	0.120	0.067	17.600	P1	31.480	33.670	38.630	[58]
5.833	0.221	0.041	6.230	P1	15.510	16.390	19.210	[59]
6.520	0.199	0.022	1.740	S2	1.810	1.840	2.100	[60]
6.520	0.207	0.025	3.110	S2	3.360	3.420	3.860	[60]
6.520	0.217	0.026	3.790	S2	4.090	4.170	4.740	[60]
6.520	0.249	0.025	4.760	S2	4.910	5.020	5.730	[60]
7.667	0.539	0.000	27.600	P1	42.220	46.130	56.520	[61]
7.667	0.194	0.023	7.700	P1	18.970	19.990	23.510	[61]
8.571	0.120	0.028	1.180	S1	1.231	1.242	1.354	[24]
8.571	0.065	0.033	2.120	S1	2.160	2.230	2.950	[24]
10.814	0.720	0.030	2.530	S2	2.690	2.770	3.170	[40]

11.724	0.116	0.007	17.000	P1	31.800	33.800	38.990	[55]
11.724	0.239	0.005	24.000	P1	39.700	42.630	49.580	[55]
11.724	0.561	0.000	32.000	P1	46.600	50.090	61.800	[55]
13.061	0.214	0.021	2.020	S2	2.020	2.120	4.380	[62]
13.061	0.166	0.024	1.020	S2	1.050	1.060	1.140	[62]
13.971	0.172	0.039	2.530	S2	2.690	2.770	3.170	[40]
15.152	0.070	0.001	1.180	S1	1.231	1.242	1.354	[24]
15.152	0.034	0.003	2.120	S1	2.160	2.230	2.950	[24]
16.296	0.345	0.035	2.530	S2	2.690	2.770	3.170	[40]
18.432	0.875	0.023	2.530	S2	2.690	2.770	3.170	[40]
25.455	0.430	0.000	12.100	P2	11.900	12.340	14.310	[63]
25.455	0.210	0.023	5.800	P2	5.910	6.050	6.930	[63]
91.509	1.708	0.005	2.530	S2	2.690	2.770	3.170	[40]
114.900	0.990	0.017	2.530	S2	2.690	2.770	3.170	[40]

Table C2 Calculated LET_D for rat or mouse cell lines.

$(\alpha/\beta)_x$ (Gy)	α (Gy^{-1})	β (Gy^{-2})	LET_D Original $(keV\mu m^{-1})$	Config.	LET_D Water $(keV\mu m^{-1})$	LET_D Cytoplasm-1 $(keV\mu m^{-1})$	LET_D Cytoplasm-2 $(keV\mu m^{-1})$	References
0.000	0.093	0.024	0.420	P2	0.450	0.460	0.510	[64]
0.000	0.088	0.013	0.420	P2	0.450	0.460	0.510	[64]
0.000	0.000	0.011	1.210	S2	1.230	1.250	1.420	[65]
0.000	0.028	0.036	1.210	S2	1.230	1.250	1.420	[65]
0.000	0.036	0.004	1.210	S2	1.230	1.250	1.420	[65]
0.051	0.140	0.044	2.690	P2	2.880	2.920	3.290	[57]
0.051	0.320	0.060	14.000	P2	12.220	12.680	14.710	[57]
0.051	0.670	0.230	26.000	P2	21.860	22.670	26.970	[57]
1.871	0.121	0.023	0.420	P2	0.450	0.460	0.510	[64]
2.174	0.073	0.049	3.400	P2	3.610	3.680	4.170	[66]
2.174	0.610	0.000	14.000	P2	12.220	12.680	14.710	[66]
3.514	0.310	0.020	3.100	P2	3.190	3.250	3.670	[57]
3.514	0.320	0.050	15.600	P2	13.740	14.280	16.620	[57]
3.514	0.690	0.260	26.000	P2	21.860	22.670	26.970	[57]
4.390	0.310	0.030	10.000	P2	10.200	10.560	12.210	[67]
5.600	0.084	0.002	0.420	P2	0.450	0.460	0.510	[68]
5.965	0.430	0.013	22.910	P2	24.330	25.230	30.290	[47]
5.965	0.430	0.013	20.270	P2	21.360	22.170	26.330	[47]
7.009	0.017	0.053	1.210	S2	0.816	0.827	0.934	[69]

7.009	0.000	0.040	1.450	S2	0.976	0.990	1.130	[69]
7.009	0.071	0.039	2.280	S2	2.240	2.300	2.640	[69]
7.009	0.139	0.044	3.050	S2	3.090	3.200	3.630	[69]
7.009	0.000	0.054	3.510	S2	4.620	4.640	5.980	[69]
7.625	0.097	0.022	0.420	P2	0.450	0.460	0.510	[68]
7.854	0.226	0.044	1.210	S2	1.230	1.250	1.420	[65]
8.032	0.212	0.025	2.200	S2	2.130	2.160	2.460	[70]
11.646	0.211	0.017	2.200	S2	2.130	2.160	2.460	[70]
11.646	0.203	0.021	1.190	S2	1.160	1.170	1.250	[70]
14.000	0.079	0.006	0.420	P2	0.450	0.460	0.510	[68]
15.000	0.470	0.019	11.000	P2	11.370	11.780	13.650	[71]
15.000	0.430	0.038	19.700	P2	21.120	21.920	26.020	[71]
15.000	0.550	0.053	28.800	P2	33.250	34.430	43.300	[71]
15.000	0.670	0.000	31.600	P2	37.700	39.330	51.820	[71]
15.000	0.750	0.000	32.500	P2	39.400	41.320	56.180	[71]
15.000	1.020	0.000	33.200	P2	40.660	42.870	59.720	[71]
15.000	0.050	0.041	1.830	P2	2.270	2.300	2.550	[71]
19.706	0.282	0.021	2.200	S2	2.130	2.160	2.460	[70]
29.448	0.195	0.005	3.940	S2	4.130	4.210	4.790	[72]
39.583	0.114	0.004	2.200	S2	2.130	2.160	2.460	[70]
49.500	0.075	0.004	0.420	P2	0.450	0.460	0.510	[68]
218.610	0.287	0.004	11.000	P2	10.780	8.470	9.110	[73]
-	0.402	0.000	11.000	P2	10.780	8.470	9.110	[73]
-	0.411	0.000	1.250	P2	1.300	1.330	1.520	[73]

Table C3 Calculated LET_D for human cancer cell lines

$(\alpha/\beta)_x$ (Gy)	α (Gy^{-1})	β (Gy^{-2})	LET_D Original $(keV\mu m^{-1})$	Config.	LET_D Water $(keV\mu m^{-1})$	LET_D Cytoplasm-1 $(keV\mu m^{-1})$	LET_D Cytoplasm-2 $(keV\mu m^{-1})$	References
0.577	0.034	0.098	2.560	S2	2.380	2.460	2.850	[74]
0.695	0.820	0.730	2.200	S2	2.530	2.620	3.080	[75]
0.754	0.215	0.058	2.600	S2	2.380	2.460	2.850	[74]
0.992	0.000	0.114	2.560	S2	2.380	2.460	2.850	[74]
1.460	0.473	0.085	2.020	S2	2.020	2.120	4.380	[62]
1.460	0.245	0.097	1.020	S2	1.050	1.060	1.140	[62]
1.833	0.140	0.064	1.110	P2	1.110	1.130	1.290	[76]
1.833	0.170	0.065	4.020	P2	4.020	4.500	5.160	[76]
1.833	0.220	0.071	7.000	P2	7.000	7.330	8.420	[76]
1.833	0.440	0.045	11.900	P2	11.900	12.610	14.630	[76]
1.833	0.770	0.008	18.000	P2	18.000	19.620	23.120	[76]
1.833	0.900	0.010	22.600	P2	22.600	25.230	30.290	[76]
1.833	0.160	0.056	1.200	S2	1.200	1.250	1.420	[76]
1.833	0.190	0.058	2.600	S2	2.600	2.640	3.040	[76]
1.833	0.220	0.064	4.500	S2	4.500	4.760	5.430	[76]
1.833	0.310	0.056	13.400	S2	13.400	14.240	16.560	[76]
1.833	0.410	0.056	21.700	S2	21.700	22.700	26.970	[76]
1.833	0.500	0.064	25.900	S2	25.900	26.700	32.200	[76]
1.851	0.036	0.010	2.420	S2	2.620	2.670	3.070	[77]
1.851	0.029	0.012	4.040	S2	4.220	4.310	4.900	[77]
1.851	0.027	0.016	6.850	S2	6.980	7.170	8.230	[77]
1.851	0.044	0.009	1.140	S2	1.120	1.121	1.140	[77]
1.851	0.044	0.009	2.740	S2	2.630	2.720	3.120	[77]
1.851	0.044	0.009	5.800	S2	5.430	5.630	6.530	[77]
2.078	0.850	0.037	22.910	P2	24.330	25.230	30.290	[47]
2.078	0.530	0.084	20.270	P2	21.360	22.170	26.330	[47]
2.392	0.054	0.017	3.940	S2	4.130	4.210	4.790	[72]
2.511	0.104	0.042	1.300	S2	1.330	1.350	1.540	[78]
2.511	0.057	0.057	2.300	S2	2.460	2.510	2.890	[78]
2.511	0.048	0.062	2.650	S2	2.940	2.990	3.370	[78]
2.511	0.035	0.072	3.750	S2	3.950	4.030	4.570	[78]
2.511	0.096	0.074	6.000	S2	6.120	6.270	7.180	[78]
2.998	0.385	0.080	2.500	S2	2.570	2.620	2.980	[79]
3.083	0.470	0.000	7.700	P2	7.840	8.070	9.290	[80]
3.763	0.344	0.044	5.100	S2	4.990	5.260	6.230	[39]
3.763	0.385	0.051	7.600	S2	8.010	8.400	10.280	[39]

3.763	0.372	0.063	8.720	S2	10.100	10.630	12.630	[39]
3.763	0.166	0.058	2.660	S2	2.950	3.000	3.380	[39]
3.763	0.286	0.044	4.300	S2	4.470	4.560	5.190	[39]
3.763	0.598	0.017	6.350	S2	6.460	6.630	7.630	[39]
3.763	0.555	0.053	8.220	S2	8.340	8.600	9.900	[39]
3.891	0.158	0.077	13.500	P2	13.930	10.580	16.630	[81]
3.891	0.048	0.088	1.300	P2	1.250	1.270	1.450	[81]
4.000	0.150	0.030	2.200	S2	2.530	2.620	3.080	[75]
4.056	0.168	0.053	1.110	S2	1.028	1.033	1.103	[82]
4.056	0.180	0.051	2.110	S2	1.950	2.010	2.210	[82]
4.056	0.176	0.052	2.540	S2	2.380	2.460	2.860	[82]
4.056	0.155	0.060	3.910	S2	3.610	3.740	4.370	[82]
4.056	0.170	0.057	4.800	S2	4.210	4.250	4.980	[82]
4.455	0.157	0.048	1.200	S2	1.192	1.200	1.290	[83]
4.455	0.164	0.048	2.030	S2	1.640	1.690	2.060	[83]
4.455	0.139	0.056	2.650	S2	2.520	2.620	3.100	[83]
4.455	0.141	0.062	4.250	S2	4.290	4.440	5.240	[83]
4.455	0.237	0.049	0.560	P2	0.590	0.596	0.670	[84]
4.455	0.348	0.047	3.190	P2	3.674	3.760	4.380	[84]
4.455	0.183	0.053	0.560	P2	0.590	0.596	0.670	[84]
4.455	0.294	0.056	3.190	P2	3.674	3.760	4.380	[84]
4.604	0.315	0.038	2.500	S2	2.380	2.460	2.850	[74]
4.999	0.273	0.046	1.140	S2	1.072	1.072	1.145	[85]
4.999	0.291	0.041	2.560	S2	2.430	2.490	2.910	[85]
5.803	0.086	0.033	2.860	S2	2.850	2.960	3.470	[86]
5.803	0.147	0.021	2.860	S2	2.850	2.960	3.470	[86]
6.023	1.010	0.000	22.910	P2	24.330	25.230	30.290	[47]
6.023	0.670	0.037	20.270	P2	21.360	22.170	26.330	[47]
6.333	0.220	0.050	2.760	S2	2.700	2.800	3.100	[87]
6.333	0.280	0.050	3.270	S2	3.170	3.280	3.790	[87]
6.333	0.250	0.050	3.615	S2	3.610	3.740	4.370	[87]
6.333	0.260	0.050	4.070	S2	3.990	4.130	4.840	[87]
6.333	0.420	0.050	4.930	S2	4.590	4.750	5.590	[87]
6.333	0.410	0.050	6.190	S2	5.830	6.060	7.200	[87]
6.333	0.380	0.050	7.900	S2	8.930	9.440	12.440	[87]
6.333	0.440	0.030	9.445	S2	13.170	13.850	16.540	[87]
6.333	0.420	0.030	10.800	S2	16.460	17.310	20.710	[87]
6.343	0.504	0.047	6.230	P1	15.510	16.390	19.210	[59]
6.897	0.253	0.024	2.420	S2	2.620	2.670	3.070	[77]
6.897	0.293	0.020	4.040	S2	4.220	4.310	4.900	[77]
6.897	0.352	0.021	6.850	S2	6.980	7.170	8.230	[77]

6.897	0.213	0.054	1.140	S2	1.120	1.121	1.140	[77]
6.897	0.213	0.054	2.740	S2	2.630	2.720	3.120	[77]
6.897	0.213	0.054	5.800	S2	5.430	5.630	6.530	[77]
7.111	0.188	0.038	0.790	P2	1.980	1.990	2.080	[52]
7.613	0.218	0.039	2.560	S2	2.380	2.460	2.860	[88]
7.647	0.150	0.011	7.700	P2	8.010	8.240	9.490	[89]
7.647	0.230	0.004	19.800	P2	20.780	21.570	25.570	[89]
7.647	0.570	0.000	30.000	P2	32.880	34.040	42.680	[89]
10.893	0.243	0.041	17.100	P1	29.120	30.930	38.290	[90]
11.333	0.110	0.024	1.930	S2	2.020	2.060	2.360	[91]
11.333	0.190	0.026	2.420	S2	2.620	2.670	3.070	[91]
11.333	0.140	0.039	6.710	S2	6.840	7.030	8.070	[91]
11.333	0.150	0.032	8.110	S2	8.230	8.480	9.770	[91]
11.333	0.340	0.150	8.830	S2	8.970	9.260	10.700	[91]
16.493	0.389	0.027	2.500	S2	2.720	2.770	3.190	[79]
17.100	0.030	0.002	6.200	P2	5.320	5.440	6.220	[92]
17.100	0.030	0.002	6.900	P2	5.280	5.400	6.170	[93]
18.387	0.410	0.092	7.700	P2	8.010	8.240	9.490	[89]
18.387	0.870	0.000	19.700	P2	20.780	21.570	25.570	[89]
18.387	0.810	0.000	29.500	P2	32.880	34.040	42.680	[89]
18.444	0.824	0.000	10.000	P2	9.700	10.020	11.580	[94]
18.444	1.260	0.000	25.500	P2	30.510	31.560	38.920	[95]
47.500	0.570	0.012	1.930	S2	2.020	2.060	2.360	[91]
47.500	0.610	0.010	2.420	S2	2.620	2.670	3.070	[91]
47.500	0.700	0.018	6.710	S2	6.840	7.030	8.070	[91]
47.500	0.830	0.001	8.110	S2	8.230	8.480	9.770	[91]
47.500	1.230	0.000	8.830	S2	8.970	9.260	10.700	[91]
51.805	0.053	0.001	9.080	P2	9.250	9.550	1.100	[96]
51.805	0.082	0.000	4.710	S2	4.780	4.900	5.600	[96]
69.500	0.320	0.060	7.700	P2	7.840	8.070	9.290	[80]
-	0.653	0.004	3.710	S2	3.910	3.990	4.530	[51]
-	0.061	0.000	2.600	S2	1.920	1.930	2.100	[97]
-	0.073	0.000	4.700	S2	2.140	2.170	2.390	[97]
-	0.104	0.000	10.100	S2	4.190	4.280	4.860	[97]
-	0.267	0.000	18.800	S2	6.960	7.150	8.210	[97]
-	0.101	0.000	4.700	S2	4.780	4.900	5.600	[98]

Table C4 Calculated LET_D for human fibroblasts and epithelial cell lines

$(\alpha/\beta)_x$ (Gy)	α (Gy^{-1})	β (Gy^{-2})	LET_D Original $(keV\mu m^{-1})$	Config.	LET_D Water $(keV\mu m^{-1})$	LET_D Cytoplasm-1 $(keV\mu m^{-1})$	LET_D Cytoplasm-2 $(keV\mu m^{-1})$	References
2.310	0.694	0.011	10.000	P2	10.200	10.560	12.210	99
4.050	0.520	0.029	0.200	S2	0.000	0.000	0.000	100
6.862	0.500	0.054	2.250	S2	2.250	2.290	2.540	101
6.862	0.493	0.054	2.930	S2	2.930	2.980	3.350	101
6.862	0.561	0.065	7.500	S2	7.500	7.850	9.030	101
8.710	0.750	0.119	1.110	P2	1.110	1.130	1.290	76
8.710	1.020	0.061	4.020	P2	4.020	4.500	5.160	76
8.710	1.290	0.041	7.000	P2	7.000	7.330	8.420	76
8.710	1.700	0.079	11.900	P2	11.900	12.610	14.630	76
8.710	1.870	0.074	18.000	P2	18.000	19.620	23.120	76
8.710	2.430	0.057	22.600	P2	22.600	25.230	30.290	76
8.710	0.660	0.117	1.200	S2	1.200	1.250	1.420	76
8.710	0.890	0.075	2.600	S2	2.600	2.640	3.040	76
8.710	1.150	0.047	4.500	S2	4.500	4.760	5.430	76
8.710	1.360	0.037	13.400	S2	13.400	14.240	16.560	76
8.710	1.610	0.023	21.700	S2	21.700	22.700	26.970	76
8.710	2.010	0.011	25.900	S2	25.900	26.700	32.200	76
10.115	1.000	0.041	2.020	S2	2.020	2.120	4.380	62
10.115	0.401	0.040	1.020	S2	1.050	1.060	1.140	62
11.192	0.620	0.041	2.350	S2	2.250	2.290	2.540	101
11.192	0.686	0.035	2.930	S2	2.930	2.980	3.350	101
11.192	0.772	0.026	7.500	S2	7.500	7.850	9.030	101
12.379	0.814	0.056	7.900	P2	7.240	7.440	8.550	101
13.063	0.630	0.062	7.900	P2	7.240	7.440	8.550	101
16.805	0.855	0.040	7.900	P2	7.240	7.440	8.550	101
19.381	0.861	0.038	2.350	S2	2.250	2.290	2.540	101
19.381	0.894	0.031	2.930	S2	2.930	2.980	3.350	101
19.381	1.096	0.010	7.500	S2	7.500	7.850	9.030	101
27.810	0.364	0.029	1.850	P2	2.260	2.290	2.540	102
-	0.500	0.000	9.100	P2	9.430	9.730	11.240	89
-	0.490	0.000	21.400	P2	22.520	23.350	27.880	89
-	0.930	0.000	33.000	P2	36.680	38.170	49.600	89
-	0.550	0.000	7.700	P2	8.010	8.240	9.490	89
-	0.540	0.000	19.500	P2	20.780	21.570	25.570	89
-	0.520	0.000	29.000	P2	32.880	34.040	42.680	89

-	0.810	0.000	28.500	P2	36.200	37.630	48.620	[103]
-	0.010	0.138	1.850	P2	2.260	2.290	2.540	[104]
-	0.156	0.169	3.900	P2	4.120	4.200	4.770	[104]
-	0.515	0.082	5.500	P2	5.570	5.700	6.520	[104]

Appendix D

Table D1 Percentage Difference at *Position* 1 (Plateau region) between $\mathrm{E}\left(\frac{\epsilon_i^2}{l}\right)$ and $\frac{\mathrm{E}(\epsilon_i^2)}{\mathrm{E}(l_i)}$ given by the second and third term of Equation 4.4, using $\mathrm{E}\left(\frac{\epsilon_i^2}{l}\right)$ as reference.

Energy	**stepMax**	**0.50 *mm***				**0.05 *mm***				**0.01 *mm***			
	setCut	$\mathrm{E}\left(\frac{\epsilon_i^2}{l}\right)$	$\frac{\mathrm{E}(\epsilon_i^2)}{\mathrm{E}(l_i)}$	$-\frac{Cov(\epsilon_i^2,l)}{(\mathrm{E}(l))^2}+\frac{Var(l)\mathrm{E}(\epsilon_i^2)}{(\mathrm{E}(l))^3}$	**% Difference**	$\mathrm{E}\left(\frac{\epsilon_i^2}{l}\right)$	$\frac{\mathrm{E}(\epsilon_i^2)}{\mathrm{E}(l_i)}$	$-\frac{Cov(\epsilon_i^2,l)}{(\mathrm{E}(l))^2}+\frac{Var(l)\mathrm{E}(\epsilon_i^2)}{(\mathrm{E}(l))^3}$	**% Difference**	$\mathrm{E}\left(\frac{\epsilon_i^2}{l}\right)$	$\frac{\mathrm{E}(\epsilon_i^2)}{\mathrm{E}(l_i)}$	$-\frac{Cov(\epsilon_i^2,l)}{(\mathrm{E}(l))^2}+\frac{Var(l)\mathrm{E}(\epsilon_i^2)}{(\mathrm{E}(l))^3}$	**% Difference**
80 MeV	**10 *μm***	0.084	0.171	-0.123	42.423	0.029	0.029	1.09E-04	0.075	0.008	0.007	1.89E-04	2.303
	50 *μm*	0.223	0.309	-0.036	22.152	0.037	0.037	-1.16E-05	0.463	0.010	0.010	2.75E-05	0.389
	100 *μm*	0.274	0.344	-0.022	17.056	0.040	0.040	-1.28E-05	0.253	0.012	0.012	1.31E-05	0.153
150 MeV	**10 *μm***	0.053	0.079	-0.028	3.429	0.014	0.012	5.64E-04	8.118	0.004	0.003	1.45E-04	4.437
	50 *μm*	0.095	0.118	-0.010	13.153	0.015	0.015	1.05E-04	0.877	0.005	0.005	2.57E-05	0.864
	100 *μm*	0.108	0.128	-0.008	11.464	0.016	0.016	6.02E-05	0.443	0.006	0.005	1.44E-05	0.412
200 MeV	**10 *μm***	0.044	0.057	-0.014	2.663	0.011	0.009	5.43E-04	11.077	0.003	0.003	1.19E-04	5.006
	50 *μm*	0.069	0.081	-0.006	8.856	0.011	0.011	1.07E-04	1.463	0.004	0.003	2.18E-05	1.020
	100 *μm*	0.076	0.087	-0.005	8.182	0.012	0.012	6.435E-05	0.755	0.004	0.004	1.299E-05	0.500

List of Publications

1. Hong Qi Tan[1†], Wei Yang Calvin Koh[2†], Lloyd Kuan Rui Tan[1], Jun Hao Phua[1], Khong Wei Ang[1], Sung Yong Park[1], Wen Siang Lew[2], James Cheow Lei Lee[1,2], Dependence of LET on Material and its Impact on Current RBE Model, Physics in Medicine & Biology, 64(13), 135022 Jul 29.

2. Tan HQ, Koh WYC, Yeo ELL, Ang KW, Poon DJJ, Lim CP, Vajandar SK, Chen CB, Ren M, Osipowicz T, Soo KC, Chua MLK, Park SY. Dosimetric uncertainties impact on cell survival curve with low energy proton. Phys Med. 2020 Aug;76:277-284. doi: 10.1016/j.ejmp.2020.07.005. Epub 2020 Jul 29. PMID:32738775

3. Wei Yang Calvin Koh[1], Hong Qi Tan[2], Khong Wei Ang[2], Sung Yong Park[2], Wen Siang Lew[1] and James Cheow Lei Lee[12], Standardizing Monte Carlo Simulation parameters for a reproducible Linear Energy Transfer, The British Journal of Radiology, 93(1112), 20200122

4. Koh, W. Y., Tan, H. Q., Ng, Y. Y., Lin, Y. H., Ang, K. W., Lew, W. S., Lee, J. C., & Park, S. Y. Quantifying systematic RBE-weighted dose uncertainty arising from multiple variable RBE models in organ-at-risk. *Advances in Radiation Oncology*, 100844. https://doi.org/10.1016/j.adro.2021.100844

[†]These authors contributed equally to the work

List of Conference Presentations

1. PTC17-0071: Initial Experience in Calibration of CT for Proton Therapy. Poster presented at 56th Annual Meeting of the Particle Therapy Cooperative Group (PTCOG); 2017 May 8-13; Japan, Yokohama and Chiba.

2. W.Y.C. Koh, H.Q. Tan, W.S. Lew, S.Y. Park, C.L.J. Lee, Stochastic RBE in CNS clinical SOBP- A novel approach, Poster presented at 58th Annual Meeting of the Particle Therapy Cooperative Group (PTCOG); 2019 June 10-15; United Kingdom, Manchester.